On the Relation Between Exciton Dynamics and Nano-Morphology in Organic Semiconductor Blends

Prifysgol Abertawe
Swansea University

Drew B. Riley

Submitted to Swansea University in partial fulfilment of the requirements for the Degree of

Ph.D. in Physics

2023

Abstract

Optoelectronic processes in semiconductor-based devices are widely understood through the constructs of highly-symmetric crystalline inorganic systems, where the lattice periodicity allows significant simplification. Emerging technologies, such as organic semiconductor-based devices, share many qualities with crystalline inorganic semiconductors; however, they diverge in subtle yet important ways. Optical absorption in organic semiconductors gives rise to long-lived and tightly-bound excitons, which migrate in manner often disregarded in the understanding of highly-symmetric crystalline inorganic semiconductors. Further, 'free' charge carriers in organic semiconductors 'hop' between organic molecules in a disordered film rather than the undergo band transport that delocalised carriers in periodic lattices do. This hopping transport leads to lower charge carrier mobilities which have far-reaching ramifications to device operation.

In the work summarised in this thesis the effect that excitonic and charge transport have on device performance of solar cells based on organic photovoltaics will be explored. Experimental techniques are designed and developed to gain insight into the efficiency of exciton transport, the nanostructure of organic-semiconductor blends, and the relation between charge injection and extraction. Utilising these techniques, various state-of-the art systems are examined in detail and various pathways for improving device performance are voiced.

Specifically, a technique to measure the exciton diffusion length in organic semiconductors is developed and shown to have many advantages over established techniques while improving the accuracy of the measurement. This technique is expanded to blends of organic semiconductors to quantify the efficiency of diffusion and quenching occurring between semiconductors in blends. This, along with a developed theoretical understanding, allows for the size of the phase separated domains to be quantified. Relationships between the excitons generated in organic semiconductors, charge carriers created in the blends, and the transport of charges to and extraction at the electrodes is considered in detail. Finally, a technique to distinguish between the nonradiative recombination occurring within an organic semiconductor blend and at the interface between the blend and the larger device structure is introduced. This technique utilises the well-establish reciprocity theory to reconcile the imbalance between charge injection and extraction unique to low-mobility organic semiconductors.

The insights developed here contribute to a comprehensive understanding of device operation in organic optoelectronics. The addition of these techniques to the wide variety available will aid researchers in understanding the fundamental photophysics occurring in organic semiconductors. Which will potentially lead to improvements in device performance as well as aid in the search for novel device architectures based on organic semiconductors.

Declaration

This work has not previously been accepted in substance for any degree and is not being concurrently submitted in candidature for any degree.

Signed: .....[redacted].....(candidate)
Date: .....06/01/2023.....

This thesis is the result of my own investigations, except where otherwise stated. Where correction services have been used, the extent and nature of the correction is clearly marked in a footnote(s). Other sources are acknowledged by footnotes giving explicit references. A bibliography is appended.

Signed: .....[redacted].....(candidate)
Date: .....06/01/2023.....

I hereby give consent for my thesis, if accepted, to be available for photocopying and for inter-library loan, and for the title and summary to be made available to outside organisations.

Signed: .....[redacted].....(candidate)
Date: .....06/01/2023.....

The University's ethical procedures have been followed and, where appropriate, that ethical approval has been granted.

Signed: .....[redacted].....(candidate)
Date: .....06/01/2023.....

Acknowledgement

First and foremost I would like to acknowledge the incredible work of those that have come before me in this field. Crucially, this is not limited the giants of research and industry that have become household names (depending on your household), but each researcher's incremental contribution to the field that I have joined. It is a privilege to add my complementary piece to this intractable puzzle. Amongst those that have contributed much I would predominantly acknowledge my supervisors, Prof. Paul Meredith and Prof. Ardalan Armin. Their work, both in research and establishing the Sêr SAM program, have allowed me to carry out this work in a supportive and au courant environment. I would also like to thank Dr. Oskar J. Sandberg for his leadership and supervision throughout my research. This work would not be possible without these three men.

The Sêr SAM program has facilitated my interaction with some incredible graduate students and Post-docs. I would to thank them all for their support and training in the laboratory, their patience with and ruination of my ignorance, and their continued support through my writing process. Prof. Wei Li and Dr. Yong Ryun Kim for their help with device fabrication, Dr. Stefan Zeiske for his help with all things optoelectronic, and Dr. Nasim Zarrabi for her vast understanding of the field of organic electronics. I would also like to acknowledge all the difficult and hard work done by the non-academic staff in the Sêr SAM program. We would all be lost without Rhian Jones' command of the Dantean circles of the University and Welsh Government. The labs would have lit on fire many times without the constant due diligence of Paul Hughes and his many minions including Dr. Ryan Bingham and Mark Williams. I would like to thank all the other group members in the Sêr SAM program who have provided me with the inspiration and coffee required to complete this task including: Dr. Sahar Basiri-Esfahani, Dr. Bernard Mostert, Dr. Gregory Burwell, Klaudia Rejnhard, Nick Burridge, John Hudson, and Dr. Christina Kaiser. Finally, I would like to thank all the previous academics that I have worked with and been taught by, I would not be here without them, including; Prof. Kimberly C. Hall, Dr. Sam March, Dr. Ajan Ramachandran, Prof. Thomas Duck, Dr. Jordan Kyriakidis, Dr. S. Abaddon, Prof. Jesse Maassen, Prof. Theodore Monchesky, and Prof. Ian Hill.

Beyond the academics that I have encountered on my journey, I would like to thank those that have supported me from the beginning, my family. To my

mother, Susan, you have always supported me in my many rash adventures, and the journey through academics has been no exception. Thank you for your love and care for me all these years. To my sister, Chloe, you have always been a guiding force in my life. Thank you for all you have done in helping me open my eyes and see the world in different lights. Without your example I would not be where I am today. To my grandmother, Dorothy, although you are not here to witness this know that this work is dedicated to you. You guided our family and held us together before and after my arrival. Finally, to Heather, thank you for all your love, support, and guidance throughout the time we have spent together. L'aventure commence!

Author's Contributions

This thesis is based on three publication which contribute to Chapter4, 5, and 7. Chapter 6 is based on an unpublished manuscript to be submitted shortly after this thesis is completed [1–3].

In the work contributing to Chapter 4 the author contributed to the development of the detailed balance model, headed by Dr. Oskar J. Sandberg; wrote the software for and performed the 1-dimensional Monte-Carlo simulations and analysis; and designed and wrote the subsequent manuscript with the aid Dr. Oskar J. Sandberg, Prof. Armin Ardalan, and Prof. Paul Meredith. The work contributing to Chapter 4 was published in *JPCL* under the title *Role of Exciton Diffusion and Lifetime in Organic Solar Cells with a Low Energy Offset* [1].

In the work contributing to Chapter 5 the author wrote the software for and performed the 3-dimensional Monte-Carlo simulations and analysis; designed, built, and carried out the experiments utilising thin film OSCs fabricated with the help of Dr. Wei Li; and designed and wrote the manuscript with the aid of Dr. Oskar J. Sandberg, Prof. Armin Ardalan, and Prof. Paul Meredith. The work contributing to Chapter 5 was published in *Phys.Rev.App.* under the title *Quasi-Steady-State Measurement of Exciton Diffusion Lengths in Organic Semiconductors* [2].

In the work contributing to Chapter 6 the author modified the Monte-Carlo software used in Chapter 5 and performed and analysed the simulations; fabricated both thin film OSCs and OPV-based solar cells with the aid of Dr. Yong Ryun Kim; designed, built, and carried out the optical experiments; carried out the resistance dependent photovoltage experiments with the aid of Dr. Nasim Zarrabi; and designed and wrote the manuscript with the aid of Dr. Oskar J. Sandberg, Prof. Armin Ardalan, and Prof. Paul Meredith (work yet to be published).

In the work contributing to Chapter 7 the author implemented the drift-diffusion software, and preformed and analysed the simulations; designed, built, and carried out the experiments utilising OPV-based solar cells fabricated by Dr. Wei Li, carried out the $\mathrm{EQE_{PV}}$ measurements with the aid of Dr. Stefan Zeiske; and designed and wrote the manuscript with the aid of Dr. Oskar J. Sandberg, Prof. Armin Ardalan, and Prof. Paul Meredith. The work contributing to

Chapter 7 was published in *Phys.Rev.App.* under the title *Direct Quantification of Quasi-Fermi-Level Splitting in Organic Semiconductor Devices* [3].

Dedication

For Dorothy

Contents

1 Introduction **1**
1.1 Structure and Scope of Thesis 4

2 Fundamentals of Semicondcutors **7**
2.1 Inorganic Semiconductors 7
2.2 Thermodynamics of Semiconductors 11
2.2.1 Generalized Plank Radiation 11
2.2.2 Electronic Transitions and Photon Currents 11
2.2.3 Radiative Relaxation and Photoluminescence 13
2.2.4 Non-Radiative Relaxation 14
2.3 Thermodynamics of Solar Cells 15
2.3.1 Thermodynamic Limit of Power Conversion Efficiency . . . 16
2.3.2 Non-Radiative Photovoltage Losses 19
2.3.3 Optoelectronic Reciprocity and Electroluminescence 19

3 Optoelectronics of Organic Semiconductors **21**
3.1 Organic Semiconductors 21
3.1.1 Förster Resonance Energy Transfer 23
3.1.2 Exciton Transport in Organic Semiconductors 26
3.2 Organic Photovoltaic Devices 27
3.2.1 The Bulk-Heterojunction 27
3.2.2 FRET in OSC Bulk-Heterojunctions 29
3.2.3 Separated Charge-Carrier Dynamics 29
3.2.4 Charge Extraction 33
3.3 Thermodynamic Limits of OPV-Based Solar Cells 35
3.4 Reciprocity in Organic Photovoltaic Devices 38

4 Role of Exciton Diffusion and Lifetime in Low Energy Offset Systems **40**
4.1 Diffusion and Charge Transfer State Generation in Low-Offset Systems 41
4.2 Theoretical Treatment of Steady-State Diffusion 42
4.3 Considerations for CT-state Generation 45
4.4 Influence of Exciton Lifetime and Diffusion on Charge Generation Yield 48
4.5 Conclusion 50

5 Quasi-Steady-State Measurement of Exciton Diffusion Lengths 52
5.1 Measuring Exciton Diffusion Lengths 53
5.2 Exciton-Exciton Annihilation 54
5.3 Monte-Carlo Modelling of Photoluminescence Experiments 55
5.4 Experimental Validation of Pulsed-PLQY 59
5.5 Conclusion 65

6 Relationship Between Charge Carrier Dynamics and Exciton Dynamics 67
6.1 Pulsed-PLQY in Bulk-Heterojunction Films 69
6.2 Validation of Domain Size Measurement 70
6.3 Donor and Acceptor Domains in High Efficiency Systems 73
6.3.1 Acceptor Phase 75
6.3.2 Donor Phase 75
6.4 Discussion of Domain Size in BHJ Thin Films 77
6.5 Domain Size and Langevin Recombination 77
6.6 Conclusion 79

7 Direct Quantification of Quasi-Fermi Level Splitting in Organic Semiconductor Devices 81
7.1 Radiative and Non-Radiative Losses to the Open-Circuit Voltage . 82
7.2 Deviations from Reciprocity 83
7.3 Experimental Approaches to Measuring Open-Circuit Voltage Losses 87
7.4 Drift Diffusion Simulations of EL-QY and EM-PLQY 89
7.5 Device Structures with Increasing Non-Radiative Losses 91
7.6 Experimental Calculation of QFLS 92
7.7 Conclusions 95

8 Conclusion 96

9 Outlook 98

Appendices 100

Appendix A Role of Exciton Diffusion and Lifetime in Low Energy Offset Systems 101
A.1 1D-Monte-Carlo Simulations 101
A.2 Charge Generation Yield Calculations 101

Appendix B Quasi-Steady-State Measurement of Exciton Diffusion Lengths 104
B.1 Materials 104

B.1.1 Chemical Definitions . . . 104
B.1.2 Film Fabrication . . . 105
B.2 Time Resolved Photoluminescence . . . 106
B.3 Spotsize Measurement . . . 106
B.4 Error Analysis . . . 107
B.5 Pulsed-PLQY Measurements . . . 108
B.6 Monte-Carlo Simulation Parameters . . . 114

Appendix C Relationship Between Charge Carrier Dynamics and Exciton Dynamics 115
C.1 Materials . . . 115
C.1.1 Chemical Definitions . . . 115
C.2 Materials Fabrication . . . 116
C.2.1 Thin Film Fabrication . . . 116
C.2.2 Bi-layer Film Fabrication . . . 117
C.2.3 Device Fabrication . . . 117
C.3 Experimental Techniques . . . 121
C.3.1 Domain Size Measurements . . . 121
C.3.2 Current-Voltage Characteristics . . . 123
C.3.3 Absolute Photoluminescence Quantum Yield . . . 123
C.3.4 Thickness Measurements . . . 124
C.3.5 Index of Refraction Measurements . . . 124
C.4 Verifying Domain Size Measurements . . . 124
C.4.1 Monte-Carlo Simulations . . . 124
C.4.2 Bi-Layer Measurements . . . 127
C.5 Experimental Data . . . 129
C.5.1 J-V Charactersitics . . . 129
C.5.2 Quasi-Steady-State Photoluminescence . . . 130
C.5.3 Absolute-PLQY . . . 131
C.5.4 Pulsed-PLQY Data . . . 132
C.5.5 Förester Resonant Energy Transfer Rate and Radii . . . 133
C.5.6 Resistance-Dependent Photovoltage Measurements . . . 135
C.6 Calculating Encounter Rates . . . 136
C.7 Error Analysis . . . 137
C.7.1 Diffusion Length . . . 137
C.7.2 Exciton Quenching Efficiency . . . 137
C.7.3 Domain Size . . . 137

Appendix D Direct Quantification of Quasi-Fermi Level Splitting in Organic Semiconductor Devices 140
D.1 Simulations . . . 140

D.2 Calibration of Apparatus . . . 143
D.2.1 In Situ Calibration . . . 143
D.2.2 Perturbation Strength . . . 144
D.2.3 Modulation Frequency . . . 144
D.3 Devices . . . 145
D.3.1 Measuring V_{OC}^{rad} . . . 145
D.3.2 Device Architectures . . . 145
D.4 Materials . . . 147
D.5 Error Analysis . . . 148

Appendix E Transfer Matrix Modelling **149**
E.1 Incoherent Glass Layer . . . 150
E.2 Coherent Stack . . . 150
E.3 Simulation . . . 152

Appendix F Monte-Carlo Modelling **153**
F.1 Initialising the Lattice . . . 153
F.2 Populating the Lattice . . . 154
F.3 Evolving in Time . . . 154
F.3.1 Gillipse Algorithm . . . 155
F.3.2 Extraction and Reinjection . . . 155
F.4 Scaling of Algorithm . . . 156
F.5 Physical Parameters . . . 156

Appendix G Drift-Diffusion Modelling **159**
G.1 Discretizing and Solving the Poisson equation . . . 160
G.2 Discretizing and Solving the Continuity Equations . . . 162
G.3 Boundary Conditions . . . 164
G.4 Calculating Physical Quantities . . . 165

List of Figures

1.1 Architecture, Equivalent Circuit, and Current-Voltage Characteristics of Solar Cells 4

2.1 Origins of Conduction and Valence Bands 8
2.2 Thermodynamic Processes Occurring in Semiconductors. 12
2.3 Solar Spectrum and Thermodynamic Limits of Solar Cells 16

3.1 Electronic Structure of Benzene 22
3.2 Förster Resonance Energy Transfer Coupling and Probability . . . 24
3.3 Architecture of Organic Photovoltaic Devices 28
3.4 Energetics of Semiconductor-Metal Interfaces 33
3.5 Entropic Limit of Excitonic Solar Cells 35
3.6 Energetics and Kinetic Rate Constants in OPV Devices 36
3.7 Detailed Balance Limit of OPV-Based Solar Cells 37
3.8 Mobility Dependence of Deviation from Reciprocity 39

4.1 Energetics and Kinetic Rate Constants in Exciton Diffusion . . . 43
4.2 Effective Charge-Transfer Rate and Dissociation Efficiency 46
4.3 Surface Plots of Exciton Dissociation Rate Constant and Dissociation Efficiency 47
4.4 Charge generation yield as a Function of Exciton-to-CT State Energetic Offsets 49

5.1 Monte-Carlo Simulations of Time-Resolved Photoluminescence . . 56
5.2 Monte-Carlo Simulation of Pulsed-PLQY 57
5.3 Time-Resolved Photoluminescence and Pulsed-PLQY Apparatuses 60
5.4 Time-Resolved and Spectral Photoluminescence of P3HT 62
5.5 Pulsed-PLQY and Diffusion Length in P3HT 63

6.1 Domain Structure in FRET Activated Bulk-Heterojunction 68
6.2 Validation of Domain Size Measurements 71
6.3 Device Characteristics and Pulsed-PLQY in BQR:$PC_{71}BM$ film . 72
6.4 Pulsed-PLQY on PM6:Y6 74
6.5 FRET Calculations for PM6:Y6 Bulk-Heterojunction 76
6.6 Domain Size Dependency of Encounter Reduction Factor 78

7.1 Mobility Dependence of Deviation from Reciprocity 84

7.2 Generation Dependence of Deviation from Reciprocity 85
7.3 Injection Barrier Dependence of Deviation from Reciprocity . . . 86
7.4 Electroluminescence and Electro-modulated Photoluminescence Apparatuses and Band Structures 87
7.5 Simulated Injection Barrier dependence of Quasi-Fermi Level Splitting 90
7.6 Current-Voltage Characteristics of Devices with Increasing Injection Barrier 92
7.7 Device Structure and External Quantum Efficiency of PM6:Y6-based Devices 93
7.8 Quasi-Fermi Level Splitting for Devices with Increasing Injection Barrier 94

B.1 Spot Size Measurement 107
B.2 Pulsed-PLQY on PM6 109
B.3 Pulsed-PLQY on P3HT-Regiorandom 110
B.4 Pulsed-PLQY on PTB7-Th 110
B.5 Pulsed-PLQY on PCDTBT 111
B.6 Pulsed-PLQY on $PC_{60}BM$ 111
B.7 Pulsed-PLQY on P3HT-Regioregular 112
B.8 Pulsed-PLQY on ITIC 112
B.9 Pulsed-PLQY on IT4F 113
B.10 Pulsed-PLQY on Y6 113
B.11 Pulsed-PLQY on PTB-eC9 114

C.1 BHJ Pulsed-PLQY Experimental Apparatus 124
C.2 Monte-Carlo Simulations of Domain Size Experiments 126
C.3 Validation of Pulsed-PLQY on Bi-Layer Films 128
C.4 Current Density-Voltage Characteristics 129
C.5 Photoluminescence of BHJ Films 130
C.6 Absolute PLQY Measurements 131
C.7 Damage Assessment of Pulsed-PLQY in Donor Phases 132
C.8 Pulsed-PLQY Data on BHJ Films 133
C.9 FRET analysis of PM6:Y6, PM6:BTP-eC9, and Ptb7-Th:Y6 . . . 135
C.10 Mobility Measurements 136
C.11 Error Analysis of Pulsed-PLQY 138

D.1 Simualted Device Response Under Electro-modulated Photoluminescence 141
D.2 Simulated Current-Voltage Characteristics and Quasi-Fermi Level Splitting 142

D.3 Calibration of Electro-Modulated Photoluminescence Apparatus . 143
D.4 Electro-Modulation Photoluminescence Signal as a Function of Perturbation Strength 144
D.5 Electro-Modulation Photoluminescence Signal as a Function of Modulation Frequency 145
D.6 Photovoltaic External Quantum Efficiency and Radiative Open-Circuit Voltage 146

E.1 Transfer Matrix Model Schematic 149
E.2 Transfer Matrix Model Flow Chart 152

F.1 Flow Chart for Monte-Carlo Algorithm 158

G.1 Drift-Diffusion Flow Chart 164
G.2 Energy Levels of Drift-Diffusion Simulations 166

List of Tables

5.1 Material Parameters Extracted from Pulsed-PLQY 66

6.1 Exciton L_D and Domain Size Measured with Pulsed-PLQY 80

B.1 Deposition Parameters for Organic Semiconductors 106
B.2 Monte-Carlo Simulation Parameters 114

C.1 BHJ Film Deposition Parameters 118
C.2 Bi-layer Film Deposition Parameters 119

D.1 Drift Diffusion Simulation Parameters used in Figure 7.4 140
D.2 Drift Diffusion Simulation Parameters used in Figure 7.5 142
D.3 Device Properties for Increasing Injection Barrier 146

Acronyms

BHJ Bulk-heterojunction 5

β Total bimolecular recombination rate 31

CS Separated charge carrier 5

CT Charge transfer 27

CGY Charge generation yield 5

$q\delta V_{\mathbf{OC}}$ Deviation from reciprocity 84

d Active-layer thickness 84

$d_{\mathbf{100}}$ Lamellar spacing 53

D Exciton diffusion constant (Diffusion constant) 5

$D_{\mathbf{n/p}}$ Separated charge carrier diffusion constant 31

DOS Density of states 8

D_C Effective density of states of conduction band 9

D_V Effective density of states of valence band 9

E_G Bandgap 7

$\eta_{\mathbf{EMPL}}$ Electro-modulated photoluminescence quantum efficiency (EM-PLQY) 6

$\mathbf{EQE_{PV}}$ Photovoltaic external quantum efficiency viii

$\eta_{\mathbf{LED}}$ LED quantum efficiency 19

$\eta_{\mathbf{EL}}$ Electroluminescence quantum efficiency 91

$\eta_{\mathbf{PL}}$ Photoluminescence quantum efficiency 53

$\eta_{\mathbf{diff}}$ Diffusion efficiency 44

$\eta_{\mathbf{CT}}$ Charge transfer efficiency 42

EEA Exciton-exciton annihilation 53

E_γ Photon energy . . . 11

FF Fill-factor . . . 2

FRET Förster Resonance Energy Transfer . . . 23

γ Exciton-exciton annihilation coefficient . . . 53

HOMO Highest occupied molecular orbital . . . 22

IP Ionization potential . . . 27

$J_0^{\mathbf{Rad}}$ Radiative dark-saturation current . . . 17

$J_{\mathbf{SC}}$ Short-circuit current . . . 2

$k_{\mathbf{CT,eff}}$ Effective charge transfer rate constant . . . 42

$k_{\mathbf{eff}}$ Effective charge or energy transfer rate constant . . . 69

$k_{\mathbf{CT,0}}$ Interfacial charge transfer rate constant . . . 42

k_L Langevin recombination rate constant . . . 30

L Phase separated domain size (Domain size) . . . 5

LUMO Lowest unoccupied molecular orbital . . . 22

n Index of refraction . . . 26

NFA Non-fullerene acceptor . . . 3

L_D Exciton diffusion length (Diffusion length) . . . 5

OPV Organic photovoltaic device . . . viii

OSC Organic semiconductor . . . viii

PCE Power Conversion Efficiency . . . 2

$P_{\mathbf{CGY}}$ Charge generation yield calculated from detailed balance . . . 48

P_S Exciton dissociation efficiency (Dissociation efficiency) . . . 42

pulsed-PLQY Pulsed-photoluminescence quantum yield . . . 5

ρ Exciton density . . . 54

ρ_0 Initial exciton density . . . 55

QFLS Quasi-Fermi level splitting (E_{QFLS}) 10

QFLS$_{\mathbf{bulk}}$ Quasi-Fermi level splitting in the bulk of the active layer ($E_{\mathrm{QFLS,bulk}}$) 83

E_{F_n} Electron quasi-Fermi level 9

E_{F_p} Hole quasi-Fermi level 9

R_0 Intermolecular spacing 24

$R_{\mathbf{FRET}}$ FRET Radii 25

σ_d Static disorder 23

τ Exciton lifetime (Lifetime) 27

τ_0 Molecular lifetime 25

T_S Temperature of the sun 15

T_C Temperature of the cell 15

TRPL Time-resolved photoluminescence 52

μ Chemical potential 9

μ_γ Chemical potential of radiation 11

$\mu_{\mathbf{CT}}$ Chemical potential of charge-transfer states 28

$\mu_{\mathbf{CS}}$ Chemical potential of separated charge carrier states 35

$\mu_{\mathbf{e}}$ Chemical potential of electron 12

μ_h Chemical potential of holes 12

$\mu_{\mathbf{n}}$ Electron mobility 9

$\mu_{\mathbf{p}}$ Hole mobility 9

μ_x Chemical potential of excitons 35

$V_{\mathbf{OC}}$ Open-circuit voltage 2

$V_{\mathbf{OC}}^{\mathbf{Rad}}$ Radiative limit to the open-circuit voltage 18

$\Delta V_{\mathbf{OC}}^{\mathbf{NR}}$ Non-radiative losses to the open-circuit voltage 19

$\Delta V_{\mathbf{OC}}^{\mathbf{NR,Electrode}}$ Electrode-induced non-radiative losses to the open-circuit voltage . . . 85

$\Delta V_{\mathbf{OC}}^{\mathbf{NR,Intrinsic}}$ Intrinsic non-radiative losses to the open-circuit voltage . . 85

$\Phi_{\mathbf{AM1.5}}$ AM1.5 standard spectrum . . . 18

$\Phi_{\mathbf{bb}}$ Black-body radiation . . . 11

$\Phi_{\mathbf{em}}$ Emitted photon flux . . . 14

α Absorption coefficient . . . 12

$\gamma_{\mathbf{CT}}$ CT-state Langevin reduction factor . . . 31

$\gamma_{\mathbf{enc}}$ Encounter Langevin reduction factor . . . 31

Chapter 1

Introduction

It is difficult to overstate the impact technological revolutions have on society, the last hundred years is no exception and has been characterised by the semiconductor revolution. The lineage of semiconductor physics can be traced all the way back to the coining of the phrase 'semicoibente' (semi-insulating) or semiconducting by Alessandro Volta in 1782 [4]. Continuing into the 19^{th} century, the work of Seebeck (1821) [5] and Faraday (1833) [6] eventually culminated in the discovery of the rectification effect by Karl Ferdinand Braun in 1874. Braun's discovery lead to the harnessing of radio waves and the first Nobel Prize rewarding work in solid-state physics [7]. Continued into the 20^{th} century, the dual inventions of the point-contact (1947) and junction (1948) transistors by John Bardeen, Walter Brattain, and William Shockley (shared Nobel Prize 1956) launched the solid-state transistor era [8, 9].

Logic, being the easiest and most well understood application of transistors, developed the computer industry into a multi-billion dollar industry with the introduction of integrated circuit, first designed by Jack Kilby (Nobel Prize in Physics 2000) at Texas Instruments [10], and the silicon monolithic integrated circuit, developed by Robert Noyce (founder of Intel).

A contemporary to William Shockley at Bell Laboratories, John Shive demonstrated that current could be passed through the bulk of a point-contact transistor, confirming the viability of William Shockley's junction transistor. Utilising a light source as the emitter in this new point-contact transistor modality, John Shive demonstrated the first phototransistor (first announced by Bell Laboratories in 1950) [11]. First used as 'electronic eyes' in Bell's switching systems, phototransistors, later renamed photodiodes, now have many applications from fire detectors to astrophysics [12].

Congruently, in the late 19^{th} century, Charles Fritts was working towards a light harvesting selenium solar cell [13]. In 1939 Russell Ohl inadvertently discovered the p-n junction and filed the first patent for a p-n based solar cell [14]. Further work understanding the effect dopants, impurities, and contacts have on solar cells at Bell Laboratories led to additional interest in the p-n junction and eventually inspired the work of William Shockley. William Shockley's seminal work at Bell Laboratories laid the ground work for our modern understanding

of p-n type semiconductors, which drives our modern understanding of the operation of all semiconductor based devices including transistors, photodetectors, and solar cells. Although the work described in this thesis concerns fundamental optoelectronic processes occurring in semiconductors, often agnostic of device application, it is motivated by recent surges in demand for and deliverance of novel photovoltaic light harvesting materials. Hence, in order to guide the reader towards the relevant applications motivating the remainder of the thesis, the next section will establish the basic operating principles of a solar cell.

Solar Cells

Today, the rise in solar power consumption around the world has driven research into ever improving solar harvesting ability. Characterised by the maximal power that a solar cell can provide to a load, the Power Conversion Efficiency (PCE) can be expressed through the open-circuit voltage (V_{OC}) and short-circuit current (J_{SC}) reduced by the so-called fill-factor (FF < 1) as

$$\mathrm{PCE} = \frac{J_{\mathrm{SC}} V_{\mathrm{OC}} \mathrm{FF}}{P_{\mathrm{Sun}}}, \tag{1.1}$$

where P_{Sun} is the power delivered by the sun to the solar cell, typically described by the AM1.5 spectrum for solar panels on the Earth's surface (shown in Figure 2.3a). The most common architecture for a solar cell is an active layer sandwiched between two electrodes, as shown in Figure 1.1a. However, various alternative architectures have been developed such as the interdigitated back contacts [15]; additionally, much development has gone into the design and deposition of both the active layer and the electrical contacts [16, 17]. In all designs the active layer serves a two-fold purpose, to create pairs of positive and negative charges, known as electron-hole pairs, and transport these charges to opposite electrodes to be extracted as current. The voltage and current that a solar cell can produce will depend on the optoelectronic properties of the active layer as well as the overall architecture of the cell, including additional interlayers between the active layer and metal electrodes. The current delivered by a solar cell can be described by the Shockley diode equation

$$J(V) = J_0 \left\{ \exp\left[\frac{q\left(V - JR_{\mathrm{S}}\right)}{m_i k_B T} \right] - 1 \right\} + \frac{V - JR_{\mathrm{S}}}{R_{\mathrm{Sh}}} - J_{\mathrm{Ph}}. \tag{1.2}$$

In which J_0 is the current associated with unwanted, but inevitable, charge carrier recombination, known as the dark saturation current, J_{Ph} is the photocurrent generated when the cell is exposed to the AM1.5 spectrum, R_{S} is the series resistance of the load circuit including the solar cell contacts, R_{Sh} is the resistance associated with leakage currents caused by defects within the device, m_i is the

ideality factor describing how closely a cell performs to the ideal Shockley type cell ($m_i = 1 \rightarrow$ Shockley type), k_B is the Boltzmann constant, q is the elementary charge, and T is the temperature. Figure 1.1c shows the equivalent circuit diagram for a solar cell in which J_{Ph} is a steady current source and $J_d(V)$ is a diode with ideality factor m_i.

Equation 1.2 is plotted as a function of applied voltage in Figure 1.1b. The black curve represents the current density output of a cell, while the red dashed line represents the power output of a cell, positive numbers representing power delivered to the load. The FF is defined as the ratio of the maximum output power (MPP = $V_{\mathrm{MPP}} \times J_{\mathrm{MPP}}$) to the product of the V_{OC} and J_{SC}, or the ratio of the area of yellow to blue rectangles, ultimately determined by the various material and device properties.

The most common p-n type solar cells on the market today use silicon as the active layer due to silicon's earth abundance, well understood electronic properties, and well established and widespread fabrication and supply chains [18]. The record efficiency for a crystalline silicon solar cell is 26.7%, however; most commercial modules use multicrystalline silicon with a maximum laboratory efficiency of 21.9% [15, 19]. Other inorganic active layers have been utilised such as gallium arsenide (28.8%), indium phosphate (24.2%), and cadmium telluride (21.0%) [20–23].

Although these materials show high PCEs with remarkable stability they require energy intensive fabrication and heavy mounting brackets, often are composed of rare earth elements, a few show (relatively) weak absorption of sunlight, and their crystalline nature makes them brittle. Future applications including solar windows, light weight and flexible solar cells, semi-transparent solar cells, and indoor solar cells require materials that are light weight and flexible, with tunable and strong spectral absorption, and utilise earth abundant materials with low cost and scalable fabrication techniques [17, 24–26].

One promising candidate to fulfil this emerging market are known as organic photovoltaics (OPVs) made of blends of organic semiconductors (OSC). OSCs are comprised of organic molecules which absorb and emit photons (as all organic molecules do) as well as conduct electricity in a similar manner to the inorganic semiconductors listed above. Although OPVs can be utilised in many different applications such as light-emitting diodes [27], photo-detectors [28], and lasers [29], the discussion in this thesis will focus on OPV-based solar cells, which have shown promising development in recent years [17]. The majority of OPV-based solar cell development has historically been based on blends of a polymer with C60 derivative, known as fullerene OPVs, which has reached PCEs as high as 12% [17, 30]. In parallel, research into alternative blends was ongoing, and, in 2017, the emergence of high-efficiency non-fullerene acceptor (NFA) based blends quickly propelled PCEs of OPVs-based solar cells from 13% to the current state,

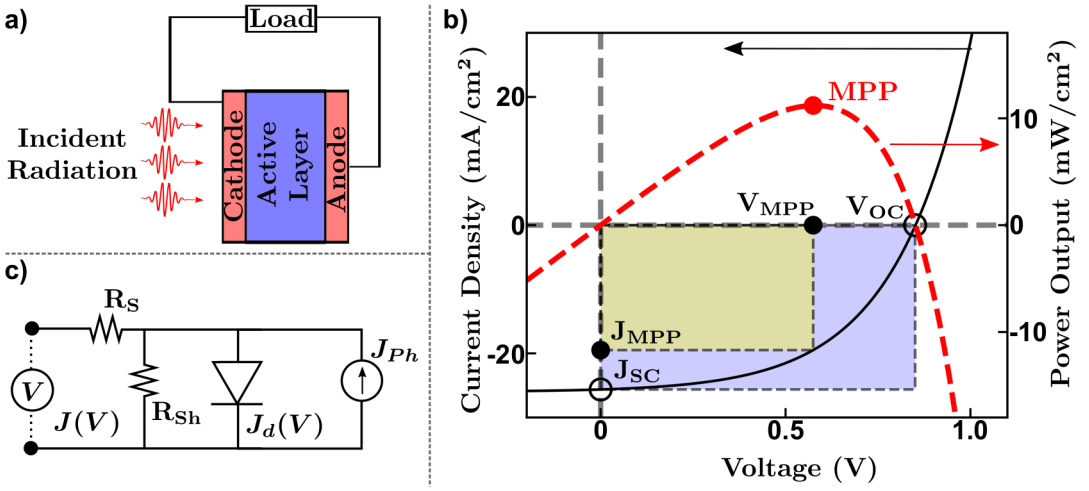

Figure 1.1: (a) Basic architecture of a solar cell. (b) Equation 1.2 (black line) and output power (red dashed line), indicated is the power delivered by the cell (yellow shading) defined by the maximum power point voltage (V_{MPP}) and current density (J_{MPP}) as well as the maximum possible output power (blue shading) defined by the V_{OC} and J_{SC}. (c) Equivalent circuit diagram of a solar cell connected to a load of series resistance R_S delivering current $J(V)$. R_{Sh}-shunt resistance of cell. J_{Ph}-Photocurrent generated by the cell. $J_d(V)$-voltage dependent dark current of the cell.

where many polymer-NFA blends consistently achieve PCEs above 18% with 20-25% predicted [31–38].

In this thesis fundamental processes that underlie the power conversion process in solar cells will be examined utilising the (historic) crystalline inorganic understanding before comparing with OPV-based solar cells. However, the processes examined have wide-ranging implications in other OPV-based applications and the experimental techniques introduced and discussed will be relevant to researchers pursuing alternative applications of OPVs.

1.1 Structure and Scope of Thesis

In Chapter 2 fundamental processes occurring in crystalline inorganic semiconductors are discussed in detail. Section 2.1 discusses how conductivity arises in solids and offers an overview of basic semiconductor processes. Section 2.2 introduces various thermodynamic processes that occur in semiconductors. Finally, Section 2.3 focuses on the thermodynamic processes limiting PCEs in semiconductor-based solar cells.

In Chapter 3 the reader's focus is brought to OSCs. Section 3.1 introduces the structure and transport properties of OSCs. Section 3.2 describes how OSCs can be used to create OPV devices and contrasts the thermodynamic processes occurring in OPV devices with those introduced in Section 2.2. Finally Section 3.3 compares the thermodynamic limit of OPV-based solar cells to that described in Section 2.3.

Two key fundamental differences that will be developed between inorganic semiconductors and OSCs are the excitonic nature of the charge generation process, developed in Section 3.1.2 and 3.2.1, and the low mobility nature of the separated charge carriers, as outlined in Section 3.2.3 and 3.2.4. These differences culminate in the independent thermodynamic limits for inorganic solar cells, expressed in Section 2.3, and OPV-based solar cells, outlined in Section 3.3. In the remaining chapters of this thesis, simulation and experimental investigation of these two unique processes occurring in OSCs will be discussed.

In Chapter 4 the role that exciton diffusion and dissociation plays in the charge generation process of OPV devices will be explored with a focus on modern low-offset NFA-based solar cells. Expressions for the exciton dissociation efficiency and effective dissociation rate will be derived depending on the size of the phase separated domains and the exciton diffusion length. The effect diffusion has on charge generation yield will be examined for both low-and high-offset systems, contrasting the two.

In Chapter 5 various experimental methods used to measure exciton diffusion length and exciton diffusion constant in OSCs will be discussed. The limitations of these techniques will be explored through the use of Monte-Carlo simulations. An alternative method, called pulsed-photoluminescence quantum yield, will be introduced through the same Monte-Carlo simulations and validated on a well studied OSC. It will be shown that pulsed-photoluminescence quantum yield is faster, easier, requires less equipment specialisation, and is less prone to experimental errors than well established techniques.

In Chapter 6 the use of pulsed-photoluminescence quantum yield will be expanded to OSC-based bulk-heterojunctions (BHJs). It will be shown that pulsed-photoluminescence quantum yield is a powerful tool in determining the phase separated domain size of OSC-based BHJs. This experimental technique will be validated by measuring the phase separated domain size of bi-layer systems with known thickness. After which, the phase separated domain size will be measured on a variety of technologically relevant bulk-heterojunction films. Beyond establishing this new methodology, the link between the phase separated domain size and the recombination of separated charge carriers will be discussed.

Finally, in Chapter 7 the extraction of separated charge carriers will be considered and the conditions under which reciprocity can be broken will be analysed. The relationship between electroluminescence, photoluminescence, and

non-radiative photovoltage losses will be illustrated and examined in detail through the use of drift diffusion simulations. The result of this analysis will be the introduction of an experimental technique called electro-modulated photoluminescence quantum efficiency, which, when coupled with traditional measurement techniques, will allow for a full description of non-radiative photovoltage losses. Additional information about simulations and experimental procedures are included in the Appendices.

Chapter 2

Fundamentals of Semicondcutors

2.1 Inorganic Semiconductors

Covalent bonds are formed due to quantum mechanical forces between nearby atoms creating an energy well with energetic minima at a interatomic spacing $a \sim 1$ Å [39]. When several electrons are available for bonding directional bonds are created resulting in a periodic, ordered solid. The arrangement of atoms in a solid is known as a lattice, where the interatomic spacing is referred to as the lattice constant. The highly symmetric nature of a lattice can be exploited to gain insight into its electronic and vibrational properties. In momentum ($\vec{k}$) space the periodicity of the lattice creates a space of unique electronic and vibrational solutions known as the first Brillouin zone (BZ), with BZ boundaries at $\left|\vec{k}\right| = \pi/a$. Further, the periodicity of the lattice leads to a delta function potential of height V_G in momentum space. The Schrödinger equation for an electron wavefunction (Ψ_k) with mass m_e in momentum space is

$$\left[\frac{\hat{p}^2}{2m_e} + U\left(\vec{k}\right)\right]\Psi_k\left(\vec{k}\right) = E_k\left(\vec{k}\right)\Psi_k\left(\vec{k}\right), \tag{2.1}$$

where $\hat{p}$ is the momentum operator. Equation 2.1 has energy eigenstates $E_k = \hbar^2 k^2/2m_e$, where $\hbar$ is the reduced Plank's constant, for a free-electron $\left(U\left(\vec{k}\right) = 0\right)$. A weak periodic potential (a delta function $U\left(\vec{k} = \pi/a\right) = V_G$) leads to eigenstates in the vicinity of the BZ boundary varying away from the free electron case [40]. Figure 2.1a shows the free-electron energy and the so called nearly-free electron energy over the first and second BZ. Under a periodic potential, electrons with momentum k are equivalent to those of $k \pm 2z\pi/a$ for any integer z. To account for this, all BZ are typically 'folded' into the first BZ, known as the 'reduced' zone scheme, as shown in Figure 2.1b. Under the periodic potential, an energetic gap of $2V_G$ forms at the BZ boundary creating a 'band' of forbidden energetic states, where the size of this energetic gap is known as the bandgap (E_G). Electronic states above (below) the bandgap are known as conduction (valence) band states [39–41]. Under circumstances where an electron is promoted from the valence band to the conduction band an overall positive charge is left behind

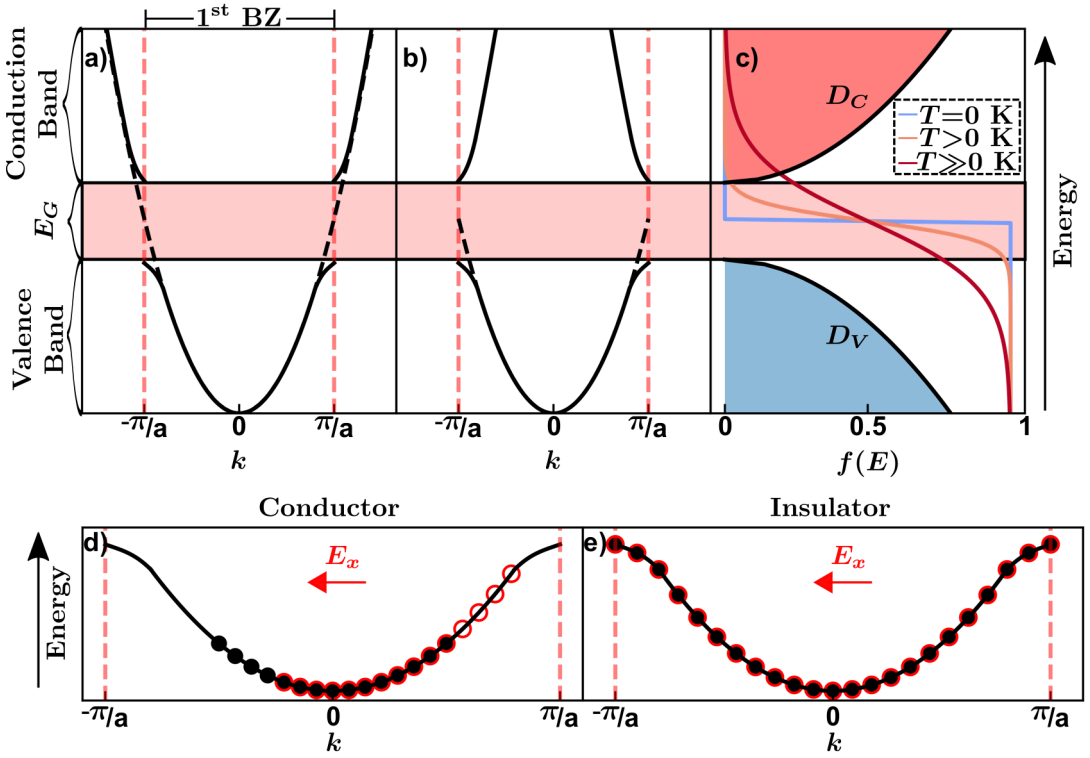

Figure 2.1: Conduction and valence bands determined by the nearly free electron model in the (a) extended and (b) reduced zone schemes. Dashed line-free electron energies, solid line-nearly-free electron model. (c) Density of states in the conduction (D_C) and valence bands (D_V) and Fermi-Dirac distribution for various temperatures.(d-e) Energetics of highest lying electrons in equilibrium (black circles) and under an external electric field (E_x) (open red circles) for (d) a conductor and (e) an insulator.

in the valence band, known as a hole (as it is in fact the absence of an electron from an atomic orbital).

Although it is common (and useful) to consider bands to be continuous, the finite nature of the lattice means that each band is made up of unique energy states which, according to the Aufbau principle, will be filled from lowest to highest energy. The number of conduction (valence) states per unit energy and volume is known as the density of states (DOS). In a 3D semiconductor the DOS

for electrons (holes) in the conduction (valence) band, D_C (D_V), can be written

$$D_C(E) = \frac{(2m_e^*)^{3/2}}{2\pi^2\hbar^3}\sqrt{E - E_C}, \tag{2.2}$$

$$D_V(E) = \frac{(2m_p^*)^{3/2}}{2\pi^2\hbar^3}\sqrt{E_V - E}, \tag{2.3}$$

where E_C (E_V) is the lowest (highest) conduction (valence) state known as the conduction (valence) band edge, m_e^* (m_p^*) is the effective mass of an electron (hole) in the conduction (valence) band, defined from the curvature of the respective band as $m_{e/h}^* = \hbar^2 \left(\partial^2 E/\partial k^2\right)^{-1}$. The D_C and D_V are plotted as the red and blue shaded areas in Figure 2.1c.

The occupation of electrons (holes) across the conduction (valence) states is governed by the Fermi-Dirac distribution [41]

$$f(E) = \frac{1}{\exp\left(\frac{E - E_{F_{n/p}}}{k_B T}\right) + 1}, \tag{2.4}$$

where E_{F_n} (E_{F_p}) is known as the electron (hole) quasi-Fermi level, representative of the chemical potential (μ) of the highest (lowest) energy electrons (holes).

In an electrical conductor the Fermi level lies within the conduction states. In equilibrium (no external potential applied) electrons relax to the lowest energy states as shown by the black circles in Figure 2.1d. When an external electric field (E_x) is applied for some time δt each $\vec{k}$ will shift by $\delta k = -qE_x\delta t/\hbar$ leading to an uneven distribution of electron momenta, as shown by the red circles in Figure 2.1d and current flows. In an insulator the Fermi level lies within the bandgap. At $T = 0$ K, due to Equation 2.4, the valence states are completely full, as shown by the black circles in Figure 2.1e, while the conduction states are completely empty. When E_x is applied the DOS is full and electrons cannot change momenta, hence no current flows, exemplified by the red circles in Figure 2.1e. The responsivity of electrons (holes) to an external electric field is known as the mobility μ_{n} (μ_{p}) and is directly proportional to the curvature of the bands in k-space, such that a band with high curvature will have low effective mass and high mobility. With regards to Figure 2.1d, larger μ_{n} would result in a larger energetic increase with equivalent momenta change.

As the temperature increases the Fermi-Dirac distribution expands and, depending on E_G, electrons could occupy the conduction states. $f(E)$ is plotted for $T = 0$ K (blue curve) and $T > 0$ K (orange and red curve) in Figure 2.1c. Under conditions where the electron (hole) quasi-Fermi level is far away from the band edges, the Fermi-Dirac distribution can be approximated with Boltzmann statistics [41, 42]. The total number of electrons (holes) in the conduction (valence)

states can then be found as

$$n = \int_{E_C}^{\infty} D_C(E) f\left(E, E_{Fn}\right) dE = N_C \exp\left(\frac{E_{F_n} - E_C}{k_B T}\right) \tag{2.5}$$

$$p = \int_{-\infty}^{E_V} D_V(E) \left[1 - f\left(E, E_{Fp}\right)\right] dE = N_V \exp\left(\frac{E_V - E_{F_p}}{k_B T}\right), \tag{2.6}$$

where N_C (N_V) is the number of states within a few $k_B T$ of the conduction (valence) edge, known as the effective DOS. The carrier concentrations can be related to the bandgap and quasi-Fermi levels as

$$np = N_C N_V \exp\left(\frac{E_{F_n} - E_{F_p} - E_G}{k_B T}\right) = {n_i}^2 \exp\left(\frac{E_{F_n} - E_{F_p}}{k_B T}\right), \tag{2.7}$$

where ${n_i}^2$ is the concentration of electrons (holes) in the conduction (valence) band at temperature T, known as the intrinsic carrier concentration. Under thermal equilibrium ($E_{F_n} = E_{F_p}$) recombination and generation are equal and Equation 2.7 becomes the well-known law of mass action, under which np is a constant. The difference between the electron and hole quasi-Fermi levels ($E_{F_n} - E_{F_p}$) is known as the quasi-Fermi level splitting (QFLS or E_{QFLS}) and has many implications in the performance of semiconductor-based devices [42, 43].

A semiconductor is defined as an electrical insulator that allows for an electron to be excited into the conduction band from the valence band through an external input, such as absorption of a photon or application of an external field. This external input creates a bound electron-hole pair, which, depending on the electronic properties of the semiconductor may stay bound together or dissociate into an unbound electron and hole pair [39–41]. Once an electron-hole pair has been created the electrical conductivity of the solid changes dramatically, as the conduction (valence) electron (hole) is now able to change momenta in response to an external field.

The bandgap requirements for a material to be considered a semiconductor are not well defined and can range from to near zero to 6 eV [44, 45]. However, semiconductors useful in light harvesting applications typically have bandgaps from the infrared to the visible spectrum of light ($\sim$ 0.43 to 3.1 eV). Semiconductors with bandgap larger than this are known as wide-gap semiconductors and have applications in high power [46–48] and high switching frequencies [49–51] electronics.

Although this discussion has centred on inorganic, including elemental (such as silicon) and compound (such as gallium arsenide) semiconductors, many of the ideas developed in this section are applicable to other semiconductor systems such as; quantum dot [52], 2-dimensional [53], and molecular semiconductors such as perovskite [54] and organic [17] semiconductors. In Section 2.2 and 2.3

the thermodynamics of semiconductors and semiconductor-based solar cells will be discussed, for which many of these concepts will be pertinent. In Chapter 3 organic semiconductors will be introduced and discussed, comparing them to the ideas developed here. Finally, a detailed description of how the ideas discussed in this section can be used to model charge transport and collection in photovoltaic devices is given in Appendix G.

2.2 Thermodynamics of Semiconductors

2.2.1 Generalized Plank Radiation

The thermal emission energy density of any black-body at temperature T, known as the black-body radiation, can be expressed as

$$\Phi_{\mathrm{bb}}(E_\gamma) = \Omega \frac{(E_\gamma)^2}{4\pi^2\hbar^3c^3}\left[\exp\left(\frac{E_\gamma}{k_BT}\right) - 1\right]^{-1}, \tag{2.8}$$

in which Ω is the solid angle subtended by the surface the radiation is illuminating, E_γ is the energy of the emitted photon, and c is the speed of light in vacuum. Combining this with Gibbs' observation that the changes in energy are related to the changes in the relevant extensive variables, photons confined to a cavity with constant volume ($\partial V = 0$) and entropy ($\partial S = 0$) exhibit an energetic change dependent on the chemical potential of the radiation (μ_γ) and the photon number (N_γ)

$$\partial E = T\cancel{\partial S} - P\cancel{\partial dV} + \mu_\gamma \partial N_\gamma, \tag{2.9}$$

where P is pressure. For the non-trivial case ($\partial N_\gamma \neq 0$) the chemical potential must vanish when the system is in equilibrium with the surrounding environment, characteristic of thermal radiation. The relationship between non-thermal radiation and the emission spectra will instead be characterised by the threshold photon energy which, as will be shown, necessitates a non-zero chemical potential of radiation.

2.2.2 Electronic Transitions and Photon Currents

To determine the emission current from a semiconductor in equilibrium with an external photon bath consider the slab of material shown in Figure 2.2a. The photon current (J_γ) flowing within the slab is contingent on the rates of absorption (r_α), spontaneous emission (r_{Sp}), and stimulated emission (r_{St}) as

$$\nabla J_\gamma = \frac{1}{4} r_{\mathrm{Sp}} - \left(r_\alpha - r_{\mathrm{St}}\right), \tag{2.10}$$

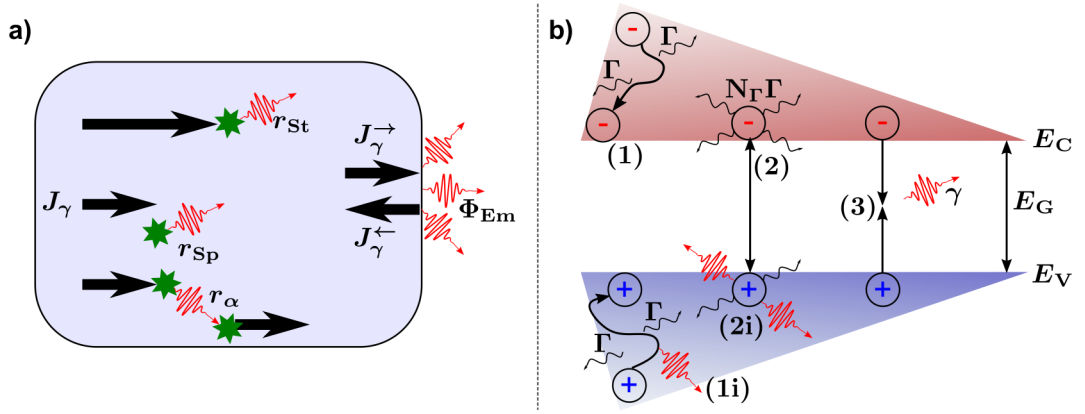

Figure 2.2: (a) Thermodynamic processes in semiconductors including rates of spontaneous emission (r_{Sp}), stimulated emission (r_{St}), and absorption (r_α). J_γ-Photon current, Φ_{em}-Photoluminescence emission. (b) Electron and hole processes occurring in semiconductors. Intraband thermal relaxation resulting in (1) phonons and (1i) photons, interband relaxation resulting in (2) phonons and (2i) photons, (3) interband recombination resulting in photons.

where the factor of 1/4 is due to Lambert's Law [55]. The net absorption rate can be expressed as the product of the absorption coefficient (α) and the photon current ($r_\alpha - r_{\mathrm{St}} = \alpha J_\gamma$). Leading to the solution to Equation 2.10

$$J_\gamma(x) = \frac{r_{\mathrm{Sp}}}{4\alpha}\left(1 - e^{-\alpha x}\right). \tag{2.11}$$

At the interface, the fraction of the photon current transmitted into the surrounding media will depend on the reflection coefficient at the interface ($R(E_\gamma)$). Allowing for multiple reflections through a slab of length L and refractive index n, the photon current emitted through the surface,

$$J_\gamma(L, E_\gamma) = [1 - R(E_\gamma)]\left[\frac{1 - \exp\left(-\alpha(E_\gamma)L\right)}{1 - R(E_\gamma)\exp\left(-\alpha(E_\gamma)L\right)}\right]\frac{r_{\mathrm{Sp}}}{4\alpha(E_\gamma)n^2}, \tag{2.12}$$

is dependent only on material parameters as well as the coupling strength between the material and the exterior photon bath, determined by the rate of spontaneous emission.

Figure 2.2b shows the various processes an electron-hole pair can undergo in a semiconductor. Each electron or hole is characterised by a chemical potential increasing away from the energy gap region such that an electron and hole with the same energy will have chemical potentials $\mu_{\mathrm{e}} = -\mu_h$. Reactions can be either radiative (such as processes (1i), (2i), and (3)), meaning the energy exchange results in photon emission, or non-radiative (such as processes (1) and

(2)), meaning the energy exchange results in phonon emission. Further, reactions can be interband, meaning they occur between conduction and valence states, or intraband, meaning they occur fully within either conduction or valence states.

2.2.3 Radiative Relaxation and Photoluminescence

Radiative interband relaxation processes (process 3 in Figure 2.2) are recombination events between conduction electrons and valence holes that result in photon emission

$$e + h \rightarrow \gamma. \tag{2.13}$$

The Gibbs free energy exchange,

$$\partial E = \mu_{\mathrm{e}} \partial N_e + \mu_h \partial N_h + \mu_\gamma \partial N_\gamma = 0, \tag{2.14}$$

indicates that $\partial N_e = \partial N_h = -\partial N_\gamma$ and $\mu_{\mathrm{e}} + \mu_h = \mu_\gamma$. Under these conditions, $r_{\mathrm{Sp}}(E_\gamma)$ will be dependent on the number of pairs of occupied and unoccupied conduction (n_c and n_c', respectively) and valence (n_v and n_v', respectively) band states that differ by energy E_γ [56]

$$r_{\mathrm{Sp}}(E_\gamma) = A(E_\gamma) \left[\frac{n_c n_v'}{n_c' n_v - n_c n_v'} \right], \tag{2.15}$$

where A is a constant which depends on the density and velocity of photons. The DOS will be given by the Fermi-Dirac distribution, such that $E_{F_n} = \mu_{\mathrm{e}}$ and $E_{F_p} = \mu_h$. Taking this into consideration, Equation 2.12 and 2.15 can be combined and simplified to

$$J_\gamma(E_\gamma) = a(E_\gamma) \frac{(E_\gamma)^2}{\pi^2 \hbar^3 c^2} \left[\exp\left(\frac{E_\gamma - (\mu_{\mathrm{e}} - \mu_h)}{k_B T} \right) - 1 \right]^{-1}, \tag{2.16}$$

in which $a(E_\gamma)$ is the total absorption of the material, described by the prefactors in Equation 2.12 and 2.15. Equation 2.16 indicates that the emitted photon flux is in equilibrium with the excited species (μ_{e} and μ_h) in the semiconductor. Substituting μ_γ from the Gibbs free-energy conservation leads to the radiation formula

$$J_\gamma(E_\gamma) = a(E_\gamma) \frac{(E_\gamma)^2}{\pi^2 \hbar^3 c^2} \left[\exp\left(\frac{E_\gamma - \mu_\gamma}{k_B T} \right) - 1 \right]^{-1}, \tag{2.17}$$

which indicates that transitions resulting in photons of energy below $E_\gamma < \mu_\gamma$ are forbidden. Therefore, interband radiative recombination is characterised by emission of photons with $E_\gamma > E_G$ and a non-zero chemical potential.

The excess photon flux (Φ_{em}), or measurable photoluminescence, can be found from the difference between Equation 2.17 and the black-body radiation given by Equation 2.8

$$\Phi_{\text{em}} = a(E_\gamma)\Phi_{\text{bb}} \left[\exp\left(\frac{\mu_\gamma}{k_B T}\right) - 1\right], \tag{2.18}$$

in which the Laurent series expansion is used. The photoluminescence of OSCs will be considered in Chapter 5 and 6, while the relationship between photoluminescence, QFLS, and photovoltaic device properties will be discussed in Chapter 7.

2.2.4 Non-Radiative Relaxation

Non-radiative energy loss can be due to intraband thermalization of electrons or holes in their respective bands

$$e + e' \rightarrow \Gamma, \qquad h + h' \rightarrow \Gamma \tag{2.19}$$

or interband electron and hole exchange

$$e + h \rightarrow N_\Gamma, \tag{2.20}$$

mediated either by a single phonon (Γ) or a host of phonons (N_Γ) of total energy E_Γ.

Intraband Relaxation

The Gibbs free energy exchange for a thermally relaxing electron,

$$\partial E = -\mu_{\text{e}}\partial N_e + \mu_{e'}\partial N_{e'} + \mu_\Gamma \partial N_\Gamma = 0, \tag{2.21}$$

indicates that $-\partial N_e = \partial N_{e'} = \partial N_\Gamma$ and $\mu_{\text{e}} = \mu_{e'} + N_\Gamma \mu_\Gamma$. The rate of spontaneous emission will be characterised by the rate of phonon emission and Equation 2.15 can be modified to

$$r_{\text{Sp},\Gamma}(E_\Gamma) = A(E_\Gamma)\left[\frac{n_c n_c'}{n_c' n_c - n_c n_c'}\right], \tag{2.22}$$

where each pair of states differs by the energy of the emitted phonon. The differential phonon current leaving any slice of the material can be found to be

$$\partial J_\Gamma(E_\Gamma) = a(E_\Gamma)\frac{E_\Gamma^2}{\pi^2\hbar^3 c^2}\left[\exp\left(\frac{E_\Gamma - \mu_\Gamma}{k_B T}\right) - 1\right]^{-1}. \tag{2.23}$$

Since the intraband transitions are always low energy exchanges $\mu_\Gamma \sim 0$.

Interband Relaxation

When an electron-hole interaction is mediated by the available phonon states, the equilibrium condition is given by $\mu_{\mathrm{e}} + \mu_h = N_\Gamma \mu_\Gamma$ and Equation 2.15 can be re-modified to

$$r_{\mathrm{Sp},\Gamma}(E_\Gamma) = A(E_\Gamma)\left[\frac{n_c n'_v}{n'_c n_v - n_c n'_v}\right]. \tag{2.24}$$

The phonon current generated in a differential slice of the material will be the summation of all the participating phonon modes

$$\sum \partial J_\Gamma(E'_\Gamma) = \sum a(E'_\Gamma)\frac{n^2(E'_\Gamma)^2}{\pi^2\hbar^3c^2}\left[\exp\left(\frac{E'_\Gamma - \mu_\Gamma}{k_B T}\right) - 1\right]^{-1}, \tag{2.25}$$

for a total energy equal to the energy of the recombining electron-hole pair. As each individual phonon is a low energy excitation, $\mu_\Gamma \sim 0$ for each term in the summation.

Similar relaxation processes to Equation 2.23 and 2.25 resulting in a host of photons are allowed (indicated by process (1i) and (2i) in Figure 2.2) [55]; however, the energy exchange is equivalently small leading to $\mu_\gamma \sim 0$. Therefore, these radiative interband and intraband transitions result in the thermal radiation predicted by Equation 2.8 [55].

The thermal radiation of a semiconductor, described by Equation 2.8, is ascribable to intraband transitions resulting in photons of $\mu_\gamma = 0$, while the radiative interband transitions result in photons with $\mu_\gamma \neq 0$. The impact of radiative and non-radiative recombination to photovoltaic device properties will be discussed in the following sections.

2.3 Thermodynamics of Solar Cells

The process of converting thermal radiation energy from the sun into usable electrical energy is limited by a number of thermodynamic factors. If all the incident solar radiation could be transferred into usable electrical energy the PCE would simply be limited by the heat transfer efficiency described by the Carnot cycle, characterised by the ratio of the temperature of the sun (T_S) to the temperature of the cell (T_C) as PCE $= 1 - T_C/T_S$ [57, 58]. In p-n junction type solar cells, the exchange of energy depends primarily on the energy of the bandgap, limiting the number of photons that can be converted into electrical energy.

The probability that a photon of energy E_γ incident on a solar cell will create an electrical current is known as the photovoltaic external quantum efficiency

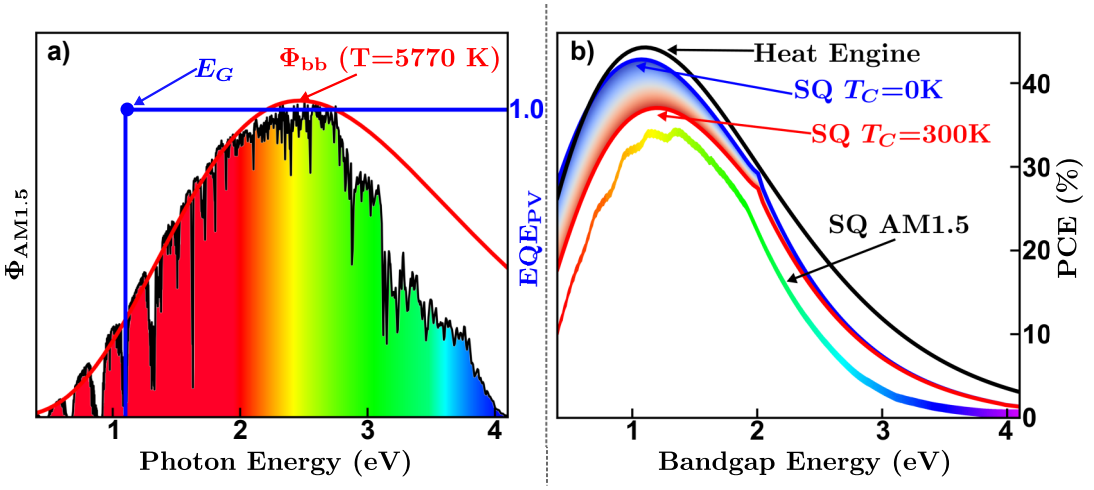

Figure 2.3: (a) AM1.5 spectrum along with (solid red line) the black-body radiation spectra (Equation 2.8) for the temperature of the sun (5770 K) . (Solid blue line) illustration of the step function $\mathrm{EQE_{PV}}$ used to calculate the thermodynamic limit of the power conversion efficiency. (b) Thermodynamic limits to the power conversion efficiency calculated for a (solid black line) Heat Engine, from the Shockley-Queisser limit (SQ) for a cell temperature of (blue line) 0 K and (red line) 300 K, and from the (multicoloured line) AM1.5 spectra shown in panel a.

($\mathrm{EQE_{PV}}$), the ideal form of which is a step-function where any photon with $E_\gamma \geq E_G$ give rise to $\mathrm{EQE_{PV}} = 1$ resulting in an electron-hole pair with energy E_G, while photons of $E_\gamma < E_G$ give rise to $\mathrm{EQE_{PV}} = 0$. This ideal $\mathrm{EQE_{PV}}$ is given by the blue line in Figure 2.3a.

2.3.1 Thermodynamic Limit of Power Conversion Efficiency

The ultimate efficiency of a heat engine with the $\mathrm{EQE_{PV}}$ characteristics described above ($\mathrm{PCE_{HE}}$) would be the ratio of the total energy absorbed by the cell ($E_\gamma > E_G$) compared to the incident power density, each found through Equation 2.8 with $T = T_S$. Φ_{bb} for $T = T_S$ is given by the red line in Figure 2.3a, while the heat engine limit of the PCE is given by the black dashed line in Figure 2.3b. A maximum PCE of 44% occurs at a bandgap of 1.09 eV. Developing a more sophisticated limit requires consideration of the generation, and radiative and non-radiative recombination properties of the electrons and holes in the cell.

Generation

When a photovoltaic cell is in the thermal equilibrium the only form of carrier generation will be due to reabsorption of the cell's own black-body radiation. The flux of generated charges will be given by $n_{\mathrm{bb}} = \int_{E_G}^{\infty} \Phi_{\mathrm{bb}}(T = T_C)dE$. While the flux of charges generated under illumination by the sun will be $n_{\mathrm{sun}} = \int_{E_G}^{\infty} \Phi_{\mathrm{bb}}(T = T_S)dE$.

Radiative Recombination

The number of electron and hole pairs recombining radiatively ($n_R(V)$) will depend on the distribution of electrons and holes in the semiconductor and ultimately be proportional to the product of the distributions (np) [40]. Further, thermal equilibrium requires the current generated by the cell's black-body radiation be balanced by an according recombination current, meaning $n_R(0)_{\mathrm{dark}} = n_{\mathrm{bb}}$. The law of mass-action requires that $np_{\mathrm{dark}} = {n_i}^2$ (when $E_{F_n} = E_{F_p}$), and, consequentially, $n_R(V) = n_{\mathrm{bb}} np/{n_i}^2 = n_{\mathrm{bb}} \exp(qV/k_B T_C)$.

Non-Radiative Recombination

The number of non-radiative generation ($n_{NR,0}$) and recombination events ($n_{NR}(V)$) must balance at thermal equilibrium, leading to $n_{NR}(0) = n_{NR,0}$. The voltage dependence of $n_{NR}(V)$ can be approximated with the ideal rectifier equation $n_{NR}(V) = n_{NR,0} \exp(qV/k_B T_C)$ [59]. Further, the proportion of recombination which is radiative can be described by the factor f_r.

Steady-State Considerations

Under steady-state illumination the total generation and recombination of electron-hole pairs must result in an overall current ($J(V)$), leading to

$$J(V) = q\left(n_{\mathrm{bb}} - n_{\mathrm{sun}}\right) + q\left(\frac{n_{\mathrm{bb}}}{f_r}\right)\left[\exp\left(\frac{qV}{k_B T_C}\right) - 1\right], \tag{2.26}$$

where $J(V)$ is the current delivered to the load, $q\left(n_{\mathrm{bb}} - n_{\mathrm{sun}}\right)$ defines the short-circuit current and $q\left(n_{\mathrm{bb}}/f_r\right)$ defines the J_0 in Equation 1.2. When all recombination is radiative ($f_r = 1$) J_0 is minimised, known as the radiative dark-saturation current (J_0^{Rad}). In practice, $f_r < 1$ due to the presence of nonradiative recombination. At the same time $\mathrm{EQE_{PV}}$ is less than unity and has complex spectral characteristics due to the optical properties of the active layer as well as cavity effects due to the overall structure of the device [60]. With these considerations

in mind, the J_{SC} and J_0^{Rad} are formally defined for solar cells exposed to AM1.5 spectra as

$$J_{\mathrm{SC}} = q \int_0^{\infty} \mathrm{EQE}_{\mathrm{PV}}(E_\gamma) \Phi_{\mathrm{AM1.5}} dE \tag{2.27}$$

$$J_0^{\mathrm{Rad}} = q \int_0^{\infty} \mathrm{EQE}_{\mathrm{PV}}(E_\gamma) \Phi_{\mathrm{bb}} \left(T = T_C\right) dE. \tag{2.28}$$

The highest possible V_{OC}, occurring when all the recombination is radiative, known as the radiative limit to the V_{OC} ($V_{\mathrm{OC}}^{\mathrm{Rad}}$) can be found by solving Equation 2.26 for $J(V_{\mathrm{OC}}^{\mathrm{Rad}}) = 0$, leading to

$$V_{\mathrm{OC}}^{\mathrm{Rad}} = \frac{k_B T_C}{q} \ln \left[\frac{J_{\mathrm{SC}}}{J_0^{\mathrm{Rad}}} + 1 \right]. \tag{2.29}$$

Which ultimately results in an open-circuit voltage of E_G for $T_C = 0$ K [59]. As the temperature rises additional radiative decays will occur reducing the chemical potential of the remaining electron-hole pairs. Accordingly, the V_{OC} will be a fraction of E_G, dependent on the relative absorption of the black-body and solar radiation expressed as $f_{\mathrm{T}} = (T_S/T_C)^3 \int_{E_G}^{\infty} \Phi_{\mathrm{bb}}(T = T_S) dE \big/ \int_{E_G T_s/T_c}^{\infty} \Phi_{\mathrm{bb}}(T = T_C) dE$ [59].

Finally, the fill-factor of a cell can be calculated by solving $d(IV)/dV = 0$, using Equation 2.26, for V_{MPP} and J_{MPP}. Ultimately, the thermodynamic limit to the PCE of a solar cell is

$$\mathrm{PCE} = \mathrm{PCE}_{\mathrm{HE}} \times f_{\mathrm{T}} \times \mathrm{FF}, \tag{2.30}$$

where f_{T} and FF are less than unity. Equation 2.30 is known as the Shockley-Queisser (SQ) limit and can be used to calculate the thermodynamic limit to the efficiency of a solar cell based on the material parameters (E_G, $\mathrm{EQE}_{\mathrm{PV}}$, T_C) and the incident radiation spectrum.

Figure 2.3b shows the power conversion efficiency for a heat engine, along with the SQ limit calculated using the black-body spectra at the temperature of the sun when $T_C = 0$ K, $T_C = 300$ K, and using the AM1.5 spectra. At $T_C = 0$ K the SQ limit approaches the heat engine limit, as the T_C is raised the PCE is reduced following the blue-red gradient until $T_C = 300$ K. Finally, the realistic SQ limit, calculated using the AM1.5 spectra shown in Figure 2.3a in place of Equation 2.8, is given by the colored line. The reduction in PCE from $T_S = 5770$ K to AM1.5 is ascribable to the overestimation of high energy radiation in the $\Phi_{\mathrm{bb}}(T = T_S)$ compared to the AM1.5 spectra shown in Figure 2.3a, due to atmospheric effects such as Mie scattering [61]. Under these conditions, the maximum value of PCE (33.7%) occurs using a step-function $\mathrm{EQE}_{\mathrm{PV}}$ with E_G of 1.33 eV, while an additional maximum (32.6%) occurs at a E_G of 1.09 eV.

2.3.2 Non-Radiative Photovoltage Losses

Equation 2.29 indicates that the highest possible V_{OC} for a cell occurs when there is no voltage losses due to non-radiative decays. Introducing non-radiative voltage losses reduces the chemical potential of the ensemble of electrons-hole pairs in the semiconductor by reducing the QFLS of the recombining species, as outlined in Section 2.2.4. This results in a further potential loss across the device leading to a reduction in V_{OC} known as non-radiative losses to the V_{OC}, expressed as

$$\Delta V_{\mathrm{OC}}^{\mathrm{NR}} = V_{\mathrm{OC}}^{\mathrm{Rad}} - V_{\mathrm{OC}}. \tag{2.31}$$

As $\Delta V_{\mathrm{OC}}^{\mathrm{NR}}$ is due to non-radiative recombination events, the important parameter is the competition between the radiative ($q\Phi_{\mathrm{em}}$) and non-radiative ($q\Phi_{NR}$) components of the recombination current, known as the LED External Quantum Efficiency ($\eta_{\mathrm{LED}} = q\Phi_{\mathrm{em}}/(q\Phi_{\mathrm{em}} + q\Phi_{\mathrm{NR}})$) where Φ_{em} is the emitted photon flux due to the total injected current at V_{OC} ($J_{\mathrm{inj}}(V_{\mathrm{OC}})$). At open-circuit conditions $J_{\mathrm{inj}}(V_{\mathrm{OC}})$ is equal to J_{SC} and $\Delta V_{\mathrm{OC}}^{\mathrm{NR}}$ can be found through Equation 2.29 as

$$\Delta V_{\mathrm{OC}}^{\mathrm{NR}} = -\frac{k_B T}{q} \ln\left[\eta_{\mathrm{LED}}\right]. \tag{2.32}$$

2.3.3 Optoelectronic Reciprocity and Electroluminescence

The functional form of Φ_{em} can be found by recalling that, at thermal equilibrium, the current generated by the black-body radiation must be balanced by a recombination current (J_0^{Rec}) injected from the electrodes

$$J_0^{\mathrm{Rec}} = J_0^{\mathrm{Rad}} = q\int_0^{\infty} \mathrm{EQE}_{\mathrm{PV}}(E_\gamma)\Phi_{\mathrm{bb}}(E_\gamma)dE. \tag{2.33}$$

Indicating that the emission of semiconductor operated as a light emitting diode is dependent on the optical generation and carrier collection properties when operated as a solar cell (and vice versa), known formally as a reciprocity relation [62–67]. When the voltage is increased away from equilibrium, the excess photon flux will be given by the difference between the current contributing to the radiation less the J_0^{Rad} as

$$\Phi_{\mathrm{em}} = \frac{J_0^{\mathrm{Rec}}}{q}\exp\left(\frac{qV}{k_B T}\right) - \frac{J_0^{\mathrm{Rad}}}{q} = \frac{J_0^{\mathrm{Rad}}}{q}\left[\exp\left(\frac{qV}{k_B T}\right) - 1\right]. \tag{2.34}$$

Equivalently the spectral flux,

$$\Phi_{\mathrm{em}}(E_\gamma) = \mathrm{EQE}_{\mathrm{PV}}(E_\gamma)\Phi_{\mathrm{bb}}(E_\gamma)\left[\exp\left(\frac{qV}{k_B T}\right) - 1\right], \tag{2.35}$$

will depend on the spectral properties of the cell's EQE_{PV} and black-body radiation. Although the principle of detailed balance from which Equation 2.33 is derived is universal, the reciprocity relation relies on the linearity of the system away from equilibrium, effectively implying that the emission is due to linear band-to-band recombination, as described in Section 2.2.3 [67, 68].

In the following chapter organic semiconductors will be introduced and discussed utilising the concepts developed in Section 2.1 and 2.2. The applicability of Equation 2.33 to organic photovoltaic devices will be discussed in Section 3.4 and, based on this understanding, the relationship between the electroluminescence emission, photoluminescence emission (described by Equation 2.18), and QFLS will be discussed in Chapter 7. Utilising this analysis, methods for measuring distinct non-radiative recombination pathways will be developed and examined.

Chapter 3

Optoelectronics of Organic Semiconductors

3.1 Organic Semiconductors

In contrast to crystalline inorganic semiconductors discussed in Section 2.1, organic semiconductors are not composed of atoms in a well ordered crystal lattice of high permittivity. Instead, their constituent elements are conjugated (derived from the Latin 'to link together') chains of carbon (C) atoms bonded to Hydrogen (H) atoms and the occasional functional group (those with Oxygen, Nitrogen, Sulphur, Fluorine, or Chlorine). A single carbon atom has the electronic configuration of $1s^2 2s^2 2p^2$, which can form sp, sp^2, or sp^3 hybridized orbitals when bound to nearby elements, depending on the electronic structure of the elements surrounding it [69].

For example, one of the most important conjugated configurations in organic chemistry is the benzene ring, as shown in Figure 3.1a. In this configuration each C-atom is involved in bonding to two C-atoms and one H-atom. To accomplish this, each C-atom promotes an electron from the $2s$ to the $2p$ orbital forming a state $1s^2(2s^1 2p_x^1 2p_y^1)2p_z^1$. The $(2s^1 2p_x^1 2p_y^1)$ forms a superpositional state known as a hybridized orbital (in this case sp^2 hybridized). sp^2 hybridized orbitals are 2-fold degenerate, one lower energy consisting of constructive interference between the s and p orbitals while the higher energy consists of destructive interference; known as bonding and anti-bonding (denoted with a $*$) orbitals, respectively. The bonding sp^2 orbitals lie in-plane with 120° arc between bond angles, while the remaining $2p_z$ orbital will lie out-of-plane [69].

Figure 3.1b shows the shape of the $2p_z$ and sp^2 orbitals between two C-atoms in benzene, where red (blue) represents positive (negative) wavefunction values. Each sp^2 orbital points towards a neighbouring C-atom, the strong overlap region between C-atoms causes the formation of a σ bond. This wavefunction overlap leads to a large exchange integral between sp^2 orbitals on neighbouring C-atoms, causing a large energetic splitting between the σ-and σ^*-orbitals. Meanwhile, the overlap between the out-of-plane $2p_z$ orbitals leads to a π bond forming with a comparatively smaller splitting between π-and π^*-orbitals [40]. The orbitals are

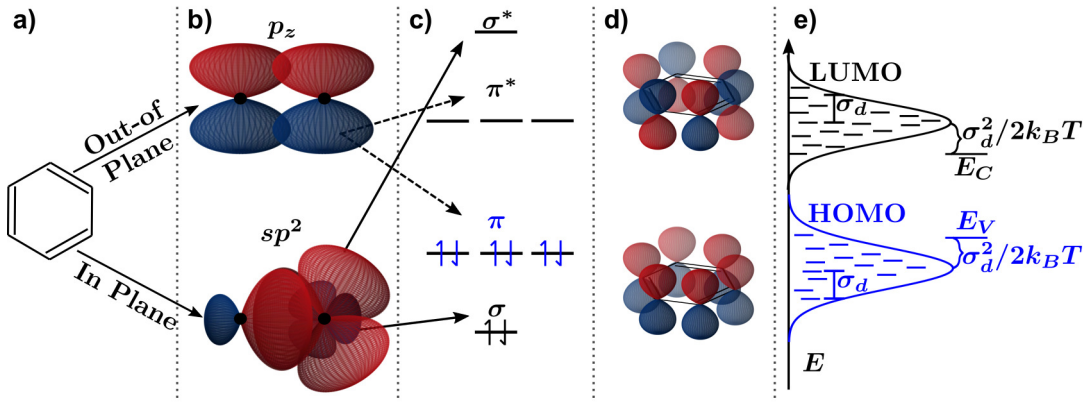

Figure 3.1: (a) The Benzene ring. (b) In- and out-of- plane orbital configurations of sp^2 hybridization. Red (blue) indicates positive (negative) wavefunction values, black circles indicate carbon atoms, additional sp^2 orbitals have been removed from left hand image for clarity. (c) Energetic landscape of bonding and anti-bonding states in Benzene. (d) Wavefunction configuration for bonding and anti-bonding $2p_z$ orbitals. (e) Energetic disorder in organic semiconductors. E_C-conduction band edge, E_V valence band edge, E_G-bandgap

filled according to the Aufbau principle such that the lowest lying σ-orbitals will be filled first followed by the lowest lying π-orbitals, as shown in Figure 3.1c. In this picture, the highest occupied molecular orbital (HOMO) plays the part of the valence state while the lowest unoccupied molecular orbital (LUMO) plays the role of the conduction state.

When an electron is promoted from the HOMO to the LUMO state (for example, by the absorption of a photon) the molecule reorganises from a ground-state configuration to an excited-state configuration through re-orientation of the $2p_z$ orbitals. Two example wavefunction configurations are shown for the π- and π^*-orbitals in Figure 3.1d, the lowest lying configuration of π-orbitals has constructive interference between all the $2p_z$ orbitals of the C-atoms while the highest lying configuration of π^*-orbitals has destructive interference between all the $2p_z$ orbitals of the C-atoms. This reorientation can be viewed as an electron (in the π^*-orbital) bound to a hole (in the π-orbital) localised to, but delocalised within, the benzene ring, commonly referred to as a Frenkel exciton [70, 71]. These excited states can decay back to the ground state through additional reorganisation of the $2p_z$ orbitals and the emission of a phonon or photon, known as geminate exciton recombination.

An organic semiconductor is created when many molecules, bound together through weak Van der Walls forces, form a polycrystalline or amorphous film. Variations in molecular conformation, polydispersity, random orientations of molecules within the solid, and chemical impurities results in a great deal of (static) disorder with the HOMO and LUMO states. Therefore, the DOS in the HOMO and LUMO levels of an organic semiconductor can be described by a Gaussian distribution with total density of states N_0, width σ_d, and mean value ($E_{C/V}$)

$$g\left(E\right) = \frac{N_0}{\sqrt{2\pi\sigma_d}} \exp\left(-\frac{\left(E - E_{C/V}\right)^2}{2\left(\sigma_d\right)^2}\right). \tag{3.1}$$

Figure 3.1e shows the conduction and valence DOS for a disordered semiconductor. As a consequence of the static disorder, electronic transitions can occur over a range of energies broadening the spectral absorption and emission of organic semiconductors from their molecular constituents. In this picture the range of HOMO (LUMO) states plays the role of valence (conduction) levels. However, as a result of the heavily localised excitons combined with the asymmetry of the polycrystalline film, the concept of continuous energy bands, introduced in Section 2.1 does not apply to excitonic transport. Further, the asymmetry in the film limits electrostatic screening between excited states, leading to a much larger exciton binding energy of the Frenkel excitons, compared to the Wannier-Mott excitons generated in inorganic semiconductors [72]. Therefore, a new approach will be needed to understand excitonic transport in OSCs.

3.1.1 Förster Resonance Energy Transfer

The low dielectric constants present in organic semiconductors creates strong electronic dipole moments within excited state configurations. These strong dipole moments result in dipole-dipole coupling to nearby ground state molecules. This coupling provides the possibility of resonance energy transfer from one molecule to another known as Förster Resonance Energy Transfer (FRET) [73–75]. The development of FRET theory requires both a quantum mechanical and classical treatment to fully comprehend. In the quantum mechanical view two static dipoles can interact when they are in resonance with one another through the electromagnetic force. The energy of this interaction (U) is dependent on the electric field created by the oscillating dipole ($\vec{E}$) and the dipole moment of the two dipoles ($\vec{\mu_{1/2}}$). In the near field this is

$$U = -\vec{E}\cdot\vec{\mu_2} = \frac{1}{4\pi\epsilon\epsilon_0}\left[\frac{\vec{\mu_1}\cdot\vec{\mu_2}}{r^3} + \mathcal{O}\left(r^{-5}\right)\right], \tag{3.2}$$

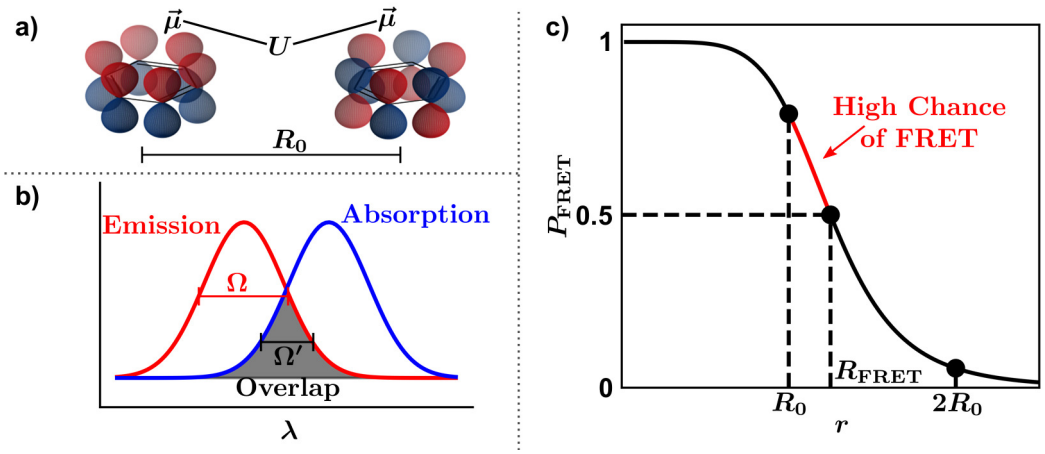

Figure 3.2: (a) Förster Resonance Energy Transfer coupling between two benzene rings with intermolecular spacing R_0. (b) Emission and absorption overlap including width of emission Ω and overlap Ω'. (c) Probability of FRET occurring R_0-intermolecular spacing, R_{FRET}-FRET Radii.

where r is the separation between dipoles. The transfer rate of a such a dipole-dipole interaction is given by $k_{d-d} = \hbar\vec{\mu}^2/r^3$ [76, 77]. However, this treatment assumes that the spectral lines of the dipoles are very sharp, which, as has been discussed, is not the case for OSCs. Figure 3.2a shows a pair of Benzene molecules and the relevant interaction energy separated by an intermolecular spacing (R_0). Figure 3.2b shows the emission and absorption (estimated as Gaussian distributions) with width Ω and overlap region Ω'. For an emitter and absorber with a broad line-shape the probability that they will be in resonance at any time is low, however; the assumption of resonance need only be valid for a small amount of time for energy transfer to occur. The interaction of a broad emitter-absorber pair can be estimated by a sharp quantum mechanical dipole multiplied by the probability that the emitter and absorber will be in resonance [78, 79]. For this to be true the pair of dipoles must have spectral overlap between the emission and absorption of electromagnetic waves, with probability Ω'/Ω. Further, the absorber must be be oscillating with identical frequency (ω) to the emitter within Ω', such that $\hbar\omega = U$. The probability that ω is within Ω' at the same time as $\hbar\omega = U$ is $\omega/\Omega' \times \Omega'/\Omega = U/\hbar\Omega$. Therefore, the rate of energy transfer is given by

$$k_{\mathrm{FRET}} = \left(\frac{\Omega'}{\Omega}\right)\left(\frac{U}{\hbar\Omega}\right) \times k_{d-d} \propto \left(\frac{\Omega'}{(\hbar\Omega)^2}\right)\left(\frac{\vec{\mu}^4}{2r^6}\right). \tag{3.3}$$

Which drops off at a much faster rate than the spectrally narrow dipoles ($k_{d-d} \propto r^{-3}$). The spectral overlap is typically quantified by the so-called FRET Radii (R_{FRET}), defined as the distance that FRET competes equally with excited state to ground state decay

$$k_{\mathrm{FRET}} = \frac{1}{\tau_0}\left(\frac{R_{\mathrm{FRET}}}{r}\right)^6, \tag{3.4}$$

where τ_0 is the excited state lifetime of the lone emitter. Although it may be necessary to amend Equation 3.4 when the size of the molecule becomes similar to the intermolecular spacing [80].

Careful quantum mechanical treatment reveals that the transition dipole moment will be dependent on the relative orientation of the dipoles (κ) and the Coulomb potential, while the resonance overlap will be dependent on the Frank-Condon Factors and the occupational probability between the excited and ground states [77, 81–83]. This treatment allows the spectroscopic transition frequencies to be correlated to the overlap integral of the photoluminescence emission and absorption spectra ($J(\lambda)$) of the two dipoles leading to a FRET rate governed by Equation 3.4 and an R_{FRET} defined by

$${R_{\mathrm{FRET}}}^6 = \left(\frac{9\ln[10]}{128\pi^2 N_A}\right)\left(\frac{\kappa^2\Phi_D}{n^4}\right) \times J(\lambda), \tag{3.5}$$

where R_{FRET} is in cm, Φ_D is the fluorescence quantum yield of the lone emitter, n is the refractive index of the medium, N_A is Avagadro's number, the overlap integral is

$$J(\lambda) = \int_0^\infty F_E(\lambda)\,\epsilon_A(\lambda)\,\lambda^4 d\lambda \Big/ \int_0^\infty F_E(\lambda)\,d\lambda, \tag{3.6}$$

in which $F_E(\lambda)$ is the emitter fluorescence per unit wavelength, and $\epsilon_A(\lambda)$ is the molar extinction coefficient of the absorber. In this view, FRET can occur between any emitter-absorber pair as long as the emitter couples strongly to the electromagnetic field (high Φ_D), the absorber is in an orientation to oscillate with the electromagnetic field (via κ), the space between emitter and absorber has low permittivity (low n), and high probability that the emitter and absorber will be in resonance (high $J(\lambda)$).

The probability FRET will occur (P_{FRET}) between two identical molecules, will depend on the competition between k_{FRET} and τ_0 as $P_{\mathrm{FRET}} = k_{\mathrm{FRET}}/(k_{\mathrm{FRET}} + 1/\tau_0)$. In Figure 3.2c P_{FRET} is plotted as a function of distance away from the excited molecule. When $R_0 < R_{\mathrm{FRET}}$ the probability that an excited state configuration will be transferred to an adjacent molecule will be greater than 0.5. The smaller R_0, or the larger the R_{FRET}, the greater the probability of FRET occurring.

3.1.2 Exciton Transport in Organic Semiconductors

When FRET occurs between molecules in an organic semiconductor the exciton is effectively transferred from one molecule to another. This type of excited-state energy transfer is often referred to as 'hopping' transfer, since, from a macroscopic viewpoint, the exciton appears to be moving around in a collection of molecules [84, 85]. Similar hopping transport occurs between defect sites in inorganic semiconductors, known as thermally activated hopping transport [86]. Formalised by Miller and Abrahams, thermally activated hopping transport consists of two characteristics; the probability that resonance energy transfer will occur and the energetic barrier between sites [87]. In the Miller-Abraham formalism, hopping from a lower to higher energy state in the DOS is thermally activated and is mediated by phonon modes while hoping from a higher to lower energy state is energetically favourable and; therefore, is only dependent on the wavefunction overlap between the two sites. The Miller-Abrahams hopping rate from site i to j can be expressed as

$$k_{ij} = \nu \exp\left(-2SR_{ij}\right) \times \begin{cases} \exp\left(-\frac{E_j - E_i}{k_B T}\right), & E_j > E_i \\ 1, & E_i < E_j \end{cases} \tag{3.7}$$

where ν is the maximum hopping attempt frequency, determined by the high frequency phonon modes, R_{ij} is the distance between site i and j, E_i and E_j are the site energies, and S is the inverse localisation length describing how quickly an excited state wavefunction drops off outside the defect site. The first exponential accounts for the degree of coupling between the two sites, while the second exponential is a Boltzmann factor requiring an 'uphill' jump to be thermally activated. In this picture a charge-carrier undergoes a random walk throughout a collection of sites according to their (spacial and energetic) distribution. Although FRET is the underlying mechanism of intra-molecular energy transfer between organic molecules, combining FRET with Miller-Abrahams rates (by replacing the prefactor in Equation 3.7 with k_{FRET}) has been shown to account for excitonic diffusion in disordered organic semiconductors [88].

In an organic semiconductor, FRET, in principle, can occur between molecules that are not nearest neighbours. However, as $k_{\mathrm{FRET}} \propto r^{-6}$, the probability of hops further than R_0 drops off dramatically as shown in Figure 3.2c, where the probability of hopping $2R_0$ is significantly reduced from the probability of hopping R_0. Further, n will most likely be smaller between nearest neighbour pairs than long-range pairs, and $k_{\mathrm{FRET}} \propto n^{-4}$, indicating that the probability of long-range hops will be further diminished by the presence of nearest neighbours.

Therefore, the D can be calculated assuming that most hops happen between nearest neighbour pairs within the time $\tau_{\mathrm{hop}} = 1/k_{\mathrm{FRET}}$. In m dimensions this

is [89]

$$D = \frac{{R_0}^2}{2m\tau_{\text{hop}}} = \frac{1}{\tau_0}\frac{{R_{\text{FRET}}}^6}{2m{R_0}^4}. \tag{3.8}$$

The average distance travelled by an exciton during a random walk is known as the exciton diffusion length (L_D) and can be calculated from D, and the average lifetime of an ensemble of excitons in the organic semiconductor (τ) as

$$L_D = \sqrt{2m \times D\tau}, \tag{3.9}$$

although sometimes the factor of 2 (or $2m$) is dropped. Since L_D is dependent on both the excited state configuration of the base molecules and the structure of the polycrystalline film making up the organic semiconductor, it will be sensitive to many factors and; therefore, not readily calculable from first principles. In Chapter 4, the role that exciton diffusion plays in OPV devices will be discussed, in Chapter 5 various way of measuring D and L_D will be introduced and considered, and in Chapter 6 description of how these measurements can be utilised to gain insight into the nano-structure of OPV devices will be presented.

3.2 Organic Photovoltaic Devices

3.2.1 The Bulk-Heterojunction

All electronic applications require unbound (free) electrons and holes to be present in the system to generate an electrical current. In OPV devices the high binding energy of the Frenkel excitons must be overcome before any unbound charge carriers can be utilised. The separation of electron-hole pairs in OPV devices is accomplished by creating energetically favourable pathways from excitonic states to CS states, enabled by an intermediate step known as a charge transfer (CT) state. The most common way of establishing energetically favourable pathways is by creating an interdigitated network of two OSCs known as a bulk-heterojunction (BHJ).

Figure 3.3a shows the basic structure of a BHJ OPV device. The BHJ is sandwiched between a transparent conductive electrode and a reflective (or transparent) electrode. The interlayers between the BHJ and the electrodes are chosen to enhance the electron (hole) extraction at the BHJ-cathode (-anode) interface, as will be described in detail in Section 3.2.4.

The two OSCs that make up the BHJ are chosen according to their ionization potential (IP) and electron affinity (χ) as well as their optical-excitation gap, ultimately determined by the HOMO-LUMO gaps of the various molecules making

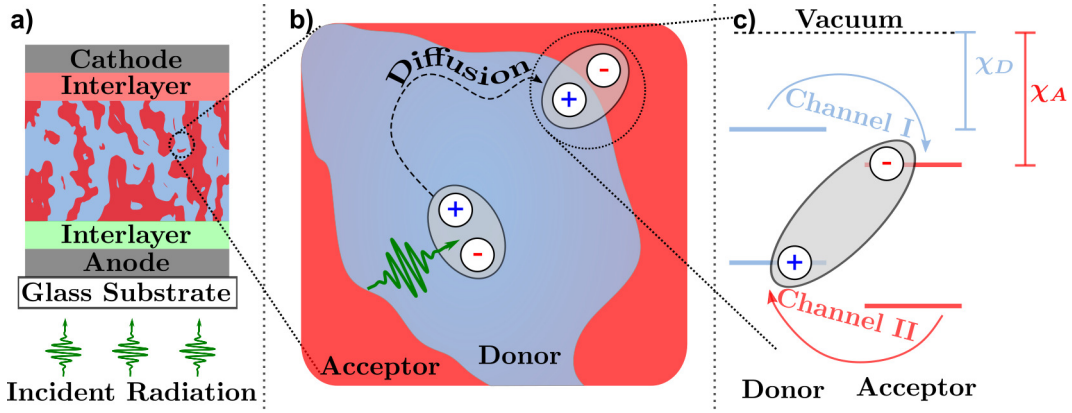

Figure 3.3: (a) Architecture of organic photovoltaic devices. (b) Structure of a phase separated donor acceptor interface including exciton diffusion and charge transfer. (c) Energetics of channel I (II) charge transfer for excitons localised to the donor (acceptor) molecule, χ-electron affinity.

up the polycrystalline or amorphous film. One of the OSCs is chosen to have a relatively high χ called the acceptor while the other has a lower χ, called the donor. In a BHJ the absorption of light will depend on the optical-excitation gap of each OSC since, as described in Section 3.1, optical excitations are localised to a single molecule. However, as will be illustrated in Section 3.3, the V_{OC} of an OPV-based solar cell is limited by the chemical potential of the CT state (μ_{CT}). This, in turn, will ultimately be determined by the difference between the IP of the donor and the χ of the acceptor.

Within the BHJ, areas rich in donor (acceptor) molecules are formed, known as donor (acceptor) phases, as shown in Figure 3.3b. Once an exciton is generated within a phase, it is able to diffuse throughout that particular phase as described in Section 3.1.2. Occasionally, and dependent on the size of the phase separated domains, the exciton will arrive at the interface between donor and acceptor phases. An exciton in the donor (acceptor) phase may form an interfacial CT state through the transfer of an electron (hole) to the acceptor (donor) phase in a process known as channel I (II) charge transfer, as shown in Figure 3.3c [90]. The binding energy of the CT state is reduced from the exciton binding energy by a factor dependent on the difference between the χ (IP) of the two OSCs in channel I (II) charge transfer, reducing the energetic barrier associated with CT-to-CS state generation [91]. In fact, in state-of-the art OPV-based solar cells near unity CT state-to-separated charge carrier generation has been observed [92].

CT state mediated separated charge carrier generation is thought to be the primary route for charge generation in OPV devices and is therefore central to the understanding of any organic-based optoelectronic device [17]. However, alterna-

tive and/or supplementing theories have been proposed to explain the high charge generation yields in state-of-the art OPV devices. It has been proposed that increased delocalisation of excitonic states can account for increased electrostatic quadrapole moments in certain donor-acceptor systems leading to increases in separated charge carrier generation [93,94]. Supporting this view, kinetic Monte-Carlo simulations have shown that even a small amount of delocalisation can lead to a large reduction in CT state binding energy [95, 96]. Additionally, when the difference in IPs between donor and acceptor phases is small, the excited state kinetics begin to play a much larger role and could be responsible for increases in charge generation yield [37]. Further, it has been conjectured that FRET can occur between donor and acceptor molecules in a BHJ, leading to a possible suppression of one charge generation pathway [97].

3.2.2 FRET in OSC Bulk-Heterojunctions

For FRET to occur between donor and acceptor molecules in a BHJ there must be significant overlap between the emission spectra of the donor and absorption spectra of the acceptor. R_{FRET} can be calculated in donor acceptor pairs with Equation 3.5 and 3.6, where the F_E is the normalised photoluminescence emission from a neat donor film and ϵ_A is the absorption coefficient from a neat acceptor film, and n can be taken as an effective index of refraction (n_{eff}) of the BHJ film weighted by the overlap integral [97]

$$n_{\mathrm{eff}} = \int_0^\infty \epsilon_A(\lambda)\, n(\lambda)\, F_D(\lambda)\, \lambda^4 d\lambda \Big/ J(\lambda)\,. \tag{3.10}$$

In which $n(\lambda)$ is the spectral index of refraction of the BHJ film. In this process an exciton may undergo FRET from the donor to acceptor phase of a BHJ without forming a CT state. The transferred exciton will most likely undergo FRET to an acceptor molecule very near the donor-acceptor interface and; therefore, will likely diffuse to the interface to form a CT state via channel II charge transfer. In Chapter 6 the effect of FRET between BHJ donor and acceptor molecules on the free-charge generation will be discussed and R_{FRET} will be calculated for various OSC BHJ systems. Appendix C.5.5 provides additional details and R_{FRET} measurements for various donor-acceptor BHJs.

3.2.3 Separated Charge-Carrier Dynamics

Once excitons have migrated to the donor-acceptor interface and a CT state is formed through channel I or II charge transfer the CT state may undergo geminate recombination, or dissociate into separated charge carrier, which may undergo non-geminate recombination, or carrier transport [17, 98].

Geminate Recombination

Geminate (meaning 'of the same pair') recombination refers to the process of a CT state recombining to the ground state via radiative or non-radiative decay, with rate constant k_f. Considering the CT state to have only recombination and separation pathways leads to the dissociation efficiency $P_{\mathrm{CT}} = k_d/(k_d+k_f)$, where k_d is the rate at which CT states are thermally driven to dissociate into separated charge carriers, given by [99]

$$k_d = \frac{3q\mu_{\mathrm{n}}}{4\pi\epsilon\epsilon_0\ell^3}\exp\left(-\frac{\Delta E}{k_B T}\right)\frac{J_1\left(2\sqrt{2b}\right)}{\sqrt{2b}}. \tag{3.11}$$

In which ϵ is the relative dielectric permittivity of the BHJ, ℓ is the donor acceptor separation at the donor acceptor interface, ΔE is the CT state-to-separated charge carrier energy barrier, J_1 is the Bessel function of the first order, and b accounts for the electric field (E_x) dependence of the dissociation as $b = q^3E_x/8\pi\epsilon\epsilon_0(k_BT)^2$. ΔE is highly dependent on the system in question and evidence of near zero ΔE has been demonstrated in certain donor acceptor combinations [91].

Non-Geminate Recombination

Non-geminate (meaning 'not of the same pair') recombination occurs when two oppositely-charged separated charge carriers meet, form a CT state, and recombine as described above. The additional barrier of the charges meeting is typically understood through the Langevin recombination model [100]. In this model, the carriers must be within a critical radius such that the Coulomb attraction is greater than the kinetic energy pulling them apart, guaranteeing that they will meet. The critical radius is known as the Coulomb capture radius, ($r_c = q^2/4\pi\epsilon\epsilon_0 k_BT$) expected to be between 14-18 nm for typical organic semiconductors [101]. The upper limit to the rate of recombination, known as the Langevin recombination rate constant, can be found by considering the time it takes carriers to diffuse towards one another

$$k_L = \frac{q\left(\mu_{\mathrm{n}}+\mu_{\mathrm{p}}\right)}{\epsilon\epsilon_0}. \tag{3.12}$$

However, in OPV devices recombination rates many orders of magnitude lower than the Langevin limit have been observed, often referred to as suppressed recombination [17, 92, 102–107]. The origins of this suppressed recombination is a debated subject and has been attributed to CT state kinetics including: electrostatic quadrapole moments [93, 97], static disorder [108], delocalisation of excitonic wavefunctions over multiple molecules in the film [95], and re-dissociation

of CT states [92, 109]; as well as hindrances to electron-hole encounters such as: polaronic distortion of the surrounding media [110], imbalances in separated charge carrier mobilities [111], and confinement of electrons (holes) to the acceptor (donor) domain [105, 112]. The total bimolecular recombination rate for CS-to-CT state transfer is expressed as the Langevin recombination rate constant reduced by the CT state (γ_{CT}) and encounter (γ_{enc}) kinetics as

$$\beta = \frac{k_L}{\gamma_{\mathrm{CT}}\gamma_{\mathrm{enc}}} = \frac{q\left(\mu_{\mathrm{n}} + \mu_{\mathrm{p}}\right)}{\gamma_{\mathrm{CT}}\gamma_{\mathrm{enc}}\epsilon\epsilon_0}, \tag{3.13}$$

where both γ_{CT} and $\gamma_{\mathrm{enc}} > 1$.

Carrier Transport

Separated charge carriers in an OPV device move throughout their respective domains driven by an internal electric field induced by the difference in work function between the cathode and anode (often identified with the built-in voltage, V_{bi}). As with inorganic semiconductors the responsivity of the separated charge carriers to an electric field is determined by the charge carrier mobility. However, since the separated charge carriers are being transported between discrete sites they undergo hopping transport similar to that of excitons discussed in Section 3.1.2. Unlike excitons, separated charge carriers are not electrically neutral and when they hop between sites the surrounding media reorients to account for this electric monopole, resulting in a quasi-particle known as a polaron [17]. The hopping rate of a polaron can be described by a Marcus-Hush charge transfer process with rate [113–115]

$$k_{ij} = \frac{2\pi\left|V_{ij}\right|}{\hbar\sqrt{4\pi\lambda^* k_B T}} \exp\left(-\frac{\left(E_j - E_i + \lambda^*\right)^2}{4k_B T\lambda^*}\right), \tag{3.14}$$

where λ^* is the energy associated with reorganisation of the surrounding molecules, and V_{ij} relates to the coupling between sites. The average separated charge carrier diffusion constant ($D_{\mathrm{n/p}}$) for such a hopping mechanism can be found in a similar manner to Equation 3.8 utilising Equation 3.14 but with each pathway weighted by the distance over which a hop occurs (r_l) and its corresponding probability (P_l)

$$D_{\mathrm{n/p}} = \frac{1}{2z}\sum_{l=0}^{z} r_l^2 k_l P_l, \tag{3.15}$$

where z is the total number of available sites, $P_l = k_l/\Sigma_i k_i$, while k_l is the rate along path l and $\Sigma_i k_i$ is the total hopping rate away from the site [116, 117].

The separated charge carrier mobilities can be determined from $D_{\mathrm{n/p}}$ utilising Einstein's diffusion equation as

$$\mu_{\mathrm{n/p}} = \frac{qD_{\mathrm{n/p}}}{k_B T}. \tag{3.16}$$

Therefore, as with excitons, the separated charge carrier mobilities will be dependent on the degree of coupling and distance between molecules; however, unlike excitons, the separated charge mobilities will depend on the electrostatic interactions between the charged carrier and the uncharged media surrounding it.

The total electron current flowing between sites i and j can be calculated from the continuity equation as a function of the electron density at those sites (n_i,n_j) as

$$J_n = qrk_{ji}n_j - qrk_{ij}n_i, \tag{3.17}$$

which can be compared to the discretized drift-diffusion equation

$$J_n = q\mu_{\mathrm{n}} n E_x + qD_{\mathrm{n}}\frac{dn}{dx} = q\mu_{\mathrm{n}}\left(\frac{n_i + n_j}{2}\right)E_x + qD_{\mathrm{n}}\left(\frac{n_j - n_i}{R_0}\right). \tag{3.18}$$

Equating 3.17 and 3.18 and solving for μ_{n} and D_{n} gives

$$\mu_{\mathrm{n}} = \frac{r}{E_x}\left(k_{ji} - k_{ij}\right), \tag{3.19}$$

$$D_{\mathrm{n}} = \frac{r^2}{2}\left(k_{ij} + k_{ji}\right), \tag{3.20}$$

while similar expressions can be derived for holes. In this picture, μ_{n} appears to be inversely related to the field, however, the drift current has no explicit field dependence. In fact, the field dependence returns in the hopping rates. If site j is a lower energy than site i, $k_{ji} - k_{ij} < 0$ and the carrier will likely move $i \rightarrow j$. However, as an electric field will alter the energetic landscape between sites, the rates k_{ij} and k_{ji} will change with E_x and thereby alter the carriers trajectory [118, 119].

When the electric field strength and carrier concentration are relatively low the average carrier energy is independent of carrier concentration and the mobility can be approximated from a Miller-Abrahams rate as

$$\mu_{\mathrm{n}} = c_1 \frac{R_0^2 \nu q}{\sigma_d} \exp\left(-c_2\left(\frac{\sigma_d}{k_B T}\right)^2\right), \tag{3.21}$$

with $c_1 = 1.8 \times 10^{-9}$ and $c_2 = 0.42$ being empirical parameters [120]. In this picture, separated charge carriers quickly move throughout the polymer film to fill

the lowest lying states in the DOS after which, subsequent carriers are able to hop readily throughout the remaining states in the film with average energy $\sigma_d{}^2/k_BT$ below the center of the DOS. Known as the Gaussian disorder model, this understanding allows for the use of the effective mobilities described by Equation 3.21, and suggests that the donor IP and acceptor χ can be treated as conduction and valence levels respectively while the difference between them can be considered as an effective bandgap when describing carrier transport in OPV devices under steady-state conditions [120–123]. Once initial thermalization occurs the separated charge carriers are transported along a conduction edge between their average energy and the DOS centre, similar to that described in Equation 2.2 and 2.3, allowing for the calculation of separated electron and hole densities as described in Equation 2.5 and 2.6. Figure 3.1e shows the average energy and conduction and valence edges for a disordered semiconductor DOS.

3.2.4 Charge Extraction

Electrons and holes at the semiconductor-electrode (or interlayer) interface must be extracted from their respective phase of the BHJ through the electrodes and into the external circuit. However, when a semiconductor is brought into contact with a metal, the Fermi level of the semiconductor will bend to equilibrate with that of the metal, accomplished through the transfer of charge between the two materials [40, 41].

Figure 3.4 shows the energetic diagram for a semiconductor-metal interface (a) before and (b) after contact. The energy is referenced to the material Fermi levels to convey the thermodynamic equilibrium. The equilibrium carrier density in the semiconductor at the cathode interface will be given by

$$n_{\mathrm{Cat}} = N_c \exp\left(-\frac{\phi_{n,\mathrm{cat}}}{k_BT}\right), \quad (3.22)$$

$$p_{\mathrm{Cat}} = N_v \exp\left(-\frac{\phi_{p,\mathrm{cat}}}{k_BT}\right), \quad (3.23)$$

where $\phi_{n,\mathrm{cat}}$ ($\phi_{p,\mathrm{cat}}$) is the electron (hole) barrier at the cathode. Given by the difference between the cathode work function, $\mathrm{WF_{cat}}$, and the acceptor electron affinity, χ_{A} (donor ionization potential, $\mathrm{IP_D}$), of the OSC blend

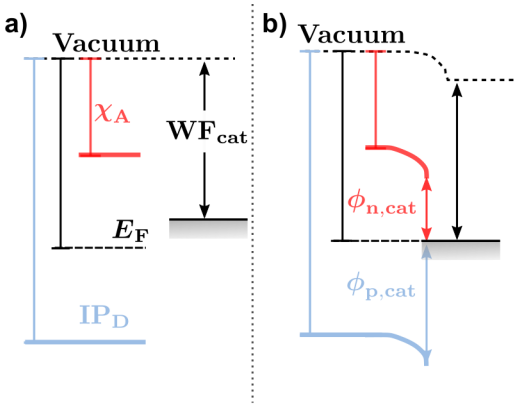

Figure 3.4: Energetics of a semiconductor-metal interface (a) before and (b) after making contact referenced to the Fermi levels.

as

$$\phi_{n,\mathrm{cat}} = \mathrm{WF}_{\mathrm{cat}} - \chi_{\mathrm{A}}, \tag{3.24}$$

$$\phi_{p,\mathrm{cat}} = -\mathrm{WF}_{\mathrm{cat}} + \mathrm{IP}_{\mathrm{D}}, \tag{3.25}$$

as shown in Figure 3.4b. In general, interfacial properties including subgap surface states or impurities at the interface may cause changes in the work function when brought into contact with a semiconductor, further modifying n_{cat} and p_{cat} [43, 124–126].

In the case of the cathode, decreasing $\phi_{p,\mathrm{cat}}$ increases the number of holes, while simultaneously decreasing the number of electrons (by increasing $\phi_{n,\mathrm{cat}}$) at the interface, assuming ideal band transport. The current of holes flowing between the cathode and the valence band in devices accurately represented by band transport can be found from thermionic emission theory as

$$J_{\mathrm{cat}\to V} = A_{\mathrm{R}} T^2 \left(1 - Q\right) \exp\left(-\frac{\phi_{p,\mathrm{cat}}}{k_B T}\right), \tag{3.26}$$

in which A_{R} is the effective Richardson Coefficient ($A_{\mathrm{R}} \sim 120$ A/cm^2/K), and Q is the reflection factor [127].

In contrast, the hole current flowing from the valence band to the cathode is typically expressed as a non-radiative relaxation process given by $J_{V\to\mathrm{cat}} = qS_{\mathrm{R}}p$, where S_{R} has units of cm/s and is known as the surface recombination velocity. Often described as carriers being removed at the 'wrong' electrode (in this case, holes at the cathode), this non-radiative loss pathways is known as surface recombination [128–136]. At thermal equilibrium these currents must be balanced indicating that the total hole current exiting the semiconductor is

$$J_p = qS_{\mathrm{R}}\left(p - p_{\mathrm{cat}}\right), \tag{3.27}$$

where p is the density of holes in the semiconductor at the interface. The associated surface recombination velocity ($S_{\mathrm{R}} = \frac{A_{\mathrm{R}}T^2}{qN_c}\left(1 - Q\right)$) has an ideal ($Q = 0$) upper limit of $\sim 10^6$ cm^2/s at 300 K, calculated from the ideal band transport-type injection expressed in Equation 3.26 [127, 135].

An electrode is considered to be ideal (Ohmic) when it is not limiting the current a device produces. To ensure this condition, the impedance of the semiconductor-electrode interface must be negligible compared to the bulk semiconductor. The primary route to accomplishing this in OPV devices is to engineer interlayers that increase the conductivity of majority carriers between the device and electrodes, effectively reducing the injection barrier [124, 125, 135]. In Chapter 7 the effect of surface recombination on the photoluminescence and electroluminescence of OPV devices will be discussed in detail.

3.3 Thermodynamic Limits of OPV-Based Solar Cells

In Section 2.3 the thermodynamic limit of a step function EQE_{PV} solar cell was found through a detailed balance approach, under the assumption that the photon interactions with the cell occur between free electron-hole pairs ($\mu_\gamma = qV_{OC}$). This is a valid assumption for inorganic semiconductors as photon absorption leads to Wannier-Mott excitons with binding energy $< k_BT$ at room temperature, easily dissociating into free charge carriers [17]. As discussed in Section 3.1, optical excitation in organic semiconductors results in tightly bound Frenkel excitons. As a result, the associated radiation field will be in equilibrium with the exciton, resulting in a separated charge carrier with chemical potential (μ_{CS}) lower than the optical gap of either organic semiconductor. The difference between chemical potential of excitons (μ_x) and μ_{CS} will depend on the binding energy of the exciton (E_B) and the entropic change due to converting excitons into separated charge carriers (ΔS) as

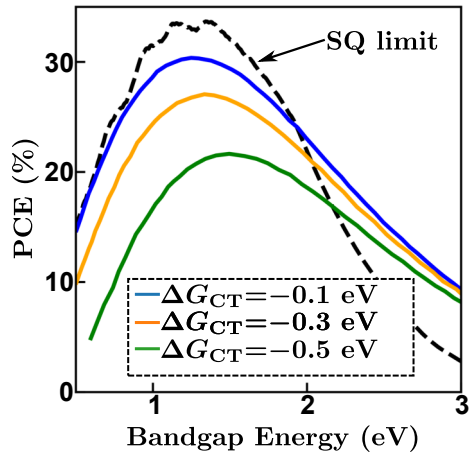

Figure 3.5: The entropic limit of excitonic solar cells calculated for various driving forces for charge separation (ΔG_{CT}).

$$(\mu_x - \mu_{CS}) = -E_B + \frac{qT_c\Delta\dot{S}}{J}, \quad (3.28)$$

where J/q is the carrier flux created by converting excitons into separated charge carriers and the dot indicates the temporal derivative, assuming every exciton reaches the donor acceptor interface [137, 138]. This change in chemical potential between excitons and separated charge carriers results in a trade off between optical gap requirements (as laid out in Section 2.3) and V_{OC}, as well as a current dependent on the difference between μ_x and μ_{CS}. Assuming exciton-to-CT state formation is the limiting reaction in OPV-based solar cells, the PCE for given exciton-to-CT state energy offset (ΔG_{CT}) can be calculated and compared to experimental results. Figure 3.5 shows the PCE calculated as a function of the optical gap for various values of ΔG_{CT}. As ΔG_{CT} approaches 0 the PCE approaches the Shockley-Queisser (free-carrier)

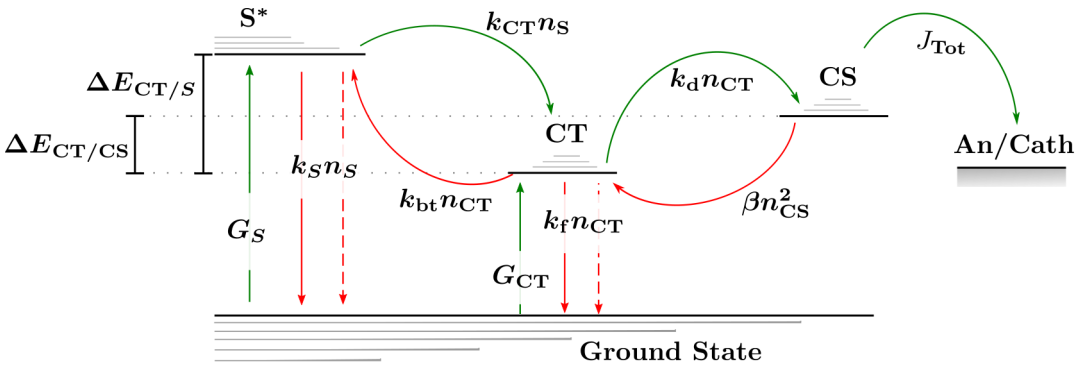

Figure 3.6: Schematic energy levels and kinetics processes for interfacial exciton S^*, charge-transfer (CT) states, and separated charge carrier (CS) states.

limit. However, experiments reveal that 0.5 eV is a more realistic value for ΔG_{CT} for fullerene OPV-based solar cells [139]. As shown in Figure 3.5, increases in ΔG_{CT} reduce the PCE significantly as well as shift the peak maximum to a bandgap of 1.5 eV [137].

This analysis assumes that PCE is dependent only on the energetics of the various states leading from excitons to separated charge carriers. However, recent advances in low-offset (low ΔG_{CT}) donor-acceptor material combinations have shown dramatic improvements in both V_{OC} and J_{SC}. On top of this, evidence suggests that separated charge carriers may be in thermal equilibrium with excitons implying that $\Delta G_{\mathrm{CT}} = 0$ [94, 140, 141]. The previous analysis would suggest that this is due to free-carrier generation in the BHJ, indicative of Wannier-Mott excitons; however, the measured binding energy of excitons in these low-offset systems indicate the opposite to be true [142–144]. It has been suggested that long enough exciton lifetimes could compensate for this lack of a driving force by increasing the time the exciton is near the interface [97]. To explore this idea, and to fully understand the factors contributing to the thermodynamic limit of PCE in OPV-based solar cells, the interplay between the excited states must be evaluated considering not only the energetics (as before) but the kinetics between states as well.

Figure 3.6 shows the stepwise process and the various rates from photon absorption to separated charge carrier extraction in BHJ OPV-based solar cells. The green arrows indicate processes that move towards separated carrier extraction while the red arrows indicate loss pathways. In the notation here S^* denotes interfacial excitonic states, G denotes rates of generation, k denotes rate constants for various processes, n denotes carrier densities in the particular state, N is the DOS of that state, β is given by Equation 3.13, $\Delta E_{i/j} = E_j - E_i$, and J_{Tot} accounts for the total charge flux between the active layer and the electrodes.

Using a detailed balance approach, the difference between μ_x and μ_{CT} can be found as [37]

$$\mu_x - \mu_{\mathrm{CT}} = k_B T \ln\left(P_S + \frac{P_s G_S}{\tilde{G}_{\mathrm{CT}}}\left[1 - P_s + \frac{k_{\mathrm{f}} N_{\mathrm{CT}}}{k_{\mathrm{CT}} N_S}\exp\left(\frac{\Delta E_{\mathrm{CT}/S}}{k_B T}\right)\right]\right), \quad (3.29)$$

where $P_S = k_{\mathrm{CT}}/(k_S + k_{\mathrm{CT}})$ and $\tilde{G}_{\mathrm{CT}}$ is the total rate at which CT states are formed from all pathways. In this picture, the difference between qV_{OC} and μ_x approaches zero when $\Delta E_{\mathrm{CT},S} = 0$ (assuming a small difference between μ_{CT} and μ_{CS}). However, even at low-offsets the imbalance between G_S and $\tilde{G}_{\mathrm{CT}}$ leads to a difference between μ_x and μ_{CT}. Further, under the influence of even a small offset, the rate of decay (k_{f}) and charge transfer (k_{CT}) play an important role in determining μ_x.

Taking this into account, the V_{OC} will depend primarily on the energy of the CT state, but with dependence on the interplay of both the kinetics (k_{f} and k_s) and energetics ($\Delta E_{\mathrm{CT}/S}$) of the exciton and CT state

$$qV_{\mathrm{OC}} = E_{\mathrm{CT}} - k_B T \ln\left(\frac{k_{\mathrm{f}} N_{\mathrm{CT}}}{\tilde{G}_{\mathrm{CT}}}\right) - k_B T \ln\left(1 + \frac{P_S k_S N_S}{k_{\mathrm{f}} N_{\mathrm{CT}}}\exp\left(-\frac{\Delta E_{\mathrm{CT}/S}}{k_B T}\right)\right). \quad (3.30)$$

While the J_{SC} can be found from the V_{OC}, the generation of charge transfer states ($J_{\tilde{G}_{\mathrm{CT}}}$), and the chemical potential of the separated charge carriers $\mu_{\mathrm{CS}} = q\left(V + \alpha V_{\mathrm{OC}}\right)/\left(1+\alpha\right)$ where $\alpha^2 = \beta G_{\mathrm{CT}} d^4 q^2 / 4\mu_n \mu_p \left(k_B T\right)^2$ as

$$J_{\mathrm{SC}} = -J_{\tilde{G}_{\mathrm{CT}}} + J_{\tilde{G}_{\mathrm{CT}}} \exp\left(V \frac{q}{\left(1+\alpha\right) k_B T}\right). \quad (3.31)$$

Finally, the FF is given by [145, 146]

$$\mathrm{FF} = \frac{V_{\mathrm{OC}}/k_B T - \ln\left(1 + V_{\mathrm{OC}}/k_B T\right)}{1 + V_{\mathrm{OC}}/k_B T}. \quad (3.32)$$

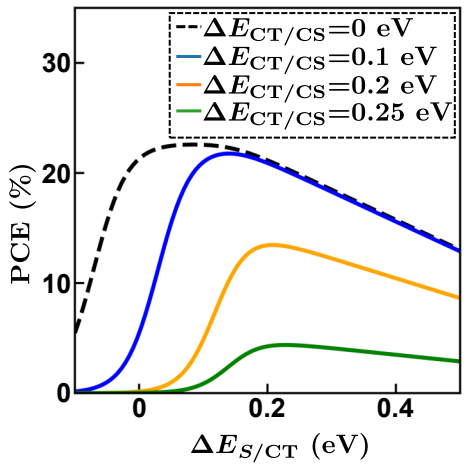

Figure 3.7: Detailed balance limit for OPV-based solar cells for various CT-to-CS state offsets as a function of exciton-to-CT state offset.

Figure 3.7 shows the calculation of PCE as a function of the exciton-to-CT state energy offset for various values of CT-to-CS state offset. As $E_{\mathrm{CT}} \to E_{\mathrm{CS}}$ this solution approaches the 'realistic' analysis in Figure 3.5 ($\Delta G_{\mathrm{CT}} \sim -0.5$ eV). In addition, as $\Delta E_{\mathrm{CT/CS}}$ increases

the maximum PCE shifts to higher $\Delta E_{\mathrm{CT}/S}$, similar to Figure 3.5. For realistic CT state binding energies ($\Delta E_{\mathrm{CT/CS}} \sim 0.15$ eV) this analysis ultimately leads to a maximum PCE $> 25\%$ with $\Delta E_{\mathrm{CT}/S} = 0.1$ eV at an optical gap of 1.5 eV [37].

This analysis indicates that both the energetics and kinetics play an important role in determining the various figures of merit in OPV-based solar cells. It demonstrates that the thermodynamic limit of an excitonic solar cell is not only dependent on the optical gap energy (as outlined in Section 2.3) but depends strongly on the interaction between the energetics of the various excited states and the kinetics occurring between them.

In Chapter 4 the role that exciton diffusion plays in the generation of charges will be explored in detail, expanding on the state diagram shown in Figure 3.6. Additional information relating to the thermodynamic calculations are included in Appendix A and reference [37].

3.4 Reciprocity in Organic Photovoltaic Devices

Equation 2.32 was derived assuming that the spatially averaged injection (F_i) and collection (F_c) efficiencies are equal across the range of voltages used [67]. A statement which is equivalent to the reciprocity relation between charge injection and extraction expressed by Equation 2.33. Both these phrasings of the injection-emission reciprocity rely on the linearity of minority carriers as the system is moved away from equilibrium (in this case as a voltage is applied) [62,67]. However, the low separated charge carrier mobilities in OPV devices present a situation where, despite the thin nature (< 100 nm) of OPV active layers, the efficiencies of injection and collection may be unequal.

A more general form of Equation 2.32 can be found by noting that the V_{OC} can be expressed as $V_{\mathrm{OC}} = k_B T/q \ln\left(J_{\mathrm{SC}}/J_0(V)\right)$, where $J_0(V)$ is the voltage-dependent dark-current. In this formulation $\eta_{\mathrm{LED}} = q\Phi_{\mathrm{em}}(V)/J_0(V)$, with $q\Phi_{\mathrm{em}}(V)$ being the voltage dependent recombination current. Which can be can be written as a function of F_i and the black-body radiation as

$$q\Phi_{\mathrm{em}}(V) = q\int_0^\infty F_i(V)\Phi_{\mathrm{bb}}dE. \tag{3.33}$$

Utilising the definition for η_{LED}, $J_0(V)$ can be written in terms of F_i as

$$J_0(V) = \frac{q\Phi_{\mathrm{em}}(V)}{\eta_{\mathrm{LED}}} = \frac{q\int_0^\infty F_i(V)\Phi_{\mathrm{bb}}dE}{\eta_{\mathrm{LED}}}. \tag{3.34}$$

Accordingly, the exact V_{OC} found from η_{LED} measurements, assuming that F_i is

known, would be given by

$$V_{\mathrm{OC}} = \frac{k_B T}{q} \ln\left(\frac{J_{\mathrm{SC}}\eta_{\mathrm{LED}}}{q\int_0^\infty F_i\left(V_{\mathrm{OC}}\right)\Phi_{\mathrm{bb}}dE}\right). \tag{3.35}$$

Under the assumption that reciprocity holds ($F_c = F_i$), the predicted V_{OC} will be given by

$$V_{\mathrm{OC,Predicted}} = \frac{k_B T}{q} \ln\left(\frac{J_{\mathrm{SC}}\eta_{\mathrm{LED}}}{q\int_0^\infty F_c\left(V_{\mathrm{OC}}\right)\Phi_{\mathrm{bb}}dE}\right). \tag{3.36}$$

The deviation of $V_{\mathrm{OC,Predicted}}$ from the actual V_{OC} can then be expressed in terms of F_c and F_i as

$$\delta V_{\mathrm{OC}} = V_{\mathrm{OC,Predicted}} - V_{\mathrm{OC}} = \frac{k_B T}{q} \ln\left(\frac{F_i\left(V_{\mathrm{OC}}\right)}{F_c\left(V_{\mathrm{OC}}\right)}\right). \tag{3.37}$$

Equation 3.37 indicates that while reciprocity holds $\delta V_{\mathrm{OC}} = 0$. However, when the injection and collection efficiencies diverge the electroluminescence no longer accurately represents the non-radiative photovoltage loss under steady-state illumination, open-circuit conditions. Figure 3.8 shows the V_{OC}, $V_{\mathrm{OC,Predicted}}$, and the δV_{OC} calculated as a function of separated charge carrier mobility [67]. As electron and hole mobilities are decreased carriers near the center of the device are no longer extracted, decreasing F_c. At the same time, injected carriers will decay with a similar efficiency leading to $\delta V_{\mathrm{OC}} < 0$.

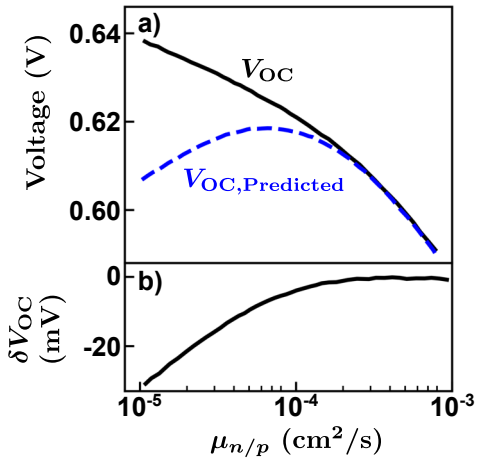

Figure 3.8: (a) V_{OC} and $V_{\mathrm{OC,Predicted}}$ calculated from Equation 3.35 and 3.36. (b) Deviation between V_{OC} and $V_{\mathrm{OC,Predicted}}$.

Chapter 7 will expand on the idea that reciprocity can be invalid in certain systems relevant to OPV devices. The deviation from reciprocity will be examined as a deviation in QFLS from the ideal case in which the separated charge carriers are in equilibrium with μ_γ across the device and the contacts. Traditional measurements of η_{LED} will be compared to an alternative technique which, as will be shown, can accurately quantify the QFLS of a photovoltaic device under steady-state illumination at V_{OC}

Chapter 4

Role of Exciton Diffusion and Lifetime in Low Energy Offset Systems

Despite general agreement that the generation of separated charge carriers in organic photovoltaic device devices is driven by an energetic offset, power conversion efficiencies have been improved using low-energy offset blends. In this chapter, the interconnected roles that exciton diffusion and lifetime play in the charge generation process under various energetic offsets is discussed. A detailed balance approach is used to develop an analytic framework to discuss exciton dissociation and separated charge carrier generation accounting for exciton diffusion to and dissociation at the donor-acceptor interface. For low-offset systems, it is found that the exciton lifetime is a pivotal component in the charge generation process, as it influences both the exciton and charge transfer state dissociation. These findings suggest that any novel low-offset material combination must have long exciton diffusion lengths with long exciton lifetimes to achieve optimum charge generation yields. The work presented in this chapter (in conjunction with Appendix A) is the same as that published in *Role of Exciton Diffusion and Lifetime in Organic Solar Cells with a Low Energy Offset* [1].

4.1 Diffusion and Charge Transfer State Generation in Low-Offset Systems

The recent rise in PCEs of OPV-based solar cells has been driven by the introduction of narrow-gap NFA molecules, which show enhanced photon absorption of the solar spectrum when used in conjunction with an appropriate and complementary donor molecule [17]. This increase in absorption combined with a superior CGY observed in state-of-the-art NFA-based BHJs ultimately cumulates in short-circuit currents much higher than their fullerene-based predecessors [17, 147–149]. Concurrently, the reduction of energetic offset between donor and acceptor molecules in low-offset NFA BHJs has reduced losses associated with the V_{OC} [140, 150]. Specifically, low-offset NFA systems have small energetic differences between the IPs of the donor and acceptor molecules. As such, the increase in PCE of NFAs, compared to fullerene blends, is ascribable to both the reduction of losses to the V_{OC}, brought about by low IP-offsets, and the increase in J_{SC}, supported by high CGYs.

The charge generation process in OPV devices, as described in Chapter 3, and the thermodynamic treatments of OPV-based solar cells, as presented in Section 3.3, ignore the role that exciton diffusion plays in generating separated charge carriers. Authors often assume that the exciton diffusion length is much larger than the phase separated domains making diffusion to the interface efficient, or that all excitons are generated near enough the donor-acceptor interface to undergo charge transfer [37, 137, 138]. While it is widely accepted that increasing the exciton diffusion length enhances the exciton dissociation (via more efficient transfer of excitons to the interface), the influence of exciton diffusion on the charge transfer efficiency at the interface is not fully understood. During exciton dissociation, the transfer of an electron (hole) from the donor (acceptor) to the acceptor (donor) phase during channel I (II) charge transfer has been historically understood to be driven by an energetic offset between the χ (IP) levels of the two materials [17, 90, 141, 151, 152]. In NFA-based low-offset systems, the driving force to dissociate excitons into CT states at the interface is expected to be small due to the reduced energetic offset. Nonetheless, this has not resulted in a reduction in the CGY, but instead, near unity CGYs have been observed in state-of-the-art low-offset systems [149]. Contributing to the understanding of how NFA BHJs can achieve high CGY in the absence of a significant IP-offset is the motivation behind the work presented in this chapter and a necessary step to further progressing the PCEs of OPV-based solar cells past 20%.

While a decreasing IP-offset is expected to reduce energetic losses to the V_{OC}, recent studies have also shown reduced nonradiative voltage losses in low-offset NFA OPV-based solar cells attributable to an equilibrium between excitons lo-

calised to the acceptor phase and CT states [94, 141]. On the other hand, it has been suggested that the decreasing driving force for exciton dissociation, brought about through decreasing IP-offset, can be compensated for with increasing exciton lifetime [140, 153]. Further, as presented in Section 3.3, photovoltaic parameters are contingent on not only the relative energetics of the donor and acceptor molecules but also the kinetic rate constants between excitons, CT states, and CS states. Including the interplay between the lifetimes of excitons and CT states as well as the degree of equilibrium between the two states [37]. However, these analyses assume that each exciton generated in the bulk dissociates into a CT state via charge transfer at a rate independent of exciton diffusion.

In the work summarised in this chapter, the role of exciton diffusion in exciton dissociation and charge generation yield of low-offset OPV devices is investigated. An expression for the exciton dissociation efficiency and effective charge transfer rate constant is derived accounting for exciton diffusion to and dissociation at the interface. Using this expression, it is clarified under what conditions a system with low driving force for CT state formation can achieve high charge generation yield. It is found that, in low-offset systems, long exciton lifetimes serve a twofold purpose: to increase diffusion to the interface and to reduce the rate of back-transfer of CT states to excitons. Therefore, large exciton diffusion lengths supported by long exciton lifetimes are required for efficient charge generation in low-offset systems.

4.2 Theoretical Treatment of Steady-State Diffusion

The process of singlet exciton dissociation is mediated by two steps: (i) diffusion of excitons to the donor-acceptor interface and (ii) charge transfer at the interface with rate constant $k_{\mathrm{CT},0}$. In the case of excitons in the donor (acceptor) phase, $k_{\mathrm{CT},0}$ is the electron (hole) transfer rate constant associated with channel I (II) charge generation. In the limit where diffusion to the interface is efficient the exciton dissociation rate is independent of diffusion. In this limit, the exciton dissociation efficiency (P_S or dissociation efficiency) is given by the charge transfer efficiency (η_{CT}) of excitons at the interface, described by the competition between the interfacial charge transfer rate constant and the exciton lifetime within the limiting phase as

$$\eta_{\mathrm{CT}} = \frac{k_{\mathrm{CT},0}}{1/\tau + k_{\mathrm{CT},0}}. \tag{4.1}$$

In general, away from the diffusion independent limit, the effective rate of exciton dissociation will be given by processes (i) and (ii) occurring in series. To

derive an expression for P_S and effective charge transfer rate constant, accounting for exciton diffusion to and charge transfer at the interface, consider a domain of length L, spanning $0 < x < L$, in which excitons are uniformly generated at rate G. Figure 4.1 shows a schematic state diagram and the relevant rates of diffusion, decay, charge transfer, and CT state-to-exciton back-transfer for a singlet exciton in either the donor or acceptor phase. Under these conditions, the diffusion equation for excitons in the bulk takes the form

$$G - \frac{n(x)}{\tau} + D\frac{d^2n(x)}{dx^2} = 0, \tag{4.2}$$

where $n(x)$ is the exciton density at position x in the domain. To account for exciton-to-CT state dissociation and CT state-to-exciton back-transfer, the exciton current leaving the domain at the interfaces can be expressed as

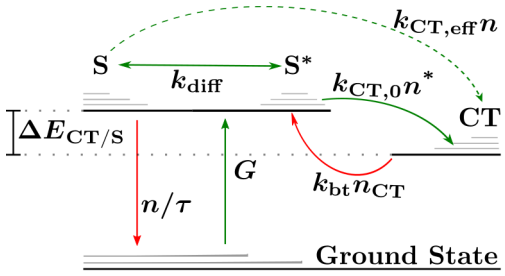

Figure 4.1: Schematic energy-level diagram showing relevant kinetics and processes occurring for bulk (S) and interfacial (S*) excitons and charge-transfer states (CT). Here, k_{diff} represents the rate constant of diffusion from bulk to interfacial excitonic states, $k_{CT,0}$ is the electron or hole transfer rate constant from interfacial excitons-to-CT states, $k_{bt}n_{CT}$ is the rate of back-transfer from CT states to excitons, τ is the exciton lifetime, G is the rate of exciton generation, and $k_{CT,eff}$ is the effective dissociation rate constant for all excitons.

$$-D\left.\frac{dn(x)}{dx}\right|_{x=L} = \nu\left[n(L) - n^*_{bt}\right], \tag{4.3}$$

$$-D\left.\frac{dn(x)}{dx}\right|_{x=0} = -\nu\left[n(0) - n^*_{bt}\right], \tag{4.4}$$

with ν being the interfacial velocity of charge transfer from one phase to the other and νn^*_{bt} being the exciton current entering the domain via back-transfer from CT states. Here, n^*_{bt} is an effective density that depends on the prevailing density of CT states at the interface but is independent of x. The solution to Equations 4.2-4.4 is obtained as

$$n(x) = G\tau - \frac{\left[G\tau - n^*_{bt}\right]\cosh\left(\frac{x-L/2}{L_D}\right)}{\cosh\left(\frac{L}{2L_D}\right)\left[1 + \frac{D}{\nu L_D}\tanh\left(\frac{L}{2L_D}\right)\right]} \tag{4.5}$$

where $L_D = \sqrt{D\tau}$ is the one-dimensional exciton diffusion length.

However, Equation 4.2 does not explicitly contain the exciton-to-CT state charge transfer and CT state-to-exciton back-transfer rates, while Equation 4.5 strongly depends on the position within the domain. Therefore, to obtain a general rate equation that relates excitons in the bulk to excitons at the interface, one can average Equation 4.2 across the domain to obtain

$$G - \frac{n}{\tau} - k_{\mathrm{CT},0}\left[n^* - n^*_{\mathrm{bt}}\right] = 0, \tag{4.6}$$

where $n = (1/L)\int_0^L n(x)dx$ is the average density of bulk excitons, n^* is the density of excitons at the interfaces, and $k_{\mathrm{CT},0} = 2\nu/L$. Evident in Equation 4.6 is that the CT state-to-exciton back-transfer rate can be equivalently expressed as $k_{\mathrm{CT},0}n^*_{\mathrm{bt}}$ or $k_{\mathrm{bt}}n_{\mathrm{CT}}$ (as shown in Figure 4.1, where n_{CT} is the density of CT states and k_{bt} is the associated back-transfer rate constant). At thermal equilibrium, the exciton-to-CT state and CT state-to-exciton rates must balance, $k_{\mathrm{bt}}n_{\mathrm{CT,eq}} = k_{\mathrm{CT},0}n^*_{\mathrm{eq}}$, leading to

$$n^*_{\mathrm{bt}} = n_{\mathrm{CT}}\frac{N_S}{N_{\mathrm{CT}}}\exp\left(-\frac{\Delta E_{\mathrm{CT}/S}}{k_{\mathrm{B}}T}\right) \tag{4.7}$$

where N_{S} (N_{CT}) are available density of states for the lowest exciton (CT) states, while $n^*_{\mathrm{eq}} = N_{\mathrm{S}}\exp\left(-\frac{E_{\mathrm{S}}}{k_{\mathrm{B}}T}\right)$, and $n_{\mathrm{CT,eq}} = N_{\mathrm{CT}}\exp\left(-\frac{E_{\mathrm{CT}}}{k_{\mathrm{B}}T}\right)$. Additionally, at thermal equilibrium, the net diffusion current of excitons must vanish such that $n = n^* = n^*_{\mathrm{bt}}$, in accordance with detailed balance.

After accounting for this, Equation 4.6 can be equivalently expressed in terms of n as

$$G - \frac{n}{\tau} - k_{\mathrm{CT,eff}}\left[n - n^*_{\mathrm{bt}}\right] = 0, \tag{4.8}$$

where

$$k_{\mathrm{CT,eff}} = \frac{k_{\mathrm{CT},0}}{1 + (\tau \times k_{\mathrm{CT},0})\left[\frac{1-\eta_{\mathrm{Diff}}}{\eta_{\mathrm{diff}}}\right]} \tag{4.9}$$

is the effective charge transfer rate constant for excitons generated within the domain, and η_{diff} is the efficiency of exciton diffusion to the interface given by

$$\eta_{\mathrm{diff}} = \frac{2L_D}{L}\tanh\left(\frac{L}{2L_D}\right). \tag{4.10}$$

Finally, the overall exciton dissociation efficiency, defined as the number of dissociated excitons relative to the total number of generated excitons can be found as

$$P_S = \frac{k_{\mathrm{CT,eff}}}{1/\tau + k_{\mathrm{CT,eff}}} = \left[\frac{1}{\eta_{\mathrm{diff}}} + \frac{1}{\eta_{\mathrm{CT}}} - 1\right]^{-1}, \tag{4.11}$$

where Equations 4.1 and 4.9 were used in the last step. Note that P_S is not given by the simple product of the diffusion and dissociation efficiencies, indicating that processes (i) and (ii) are not independent.

4.3 Considerations for CT-state Generation

To substantiate Equations 4.9 and 4.11, a 1D Monte-Carlo hopping model was implemented to simulate the exciton kinetics including diffusion, decay, and interfacial charge transfer. Monte-Carlo simulations were used, as they have been shown to accurately account for exciton dynamics within OSCs and OPV BHJs [2, 119, 154–157]. Furthermore, the use of Monte-Carlo simulations allows for the calculation of the exciton dissociation efficiency and $k_{\mathrm{CT,eff}}$ under conditions where the phase separated domain size, interfacial charge transfer rate constant, exciton lifetime, and exciton diffusion constant are known precisely. The simulated P_S and $k_{\mathrm{CT,eff}}$ can then be compared to Equation 4.9 and 4.11. Further details relating to the simulations used in this chapter are outlined in Appendix A.1. The exciton dissociation efficiency was calculated as the ratio of excitons exiting the domain at the interfaces to the total number of excitons generated in the simulation, from which the effective charge transfer rate constant can be calculated through Equation 4.11. In this formalism, the characteristic length ratio (defined as $2L_D/L$) and the lifetime-product (defined as $\tau \times k_{\mathrm{CT},0}$) can be controlled by specifying L and $k_{\mathrm{CT},0}$, respectively, while leaving the exciton lifetime and diffusion constant unaffected. It is important to note that, in general, these two metrics are not independent, as increases in the exciton lifetime will affect both the lifetime-product and the diffusion length. The effect on these metrics of changing the D and τ are discussed throughout the remainder of this chapter. In these simulations, $\tau = 300$ ps, while $D = 5 \times 10^{-3}$ cm^2/s, leading to $L_D = 12$ nm.

Figure 4.2 shows the normalised $k_{\mathrm{CT,eff}}$ and P_S as a function of the lifetime-product for selected diffusion efficiencies, determined by the characteristic length ratio through Equation 4.10, and the characteristic length ratio for various charge-transfer efficiencies, determined by the lifetime-product through Equation 4.2. The circles indicate values from the Monte-Carlo simulations, while the colored lines indicate Equations 4.9 and 4.11 plotted with the associated values of τ, $k_{\mathrm{CT},0}$,

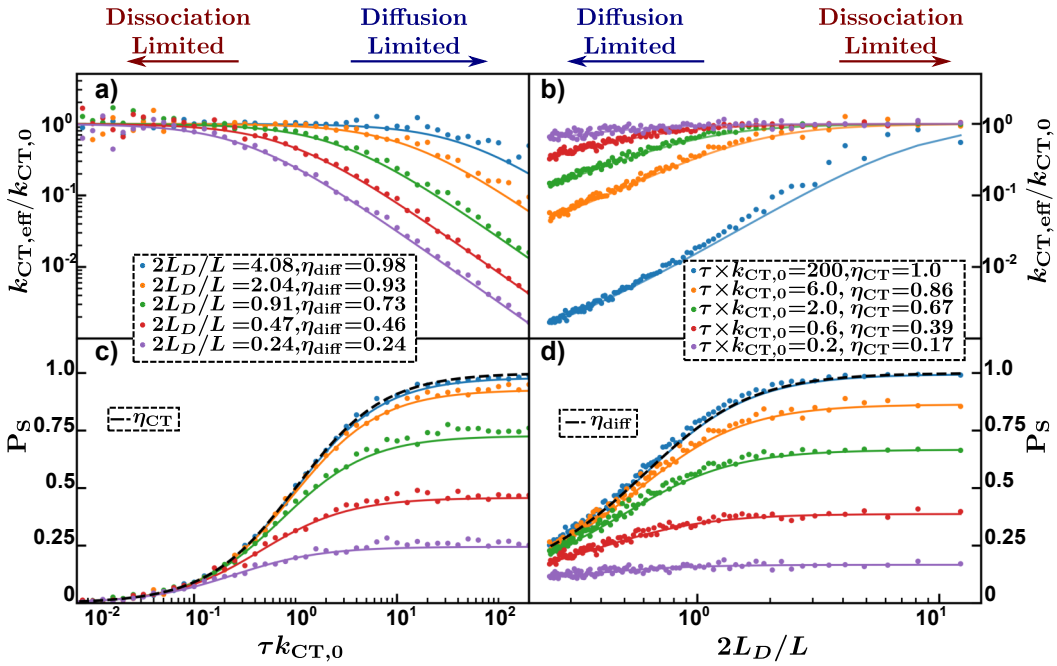

Figure 4.2: (Top) Normalised $k_{\mathrm{CT,eff}}$ and (Bottom) P_S as a function of (left) lifetime-product and (right) the characteristic length ratio. Circles indicate Monte-Carlo simulations, solid lines indicate Equations 4.9 and 4.11, black dashed lines indicate Equations 4.1 and 4.10.

L, and D. The analytic solution provided by Equations 4.9 and 4.11 reproduces the simulated P_S and $k_{\mathrm{CT,eff}}$ over the range of parameters used. As noted above, exciton dissociation can be limited by two distinct processes: diffusion to the interface and dissociation at the interface. As will be shown below, both these processes must be efficient for excitons generated in the domain to be dissociated efficiently.

Under conditions when either $\tau \times k_{\mathrm{CT,0}}$ is small or $2L_D/L$ is large, corresponding to $\eta_{\mathrm{CT}} \ll \eta_{\mathrm{diff}}$ or $\eta_{\mathrm{diff}} \to 1$, respectively, the overall dissociation rate of excitons is dissociation limited. As indicated on the left-hand side of Figure 4.2a and right-hand side of Figure 4.2b, this limit is characterised by $k_{\mathrm{CT,eff}} \to k_{\mathrm{CT,0}}$. Under these conditions, the dissociation at the interface is the rate-limiting process, and according to Equation 4.11, $P_S = \eta_{\mathrm{CT}}$ (indicated by the black dashed line in Figure 4.2c). In the dissociation limited regime, P_S is strongly dependent on lifetime-product, asymptotically approaching $P_S = 0$ with decreasing lifetime-product. Conversely, under conditions when $\tau \times k_{\mathrm{CT,0}}$ is large (right-hand side of Figure 4.2a and c) or $2L_D/L$ is small (left-hand side of Figure 4.2b and d), corresponding to $\eta_{\mathrm{CT}} \to 1$ or $\eta_{\mathrm{diff}} \ll \eta_{\mathrm{CT}}$, respectively, the exciton dissociation is

diffusion limited. In this limit, diffusion to the interface is the rate-limiting process, resulting in $k_{\mathrm{CT,eff}}/k_{\mathrm{CT,0}} \ll 1$ and $P_S = \eta_{\mathrm{diff}}$ (indicated by the black dashed line in Figure 4.2d). In this limit, P_S is dependent only on the characteristic length ratio and approaches $P_S = 0$ for a diminishing characteristic length ratio, as excitons are unable to diffuse to the interface. Finally, under conditions when both $\tau \times k_{\mathrm{CT,0}}$ and $2L_D/L$ exceed unity, shown on the right-hand sides of Figure 4.2c as $\eta_{\mathrm{diff}} \to 1$ and Figure 4.2d as $\eta_{\mathrm{CT}} \to 1$, eventually $P_S \to 1$.

This analysis is summarised in Figure 4.3, which shows the simulated P_S (Figure 4.3a) and $k_{\mathrm{CT,eff}}$ (Figure 4.3b) as a function of the lifetime-product and the characteristic length ratio. Indicated on Figure 4.3 is the diffusion and dissociation limits. For a dissociation limited system, changes to the characteristic length ratio will not significantly affect $k_{\mathrm{CT,eff}}$ or P_S. This can be recognised by moving vertically in Figure 4.3 in the dissociation limited regime. Similarly, for a diffusion limited system, changes to the lifetime-product will not significantly alter $k_{\mathrm{CT,eff}}$ or P_S. This can be recognised by moving horizontally in Figure 4.3 in the diffusion limited regime.

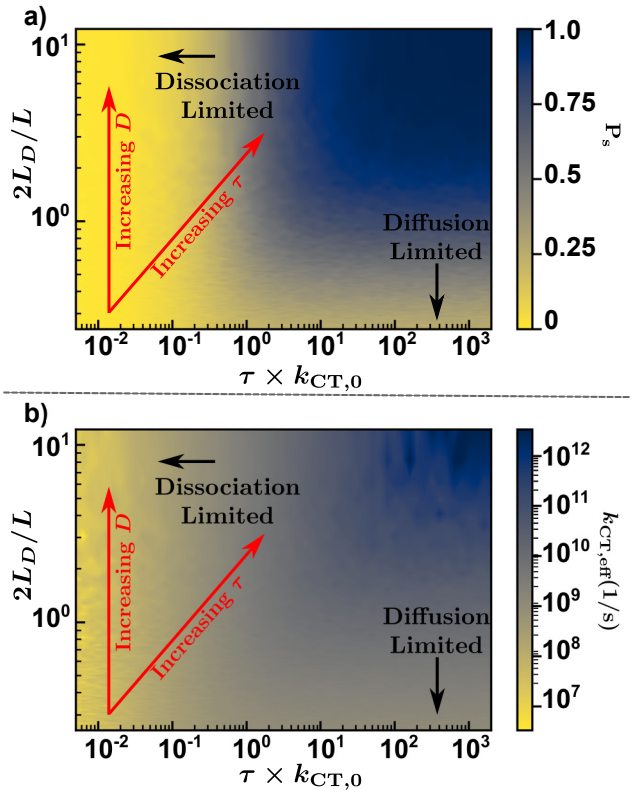

Figure 4.3: (a) Exciton dissociation efficiency and (b) effective charge transfer rate constant as a function of characteristic length ratio and lifetime-product. Red lines indicate the direction a system will move for an increasing exciton diffusion constant and lifetime.

These observations highlight the primary thesis of this chapter: to efficiently dissociate excitons into CT states, the phase limiting charge generation must simultaneously have efficient diffusion to and dissociation at the interface, enabled by high lifetime-products and characteristic length ratios. The former can be increased by increasing the exciton lifetime or increasing $k_{\mathrm{CT,0}}$. The latter can be increased by increasing L_D, via increases in τ

or D, or by decreasing the phase separated domain size [158,159]. Therefore, the exciton lifetime plays a crucial role in determining the exciton dissociation efficiency, as increases in exciton lifetime increase both the characteristic length ratio and lifetime-product. This observation agrees with previous experimental studies by other researchers [140]. Despite this, the diffusion constant plays an equally important role in determining the characteristic length ratio and therefore is important in determining the diffusion efficiency, the dissociation efficiency, and effective charge transfer rate constant. This is highlighted by the red lines in Figure 4.3. Increases in diffusion constant lead to increases in the characteristic length ratio, manifesting in a vertical transition in Figure 4.3, while increases in the exciton lifetime increase both the characteristic length ratio as well as the lifetime-product, signified by the sloped red lines in Figure 4.3.

4.4 Influence of Exciton Lifetime and Diffusion on Charge Generation Yield

To explore the effects that exciton diffusion has on the device performance of OPV devices, the charge generation yield was calculated. Here, the charge generation yield (P_{CGY}) is defined as the ratio of generated CS states to the total number of generated excitons. To calculate P_{CGY}, the kinetic interplay between excitons, CT states, and CS states is considered, as described in Section 3.3 and Appendix A.2. After accounting for the generation, recombination, reformation, and dissociation of CT states and excitons, summarised in Figure 4.4a, it is found that $P_{\mathrm{CGY}} = P_S P_{\mathrm{CT}}$ where $P_{\mathrm{CT}} = k_d/(k_d + k_f + k'_{\mathrm{bt}})$ denotes the CT state-to-CS state dissociation efficiency. Further, k_d is the CT state dissociation rate constant, k_f is the CT state recombination rate constant, and $k'_{\mathrm{bt}} = (1 - P_S)k_{\mathrm{bt,eff}}$. Finally, $k_{\mathrm{bt,eff}}$ is the effective CT-to-exciton back-transfer rate constant related to $k_{\mathrm{CT,eff}}$ via $k_{\mathrm{bt,eff}} = (n^*_{\mathrm{bt}}/n_{\mathrm{CT}})k_{\mathrm{CT,eff}}$; hence,

$$k'_{\mathrm{bt}} = \frac{P_S N_{\mathrm{S}}}{\tau N_{\mathrm{CT}}} \exp\left[-\frac{\Delta E_{\mathrm{CT}/S}}{k_{\mathrm{B}} T}\right] \tag{4.12}$$

in accordance with Equations 4.7 and 4.9. Consequentially, CT states generated directly from the ground state or via interfacial charge transfer may form excitons via this back-transfer mechanism and reform CT states many times over. The idealised case for P_{CGY} with efficient diffusion, corresponding to $\eta_{\mathrm{diff}} = 1$, is shown for a high interfacial charge-transfer rate in the dashed black line in Figure 4.4 b. The calculated P_{CGY} as a function of the exciton-to-CT state energetic offset ($\Delta E_{\mathrm{CT}/S}$) is summarised in Figure 4.4b,c for the lifetime-products $\tau \times k_{\mathrm{CT},0} \gg 1$ and $\tau \times k_{\mathrm{CT},0} = 1$, respectively, assuming a domain size of 10 nm. In the case of a

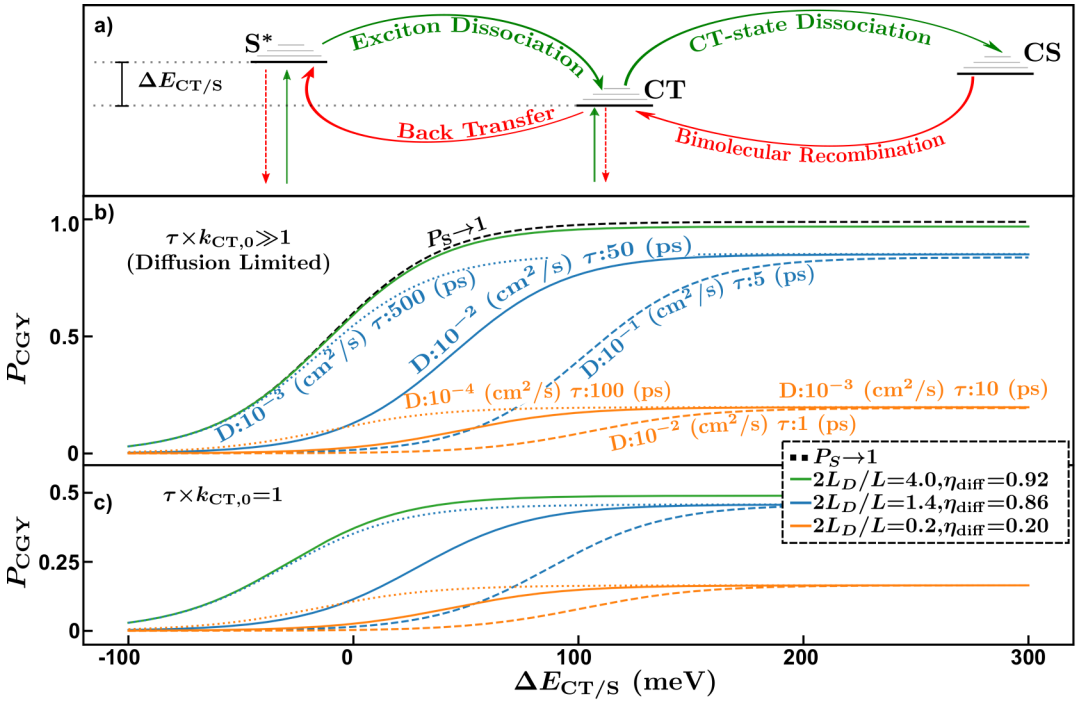

Figure 4.4: ((a) Schematic energy-level diagram summarising the work of Sandberg et al [37]. Labelled are interfacial excitonic states (S*), charge-transfer states (CT), and charge separated states (CS), as well as the varying pathways between them and to the ground state (vertical arrows). Charge generation yield calculated from detailed balance as a function of exciton-to-CT state offset for a system with (a) large and (b) unity lifetime-products. The black dashed line indicates the conclusion of Sandberg et al. Colors of lines indicate the characteristic length ratios. Moving from dotted to solid to dashed lines indicates increasing exciton diffusion constant and decreasing exciton lifetime.

high lifetime-product (equivalent to the diffusion limited regime), Equation 4.11 simplifies to $P_S = \eta_{\text{diff}}$. Therefore, as the characteristic length ratio is increased, exciton dissociation is increased. This results in an increase in P_{CGY} with an increasing characteristic length ratio independent of $\Delta E_{\text{CT/S}}$, generally seen by comparing the different colored lines in Figure 4.4b. Interestingly, in the high-offset limit ($\Delta E_{CT/S} > 200$ meV) P_{CGY} is dependent on the characteristic length ratio yet agnostic to the individual values of τ and D. This effect can be observed by comparing lines of the same color in the high offset region of Figure 4.4b,c. On the other hand, for low-offset systems ($\Delta E_{CT/S} < 200$ meV), the CT state-to-exciton back-transfer plays a more central role in determining the P_{CGY}. In this case, the rate of CT states undergoing back-transfer to form excitons is much

higher, which in turn increases the likelihood that excitons will reform and decay. Therefore, it is expected that a higher τ will decrease the number of CT states that recombine to the ground state via an excitonic state by the back-transfer mechanism and, in turn, increase the P_{CGY}. This effect is evident in comparing the dotted (longest τ), solid (middle τ), and dashed (shortest τ) lines of the same color (equivalent L_D) in the low-offset region of Figure 4.4b. In this region, P_{CGY} for identical characteristic length ratios is increased with increasing exciton lifetime due to decreasing CT state-to-exciton back-transfer.

This highlights the secondary thesis of this chapter; in low-offset systems, high exciton lifetimes increase not only the exciton dissociation through increased diffusion length, as shown by other researchers in previous experimental studies [140, 153] but additionally increase the P_{CGY} by ultimately decreasing the rate of CT state-to-exciton back-transfer. The inverse relationship between the CT state-to-exciton back-transfer rate and the exciton lifetime is expressed explicitly in Equation 4.12. Figure 4.4c shows the equivalent analysis for systems with the same characteristic length ratios but with a lifetime-product of unity, corresponding to $\eta_{\mathrm{CT}} = 0.5$. Under these conditions, the exciton dissociation efficiency is expressed as $P_S = \eta_{\mathrm{diff}}/\left(1 + \eta_{\mathrm{diff}}\right)$, resulting in a maximal efficiency of 0.5. In general, decreases in τ will decrease the exciton dissociation efficiency via decreases to both the characteristic length ratio, as described above, and the lifetime-product. This additional effect is equivalent to excitons reaching the interface but being unable to dissociate into CT states, effectively 'reflecting' off the interface. Therefore, even in the case of high characteristic length ratios and high energetic offsets, such as that shown by the green curve in Figure 4.4 c, the P_{CGY} is reduced via reductions to the $k_{\mathrm{CT,eff}}$.

4.5 Conclusion

In conclusion, the role that exciton diffusion plays in exciton dissociation in BHJ OPV devices was investigated and analytic expressions for the exciton dissociation efficiency and the effective dissociation rate constant were derived. This analysis revealed that the exciton dissociation efficiency is determined by the efficiency of exciton diffusion to the interface (determined by the characteristic length ratio, $2L_D/L$) and the charge-transfer efficiency at the interface (determined by the lifetime-product, $\tau \times k_{\mathrm{CT},0}$). The expression for exciton dissociation efficiency was used to calculate the theoretical charge generation yield in BHJ OPV-based solar cells. For high-offset systems, it was found that the charge generation yield is governed by the characteristic length ratio and that the individual values of exciton lifetime and diffusion coefficient were inconsequential. However, in low-offset systems, the exciton lifetime influences not only the characteristic

length ratio but also the rate of back-transfer from CT states to excitons. This suggests that CGY in low-offset blends could be increased by focusing on low-offset blends with long diffusion length supported by increased exciton lifetimes. Systems of this type would increase the diffusion of excitons to the interface while simultaneously reducing CT state-to-exciton back-transfer losses.

Unfortunately for researchers, measuring exciton diffusion length and exciton diffusion constant in organic semiconductor is a difficult process. In Chapter 5 various methods for determining exciton diffusion lengths and exciton diffusion constants will be discussed, highlighting experimental difficulties. An alternative technique will be introduced that avoids these difficulties while increasing the ease and speed of the measurement. Interestingly, low-offset NFAs organic semiconductors will be found to show a significant increase in exciton diffusion length compared to their fullerene predecessors, which would help to explain the improvements in CGY. However, it will be shown that, the increased L_D in non-fullerene acceptor OSCs is due to increases in D, not τ, consistent with other authors in previous experimental reports [160–162]. This result, coupled with the work developed in this chapter, indicates that the low-offset blends are not optimised to reduced CT state-to-exciton back-transfer.

Chapter 5

Quasi-Steady-State Measurement of Exciton Diffusion Lengths

In Chapter 4 the importance of exciton diffusion length in the charge generation yield process was emphasised. It was shown that optimised low-offset OPV devices would require long exciton diffusion length with maximal exciton lifetime. Established methods for quantifying exciton diffusion lengths in OSCs require specialised equipment designed for measuring high-resolution time-resolved photoluminescence (TRPL). In this chapter an approach, named pulsed-PLQY, is introduced to determine the exciton diffusion length in OSCs without any temporal measurements. Using a Monte-Carlo model the exciton dynamics within a thin-film semiconductor are simulated and the results are analysed using both pulsed-PLQY and TRPL methods. It is found that pulsed-PLQY has a larger operational window and depends less on the excitation fluence than the traditional TRPL approach. The simulated results are validated experimentally on a well-studied organic semiconductor, after which pulsed-PLQY is used to evaluate the exciton diffusion length in a variety of technologically relevant materials. It is found that the diffusion lengths in NFAs are much larger than in the benchmark fullerene and that this increase is mainly driven by an increase in exciton diffusion constant, not lifetime. The work presented in this chapter (in conjunction with Appendix B) is the mostly identical as that published in *Quasi-Steady-State Measurement of Exciton Diffusion Lengths in Organic Semiconductors* [2]. Figure 5.3 was added to the published text, along with some additional explanation, to aid the reader in their understanding of pulsed-PLQY.

5.1 Measuring Exciton Diffusion Lengths

As outlined in Chapter 4, the lack of driving force for charge separation in low-offset OPV-blends can be compensated for by an increase in exciton lifetime or diffusivity, increasing the attempt frequency of CT-state formation. Thorough understanding of exciton dynamics within the donor and acceptor lattices and exciton kinetics at the donor acceptor interface is essential to explain the high charge generation yields in low-offset NFA OPV devices.

While exciton lifetimes can be discerned from TRPL measurements, measuring exciton diffusion constants is not as straightforward. Exciton diffusion constants in OSCs can be determined through a variety of optical methods including fluorescence volume [163–165] or bi-layer [163, 166–173] quenching, and exciton-exciton annihilation (EEA) measurements [165, 173–181]. A robust quenching experiment requires the fabrication of multiple films with varying thickness, detailed measurement of optical constants, a precise understanding of both the heterostructure and the quenching mechanism, and in the case of steady-state measurements the absolute value of the photoluminescence quantum efficiency (η_{PL}). In contrast, EEA approaches require only one film with spectrally understood absorbance, do not require absolute η_{PL} measurements, and are less sensitive to both optical interference effects and long-range quenching mechanisms such as Förster energy transfer [182]. Further, EEA studies provide additional insight into exciton dynamics by observing exciton-exciton interactions at high excitation densities. This ancillary information allows for the determination of the exciton-exciton annihilation coefficient (γ), important to the field of organic lasing, and the so called exciton capture radius, defined as the average distance at which excitons annihilate.

In the majority of experimental reports employing EEA, γ is measured through linearising TRPL data at high excitation densities, while the capture radius is assumed to be on the order of the molecular spacing (R_0), allowing for the calculation of the low-density diffusion length [173, 174, 176, 177]. In some studies authors further compare diffusion length and exciton-exciton annihilation coefficient from two independent methods to gain insight into the capture radius, however; this requires the assumption of a perfect quenching molecule or interface [173,178,180]. Still others use global fitting techniques, including the capture radius as either a fitting parameter or an assumed value [165, 180, 181]. Recent studies found the lamellar spacing (d_{100}) measured by grazing-incident wide-angle X-ray scattering (GIWAX) experiments to be a close estimation of the capture radius [180]. Although a reliable method for determining the capture radius is yet to be agreed upon, EEA has been a useful tool in determining the exciton diffusion length of many organic semiconductors [182].

In the work contributing to this chapter, the limitations of EEA experiments are explored by evaluating the density dependence of the diffusion length extracted from TRPL linearisation using a Monte-Carlo hopping model. Then an alternative EEA approach, which does not require any temporal measurements and instead focuses on the photoluminescence quantum efficiency, termed pulsed-photoluminescence quantum yield (pulsed-PLQY), is proposed and demonstrated via the same Monte-Carlo simulations. The use of Monte-Carlo simulations allows for the identification of operational windows, defined as the range of densities over which each analysis of the simulated kinetics reproduces the input diffusion length. It is found that, even in the ideal case, pulsed-PLQY has a larger operational window and is less sensitive to the choice of initial exciton density compared to the traditional TRPL linearisation technique. TRPL linearisation and pulsed-PLQY are performed on the well-studied P3HT system and compared (for a list of chemical acronyms used in this chapter see Appendix B.1.1). Both experiments reproduce the trends predicted by the simulations. Overall it is found that pulsed-PLQY is less dependent on the excitation fluence, is faster, easier, and requires less specialised equipment compared to traditional EEA measurement techniques. Finally, pulsed-PLQY is used to measure the exciton-exciton annihilation coefficient, exciton diffusion length, and exciton diffusion constant in various organic semiconductors. It is found that diffusion lengths in NFAs are longer than those found in fullerene acceptors and that this difference is driven by an increase in diffusion constant.

5.2 Exciton-Exciton Annihilation

Singlet-singlet exciton annihilation can occur when two excitons interact with each other, typically assumed to be on neighbouring molecules. The result of this interaction is an exciton with excess energy, which quickly relaxes to the lowest excited state, and one nonradiative decay event to the ground state. The rate equation for the exciton density (ρ) in an organic semiconductor is determined by the sum of this second-order nonradiative decay and the first-order natural decay

$$\frac{d\rho(t)}{dt} = -\frac{\rho(t)}{\tau} - \gamma\rho^2(t), \tag{5.1}$$

where t is time. When the process of annihilation is diffusion-limited, γ can be related to the diffusion constant in the film by [183]

$$\gamma = 4\pi D R_0, \tag{5.2}$$

where R_0 is the capture radius, typically understood to be the molecular spacing in OSC films [173, 178, 180, 182]. Although interactions that result in quenching

of both excitons and lead to a value for γ twice what is derived here have been proposed [175], previous experimental reports by other authors have confirmed that the primary quenching mechanism in organic semiconductors is accurately described by Equation 5.1 and 5.2 [164, 173, 174, 176–180].

The solution to Equation 5.1 is

$$\rho(t) = \frac{\rho_0 \exp\left(-t/\tau\right)}{1 + \gamma\rho_0\tau\left[1 - \exp\left(-t/\tau\right)\right]}, \tag{5.3}$$

where ρ_0 is the initial exciton density (at $t = 0$). Equation 5.3 can be linearised as

$$\frac{1}{\rho(t)} = \left[\frac{1}{\rho_0} + \gamma\tau\right] \exp\left(t/\tau\right) - \gamma\tau. \tag{5.4}$$

Allowing for γ to be obtained from either slope or intercept of a $1/\rho$ vs $\exp(t/\tau)$ plot, assuming τ is known. Finally, the annihilation coefficient can be related to the low-density exciton diffusion length, through Equation 5.2, and Equation 3.9.

5.3 Monte-Carlo Modelling of Photoluminescence Experiments

To investigate the limits of TRPL linearisation and to introduce pulsed-PLQY the two experimental methods were simulated using a Monte-Carlo hopping model. The simulations were limited to capture only the relevant physics and to allow for each experimental method to be evaluated under ideal conditions where system parameters, such as the exciton diffusion length, are known and can be compared to the extracted values. To this end, the exciton dynamics within a lattice were simulated over a range of initial excitation densities with a 3D Monte-Carlo model including natural (linear) and exciton-exciton annihilation decay mechanisms (as shown in the inset of Figure 5.1 a). Here, exciton-exciton annihilation is assumed to occur when excitons are within one lattice spacing of one another (corresponding to an R_0 equal to the lattice spacing).

Although it is possible that exciton-exciton annihilation occurs both over greater distances and as a statistical process, the capture radius is typically understood to be the average distance over which annihilation occurs. Limiting the annihilation to one lattice spacing allows for an absolute calculation of the diffusion length through Equation 5.2 and 3.9 and a direct comparison of the diffusion length calculated from the simulated TRPL linearisation and pulsed-PLQY techniques. Further, the finding that the GIWAX d_{100} spacing is similar to the capture radius experimentally corroborates the view that annihilation, on average, happens between nearest neighbour pairs [180].

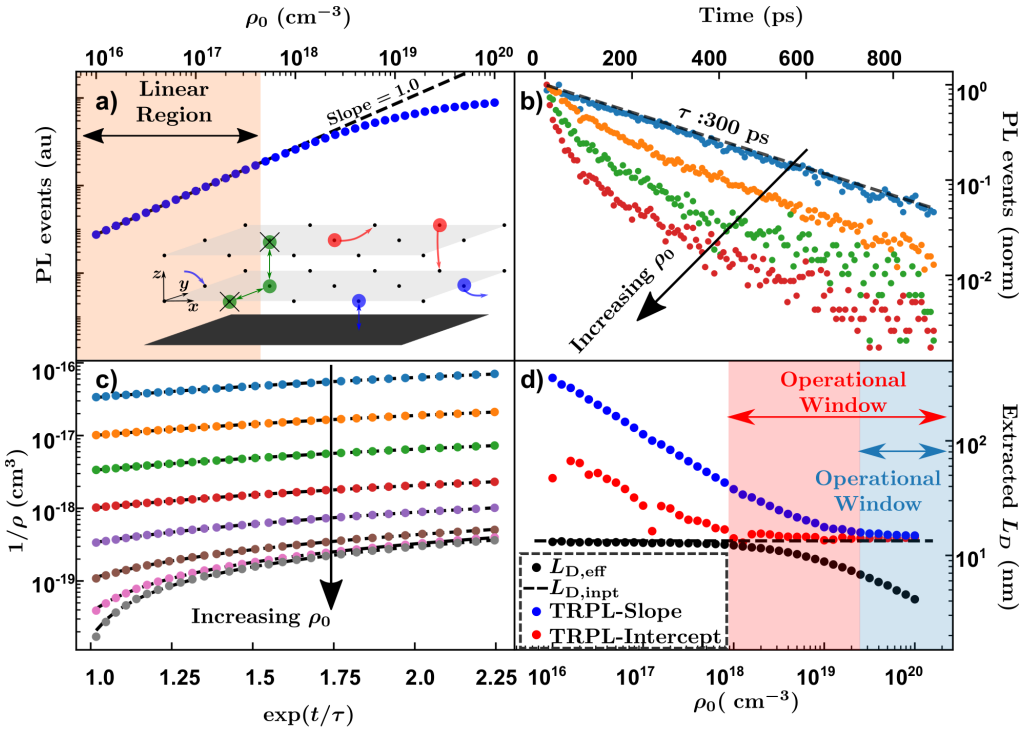

Figure 5.1: Simulated (a) PL events as a function of initial excitation density. (Inset) Cartoon depiction of various pathways for excitons to evolve in the simulation. Red circles and arrows indicate hopping transport along major axes, blue circles and arrows indicate reflecting and periodic boundary conditions, green circles and arrows indicate exciton-exciton annihilation. Simulated (b) TRPL-decays and as a function of time and (c) linearised TRPL decays for selected initial excitation densities (circles) and corresponding fit lines (black dashed lines), note that the axis in panel (c) are log-lin. (d) Diffusion lengths extracted through (blue and red circles) TRPL linearisation, (black circles) calculated from Equation F.6, or (black dashed line) calculated from input simulation parameters.

The lattice spacing (dx), temporal step size, and natural lifetime used were 0.775 nm, 1 ps, and 300 ps respectively, corresponding to a diffusion constant of 10^{-3} cm^2/s and an input 3D diffusion length ($L_{D,\text{inpt}}$) of 13.4 nm. Further details relating to the implementation of the the Monte-Carlo algorithm are provided in Appendix F.

Figure 5.1a shows the photoluminescence, determined by the number of natural decay events, as a function of initial exciton density. A transition between

first and second-order response, as expected from Equation 5.1, can clearly be seen starting around 3×10^{17} cm^{-3} and fully occurring by 3×10^{18} cm^{-3}. This is reflected in the increased quenching occurring on sub-100 ps time scale in the selected TRPL curves shown in Figure 5.1b, typical of exciton-exciton annihilation experiments [165, 173–181].

To explore the limits of Equation 5.4 the simulated TRPL data was analysed, through TRPL linearisation, to obtain the exciton diffusion length and compare with $L_{D,\text{inpt}}$. In this technique the lowest density TRPL data is fit to obtain τ as shown by the black dashed line in Figure 5.1b. Using this value of τ each TRPL decay is linearised according to Equation 5.4 and fit to a line, as shown for the selected curves in Figure 5.1c. The slope and intercept are used to obtain values of γ for each initial density and L_D is calculated from Equation 5.2 and 3.9, using $R_0 = dx$. This is equivalent to the procedure for fitting experimental data.

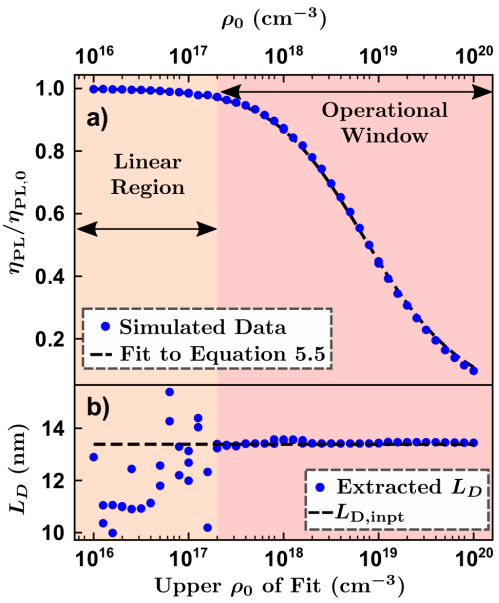

Figure 5.2: (a) Simulated η_{PL} as a function of initial excitation density (blue circles) and fit to Equation 5.5 (black dashed line). (b) Exciton diffusion length extracted from data in panel (a) as a function of the upper limit to the fit (blue circles) and input diffusion length (black dashed line).

In Figure 5.1d the black dashed line specifies $L_{D,\text{inpt}}$ while the black circles indicate the effective diffusion length ($L_{D,\text{eff}}$, calculated from simulated exciton dynamics, see Equation F.6) of the simulated excitons as a function of initial density. At low-densities $L_{D,\text{eff}}$ predicts $L_{D,\text{inpt}}$; however, $L_{D,\text{eff}}$ increasingly underestimates $L_{D,\text{inpt}}$ with increasing ρ_0. This is due to an increase in exciton-exciton annihilation occurring at large ρ_0, where, on average, excitons have a shorter effective lifetime (and therefore move, on average, less distance) than those under low-density excitations. It is therefore expected that $L_{D,\text{eff}}$ will decrease with increasing ρ_0.

In contrast to this, the blue and red circles in Figure 5.1d, respectively, show

the exciton diffusion lengths extracted from the slope and intercept of the fit to the linearised simulated TRPL data. The extracted diffusion lengths reproduce $L_{D,\mathrm{inpt}}$ at high ρ_0, where the second-order nonradiative decay dominates Equation 5.1. However, the diffusion length (or γ) extracted from the slope increasingly overestimates the input diffusion length with decreasing ρ_0. Similar reduction in extracted γ (as measured by high density TRPL experiments) with increasing excitation density has been observed by other researchers in previous studies on OSCs [174].

The apparent dependence of the slope on ρ_0 limits the range over which the true value of γ (and hence L_D) can be extracted and the extracted value converges to the expected low-density diffusion length only when $\gamma\tau \gg 1/\rho_0$. The operational window is defined as the range of densities over which this technique reliably reproduces the low-density diffusion length. The operational window for extraction from the slope is indicated by the blue shading in Figure 5.1d. On the other hand, according to Equation 5.4, the intercept does not depend on ρ_0. This is reflected in the larger operational window for the diffusion length extracted from the intercept (red shaded region in Figure 5.1d). However, in the limit where $\rho_0\gamma\tau \ll 1$ Equation 5.3 is reduced to a single exponential decay and one cannot expect to extract any second-order information, reflected in the increasing overestimation of the diffusion length as the density approaches the linear regime.

Consequently; accurate quantification of the diffusion length (or γ) from TRPL linearisation requires careful analysis of the range of excitation densities used. Implementation of this experimental procedure requires a femtosecond pulsed laser source to inject (and subsequently let evolve) the initial exciton density, accurate measurement of the exciton lifetime, and specialised equipment capable of measuring the quenching kinetics seen in Figure 5.1b, which occur on the order of picoseconds in organic semiconductors [165, 173, 175–177, 179, 180]. Furthermore, as described above, the operational window for determining the diffusion length (or γ) of these materials occurs at high excitation density where the quenching is fastest, requiring increasing resolution to resolve. Besides which, not all organic semiconductors are stable at high excitation densities and may undergo photo- or thermal-oxidation at sufficiently high excitation fluences.

To circumvent the apparent dependence of extracted values on the choice of initial density, eliminate the requirements for measuring the exciton lifetime, lower the equipment specialisation, and increase the speed of the measurement one can measure and analyse these kinetics in an alternative way by considering the normalised η_{PL} as a function of exciton density. The total number of excitons that recombine via natural decay in accordance with Equation 5.1 is $\rho_\tau = \int_0^\infty \rho(t)/\tau dt$. On the other hand, the photoluminescence quantum efficiency is given by $\eta_{\mathrm{PL}} = \rho_\tau\eta_{\mathrm{PL},0}/\rho_0$ where $\eta_{\mathrm{PL},0}$ is the low density photoluminescence quantum efficiency. From Equation 5.3, the photoluminescence quantum efficiency is then obtained

as

$$\eta_{\mathrm{PL}}\left(\rho_0\right) = \eta_{\mathrm{PL},0}\frac{\ln\left[1+\rho_0\gamma\tau\right]}{\rho_0\gamma\tau}. \tag{5.5}$$

Therefore, by measuring $\eta_{\mathrm{PL}}/\eta_{\mathrm{PL},0}$ as a function of ρ_0 one can fit to obtain the product of $\gamma\tau$ and either: (i) calculate the the diffusion length directly using Equation 5.2 and 3.9 without the need for any temporal measurements, or (ii) measure the exciton lifetime independently to calculate γ (or D).

To evaluate the validity of this procedure, $\eta_{\mathrm{PL}}/\eta_{\mathrm{PL},0}$ was calculated from the results of the Monte-Carlo simulations as the ratio of natural decay events to the initial number of excitons in the lattice. Figure 5.2a shows the results of this analysis, the blue circles indicate η_{PL} calculated for each initial density. The exciton-exciton annihilation is evident in the decrease in η_{PL} with increasing ρ_0, as observed experimentally by other researchers in studies on metal-insulator-semiconductor heterostructures [184, 185]. The linear region marked in Figure 5.1a is reproduced in Figure 5.2 as a guide.

The simulated normalised η_{PL} is fit to Equation 5.5, as shown by the black dashed line and the exciton diffusion length is calculated from the extracted product of $\gamma\tau$ through Equation 5.2 and 3.9. Figure 5.2b shows the calculated L_D as a function of the upper limit to the fitting. The operational window is defined as the densities that, when used as the upper limit to the fitting, reproduce the low-density diffusion length. The operational window for pulsed-PLQY is shown by the red shaded region in Figure 5.2a and b. The operational window for pulsed-PLQY is larger and extends to lower densities that those of TRPL linearisation and, most importantly, the confidence in the extracted value increases with increasing number of initial densities used. Whereas, in TRPL linearisation increases in the number of measurements made at varying initial densities may decrease the confidence of the extracted values, depending on the choices of ρ_0.

5.4 Experimental Validation of Pulsed-PLQY

Typical TRPL linearization techniques are accomplished through optical excitation of a sample followed by the collection subsequent decomposition of the photoluminescence response into its temporal and spectral characteristics. As the EEA-induced quenching in organic semiconductors occurs on the picosecond timescale the decomposition of light must have adequate resolution to resolve this phenomena. This is typically accomplished with a Streak Camera which can achieve the required temporal resolution and, when fitted with a spectrograph,

can decompose the photoluminescence spectra simultaneously [173,174,180,181]. Figure 5.3a shows the apparatus used to perform a TRPL measurement.

The light source (Pharos PHM02-2h-3h) generates a 300 fs pulse at a wavelength of 515 nm and a repetition rate of 25 kHz. The low repetition rate is used to ensure the time between pulses is many times longer than the natural lifetime of the sample, allowing the sample to fully decay in between pulses. Additionally, the low repetition rate allows the fundamental wavelength generated by the Pharos oscillator (1030 nm) to be converted into the second and third harmonic (515 nm, and 343 nm) through a non-linear process occurring within the Pharos. The 515 nm light is directed towards the sample with various mirrors and periscopes, not shown in Figure 5.3, passed through a neutral density filter, and focused to a spotsize of 50 μm with a 200 mm focusing lens (see Appendix B.3 for details about the spotsize measurements) before being incident on the sample which is held in a cryostat (Linkam-LTS420) under a constant flow of nitrogen gas. The resulting photoluminescence is collected, collimated, filtered to remove any scattered pump light, and focused onto the spectrograph which

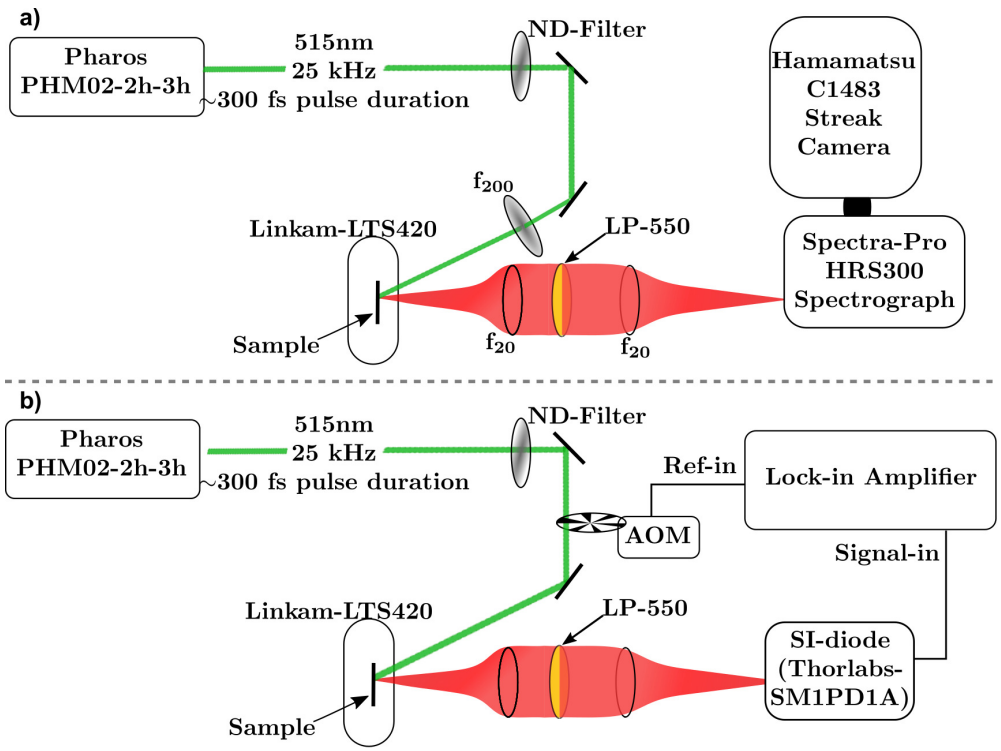

Figure 5.3: (a) Time-resolved photoluminescence and (b) pulsed-PLQY apparatuses. ND-neutral density, AOM-acousto-optic modulator, f_x indicates a lens with focal length x, LP-long pass filter.

decomposes the photoluminescence into its spectral components before directing it into the streak camera. To measured the photoluminescence decay of a sample the collected spectra is integrated across the entire spectral range to create the TRPL decays shown in Figure 5.4a.

The initial density of excitons in the film is given by

$$\rho_0 = \frac{P\alpha}{\pi\omega^2 f_{\text{rep}} E_{\text{ph}} d}, \tag{5.6}$$

where P is the average laser power incident on the sample, α is the total absorbance of the sample at the pump wavelength, f_{rep} is the repetition rate of the laser, ω is the spotsize of the laser, E_{Ph} is the incident photon energy, and d is the film thickness. Therefore, the initial density of excitons can be adjusted over many orders of magnitude simply by adjusting the power of the laser through tuning of the neutral density filter.

Realisation of pulsed-PLQY requires the same femtosecond pulsed laser as with TRPL linearisation, however; the light-collection can be accomplished with non-specialised equipment operating at a steady-state. Further, the exciton diffusion length can be calculated directly from the product $\gamma\tau$ without the need for any temporal measurements, and γ (or D) can be determined without the need for a high resolution TRPL apparatus. Due to these considerations the experimental apparatus used in pulsed-PLQY can be significantly simplified from the one used in TRPL linearisation. Figure 5.3 shows the apparatus used to measure pulsed-PLQY with a photodiode as a detector. In addition to the optical elements in Figure 5.3a, the laser is passed through an acousto-optic modulator (AOM-commonly known as a chopper) which modulates the light at 273 Hz. Additionally, as the photoluminescence does not need to be decomposed into temporal components, the pump lens is removed to increase the spot-size of the laser (see Appendix B.3 for details about spot-size measurements). The increase in spot-size has two primary benefits. The first benefit is that, for a particular ρ_0, the laser power (and therefore the collected photoluminescence) can be increased, increasing the signal to noise ratio in low ρ_0 measurements. The second benefit is related to the theory laid out in Section 5.2, which implicitly assumes a even distribution of excitons upon excitation. Increasing the spotsize of the laser spreads the initial density of excitons over a larger area increasing the validity of this assumption.

The resulting photoluminescence is collimated and focused onto the active area of the photodiode (Thorlabs-SM1PD1A). The output signal of the photodiode is fed into the lock-in amplifier (Stanford Research Systems SR860). The lock-in measures the response of the photodiode at the frequency of the chopper. This in principle is the photoluminescence of the sample, however; care must be taken to remove any scattered light from the pump laser. Not shown in Figure 5.4b are

the various solid and cloth blockers used to cover the photodiode in order to allow only the photoluminescence signal into the active area. The pump scatter can be evaluated by blocking the pump beam near the sample, such that any scattered pump light will reach the detector in the absence of the photoluminescence. The pump scatter (with the laser set at the power corresponding to the largest density used) was reduced to 100X the smallest photoluminescence signal before taking measurements. To show the simplicity of the measurement, this was carried out with the most basic optical and electrical elements, however; the apparatus can be improved by using a current-to-voltage amplifier to amplify the signal from the photodiode (such as a Fempto OE-300-Si-30) to increase the signal-to-noise ratio of the lock-in. Further, a long-pass 550 nm filter in front of the photodiode was used to filter the remaining pump scatter.

To validate the simulations outlined in Section 5.3 TRPL linearlisation and pulsed-PLQY were carried out on a P3HT thin film and the results compared. Figure 5.4b shows the resulting normalised TRPL decays, where the expected time-independent quenching dynamics can be seen, akin to other studies on sim-

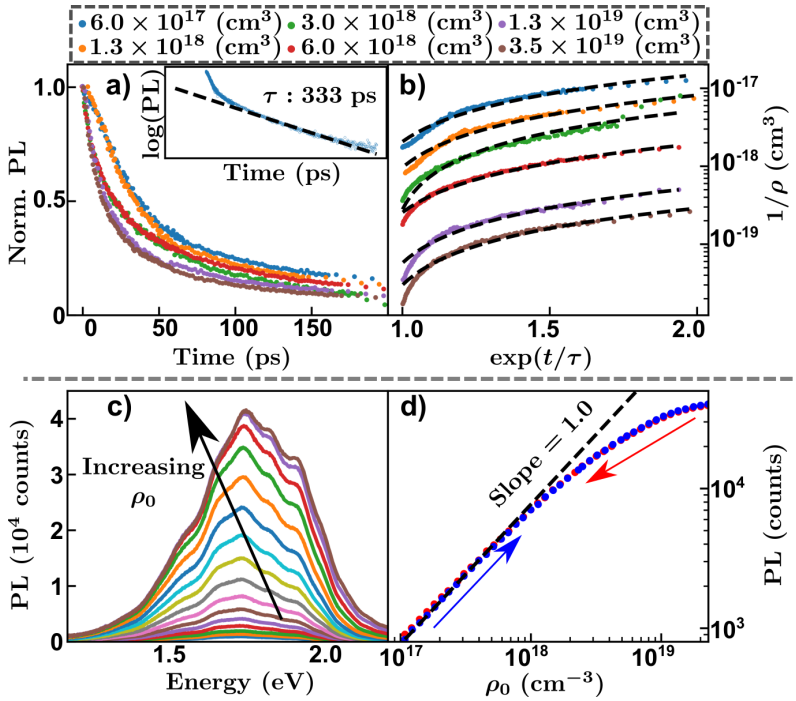

Figure 5.4: (a) Normalised TRPL decays as a function of time and (b) linearised TRPL decays for various initial excitation densities. (c) P3HT spectra for selected excitation densities. (d) P3HT peak PL counts as a function of initial excitation density.

ilar materials [165,173,174,176–178,180,181]. The exciton lifetime was measured by fitting the decay of the lowest initial density to the linear region (where exciton-exciton annihilation is minimal) on a log-lin scale as shown in the inset of Figure 5.4b. The measured τ was used to linearise all the TRPL decays in Figure 5.4b according to Equation 5.4, as shown in Figure 5.4c. The black dashed lines indicate the fits used to extract the γ from the intercept, as this was shown to be the more accurate measure.

Selected spectra obtained from the same P3HT film are shown in Figure 5.4e. These were collected with the same apparatus laid out in Figure 5.3b with the photodiode and lock-in replace with a spectrograph (Hamamatsu C10029-01). The peak values of the spectra are plotted against the excitation density in Figure 5.4f. The transition from the linear to sub-linear response can be clearly seen occurring around the same values as those in Figure 5.1a. To ensure that there was no degradation of the sample during these measurements both forward (blue circles-from low to high density) and reverse (red circles-from high to low-density) scans were performed consecutively. To calculate the relative η_{PL} the peak value of the photoluminescence data was divided by the associated ρ_0 and normalised to the η_{PL} of the lowest density points, as shown by the blue circles in Figure 5.5a. To exemplify the simplicity of this measurement a second set of data was collected where the imaging spectrograph was replaced with a silicon photodiode and the voltage response was used to calculate the relative η_{PL}. This second data set is shown as the orange squares in Figure 5.5a. Although the use of

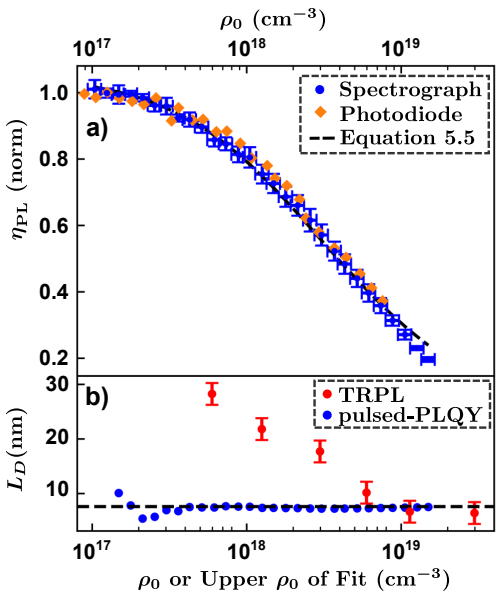

Figure 5.5: P3HT (a) pulsed-PLQY data collected using (blue circles) spectrograph and (orange squared) lock-in detection, and (black line) fitting of spectrograph data to Equation 5.5. (b) Diffusion lengths extracted from the (red circles) intercept of TRPL linearisation as a function of initial density and (blue circles) pulsed-PLQY as a function of upper limit to the fit.

a silicon photodiode does not provide spectral information, the relative η_{PL}, and therefore $\gamma\tau$ (or L_D), can be measured with a further reduction in equipment specialisation. Equation 5.5 is fit to the data collected with the spectrograph, shown by the black dashed line, and the extracted product of $\gamma\tau$ is used, with the d_{100} spacing as an estimate of R_0, to calculate L_D via Equation 5.2 and 3.9.

The results of the experiments on P3HT are summarised in Figure 5.5b which shows the 1D diffusion length extracted from TRPL linearisation as a function of initial density and pulsed-PLQY as a function of upper limit to the fit. As predicted by the simulations the diffusion length extracted from TRPL linearisation (red circles) decreases with increasing initial density. The diffusion length measured by pulsed-PLQY (blue circles) converges to a constant value with increasing upper fitting limit. These results verify the simulations and demonstrate that pulsed-PLQY is a viable and accurate alternative measurement technique for measuring L_D without the need for any temporal measurements, or γ without the need for high resolution TRPL equipment.

The product of $\gamma\tau$ found from pulsed-PLQY was $(7.2 \pm 0.2) \times 10^{-19}$ cm^3 (a detailed description of error analysis is provided in Appendix B.4), leading to a 1D diffusion length of 8 ± 1 nm, comparable to literature values [173, 182]. Using the natural lifetime, found to be 330 ± 10 ps, a value of $\gamma = (2.15 \pm 0.08) \times 10^{-9}$ cm^{-3} was found, slightly lower than previous values extracted from TRPL linearisation by other researchers [173]. However, as exemplified by the simulations, a slightly lower value of γ is expected from pulsed-PLQY than from TRPL linearisation. Finally, the diffusion constant was calculated from γ, and R_0 according to Equation 5.2 and found to be $(1.0 \pm 0.3) \times 10^{-3}$ cm^2/s, in agreement with previous values from quenching experiments [165, 173].

After pulsed-PLQY was established it was used to evaluate $\gamma\tau$ and the 1D and 3D diffusion length in a collection of OSCs, including several technologically relevant NFAs used in state-of-the-art OPV devices. Further, the exciton lifetime was measured, at low excitation density, to evaluate the annihilation and diffusion coefficients. These results are summarised in Table 5.1. The NFAs (such as ITIC, IT4F, Y6, and BTP-eC9) were found to have much longer exciton diffusion length than the benchmark fullerene acceptor $PC_{60}BM$. Measurement of the exciton lifetime shows that the increase in diffusion length is driven by increases in exciton diffusion constant. Increases in D would allow bulk excitons to form interfacial excitons many times over, increasing the probability of CT state formation regardless of IP-offset. However, this evidence does not rule out FRET playing a significant role in charge generation. The Förster radii is < 5 nm in BHJs made from these materials [97]. If FRET were to occur, suppressing one charge generation channel, increased exciton diffusion lengths would still increase charge generation by increasing the number of bulk excitons that diffuse close enough to the interface for long-range FRET to efficiently transfer the exciton to

the opposing phase. Alternatively, for excitons that have undergone FRET to the bulk of the opposing phase increased L_D would increase the chance of forming a interfacial exciton from the newly occupied phase.

5.5 Conclusion

In conclusion, pulsed-PLQY was introduced as an alternative approach to established exciton-exciton annihilation techniques. Pulsed-PLQY was used to determine the exciton diffusion length in various OSCs and the results show a dramatic increase in the diffusion length of NFA OSCs compared to fullerene-based acceptors, primarily driven by increases in exciton diffusion constant. These results support the assertation that increases in diffusion constant contribute to the charge generation efficiency in low-offset NFA OPV-based solar cells, as discussed in Section 4.4. Pulsed-PLQY is faster, easier, reduces equipment specialisation, and is less sensitive to experimental conditions than established techniques. The simplicity and ease of pulsed-PLQY measurements enables EEA to be utilised in modalities that were previously difficult to access. In Chapter 6 it will be demonstrated how pulsed-PLQY can be employed to determine the phase separated domain size in BHJ thin films.

Table 5.1: Material parameters extracted from the pulsed-PLQY fittings (γ and L_D), low-density TRPL fittings (τ), and subsequently calculated (γ, and D) for various organic semiconductors. See Appendix B.5 for all measurement data. R_0 is assumed to be the d_{100} spacing taken from the provided references, the error in R_0 is assumed to be half the value given by the d_{100} spacing. †$PC_{60}BM$ estimate for R_0 is taken as 1 nm as GIWAX d_{100} does not give intermolecular distance in this case.

Material	$\boldsymbol{\gamma\tau(\times 10^{-18})}$ **(cm^3)**	$\boldsymbol{R_0}$ **(nm)**	$\boldsymbol{{L_D}^{1D}}$ **(nm)**	$\boldsymbol{{L_D}^{3D}}$ **(nm)**	$\boldsymbol{\tau}$ **(ps)**	$\boldsymbol{\gamma(\times 10^{-9})}$ **(cm^3/s)**	$\boldsymbol{D(\times 10^{-4})}$ **(cm^2/s)**
PM6	0.088±0.002	2.1 [186]	2.6±0.3	4.5±0.3	64	1.4±0.2	5±1
P3HT-Regiorandom	0.13±0.02	1.0 [187]	5±1	8±1	175	0.76±0.05	6±3
PTB7-Th	0.144±0.004	2.4 [187]	3.1±0.3	5.4±0.3	123	1.17±0.09	3.9±0.9
PCDTBT	0.329±0.005	1.6 [188]	5.7±0.9	9.9±0.9	203	1.62±0.08	8±2
$PC_{60}BM$	0.52±0.01	1.0†	9±2	23±3	777	0.65±0.02	5±2
P3HT-Regioregular	0.72±0.02	1.7 [189]	8±1	14±1	333	2.15±0.08	10±3
ITIC (NFA)	1.23±0.03	1.6 [190]	11±2	19±2	120	10.3±0.9	50±10
IT4F (NFA)	2.54±0.07	1.8 [191]	15±2	26±2	205	12.4±0.7	60±10
Y6 (NFA)	8.5±0.2	1.5 [186]	30±5	51±5	799	10.6±0.3	60±10
BTP-eC9 (NFA)	10.6±0.3	1.6 [192]	33±5	56±5	389	27±1	140±40

Chapter 6

Relationship Between Charge Carrier Dynamics and Exciton Dynamics

In Chapter 4 the role that diffusion plays in the charge generation process of a phase separated bulk-heterojunction was described. It was found that the effective charge transfer rate constant was dependent on the exciton diffusion length and the phase separated domain size. In Chapter 5 pulsed-PLQY was introduced as a reliable method for measuring exciton diffusion length in OSCs, without the need for time-consuming temporal measurements or absolute measurements of photoluminescence quantum efficiency. In the work contributing to this chapter the charge generation process in a FRET-activated BHJ and the relation between the exciton dynamics and separated charge carrier dynamics is explored. Pulsed-PLQY is used to evaluate the size of the phase separated domains of various technologically relevant BHJs. From this, the Langevin reduction factor for encounter of separated charge carriers is estimated. It is found that the corresponding encounter Langevin reduction factor is not large enough to account for the large reduction in Langevin recombination rate constants seen in high-efficiency low-offset systems.

It has been shown that R_{FRET} from an appropriate donor to a NFA in certain NFA-based BHJs can be larger than the intermolecular spacing in the donor phase [97]. This indicates that, in these systems, FRET from the donor to acceptor phase is an efficient process provided the exciton is within a few molecular spacings of the donor acceptor interface. The charge generation process for an exciton in the donor phase of a FRET-activated BHJ is shown in Figure 6.1a. The exciton diffuses freely throughout the donor phase until it is within R_{FRET} of the donor acceptor interface, at which point the exciton is transferred to the acceptor phase, with a high probability of arriving near the interface. Hence, from the exciton's frame of reference, the donor domain size is smaller than that of the phase separation of the BHJ by twice R_{FRET}, denoted in Figure 6.1a as L_{eff}. Since FRET is inefficient from NFAs to typically donor molecules, excitons generated in the acceptor phase (or transferred there via FRET) diffuse within the acceptor phase before reaching the interface and dissociating into a CT-state.

Since the separated charge carriers are free to diffuse everywhere in their respective domains, the donor domain size in the separated charge carrier's frame of reference is equivalent to the phase separated domain size, and is, importantly, larger than the donor domain in the frame of reference of an exciton confined to the donor phase. Phase separated domains from the separated charge carrier perspective are shown in Figure 6.1b. Confinement of the electron and hole to their respective phase separated domains leads to encounter limiting reductions in total bimolecular recombination rate (given in Equation 3.13), by decreasing the ability for an electron and hole to diffuse within a Coulomb capture radius r_c (see Section 3.2.3) of one another. This reduction in total bimolecular recombination rate is most pronounced in cases of high mobility imbalances or domain sizes

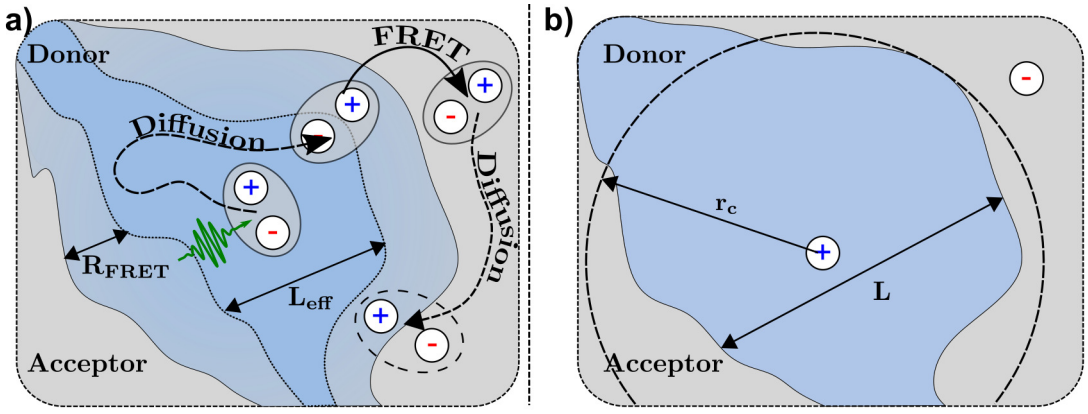

Figure 6.1: Phase separated domain geometry from the perspective of an (a) exciton in the donor phase and (b) separated charge carriers.

much greater than those observed in fullerene BHJs [105, 111, 112].

Studies of the surface morphology of many NFA-based BHJs via atomic force microscopy have revealed that the surface domains exhibit superior phase separation and larger domain sizes than fullerene blends [35, 136, 193–197]. Further studies using transmission electron microscopy have revealed that this trend extends into the bulk of NFA-based BHJs [193, 195–199]. However, these commonly used methods cannot accurately quantify the size or purity of NFA-based BHJ domains due to the low contrast of compositionally similar materials [200]. Resonant soft X-ray scattering (R-SoXS) experiments on NFA BHJs have observed scattering peaks at $q < 0.1$ nm^{-1} indicating large donor or acceptor rich areas are present in the films and suggesting the presence of acceptor domains as large as 90 nm [200–206]. Although R-SoXS is a widely used and powerful tool, many of the polymer-X-ray interactions result in high energy electrons that cause damage to the polymer structure [207]. The advent of a convenient, benign probe to quantify the size of donor and acceptor domains in phase separated BHJs would be a useful tool in understanding the relationship between charge generation yield, suppressed recombination, and device relevant figures of merit such as PCE and J_{SC}.

6.1 Pulsed-PLQY in Bulk-Heterojunction Films

As discussed in Chapter 4, the effective charge transfer rate constant for excitons in a phase separated BHJ from the occupied phase to the opposing phase is dependent on the diffusion efficiency to and the efficiency of charge transfer at the interface. Expanding on this, in FRET-activated charge generation, the effective energy transfer rate constant would depend on k_{FRET} while η_{diff} would depend on L_{eff} (on average). Amalgamating these two possible pathways into an efficiency of charge or energy transfer ($\eta_{\mathrm{CT/FRET}}$), and an effective charge or energy transfer rate (k_{eff}), the rate equation for ρ in either phase of a phase-separated BHJ is given by

$$\frac{d\rho}{dt} = -\frac{\rho}{\tau} - k_{\mathrm{eff}}\rho - \gamma\rho^2. \tag{6.1}$$

Combining the linear terms in Equation 6.1 results in

$$\frac{d\rho}{dt} = -\frac{\rho}{\tau_{\mathrm{eff}}} - \gamma\rho^2, \tag{6.2}$$

in which $\tau_{\mathrm{eff}} = \tau/(1 + k_{\mathrm{eff}}\tau)$. Similar to Equation 5.3, the solution to Equation 6.2 is

$$\rho(t) = \frac{\rho_0 \exp\left(-t/\tau_{\mathrm{eff}}\right)}{1 + \gamma\rho_0\tau_{\mathrm{eff}}\left[1 - \exp\left(-t/\tau_{\mathrm{eff}}\right)\right]}. \tag{6.3}$$

As shown in Section 5.3, a neat film ($\tau_{\text{eff}} = \tau$) has relative photoluminescence quantum efficiency given by Equation 5.5. Utilising the same procedure, each phase of a phase separated BHJ will have a η_{PL} given by

$$\eta_{\text{PL}} = \eta_{\text{PL},0} \frac{\ln\left[1 + \rho_0 \gamma \tau_{\text{eff}}\right]}{\rho_0 \gamma \tau_{\text{eff}}}, \tag{6.4}$$

where $\eta_{\text{PL},0}$ is the ratio of radiative to nonradiative events in the low density limit, including charge and FRET transfer. In general, exciton dissociation efficiency can be expressed as the competition between k_{eff} and decay rate within each phase, which can be related to η_{diff} and $\eta_{\text{CT/FRET}}$ following Equation 4.11 as

$$P_S = \frac{k_{\text{eff}}}{1/\tau + k_{\text{eff}}} = \left[\frac{1}{\eta_{\text{diff}}} + \frac{1}{\eta_{\text{CT/FRET}}} - 1\right]^{-1}. \tag{6.5}$$

Combining Equation 6.5, the definition of k_{eff}, and multiplying by γ the effective lifetime in the occupied phase can be related to η_{diff} and $\eta_{\text{CT/FRET}}$. In the limit where the charge or energy transfer is efficient ($\eta_{\text{CT/FRET}} \to 1$), the system becomes diffusion limited and, utilising Equation 4.10, Equation 6.5 becomes

$$1 - \frac{\gamma \tau_{\text{eff}}}{\gamma \tau} - \frac{2L_D}{L} \tanh\left[\frac{L}{2L_D}\right] = 0. \tag{6.6}$$

In the case where FRET from the occupied to opposing phase is efficient, L can be substituted for L_{eff}. Therefore, by measuring $\gamma\tau$ on a neat film and $\gamma\tau_{\text{eff}}$ from one phase of a phase separated BHJ film one can solve Equation 6.6 for the phase separated domain size (L), or the domain size from the excitons' perspective (L_{eff}). Appendix C.3.1 includes additional details relating to the derivation of Equation 6.6.

6.2 Validation of Domain Size Measurement

The efficacy of the technique laid out above was verified in two ways, through the use of Monte-Carlo simulations and a bi-layer experiment. The Monte-Carlo simulations were carried out in an infinite cylinder geometry to simulate a section of a single domain in a phase-separated fully-percolated BHJ, with the domain size defined as the diameter of the cylinder. Exciton dynamics were simulated within the domain including decay and annihilation, while excitons at the domain edge were additionally subject to charge-transfer and re-injection. The photoluminescence quantum efficiency of the simulation is defined as the ratio of excitons decaying radiatively to the total number of excitons in the simulation. Appendix C.4.2 provides addition details related to Monte-Carlo simulations utilised in this

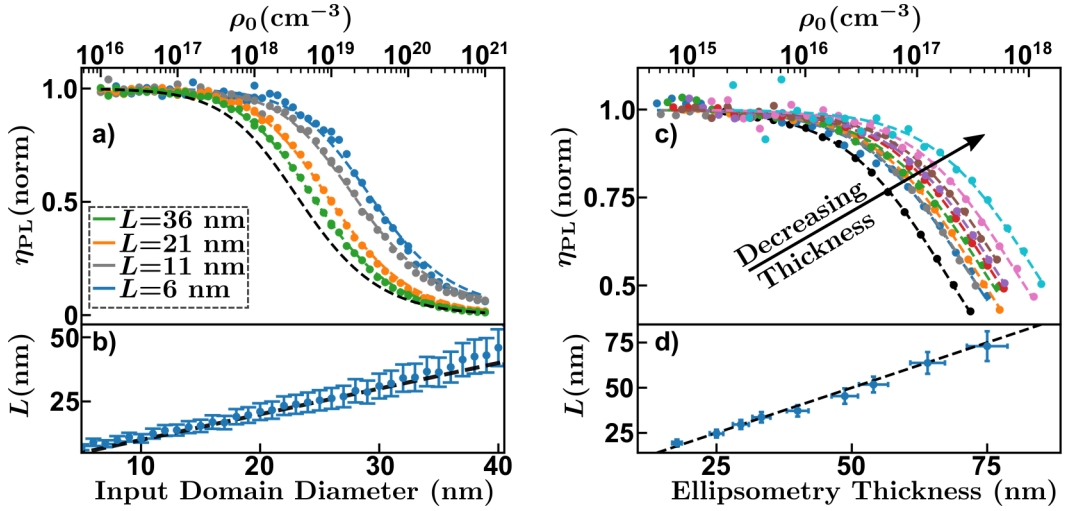

Figure 6.2: Validation of domain size measurements. (a,b) Monte-Carlo simulations. (a) Relative photoluminescence quantum efficiency as a function of initial exciton density for select domain diameters. (b) Simulated measured domain diameter as a function of input domain diameter, black-dashed line indicates $y = x$ as a guide to the eye. (c,d) Y6/Ptb7-Th bi-layer verification of domain size measurement technique. (c) Relative photoluminescence quantum efficiency as a function of initial exciton density for (black circles) neat Y6 film and (coloured circles) each bi-layer. (d) Optically measured film thickness as a function of ellipsometry measured film thickness for bi-layers, black-dashed line indicates $y = x$ as a guide to the eye.

chapter, while Appendix F describes the algorithm in detail. Figure 6.2a and b show the results of these simulations, where $L_{D,\mathrm{inpt}} = 7$ nm. Figure 6.2a shows the relative η_{PL} as a function of the initial density of excitons in the simulated domain, the black dashed line indicates Equation 6.4 for an infinite domain while the coloured circles and lines indicate the simulated relative η_{PL} and fits to Equation 6.4 for select domain sizes. When L is large, compared to L_D, such as the green curve ($L = 36$ nm), there is little charge transfer occurring. P_S and k_{eff} are small, while $\tau_{\mathrm{eff}} \sim \tau$, hence there is little change in η_{PL} from the case of an infinite film. On the other hand, when the domain size is small, such as the blue curve ($L = 6$ nm), charge transfer increases, resulting in increase of both P_S and k_{eff}. As a consequence, τ_{eff} decreases causing the onset of the reduction in η_{PL} to shift to higher densities. Each simulation was fit to Equation 6.4 for $\gamma\tau_{\mathrm{eff}}$ and, along with the simulation inputs, were used to evaluate the effectiveness of Equation 6.6 under ideal conditions. Figure 6.2b shows the domain diameter calculated

through Equation 6.6 compared to the input diameter. The calculated domain diameter reproduces the input domain diameter within error for all simulations carried out. For a detailed description of error analysis see Appendix C.7.

To experimentally validate Equations 6.4 and 6.6 a series of bi-layers films were fabricated with a glass/Y6/Ptb7-Th structure using the spontaneous spreading method (see Appendix C.4.2 for details relating to the bi-layer structure and Appendix C.1.1 for a list of chemical definitions used in this chapter) [208–210]. The resulting Y6 layers have a well defined and controllable thickness as well as a sharp interface with the thin (< 15 nm) Ptb7-Th layer. These materials were selected to ensure there is efficient charge-transfer at the interface and that, under quasi-steady-state conditions, the majority of excitons are within the Y6 phase. Pulsed-PLQY was carried out on a neat Y6 film and a series of bi-layer films with Y6 thickness varying from 17 to 75 nm. The resulting $\gamma\tau_{\text{eff}}$ were used to calculate the thickness of the Y6 layer by modifying Equation 6.6 to $1 - \gamma\tau_{\text{eff}}/\gamma\tau - L_D/L \times \tanh[L/L_D] = 0$, where L is the film thickness [172, 211]. This modification is carried out as quenching occurs only at the Y6/Ptb7-Th interface and not the glass/Y6 interface. Figure 6.2c and d show the results of these experiments. Figure 6.2c shows the relative η_{PL} as a function of the initial exciton density in the film. In a similar manner to the Monte-Carlo simulations, decreases in film thickness shifts the onset of the reduction in η_{PL} to larger ρ_0, indicating an increase in τ_{eff}. Figure 6.2b compares the optically measured film thickness to the film thickness measured via ellipsometry. The optically measured film thickness agrees with the ellipsometry measured thickness within error. Further details relating to this and subsequent pulsed-PLQY experiments on BHJs are provided in Appendix C.3.1 and Figure C.1.

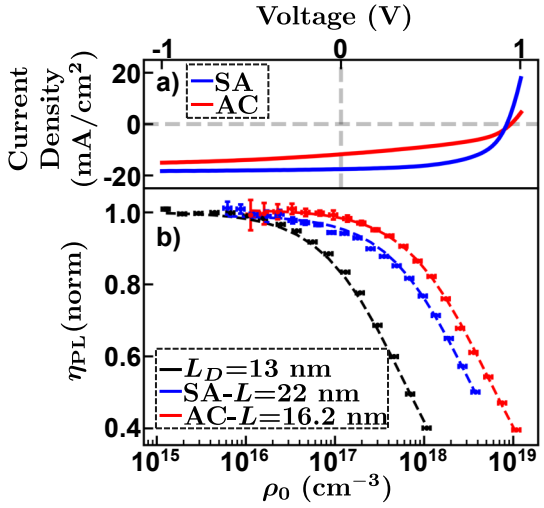

Figure 6.3: (a) Current-voltage characteristics and (b) pulsed-PLQY measurements for BQR:$PC_{71}BM$ as cast (AC) and solvent annealed (SA) devices and films.

To further substantiate the validity of pulsed-PLQY the size of the donor phase of BQR:$PC_{71}BM$ was analysed before and after a solvent annealing (SA) treatment and compared to previous experi-

mental reports by other researchers. The domain size of the BQR phase has been shown to increase with SA, increasing the J_{SC} and PCE [212]. BQR:$PC_{71}BM$ devices, and BHJ films on glass, were made through as-cast (AC) and SA processes resulting in device PCEs of 4.79% and 9.33% respectively [107,213]. The current-voltage characteristics of the devices are shown in Figure 6.3a. Pulsed-PLQY was carried out on neat BQR and BQR:$PC_{71}BM$-BHJ films, from which the L_D and L was measured, respectively, in accordance with Equation 6.4 and 6.6.

Figure 6.3b shows the results of these experiments. The black curve shows the normalised η_{PL} obtained from the neat SA-BQR film. Both SA and AC neat BQR films were found to have equivalent diffusion lengths of 13 nm, consistent with previous experimental reports [212]. The shift in the onset of the reduction in η_{PL} to lower ρ_0 moving from the AC and SA film indicates that the solvent annealing process increases the phase separated domain size of the BQR phase. The optically measured domain size was found to increase from 16.2 to 22 nm after the solvent annealing was carried out, similar to the behaviour reported by other researchers in previous experimental reports [212].

6.3 Donor and Acceptor Domains in High Efficiency Systems

To investigate the domain size in state-of-the-art high efficiency NFA systems, PM6:Y6 was investigated in detail. Devices, along with neat and BHJ thin films, were fabricated with a maximum device PCE of 15.73%. The photoluminescence spectra of neat PM6, Y6, and PM6:Y6 BHJ films is shown in Figure 6.4a. Unlike the heavily quenched high-offset fullerene systems, the photoluminescence in high efficiency low-offset systems is often composed of spectrally separated photoluminescence from both the donor and acceptor phase, as seen for the case of PM6:Y6. The presence of well separated donor and acceptor emission in the photoluminescence spectra indicates that, in the quasi-steady-state, excitons are available for exciton-exciton annihilation in both phases. Therefore, by using appropriate low- and high-pass filters in the collection pathway it is possible to collect emission from the donor and acceptor phase respectively and, in principle, utilising pulsed-PLQY, measure the domain size of both independently.

However, the relative heights of the emission from the donor and acceptor phase indicate that the absorbed light does not create an equal population of excitons in each phase. Therefore, the initial exciton density in each phase of the BHJ cannot be found simply from the experimental parameters, as was the case in Chapter 5 or the bi-layer experiments shown in Figure 6.2c and d. The density of interest here is the density of excitons available for EEA in each phase of the

BHJ under quasi steady-state conditions. To evaluate this density in each phase of the BHJ, the normalised absorption in each phase is evaluated as the ratio of the relative height of the (normalised) PL spectra in the blend film ($\Phi_{\mathrm{D/A}}$) to the absolute η_{PL} in the associated neat OSC. For example, in the PM6 phase of a PM6:Y6 BHJ this take the form

$$\begin{aligned} f_{\mathrm{PM6}} &= \frac{\Phi_{\mathrm{PM6}}/\eta_{\mathrm{PL,0\text{-}PM6}}}{\Phi_{\mathrm{PM6}}/\eta_{\mathrm{PL,0\text{-}PM6}} + \Phi_{\mathrm{Y6}}/\eta_{\mathrm{PL,0\text{-}Y6}}} \\ &= \frac{0.07/7 \times 10^{-5}}{0.07/7 \times 10^{-5} + 1/1.4 \times 10^{-5}} = 0.029. \end{aligned} \tag{6.7}$$

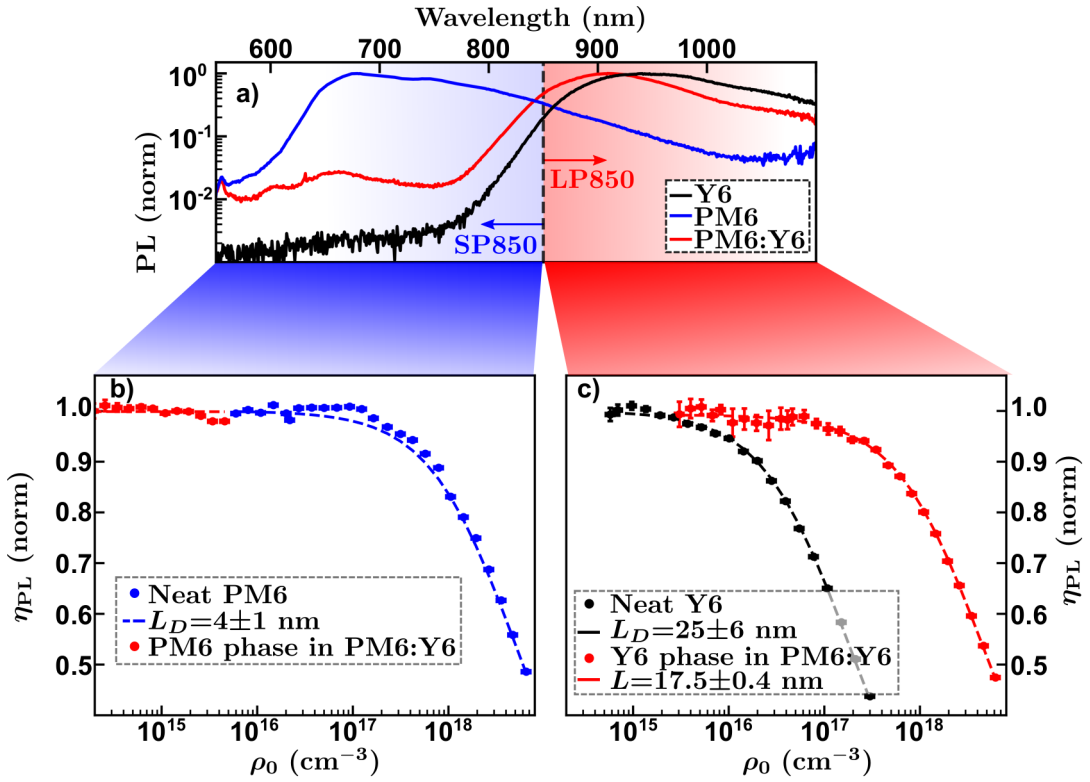

Figure 6.4: (a) Steady-state photoluminescence on (blue) neat Y6, (black) neat PM6, and (red) PM6:Y6 BHJ films excited at 515 nm. (b) Pulsed-PLQY taken on neat PM6 and PM6:Y6 BHJ films with short-pass 850 nm filter in collection pathway. (c) Pulsed-PLQY taken on neat Y6 and PM6:Y6 BHJ film with long-pass 850 nm filter in collection pathway. Circles indicate data while dashed lines indicate fits to Equation 6.4. LP850-long-pass 850 nm filter. SP850-short-pass 850 nm filter.

This indicates that 2.9% of all injected excitons are available for EEA in the PM6 phase while the remaining 97.1% were available for EEA in the Y6 phase.

6.3.1 Acceptor Phase

Figure 6.4c shows pulsed-PLQY carried out on a neat Y6 film and a PM6:Y6 BHJ with a long-pass 850 nm filter in the collection pathway to isolate the photoluminescence of the Y6 phase. The shift in the onset of the reduction in η_{PL} from the neat Y6 film to the Y6 phase of the BHJ is indicative of exciton quenching from the Y6 phase of the BHJ. The neat Y6 and long-pass filtered photoluminescence of the BHJ were fit to Equation 6.4 using $\gamma\tau$ and $\gamma\tau_{\mathrm{eff}}$, respectively, as fitting parameters. The phase separated domain size was calculated utilising Equation 6.6 (where L_D was obtained using $R_0 = 1.5$ nm [189]). L_D was found to be 25 ± 6 nm while P_S was found to be 0.960 ± 0.005, resulting in an optically measured domain size of 17.5 ± 0.4 nm. Similar phase separated domain sizes have been estimated on PM6:Y6 films by other researchers utilising R-SoXS experiments [205]. As FRET is an inefficient process from Y6 to PM6, the phase separated domain size from the perspective of the exciton is equivalent to that of the separated charge carrier's perspective (see Appendix C.5.5 for all FRET measurements).

6.3.2 Donor Phase

Due to the high absorption in the acceptor phase of the BHJ, pulsed-PLQY in the PM6 phase resulted in photo-oxidation of the BHJ film at densities below the onset of the reduction of η_{PL}, indicating that this analysis was not possible in the heavily quenched donor phase. This is shown in Figure 6.4b where the low-pass filtered photoluminescence is recorded only for densities below photo-oxidation ($\rho_0 < 10^{16}$ cm^{-3}), and detailed in Appendix C.5.4. Therefore, the size of the donor domain can only be estimated by considering the ratio of the height of the PM6 photoluminescence signal in the BHJ (Φ_{BHJ}) to the neat film (Φ_{neat}) near the PM6 peak of ~ 680 nm and calculating the domain size through Equation 6.5 with $P_S = 1 - \Phi_{\mathrm{BHJ}}/\Phi_{\mathrm{neat}}$ [172, 211], noting that $\eta_{\mathrm{CT/FRET}} = \eta_{\mathrm{FRET}}$ and $\eta_{\mathrm{FRET}} \gg \eta_{\mathrm{diff}}$ as the exciton approaches the donor acceptor interface (with $R_0 = 2.1$ nm [189]). This analysis revealed a donor phase separated domain size of 2.2 nm. It is important to note that this measurement is only an estimate as it is subject to experimental errors related to excitation density and optical alignment. Further, FRET transfer is efficient from the donor to acceptor phase in PM6:Y6 [97]; therefore, the phase separated domain size estimated from the photoluminescence quenching is the domain size as seen from the frame of reference of the exciton (L_{eff}). To calculate the domain size from the perspective of the separated charge carriers twice the FRET Radii must be added to the value found from this analysis.

Figure 6.5a shows the FRET analysis for transitions from a PM6 molecule to a Y6 molecule. As described in Section 3.2.2, R_{FRET} between a donor and acceptor molecule in a BHJ can be calculated through Equation 3.5, 3.6, and 3.10 where $F_E(\lambda)$ is determined from the donor photoluminescence and $\epsilon_A(\lambda)$ is determined from the optical constants of the acceptor. Figure 6.5a shows F_E and ϵ_A for a PM6 and Y6 film, respectively. The overlap region described by Equation 3.6 is indicated as the shaded and hatched region of the plot. This relatively large spectral overlap indicates a large R_{FRET} as described in Section 3.1.1. R_{FRET} between PM6 and Y6 molecules was found to be 2.9 nm, similar to that found by other researchers in previous reports [97].

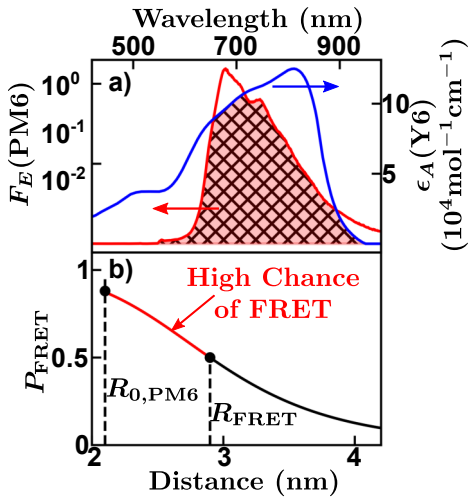

Figure 6.5: (a) (blue) Emission and (red) absorption spectra for neat PM6 and Y6 respectively. Hatched region indicates overlap region expressed in Equation 3.6. (b) Probability of FRET occurring as a function of distance between a PM6 and Y6 molecule. Labelled are the d_{100} spacing of PM6 ($R_{0,\mathrm{PM6}}$) and the R_{FRET} calculated from the data in panel a.

Figure 6.5b shows the probability that FRET will occur as a function of distance between PM6 and Y6 molecules. Marked is the intermolecular spacing between PM6 molecules ($R_{0,\mathrm{PM6}}$), taken as the GIWAX d_{100} spacing of a neat PM6 film [189], as well as the R_{FRET} for a PM6-to-Y6 transfer. Since R_{FRET} is greater than $R_{0,\mathrm{PM6}}$, there is a high chance that FRET will occur between a PM6 and Y6 molecule given that the excited PM6 molecule is within a few R_0 of the ground-state Y6 molecule. In a phase separated BHJ this is equivalent to stating that FRET will occur between a PM6 molecule within a few molecular spacings of the donor acceptor interface and a Y6 molecule near the donor acceptor interface. Considering all these phenomena, the phase separated domain size in the PM6 phase of a PM6:Y6 BHJ was calculated to be $\sim$ 10nm, comparable to fullerene-based BHJ acceptor phase-separated domain sizes [198].

6.4 Discussion of Domain Size in BHJ Thin Films

Similar analysis to that in Section 6.3.1 and 6.3.2 was carried out in a variety of fullerene and non-fullerene BHJs, the results are summarised in Table 6.1 while the associated pulsed-PLQY data can be found in Figure C.8 and the relevant FRET analysis can be found in Figure C.9. An interesting comparison can be drawn between PM6:Y6 and another high efficiency low-offset system, PM6:BTP-eC9. PM6:Y6 and PM6:BTP-eC9 have similar CS mobilities but PM6:BTP-eC9 has a PCE of 17.13%, attributable to larger fill-factor and short-circuit current. Measurements of pulsed-PLQY on PM6:BTP-eC9 BHJ and neat films reveals that, compared to PM6:Y6, neat BTP-eC9 has a larger diffusion length (36 ± 9 nm) while PM6:BTP-eC9 BHJ shows a similar P_S (0.94 ± 0.01), leading to a much larger optically measured domain size of 32 ± 1 nm in the acceptor domain. The donor domain analysis revealed a domain size $\sim$ 10 nm, equivalent to PM6:Y6. The large acceptor domain size is not an impediment to charge generation in this system due to the large diffusion length of BTP-eC9. While, in the case of PM6:Y6, the relatively small domain size allows for high P_S with a slightly reduced exciton diffusion length.

Interestingly, acceptor domain sizes similar to PM6:BTP-eC9 were measured in other NFA-based systems, indicating that NFA-based BHJs naturally form large ($\gg$ 17 nm) domains. Table 6.1 lists the exciton diffusion length and the optically measured domain size of each phase of each system studied. However, in these additional systems, small exciton diffusion lengths ($<$ 16 nm) did not support large exciton dissociation efficiencies, contributing to lower short-circuit currents and fill-factors (device performance for devices based on each BHJ studied are shown in Figure C.4). The optically measured acceptor domains in NFA-based BHJs are substantially larger than the 9.0 ± 0.6 nm measured in the fullerene system PCDTBT:$PC_{61}BM$ and, interestingly, larger than the coulomb capture radius. The consistently large phase separated domain size in NFA BHJs precipitates questions about the relevance of geometry to the device performance in state-of-the-art NFA-acceptor BHJ OPV devices.

6.5 Domain Size and Langevin Recombination

As outlined in Section 3.2.3, the origins of suppressed recombination are debated. However, the role that the phase separated domain size plays is common to all phase separated BHJ OPV devices regardless of energetic offset or chemical composition [105, 112]. Due to the interwoven geometry in an interdigitated BHJ analytic derivations of the functional form of γ_{enc} are indeterminate. Instead, a semi-classical approach is taken in which Monte-Carlo simulations produce values

for domain size dependent variables f and g such that total bimolecular recombination rate is given by

$$\beta = \frac{q}{\epsilon\epsilon_0} f(L) 2M_{g(L)}\left(\mu_\mathrm{n}, \mu_\mathrm{p}\right), \tag{6.8}$$

where $M_{g(L)}$ is the generalised mean of the electron and hole mobilities given by

$$M_{g(L)}\left(\mu_e, \mu_h\right) = \left(\frac{\mu_e^{g(L)} + \mu_h^{g(L)}}{2}\right)^{1/g(L)}. \tag{6.9}$$

From which γ_enc can be calculated from β/k_L as

$$\gamma_\mathrm{enc} = \frac{2f(L)}{\mu_\mathrm{n}/\mu_\mathrm{p} + 1}\left(\frac{(\mu_\mathrm{n}/\mu_\mathrm{p})^{g(L)} + 1}{2}\right)^{1/g(L)}. \tag{6.10}$$

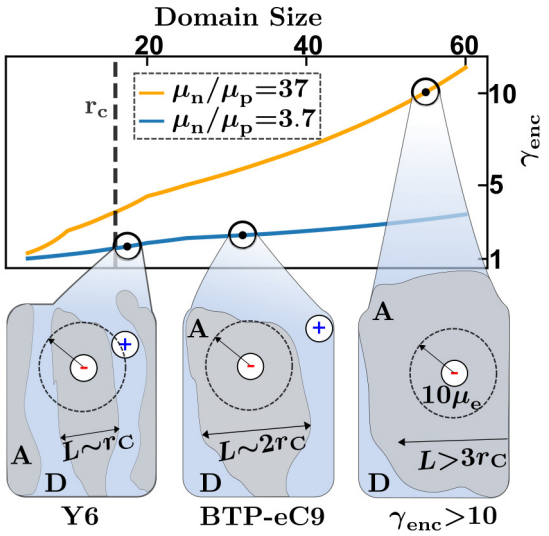

Figure 6.6: (Upper panel) γ_enc as a function of L for $\mu_\mathrm{n}/\mu_\mathrm{p}$ similar to PM6:Y6 and PM6:BTP-eC9 (blue line) and 10 times larger (orange line). (Lower panels) Cartoon depiction of phase separated domain sizes in PM6:Y6 (left), PM6:BTP-eC9 (center), and a system with $L > 3r_c$ and $10 \times \mu_\mathrm{n}/\mu_\mathrm{p}$ (right).

Thus γ_enc is dependent solely on L and the ratio of separated charge carrier mobilities.

Table 6.1 shows the results of γ_enc predicted from μ_n and μ_p and optically measured domain size for each systems studied. μ_n and μ_p are measured with resistance-dependent photovoltage measurements described in Appendix C.5.6. Given the similarities of μ_n and μ_p between PM6:Y6 and PM6:BTP-eC9 (see Table 6.1), the two-fold increase in domain size between the two systems results in an increase in γ_enc far smaller than the order of magnitude increase measured in the Langevin reduction factor through double injection experiments [149]. Figure 6.6 depicts the domain size dependency of γ_enc for two mobility imbalances, that of PM6:Y6 and PM6:BTP-eC9 as shown in the blue curve, and that 10 times greater as shown in the yellow curve. Given the similarity between μ_n and μ_p

of PM6:Y6 and PM6:BTP-eC9, γ_{enc} has a weak dependence on the domain size when moving between these two systems. In fact, to increase γ_{enc} one order of magnitude above PM6:Y6 the acceptor domain would need to increase in size 3 fold and $\mu_{\text{n}}/\mu_{\text{p}}$ would need to increase by an order of magnitude. Additionally, to maintain a similar P_S at domain sizes $> 3r_c$ would require an exciton diffusion length of > 60 nm. Despite the recent surge in acceptor molecules with $L_D > 20$ nm, materials matching these requirements are yet to be realised [180]. Therefore, even in domains as large as $2r_c$ γ_{enc} is too weak to explain the large decrease in β between PM6:Y6 and PM6:BTP-eC9 based devices.

A depiction of the domain size and carrier separation for PM6:Y6, PM6:BTP-eC9, and a system with $\gamma_{\text{enc}} \sim 10$ is shown in the lower panels of Figure 6.6. Table 6.1 lists μ_{n}, μ_{p}, and γ_{enc} for each system studied here. Even in cases of large L the resulting γ_{enc} is too small to be the determining factor in the heavily suppressed recombination seen in many of these systems. Therefore it is left to increases in the CT-state Langevin reduction factor to account for the heavily reduced recombination in these systems, enabled by the various factors discussed in Section 3.2.3.

6.6 Conclusion

In conclusion, it was shown that pulsed-PLQY can be utilised to evaluate the domain size in phase separated BHJs. The technique was validated through the use of Monte-Carlo simulations and through a bi-layer experiment. The phase separated domain size was then calculated for a variety of technologically relevant BHJs. It was found that NFA-based BHJs show a large (~ 3 fold) increase in acceptor domain compared to fullerene systems. The increase in acceptor domain size in NFA-based BHJ is compensated by an increase in exciton diffusion length, allowing for high exciton dissociation efficiency to contribute to high charge generation yields and short-circuit currents despite the large domains. The expected encounter Langevin reduction factor was calculated for each system and was found to be much smaller that the measured Langevin reduction, indicating that the limitations to electron and hole encounters brought about by the size of the domains is not the primary factor suppressing recombination. In Chapter 7 excitons will be left behind and the extraction of separated charge carriers from the BHJ will be discussed. Reciprocity between charge injection and collection will be considered and a technique for quantifying the non-radiative photovoltage loss and the bulk quasi-Fermi level splitting will be developed.

Table 6.1: Measured exciton diffusion length and L via pulsed-PLQY, μ_{n} and μ_{p} measured via resistance dependent voltage, and γ_{enc} calculated from physical parameters.

System	**Phase**	$\boldsymbol{L_D}$ **(nm)**	$\boldsymbol{L}$ **(nm)**	$\boldsymbol{\mu_e}$ **(cm²/Vs)**	$\boldsymbol{\mu_h}$ **(cm²/Vs)**	$\boldsymbol{\gamma_{\mathrm{enc}}}$
BQR:$PC_{71}BM$-AC	Donor	19 ± 5	22.9 ± 0.8	1.5×10^{-3}	4×10^{-5}	4.7 ± 0.5
BQR:$PC_{71}BM$-SA	Donor	18 ± 5	31 ± 2	3×10^{-3}	8×10^{-8}	2.3 ± 0.1
PCDTBT:$PC_{61}BM$	Acceptor	4 ± 1	9.0 ± 0.6	4×10^{-5}	6×10^{-5}	1.0 ± 0.1
PBDB-T:EH-IDTBR	Acceptor	13 ± 3	25 ± 1	4.5×10^{-3}	3.6×10^{-4}	3.2 ± 0.3
PM6:ITIC	Acceptor	14 ± 3	29 ± 3	4.9×10^{-3}	6.9×10^{-5}	7.4 ± 0.8
Ptb7-Th:Y6	Acceptor	25 ± 6	31.1 ± 0.9	1×10^{-4}	1.9×10^{-5}	2.7 ± 0.1
PM6:Y6	Acceptor	25 ± 6	17.5 ± 0.4	1.2×10^{-3}	2×10^{-4}	1.9 ± 0.1
PM6:Y6	Donor	4 ± 1	< 10	1.2×10^{-3}	2×10^{-4}	~ 1
PM6:BTP-eC9	Acceptor	36 ± 9	32 ± 1	1.5×10^{-3}	4×10^{-4}	2.3 ± 0.1
PM6:BTP-eC9	Donor	4 ± 1	< 10	1.5×10^{-3}	4×10^{-4}	~ 1

Chapter 7

Direct Quantification of Quasi-Fermi Level Splitting in Organic Semiconductor Devices

As discussed in Section 2.3.2, non-radiative losses to the open-circuit voltage are a primary factor in limiting the PCE of OPV-based solar cells. The dominant non-radiative loss is intrinsic to the active layer and can be determined from the QFLS and the radiative limit to the open-circuit voltage. However, quantification of the QFLS in low mobility OPV devices is challenging due to the excitonic nature of photoexcitation, as discussed in Section 3.1, and non-radiative photovoltage loss associated with surface recombination, as discussed in Section 3.2.4. In this chapter an experimental approach to directly measure the intrinsic non-radiative loss to the open-circuit voltage will be outlined; thereby, quantifying the QFLS. Drift-diffusion simulations are carried out to show that this method accurately predicts the QFLS in the bulk of the device regardless of surface recombination related photovoltage loss. State-of-the-art OPV-based solar cells, utilising PM6:Y6 as the active layer, are used as models to test the experimental approach. The experimental results compare well with the simulated predictions and the QFLS of PM6:Y6 is shown to be independent of device architecture. The work presented in this chapter (in conjunction with Appendix D) is largely the same as that published in *Direct Quantification of Quasi-Fermi-Level Splitting in Organic Semiconductor Devices* [3]. Section 7.2 was added to the work contributing to this chapter in order to clarify the context in which the established technique is necessary.

7.1 Radiative and Non-Radiative Losses to the Open-Circuit Voltage

The introduction of NFA OPV-based solar cells has propelled short-circuit currents consistently above 20 mA/cm^2 in state-of-the-art NFA-based blends [17, 91, 214, 215]. While open-circuit voltage losses have also decreased in NFA OPV-based solar cells, the mechanisms contributing to V_{OC} losses are not as straightforward to interpret as those contributing to the J_{SC} losses. Non-radiative losses to the V_{OC} result in proportional decreases to the PCE, making their detection and suppression a high research priority [216–223].

Non-radiative photovoltage loss can be intrinsic to the device's active layer, as described in Section 2.2.4 or dependent on the device structure, such as the surface recombination described in Section 3.2.4. As the V_{OC} is ultimately determined by both the QFLS of separated charge carriers in the device (at open-circuit conditions) and the work functions of the electrodes, an accurate quantification of the QFLS is key to understand the non-radiative recombination processes leading to photovoltage loss in semiconductor-based solar cells.

As outlined in Section 2.2 the chemical potential of an emitted photon is equal to the QFLS of recombining species of the semiconductor. Equipped with this understanding researchers have successfully employed photoluminescence measurements to evaluate the QFLS in systems where absorption and emission are dominated by free carriers [55, 224, 225], and subsequently applied this technique to OSC-based BHJs [226–228].

Regrettably, the excitonic nature of OSCs means that the absorbing state is generally not in equilibrium with the separated charge carriers, regardless of whether there is an equilibrium between the CS and CT states. Therefore, traditional photoluminescence measurements (as applied to inorganic semiconductors) are not a valid method to determine the QFLS in organic semiconductor blends. These discrepancies can be circumvented by employing the reciprocity principle between the charge collection of photogenerated carriers (under illumination) and the electroluminescent emission in the dark, as described by Equation 2.33 [65]. This has been successfully employed in conjunction with η_{LED} measurements to quantify the QFLS and related losses in a wide variety of semiconductor-based solar cells [66, 229–231]. However, the corresponding V_{OC} loss derived from this approach generally includes contributions from both intrinsic bulk-related processes and surface recombination.

In OPV devices, the presence of surface recombination is usually correlated with electrode-induced photovoltage losses at the contacts [232–234], causing a mismatch between V_{OC} and the associated QFLS in the bulk of the active layer. As such, measurements based on electroluminescence cannot differentiate be-

tween intrinsic and electrode-induced photovoltage losses, leading to a consistent underestimation the QFLS in OPV devices. A method for overcoming the difficulty in quantifying QFLS has been recently suggested using photo-induced absorption [234]. However, this method requires detailed knowledge about the absorption cross-section and charge transport parameters of the device, which must necessarily be semi-transparent. A more direct quantification of the QFLS in an optimised device would serve well to complement this method where photo-induced absorption is not trivial.

7.2 Deviations from Reciprocity

As described in Section 2.2 the emission flux from a semiconductor with flat featureless quasi-Fermi levels is described by Equation 2.18, while the electroluminescence flux is given by Equation 2.35. Note that the substitution of $\mathrm{EQE_{PV}}$ for a and qV for μ_γ in Equation 2.35 produces Equation 2.18. However, this substitution is only valid when the separated charge carriers in the semiconductor are in equilibrium with the emitted radiation across the device structure, satisfied when the quasi-Fermi levels are flat across the junction ($V = V_{\mathrm{OC}}$) and between the electrical contacts [55]. Further, Equation 2.18 and/or 2.35 may become invalid in the presence of non-equilibrium states such as radiative trap states or non-equilibrium excitons [67, 94, 107]. During a typical η_{LED} experiment the electroluminescence is measured as a function of injected current (J_{inj}) and η_{LED} is calculated at $J_{\mathrm{inj}} = J_{\mathrm{SC}}$. Under these conditions, J_{inj} will be balanced by the radiative and non-radiative recombination processes such that $J_{\mathrm{inj}} = q\Phi_{\mathrm{em}} + J_{\mathrm{nr,bulk}} + J_{\mathrm{nr,surface}}$, where $J_{\mathrm{nr,bulk}}$ ($J_{\mathrm{nr,surface}}$) is the non-radiative bulk (surface) recombination current. η_{LED} will be given by the ratio $q\Phi_{\mathrm{em}}/J_{\mathrm{inj}}$. In the dark, the total recombination current in the bulk of the active layer can be described by $q\Phi_{\mathrm{em}} = q\Phi_{\mathrm{em,0}} \exp\left(E_{\mathrm{QFLS,bulk}}/k_B T\right)$, where $q\Phi_{\mathrm{em,0}}$ is the voltage-dependent recombination current. Such that

$$E_{\mathrm{QFLS,bulk}} = k_B T \ln\left(\frac{q\Phi_{\mathrm{em}}}{q\Phi_{\mathrm{em,0}}}\right) = k_B T \ln\left(\frac{J_{\mathrm{inj}}\eta_{\mathrm{LED}}}{q\Phi_{\mathrm{em,0}}}\right), \tag{7.1}$$

is the quasi-Fermi level splitting in the bulk of the active layer while the cell is in the dark. Recalling Equation 3.33 the $\mathrm{QFLS_{bulk}}$ can be expressed as

$$E_{\mathrm{QFLS,bulk}} = k_B T \ln\left(\frac{J_{\mathrm{inj}}\eta_{\mathrm{LED}}}{q\int_0^\infty F_i\left(V_{\mathrm{OC}}\right)\Phi_{\mathrm{bb}}dE}\right). \tag{7.2}$$

Under optoelectronic reciprocity, $J_{\mathrm{inj}}\left(V_{\mathrm{OC}}\right) = J_{\mathrm{SC}}$ and the right-hand side of Equation 7.2 replicates Equation 3.35. This equivalence indicates that under

conditions where reciprocity is valid the quasi-Fermi level splitting in the bulk of the active layer is equal to qV_{OC}. Reconfirming the conditions under which Equation 2.35 and 2.18 are substitutable.

To explore this idea drift-diffusion simulations were implemented, Appendix G contains a detailed description of the drift-diffusion simulations used in the remainder of this chapter. The $\mathrm{QFLS}_{\mathrm{bulk}}$ is calculated as the bulk average QFLS at $J_{\mathrm{inj}} = J_{\mathrm{SC}}$ and compared to the simulated V_{OC}. Here $E_{\mathrm{QFLS,bulk}} = k_B T \ln\left(\overline{np}/N_c N_V\right)$, where $\overline{np} = (1/d)\int_0^d n(x)p(x)dx$, d is the active-layer thickness, and $n(x)$ and $p(x)$ are the simulated electron and hole densities, respectively. Similar to Equation 3.37, the deviation from reciprocity can be defined as

$$q\delta V_{\mathrm{OC}} = E_{\mathrm{QFLS,bulk}} - qV_{\mathrm{OC}}. \quad (7.3)$$

Figure 7.1 shows the qV_{OC}, $E_{\mathrm{QFLS,bulk}}$, and $q\delta V_{\mathrm{OC}}$ as a function of (balanced) separated charge carrier mobility. Consistent with Figure 3.8, the deviation from reciprocity increases with decreasing mobility due to a reduction in the QFLS of the recombining species.

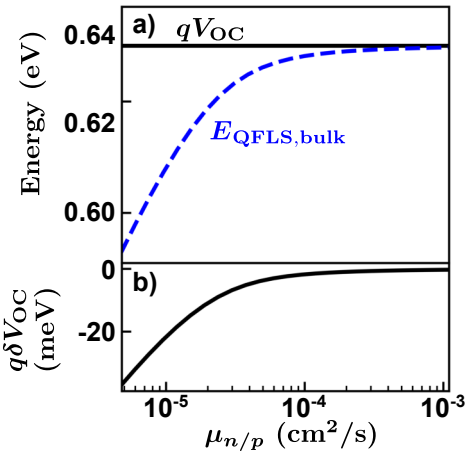

Figure 7.1: (a) (black) open-circuit voltage, (blue) quasi-Fermi level splitting in the bulk of the active layer in the dark at $J_{\mathrm{inj}} = J_{\mathrm{SC}}$., and (b) deviation from reciprocity as a function of separated charge carrier mobility for balance mobilities. These simulations use a generation rate equivalent to 1 sun, $\beta = k_L$, $d = 100$ nm, and an optical gap of 1 eV.

As discussed in Section 3.4, reciprocity is valid in situations where the minority carrier concentration is much smaller than the majority carrier concentration and linear as the system is moved away from equilibrium [63]. This can be further violated in a variety of ways in OPV devices since, as thin film systems with low mobility, the depletion region encompasses a large fraction of the active-layer thickness. In principle, this means that the carrier concentrations are both voltage and generation dependent, indicating that recombination can act as a non-linearity in the system [67]. Examining this idea further, Figure 7.2 shows the qV_{OC}, $E_{\mathrm{QFLS,bulk}}$, and $q\delta V_{\mathrm{OC}}$ as a function of generation rate. As the generation increases the V_{OC} has the form $qV_{\mathrm{OC}} = E_G - k_B T \ln\left(N_C N_V \beta/G\right)$ as shown by the comparison between the black

and red curves [235]. In general, J_{SC} increases linearly with generation, increasing the J_{inj} required to evaluate η_{LED} (in the dark). However, as J_{inj} is exponential with applied voltage the assumption that $J_{inj}(V_{OC}) = J_{SC}$ eventually fails and $q\delta V_{OC} < 0$ meV.

Figure 7.1 and 7.2 both assume perfectly Ohmic contacts. When injection barriers are increased surface recombination provides an additional non-radiative loss pathway, as described in Section 3.2.4. Under these conditions, the V_{OC} is determined by the difference between the anode and cathode work function while the $QFLS_{bulk}$ is governed by μ_γ of the recombining species. Figure 7.3 shows the qV_{OC}, $E_{QFLS,bulk}$, and $q\delta V_{OC}$ as a function of increasing injection barrier at the cathode. As the injection barrier is increased, the difference in work functions becomes smaller and large amounts of band bending occur near the contact, as depicted in Figure 3.4. This reduces the V_{OC} while μ_γ in the bulk does not change significantly [135,236]. As shown in Figure 7.3, this eventually leads to a situation where $q\delta V_{OC} > 0$ meV.

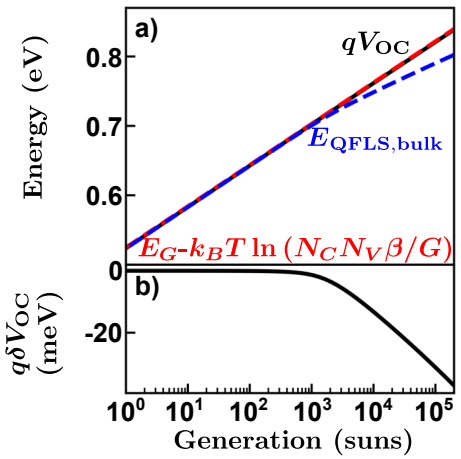

Figure 7.2: (a) open-circuit voltage, quasi-Fermi level splitting in the bulk of the active layer, and (b) deviation from reciprocity as a function of separated charge carrier generation. These simulations use $\mu = 10^{-3}$ cm^2/s, $\beta = k_L$, $d = 100$ nm, and an optical gap of 1 eV.

This analysis indicates that in systems where properties of the active layer are non-linear, as shown in Figure 7.1 and 7.2, electroluminescence measurements can lead to underestimations of the V_{OC}. Alternatively, in situations where the device structure leads to additional non-radiative pathways, as shown in Figure 7.3, electroluminescence measurements can lead to over-estimations of the V_{OC}. Realistically, both these mechanisms will occur simultaneously and could, in principle, lead to situations where it appears that reciprocity holds despite these two contrary effects.

The highest achievable V_{OC} is given by the radiative limit to the open-circuit voltage as described in Equation 2.29. However, the true V_{OC} will be the difference between radiative limit to the open-circuit voltage and the total non-radiative losses, as shown in Equation 2.31, herein defined as the sum of the intrinsic ($\Delta V_{OC}^{NR,Intrinsic}$) and electrode-induced ($\Delta V_{OC}^{NR,Electrode}$)

losses. The QFLS in the bulk of the active layer, is then determined by the difference between the radiative limit and the intrinsic non-radiative losses as

$$E_{\mathrm{QFLS}} = qV_{\mathrm{OC}}^{\mathrm{Rad}} - q\Delta V_{\mathrm{OC}}^{\mathrm{NR,Intrinsic}}. \tag{7.4}$$

In general, $\Delta V_{\mathrm{OC}}^{\mathrm{NR}}$ can be calculated from the η_{LED} via Equation 2.32; however, in order to isolate the effects of intrinsic and electrode-induced non-radiative losses one must consider the experimental conditions under which η_{LED} is measured as well as the relation between Φ_{em} and Equation 2.18 and 2.35. Directly probing the emission described in Equation 2.18 would, in the ideal case, allow for the quantification of the intrinsic non-radiative losses to the V_{OC} and subsequently the QFLS.

In the remaining sections of this chapter an experimental approach named electro-modulated photoluminescence quantum efficiency (EM-PLQY) will be established, providing a process for measuring the intrinsic non-radiative losses occurring within the active layer of an OPV device at open-circuit conditions. Through the principle of reciprocity this technique quantifies the QFLS in the active layer and subsequently the electrode-induced photovoltage loss under operational conditions. Drift-diffusion simulations are employed to simulate the proposed experiment and compare to both the results of traditional electroluminescence experiments, and the computable QFLS. Further, OPV-based solar cells utilising PM6:Y6 (see Appendix D.4 for a list of chemical acronyms used in this chapter) as an active layer are fabricated with various contacts designed to increase the non-radiative loss without modifying the QFLS in the bulk to confirm the simulated experiments. The η_{EMPL} were found to successfully predict the QFLS and related losses over the range of devices used.

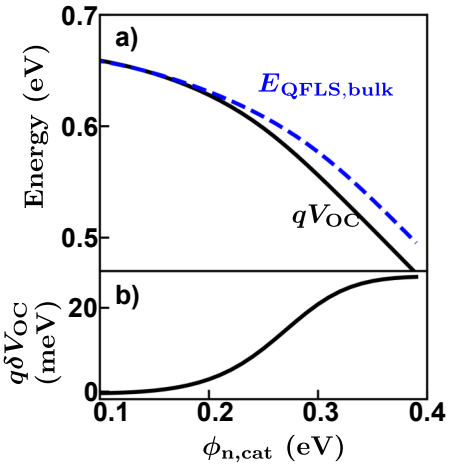

Figure 7.3: (a) open-circuit voltage, quasi-Fermi level splitting in the bulk of the active layer, and (b) deviation from reciprocity as a function of cathode injection barrier ($\phi_{\mathrm{n,Ct}}$). These simulations use a generation rate equivalent to 1 sun, $\mu = 10^{-3}$ cm^2/s, $\beta = k_L$, $d = 100$ nm, and an optical gap of 1 eV.

7.3 Experimental Approaches to Measuring Open-Circuit Voltage Losses

Figure 7.4 shows two experimental apparatuses used to measure η_{LED}, the traditional electroluminescence at applied voltage in the dark corresponding to $J_{\mathrm{inj}} = J_{\mathrm{SC}}$ (Figure 7.4a) and the alternative electro-modulated photoluminescence (Figure 7.4c). During electroluminescence measurements the device under test is held in the dark and a square-wave modulated voltage is applied to the device in forward bias by the function generator (Keysight 33500B). The current response can be measured as a square wave on the oscilloscope (Rohde & Schwarz

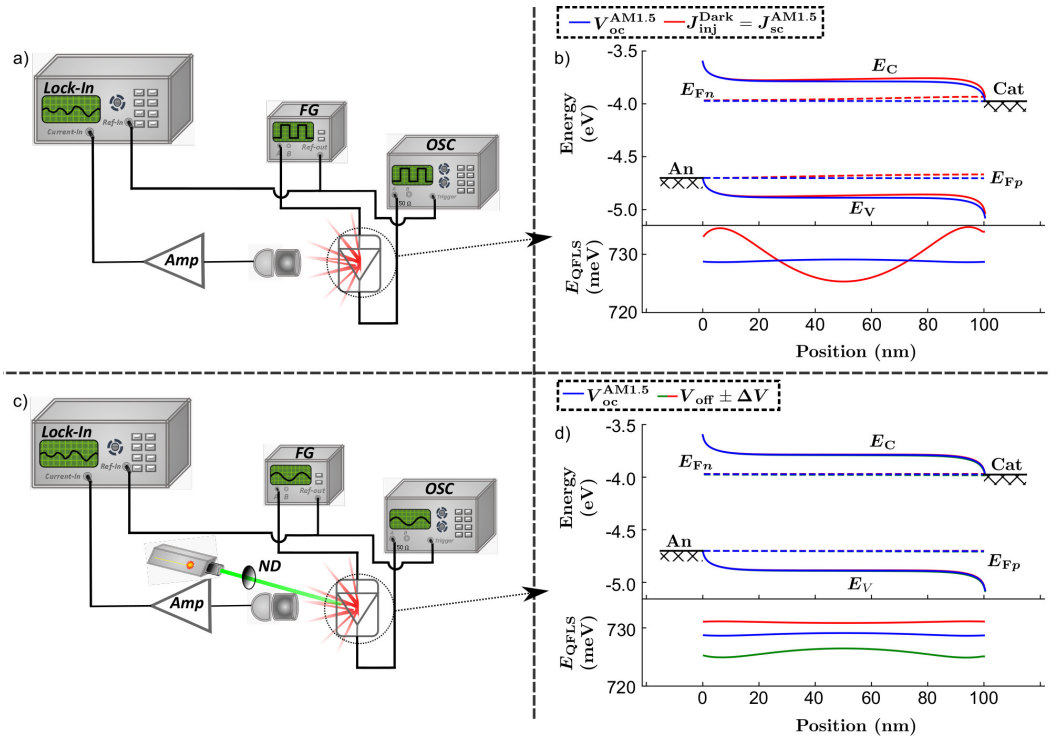

Figure 7.4: (a) Electroluminescence schematic. (b) (Solid lines) Simulated conduction (E_{C}) and valence levels (E_{V}), (dashed lines) electron ($E_{\mathrm{F}n}$) and hole ($E_{\mathrm{F}p}$) quasi-Fermi levels, and QFLS under the conditions: (blue) one-sun open-circuit and (red) dark injected current of one-sun short-circuit current. (c) Electro-modulated photoluminescence schematic. (d) Simulated conduction, valence, electron and hole quasi-Fermi levels, and QFLS under the conditions: (blue) one-sun open-circuit and (red/green) one-sun $V_{\mathrm{off}} \pm \Delta V$. An-anode, Cat-cathode, FG-function generator, Amp-current amplifier, OSC-oscilloscope, ND-neutral density wheel.

RTM3004) and the resulting electroluminescence is captured by a 50 mm lens, filtered with three low pass filters (Thorlabs FEL 600,550,550) (necessary to remove scattered pump light in the subsequent experiment), amplified by a silicon photoreceiver (FEMTO OE-300-Si-30), and measured with a lock-in amplifier (Stanford Research Systems SR860). The resulting external quantum efficiency (η_{EL}) can be calculated from the ratio of the electroluminescence intensity to the injected current at the reference frequency. This apparatus suffers from reduced geometric and spectral light collection efficiency which can be compensated for by calibrating the apparatus to an absolute measurement of η_{LED} (see Appendix D.2.1 for details). In contrast, Figure 7.4c shows the electro-modulated photoluminescence apparatus. Prior to performing an electro-modulated photoluminescence measurement the sample is illuminated with a laser (custom-made 520 nm diode laser) and the J_{SC} is measured. To perform the η_{EMPL} measurements the device is brought to open-circuit conditions where the applied time-dependent voltage, supplied by the function generator at angular frequency ω_V, resulting injected current, measured by the oscilloscope, and emitted photoluminescence have the form

$$V_{\mathrm{app}}(t) = V_{\mathrm{off}} + \Delta V \sin(\omega_V t), \tag{7.5}$$

$$J_{\mathrm{inj}}(t) = \Delta J \sin(\omega_V t), \tag{7.6}$$

$$\Phi_{\mathrm{em}}(t) = \Phi_0 + \Delta\Phi \sin(\omega_V t), \tag{7.7}$$

where ΔJ is kept smaller than $0.1 J_{\mathrm{SC}}$ by adjusting ΔV in order to keep the change in emission linear with the change in applied voltage (see Appendix D.2.2 for details related to the size of this perturbation), and V_{off} is set such that the mean current is zero. The resulting luminescence current amplitude ($\Delta\Phi$) is collected, amplified, and measured in the same manner as the electroluminescence measurement described above. The electro-modulated photoluminescence quantum efficiency is defined as the ratio between the luminescence intensity measured on the photodetector and the injected current amplitudes as

$$\eta_{\mathrm{EMPL}} = \frac{q\Delta\Phi}{\Delta J}. \tag{7.8}$$

To evaluate η_{EMPL} at conditions close to open-circuit one-sun illumination the laser power is adjusted such that the short-circuit current equals that of one-sun illumination, leading V_{off} to be approximately V_{OC} under AM1.5 spectra. As this experiment has the same spectral and geometric light collection efficiency as the electroluminescence measurement, the absolute η_{EMPL} is found by multiplying by the same calibration factor.

7.4 Drift Diffusion Simulations of EL-QY and EM-PLQY

Time-domain and steady-state drift-diffusion simulations were employed to demonstrate the difference between electroluminescence and EM-PLQY measurements in idealised systems before undertaking experiments. Figure 7.4b and d compare the simulated conduction, valence, electron and hole quasi-Fermi levels, and the QFLS across a device under one-sun open-circuit (blue), electroluminescence at applied voltage in the dark corresponding to $J_{\text{inj}} = J_{\text{SC}}$ (Figure 7.4b, red), and electro-modulated photoluminescence (Figure 7.4d, red/green) conditions. Under electroluminescence conditions the conduction and valence levels, along with the quasi-Fermi levels, deviate from the one-sun open-circuit conditions as the QFLS varies across the device. In contrast, under the maximum and minimum voltages applied during electro-modulated photoluminescence the conduction and valence levels, and quasi-Fermi levels, are indistinguishable from those of one-sun open-circuit conditions. This indicates that electro-modulated photoluminescence conditions are closer to operational conditions than electroluminescence conditions. Crucially, under electro-modulated photoluminescence conditions the QFLS varies little across the device for each voltage and much less over the applied voltage range compared with the 10 meV variance in QFLS under $J_{\text{inj}} = J_{\text{sc}}$ conditions, seen in Figure 7.4 b. The small variation in QFLS indicates that under electro-modulated photoluminescence conditions the device is very nearly in equilibrium with the emitted radiation, suggesting that the emission is described by Equation 2.18 and therefore can be used to quantify the QFLS. While the emission under electroluminescence conditions is given by Equation 2.35, reflective of both intrinsic and device related non-radiative losses.

To explore the relationship between QFLS and V_{OC} steady-state simulations of devices under open-circuit conditions were conducted. By increasing the electron injection barrier at the cathode ($\phi_{n,\text{Cat}}$), the effect of an increased electrode-induced photovoltage loss can be simulated for OPV devices [232, 233]. Figure 7.5a-c show the energy levels for devices with no (a), small (b), and large (c) injection barriers. The QFLS is defined as the difference between the electron and hole quasi-Fermi levels in the bulk of the device (here taken to mean the exact center) as indicated by the green arrow, while the V_{OC} can be determined by the difference between the electrode work functions as indicated by the black arrows [232]. As $\phi_{n,\text{Cat}}$ is increased the electron quasi-Fermi level near the cathode has to bend down in order to maintain equilibrium with the cathode work function. This leads to a considerable gradient in the electron quasi-Fermi level near the cathode ultimately reducing the V_{OC} while the QFLS inside the bulk remains predominately unaffected. Figure 7.5d summarises these data for devices with

electron injection barriers between 0 and 300 meV. In the absence of an injection barrier the QFLS and qV_{OC} are identical; however, as the injection barrier is increased the V_{OC} reduces while the QFLS is weakly affected. This is consistent with previous work where it was shown that $qV_{\mathrm{OC}} \propto E_G - \phi_{n,\mathrm{Cat}}$ for large enough electron injection barrier at the cathode [232, 236]. The size of the intrinsic and total non-radiative losses as well as those induced by the electrode ($\Delta V_{\mathrm{OC}}^{\mathrm{NR,Electrode}}$) and predicted by electroluminescence ($\Delta V_{\mathrm{OC}}^{\mathrm{NR},\eta_{\mathrm{EL}}}$) are labelled for clarity.

To uncover the relationship between the QFLS and η_{LED}, electroluminescence and EM-PLQY experiments were simulated for each system. The non-radiative losses, calculated from Equation 2.32, for both electroluminescence and electro-modulated photoluminescence are subtracted from the radiative limit; the blue curves in Figure 7.5d show the results of these calculations. The predicted losses from electroluminescence, when subtracted from $V_{\mathrm{OC}}^{\mathrm{Rad}}$, follow qV_{OC} for devices with low injection barrier, as expected from the reciprocity principle. A discrep-

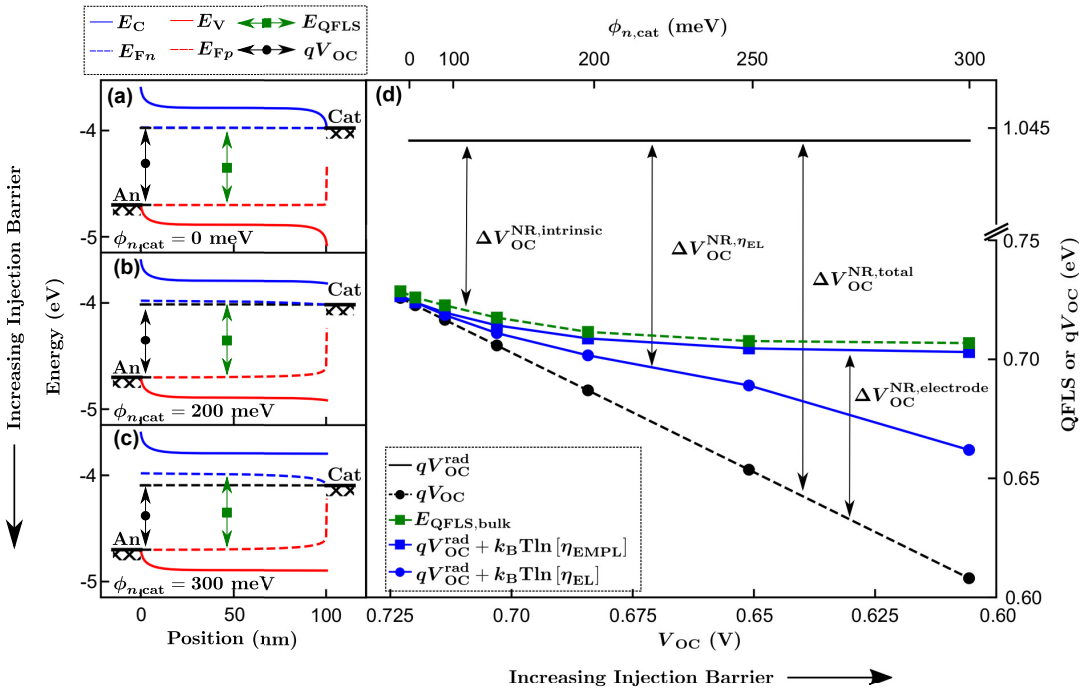

Figure 7.5: Simulated (a-c) conduction (E_{C}), valence (E_{V}), electron ($E_{\mathrm{F}n}$) and hole ($E_{\mathrm{F}p}$) quasi-Fermi levels for devices with (a) no, (b) medium, and (c) high injection barrier. (d) Simulated injection barrier dependence of (black circles) V_{OC}, (green squares) QFLS, and non-radiative losses measured by simulating (blue circles) electroluminescence and (blue squares) electro-modulated photoluminescence experiments.

ancy between the expected qV_{OC} given by electroluminescence and the actual qV_{OC} is seen for devices with large injection barrier. A possible explanation for this deviation from reciprocity is that an increased injection barrier at the cathode (reducing the number of injected electrons) generally makes the overall charge in the device uneven. In contrast, the simulated losses obtained by electro-modulated photoluminescence follow the QFLS across all devices. This indicates that η_{EMPL} is probing the intrinsic losses occurring within the active layer of the device. While electro-luminescence is sensitive to both the intrinsic and electrode-induced non-radiative losses. Consequentially, based on this analysis, the open-circuit voltage expected from reciprocity ($V_{\mathrm{OC,EL}}$), and the QFLS in the bulk can be calculated from Equation 2.31, 2.32, and 7.4 as:

$$qV_{\mathrm{OC,EL}} = qV_{\mathrm{OC}}^{\mathrm{Rad}} + k_{\mathrm{B}}T \ln\left[\eta_{\mathrm{EL}}\right], \tag{7.9}$$

$$E_{\mathrm{QFLS}} = qV_{\mathrm{OC}}^{\mathrm{Rad}} + k_{\mathrm{B}}T \ln\left[\eta_{\mathrm{EMPL}}\right], \tag{7.10}$$

where η_{EL} is η_{LED} measured through traditional electroluminescence measurements and η_{EMPL} is defined by Equation 7.8.

7.5 Device Structures with Increasing Non-Radiative Losses

To validate this proposal and the simulations (shown in Figure 7.5) devices with cathode materials of different work functions were prepared to emulate the effect of varying the electron injection barrier at the cathode. Each device was made with ITO/PEDOT:PSS as the anode and a 100 nm PM6:Y6 active layer, while the cathode was varied to alter the electrode-induced non-radiative losses. Using this architecture an optimised device with power conversion efficiency of 15.3% was created using PDINO/Ag as the cathode. Figure 7.6 shows the current-voltage characteristics for each solar cell device. Despite a relatively small shift in J_{SC} and fill factor between the different devices the power conversion efficiency is reduced due to the reduction in V_{OC}, indicative of increasing electrode-induced non-radiative losses due to surface recombination [232, 233]. While the optimised device has a V_{OC} of 0.847 V, the device using silver-only cathode exhibits a V_{OC} of 0.787 V, the added interlayers (PDNIO or PFN-Br) modify the work function to create a more ohmic cathode. Figure 7.7 a-g shows the device structures along with a sketch of the quasi-Fermi levels at open-circuit conditions. A near ohmic cathode (Figure 7.7a and b) will cause the QFLS in the bulk and the qV_{OC} to be roughly equivalent. Moving down from panel a to panel f the injection barrier is increased by increasing the cathode work function, causing a decrease in the V_{OC}

while the QFLS in the bulk of the active layer remains unchanged. The loss to the V_{OC} is due to the increasing electrode-induced non-radiative loss associated with the increasing injection barrier. Figure 7.7h-m shows the η_{LED} measured by both electroluminescence and EM-PLQY for each device as a function of dark injected current density or short-circuit current density respectively. As the injection barrier is increased, moving down the column from panel h to m, η_{EL} decreases until it is undetectable at low injected currents, while η_{EMPL} does not substantially change. This suggests that η_{EMPL} is measuring losses intrinsic to the semiconductor, while η_{EL} is influenced by the structure of the device, as predicted by the simulations in Figure 7.5. Figure 7.7g and n show the structure and external quantum efficiencies for a device without anode or cathode interlayers, severely limiting the driving force for charge extraction by creating an additional injection barrier at the anode. While electroluminescence emission was not measurable in this case, the corresponding electro-modulated photoluminescence emission was. In this low V_{OC} device η_{EMPL} was similar to the other devices. This corroborates that electro-modulated photoluminescence measurements are insensitive to device structure and are measuring an intrinsic property of the active layer.

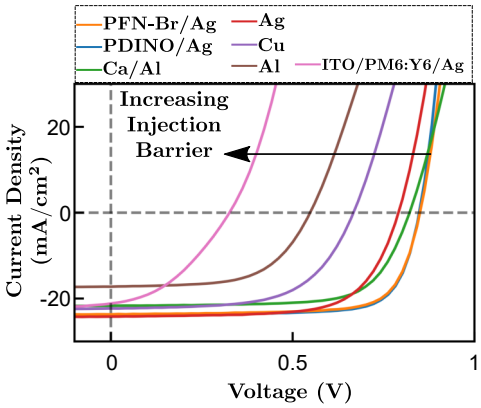

Figure 7.6: Current density-voltage curves at one-sun illumination for devices with various cathode materials. All devices have an structure ITO/PEDOT:PSS/PM6:Y6/cathode (cathode material shown in legend), except for the pink curve where the device structure is ITO/PM6:Y6/Ag.

7.6 Experimental Calculation of QFLS

The radiative limit to the V_{OC} is calculated by measuring the photovoltaic external quantum efficiency on the optimised device and was found to be 1.077 V (see Appendix D.3.1 for details). The expected V_{OC} was calculated from η_{EL} at $J_{Inj} = J_{SC}$ in accordance with Equation 7.9, and the QFLS is calculated from η_{EMPL} at J_{SC} in accordance with Equation 7.10. Figure 7.8a shows the QFLS, the expected qV_{OC}, and the measured qV_{OC} at one-sun conditions for devices with increasing

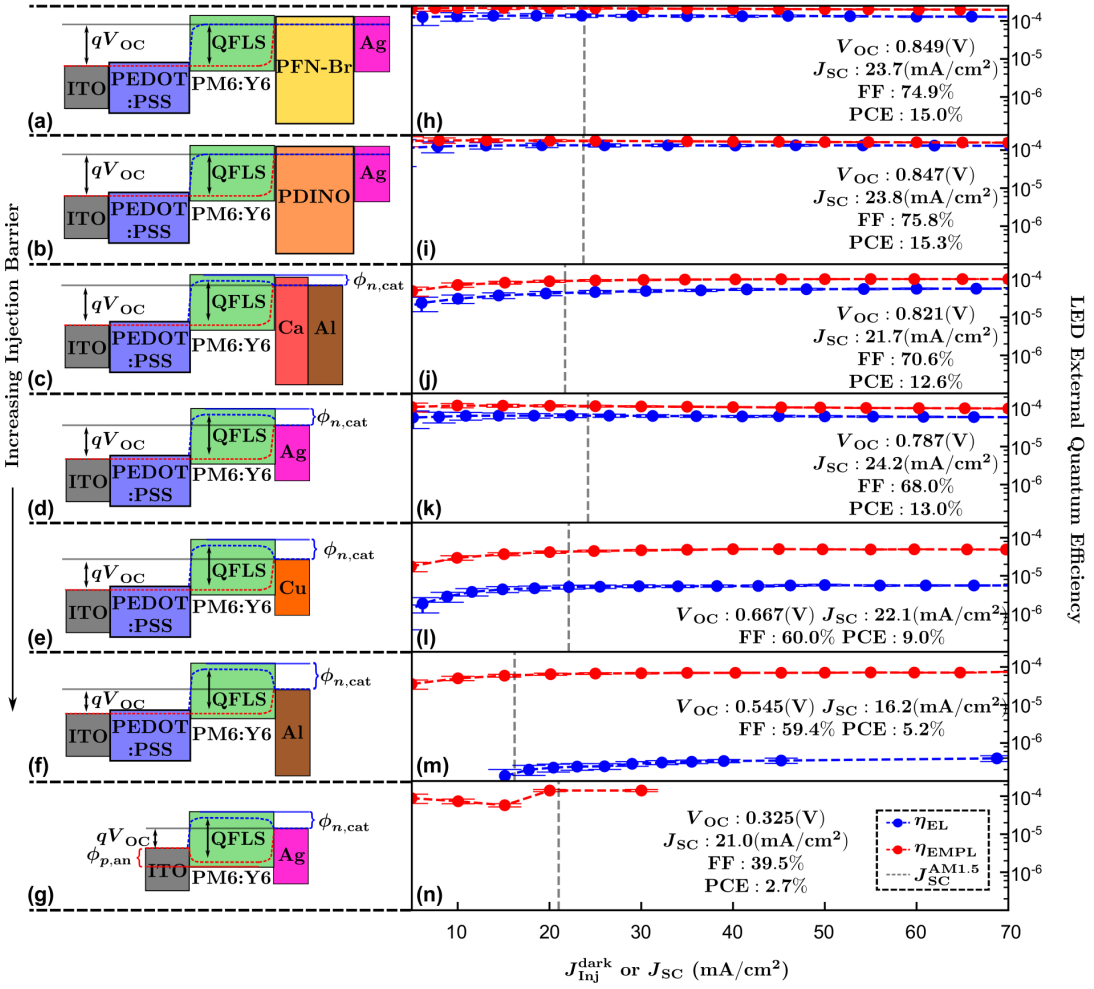

Figure 7.7: (a-g) Device structures with increasing injection barrier. (h-n) η_{LED} as measured by (blue) electroluminescence (η_{EL}) as a function of dark injected current and (red) electro-modulated photoluminescence (η_{EMPL}) as a function of short-circuit current, where the grey dashed lines indicate J_{SC} for that system. PCE-power conversion efficiency, FF-fill factor. Values of device parameters and measurements are taken from the pixel with highest V_{OC}. Error bars are calculated from measurement errors in the oscilloscope and lock-in amplifier (see Appendix D.5 for details).

non-radiative losses. The black arrows indicate the magnitude of the various non-radiative losses as a guide for the eye. Figure 7.8b through d show examples of device structures with small (b), medium (c), and large (d) injection barriers reproduced from Figure 7.7. The expected qV_{OC} based on the measured η_{EL} follows the actual qV_{OC} for devices with negligible injection barriers and occupy the region between the QFLS and qV_{OC} for devices with impractical injection barriers, as predicted by the simulations in Figure 7.5d. The calculated QFLS is constant throughout all devices as expected, demonstrating the precision of the method, and consistent with a previous study on the same material system using photo-induced absorption, further exemplifying the accuracy [234].

The inset of Figure 7.8a enhances the devices with lowest non-radiative losses. In the PDINO/Ag device ($V_{OC} = 0.847$V) the QFLS is 853 ± 5 meV, while the electrode-induced losses are not obvious due to the experimental uncertainty. However, in the PFN-Br device ($V_{OC} = 0.849$ V) the QFLS is 859 ± 4 meV while the electrode-induced losses account for a reduction in the V_{OC} of 10 ± 4 meV.

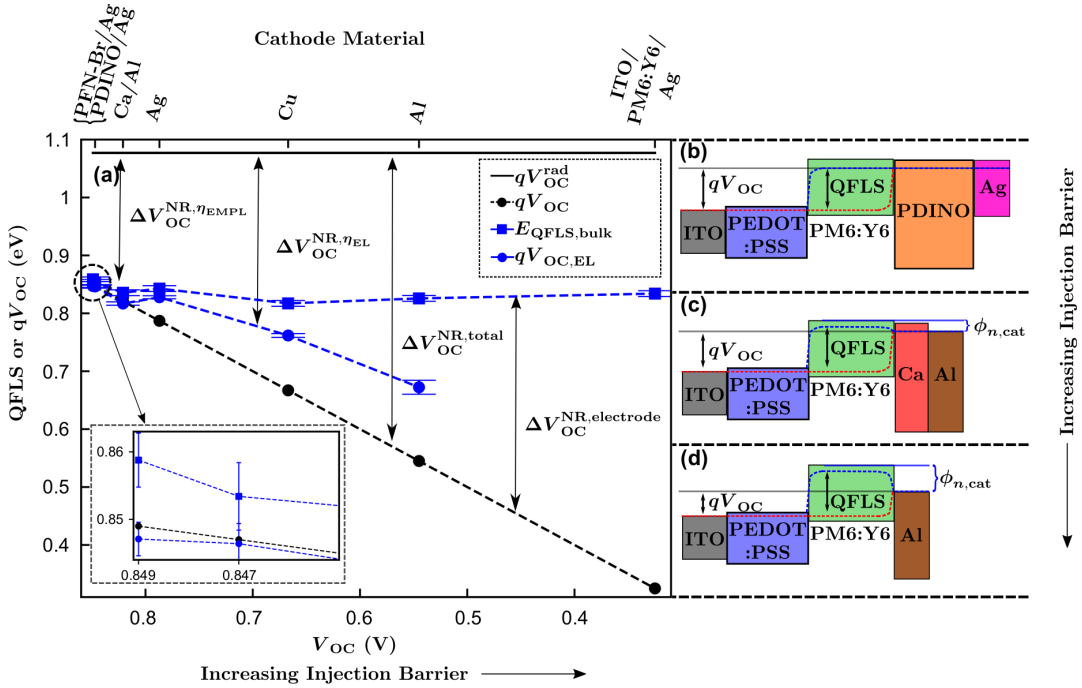

Figure 7.8: (a) QFLS measured by (blue squares) electro-modulated photoluminescence and (blue circles) expected qV_{OC} as measured by η_{EL} for PM6:Y6 systems with increasing non-radiative V_{OC} losses. Indicated on the plot is the size of the various non-radiative losses to the V_{OC}. Upper axis lists cathode materials while lower axis lists measured V_{OC}. (b-d) Device structure designed to have (b) low, (c) medium, and (d) high non-radiative losses at the cathode.

Improvements to the resolution will allow for discrepancies in the QFLS and the total non-radiative losses in an optimised cell to be distinguished, together quantifying the electrode-induced losses. This can be achieved by closely monitoring the temperature of the sample (accounting for about 3 meV of error) and decreasing the measurement error in the lock-in amplifier or the oscilloscope (accounting for about 1 meV of error each).

7.7 Conclusions

In conclusion, the conditions under which reciprocity can be invalidated in OPV devices were explored with simulation and experimentation. Distinct non-radiative recombination pathways in OPV devices were identified and disentangled using electro-modulated photoluminescence quantum efficiency measurements. It was shown that, when used in conjunction with traditional electroluminescence experiments, EM-PLQY was able to fully differentiate between the intrinsic and electrode-induced photovoltage losses and predict the QFLS in the bulk of the active layer. It was found that in a high V_{OC} optimised OPV-based solar cell the QFLS was 859±4 meV, leading to the conclusion that the electrode-induced losses accounted for 10 ± 4 mV of the total photovoltage loss. Electro-modulated photoluminescence quantum efficiency will contribute to the continual improvement of OSC based devices by allowing researchers to distinguish between intrinsic and electrode-induced losses to the open-circuit voltage.

Chapter 8

Conclusion

While the discussion in this thesis has focused attention on solar harvesting applications of OSCs it is by no means the only use case. Research into OSC-based light emitting diodes (LEDs), photodiodes, transistors, and lasers has been ongoing. These seemingly disparate fields all require a secure understanding of the fundamental photophysics and greater device architecture that underpins operation. Which, in turn, requires an array of accurate, accessible, and standardised measurement techniques. In this thesis various photophysical processes have been discussed and measurement techniques have been developed to probe specific aspects of these processes. In Chapter 1-3 the optoelectronic processes underlying operation in OPV devices have been discussed and compared to the well-established band-transport theory. Amongst the many notable differences, the excitonic nature of excitation in OSCs and the low separated charge carrier mobility were singled out. Chapter 4-6 focused on the former, while Chapter 7 focused on the latter.

In Chapter 4 a detailed balance model accounting for exciton diffusion and dissociation in OPV devices was developed and amalgamated with a established model of device operation. It was found that long exciton diffusion lengths supported by long exciton lifetimes were required for low-offset systems to achieve high CGY. The long exciton diffusion length allows for efficiency exciton transport to the interface while the long exciton lifetime reduces the CT state-to-exciton back transfer, most prominent in low-offset systems.

In Chapter 5 pulsed-PLQY was introduced as a method for measuring the exciton diffusion length through exciton-exciton annihilation. It was found that pulsed-PLQY is faster, easier, requires less equipment specialisation, and is less dependent on experimental conditions than other well established methods. Using pulsed-PLQY the exciton diffusion length and lifetime were measured in many technologically relevant systems. It was found that high-efficiency low-offset systems did have long diffusion lengths, but that this increase was driven by increases in diffusion constant, not lifetime. These results combined indicate that the high-efficiency low-offset NFA-based systems that are dominating the field today are not optimised. Further increases to CGY, J_{SC}, and PCE could be achievable by focusing on low-offset systems with long diffusion lengths supported by long

exciton lifetimes.

In Chapter 6 processes occurring in systems where FRET-activated charge generation is dominate were discussed, including charge or energy transfer, as well as bimolecular recombination; all processes that are dependent on the size of the phase separated domains. Pulsed-PLQY was demonstrated as a viable all-optical technique for experimentally determining the domain size in various BHJs. Utilising this, it was found that NFAs naturally form large phase-separated domains. Further, given the large domains, the long exciton diffusion lengths in the highest performing NFAs are requisite for them to achieve high CGYs. It was noted that the size of these domains, though substantially larger than fullerene BHJs, were insufficient to explain the large reduction in bimolecular recombination occurring in high-efficiency NFA-based devices.

In Chapter 7 optoelectronic reciprocity was examined and situations under which it can be invalid were explored. Through drift-diffusion simulations it was found that low mobilities, high separated charge carrier generation, and interface recombination can all create situations in which reciprocity is invalid. This invalidation is due to increased non-linearities in the device that uncouples the charge injection from the charge extraction processes. EM-PLQY was established and shown to reconcile these ideas with traditional reciprocity theory. Utilising EM-PLQY along with electroluminescence measurements fully characterises the non-radiative pathways in an OPV device, allowing for optimisation of the device electrodes and interlayers.

This thesis has aimed to aid researchers in understanding of the fundamental photophysics occurring in OSCs and BHJs made from OSC blends. Through the modelling, development, and validation of experimental techniques it has been shown how various fundamental properties can be quantified. The addition of these experimental modalities to the collection of widely used and highly successful techniques will assist researchers in the development of a variety of OSC-based photovoltaic devices.

Chapter 9

Outlook

As society progresses into the mid 21^{st} century many emerging technologies will compete for viability across a wide range of electronic applications. Whether application targets will be dominated by a single material system, as silicon has in the past 50 years, or be filled by purposed-built, targeted materials is yet to be determined. In the meantime there are many applications for which organic semiconductors are particularly well suited.

The thermodynamic limits laid out in Section 3.3 assume that the light harvested by the OPV-based solar cell is the AM1.5 spectra. However, many emerging technologies related to the so-called 'internet of things', require low power-consumption communication-protocols that may be achievable without the use of batteries. It is estimated that there could already be as many as 29 billion devices connected to the 'internet of things' with a total power consumption as high as 1100 TWh/year [26, 237]. Since the majority of these devices are indoor applications they will not be exposed to the AM1.5 spectra alone, rather the spectra produced by various LEDs. The versatility in optical gap engineering available with OPV-based solar cells allows for the spectral matching of various LEDs, ultimately allowing for higher efficiencies than systems optimised for the AM1.5 spectra.

Further, this spectra matching and portable nature of OPV-based solar cells are ideal for the use in agricultural areas where electrical grid access is difficult and spectral transmission engineering could be ideally utilized [238, 239]. Additionally, The light weight nature OSC based electronics including OPV-based solar cells enables their incorporation into novel, light-weight, and wearable electronics useful in both consumer and medical products [240, 241].

However, OPV devices suffer from degradation under light, especially in the presence of water and oxygen. Before OPV-based optoelectronic products can be brought to market the lifetime of the high-efficiency systems studied in laboratory environments must be systematically studied and improved [242]. The application of pulsed-PLQY to OSC-based BHJs could be used to study the morphological changes occurring under differing conditions, while η_{EMPL} could be used to study the effect various contacts have on device performance.

Parallel to the developments in OPV-based solar cells, research into the de-

velopment of OPV-based photodectors have made dramatic progress in recent years. Interestingly, the strong absorption coefficients associated with OSCs have enabled the development of device architectures with intrinsic spectral selectivity not possible with inorganic semiconductors [243, 244]. Exemplifying the unique applications possible with OSC-based systems.

Specific device architectures for both OPV-based solar cell and photodiodes rely on the long diffusion length of NFA OSCs, reinforcing the need for accurate quantification of L_D in OSCs [208, 209, 245]. Pulsed-PLQY offers researchers a low-cost, straightforward, and accurate measurement technique to quickly screen viable OSCs for long diffusion lengths. Interestingly these architectures show higher stability and are more compatible with established manufacturing techniques, as they require much thicker active layers compared with traditional BHJs.

The future development of OPV devices does not depend on the laboratory efficiencies and ideal device architectures alone. It will be influenced by broad social and technological factors, including established manufacturing techniques and supply chains. Development of consumer and industrial products on a large scale will start with inclusion into existing platforms and require small incremental victories to convince both the public and investors of the viability of the research and products.

Appendices

Appendix A

Role of Exciton Diffusion and Lifetime in Low Energy Offset Systems

A.1 1D-Monte-Carlo Simulations

With the aim of modelling the exciton dynamics within an organic semiconductor, a 1D Monte-Carlo hopping model was invoked. [157] First, a domain of size L with lattice spacing (dx) is created, and the lattice is randomly populated with an exciton and allowed to evolve in time with a temporal time step size (dt). The diffusion constant in the film is determined as $D = dx^2/2dt$. The lattice spacing, temporal step size, and exciton lifetime (τ) were 1 nm, 1 ps, and 300 ps respectively, corresponding to a diffusion coefficient of 5×10^{-3} cm^2/s and diffusion length of 12 nm ($L_D = \sqrt{D\tau}$). To explore the dependence on the characteristic length ratio ($2L_D/L$), the domain size was varied from 2 to 100 nm. To investigate the effect of the lifetime-product ($\tau \times k_{\mathrm{CT},0}$), the interfacial velocity of charge transfer was varied. This was accomplished by considering the rate of dissociation at the interface (k_{int}) to be related to the interfacial velocity as $\nu = k_{\mathrm{int}}dx/2$, and therefore, $k_{\mathrm{int}} = k_{\mathrm{CT},0}(L/dx)$. The exciton dissociation efficiency was calculated as the ratio of excitons exiting the domain at the interfaces to the total number of excitons generated in the simulation, from which the effective dissociation rate can be calculated through Equation 4.11.

A.2 Charge Generation Yield Calculations

In accordance with Equation 4.6, accounting for diffusion to and dissociation at the interface, under steady-state illumination, the kinetics of excitons and CT states is governed by the rate equations

$$G - k_{\mathrm{S}}n - k_{\mathrm{CT},0}n^* + k_{\mathrm{bt}}n_{\mathrm{CT}} = 0 \tag{A.1}$$

$$G_{\mathrm{CT}} + k_{\mathrm{CT},0}n^* - k_{\mathrm{bt}}n_{\mathrm{CT}} - k_{\mathrm{f}}n_{\mathrm{CT}} - k_{\mathrm{d}}n_{\mathrm{CT}} + \beta_0 n_{\mathrm{CS}}^2 = 0 \tag{A.2}$$

where G (G_{CT}) is the generation of excitons (CT states) from the ground state, n is the spatially averaged density of excitons in the domain, n^* is density of excitons at the interface, k_{S} is the decay rate of excitons ($k_{\mathrm{S}} = 1/\tau$), $k_{\mathrm{CT},0}$ is the dissociation rate constant of interfacial excitons, k_{bt} is the back-transfer rate constant, n_{CT} is the density of CT states, k_{f} is the decay rate constant of CT states, k_{d} is the rate constant for the dissociation of CT states into CS states, n_{CS} is the density of charge separated states, and β_0 is the bimolecular recombination rate constant of CS states to CT states. However, as established in Section 4.2, after accounting for exciton diffusion to the interface, the net exciton-to-CT rate can be equivalently expressed as $k_{\mathrm{CT},0}n^* - k_{\mathrm{bt}}n_{\mathrm{CT}} = k_{\mathrm{CT,eff}}n - k_{\mathrm{bt,eff}}n_{\mathrm{CT}}$, where $k_{\mathrm{bt,eff}} = k_{\mathrm{bt}}k_{\mathrm{CT,eff}}/k_{\mathrm{CT},0}$ and $k_{\mathrm{CT,eff}}$ is the effective dissociation rate constant described by Equation 4.9. Hence, Equations A.1 and A.2 can be rewritten as

$$G - k_{\mathrm{S}}n - k_{\mathrm{CT,eff}}n + k_{\mathrm{bt,eff}}n_{\mathrm{CT}} = 0 \tag{A.3}$$

$$G_{\mathrm{CT}} + k_{\mathrm{CT,eff}}n - k_{\mathrm{bt,eff}}n_{\mathrm{CT}} - k_{\mathrm{f}}n_{\mathrm{CT}} - k_{\mathrm{d}}n_{\mathrm{CT}} + \beta_0 n_{\mathrm{CS}}^2 = 0 \tag{A.4}$$

Then, based on eqs A3 and A4, and following the formalism of Sandberg et al., [37] the CT state-to-CS state dissociation efficiency can be calculated from the decay rate of CT states, the CT state-to-CS state dissociation, and back-transfer rate from CT states to excitons as $P_{\mathrm{CT}} = k_{\mathrm{d}}/(k'_{\mathrm{bt}} + k_{\mathrm{d}} + k_{\mathrm{f}})$, where $k'_{\mathrm{bt}} = (1 - P_{\mathrm{S}})k_{\mathrm{bt,eff}}$ is the ultimate (effective) back-transfer rate constant. Using a detailed balance approach, the back-transfer rate constant can be calculated as

$$k'_{\mathrm{bt}} = \frac{P_{\mathrm{S}}k_{\mathrm{S}}N_{\mathrm{S}}}{N_{\mathrm{CT}}} \exp\left[-\frac{\Delta E_{\mathrm{CT/S}}}{K_B T}\right] \tag{A.5}$$

where N_{S} and N_{CT} are the density of states for singlet excitons and CT states, respectively, and $\Delta E_{\mathrm{CT/S}}$ is the energetic difference between the exciton and CT state. The rate constant for CT state-to-CS state dissociation can be calculated as

$$k_{\mathrm{d}} = \frac{\beta_0 N_{\mathrm{CT}}^2}{N_{\mathrm{CT}}} \exp\left[-\frac{\Delta E_{\mathrm{CT/CS}}}{K_B T}\right] \tag{A.6}$$

where N_{CS} is the density of states for CS states and $\Delta E_{\mathrm{CT/CS}}$ is the effective CT state binding energy. The charge generation yield can then be expressed as the product of the exciton dissociation efficiency and the CT state dissociation efficiency.

$$P_{\mathrm{CGY}} = P_{\mathrm{S}} \times P_{\mathrm{CT}} = \frac{P_{\mathrm{S}}}{1 + \frac{k_{\mathrm{f}}N_{\mathrm{CT}}}{\beta_0 N_{\mathrm{CS}}^2} \exp\left[-\frac{\Delta E_{\mathrm{CT/CS}}}{K_B T}\right]\left[1 + \frac{P_{\mathrm{S}}k_{\mathrm{S}}N_{\mathrm{S}}}{k_{\mathrm{f}}N_{\mathrm{CT}}} \exp\left[-\frac{\Delta E_{\mathrm{CT/S}}}{K_B T}\right]\right]} \tag{A.7}$$

The calculations in Figure 4.4 were performed by evaluating P_S from Equation 11 and using the result to calculate P_{CGY} from Equation A.7. In this work, the default values for the parameters were taken from Sandberg et al. as $k_f = 10^{10} s^{-1}$, $\beta_0 = 5 \times 10^{-10} cm^3 s^{-1}$, $N_{CT} = 10^{18}$ cm^{-3}, $N_S = N_{CS} = 3 \times 10^{20}$ cm^{-3}, $T = 300$ K, and $\Delta E_{CT/CS} = 100$ meV. Meanwhile, the values for k_S and P_S are determined by the choice of τ and D, as shown for each calculation in Figure 4b.

Appendix B

Quasi-Steady-State Measurement of Exciton Diffusion Lengths

B.1 Materials

B.1.1 Chemical Definitions

- PM6: Poly [(2, 6-(4, 8-bis(5- (2-ethylhexyl-3-fluoro) thiophen-2-yl)- benzo [1, 2-b:4, 5-b′] dithiophene)) -alt- (5, 5-(1′, 3′-di-2-thienyl-5′, 7′-bis(2-ethylhexyl)benzo [1′, 2′-c:4′, 5′-c′] dithiophene-4, 8-dione)]
- P3HT-Regiorandom: Poly(3-hexylthiophene-2, 5-diyl)
- PTB7-Th: Poly[4, 8-bis(5-(2-ethylhexyl)thiophen-2-yl) benzo[1, 2-b;4, 5-b′] dithiophene-2, 6-diyl-alt- (4- (2-ethylhexyl)-3- fluorothieno [3, 4-b]thiophene-)-2-carboxylate-2-6-diyl)]
- PCDTBT: Poly[N-9′-heptadecanyl-2, 7-carbazole-alt-5, 5- (4′, 7′-di-2-thienyl-2′, 1′, 3′-benzothiadiazole)]
- $PC_{60}BM$: ([6, 6]-Phenyl-C_{60}-butyric acid methyl ester)
- P3HT-Regioregular: Poly(3-hexylthiophene-2, 5-diyl)
- ITIC: (5Z)-3-ethyl-2-sulfanylidene-5-[[4-[9, 9, 18, 18-tetrakis(2- ethylhexyl)-15- [7- [(Z)-(3-ethyl-4-oxo-2-sulfanylidene-1, 3-thiazolidin-5-ylidene)methyl]-2, 1, 3-benzothiadiazol-4-yl]-5, 14-dithiapentacyclo [10.6.0.03, 10.04, 8.013, 17] octadeca-1(12), 2, 4(8), 6, 10, 13(17), 15-heptaen-6-yl]-2, 1, 3- benzothiadiazol-7-yl] methylidene]-1, 3-thiazolidin-4-one
- IT4F: 3, 9-bis(2-methylene-((3-(1, 1-dicyanomethylene)-6, 7-difluoro)- indanone))-5, 5, 11, 11-tetrakis(4-hexylphenyl)-dithieno [2, 3-d:2′, 3′-d′]-s-indaceno [1, 2-b:5, 6-b′]dithiophene

- Y6: 2, 2′-[[12, 13-Bis(2-butyloctyl)-12, 13-dihydro-3, 9- dinonylbisthieno[2″, 3″:4′, 5′] thieno [2′, 3′:4, 5]pyrrolo[3, 2-e:2′, 3′-g][2, 1, 3] benzothiadiazole-2,10-diyl] bis [methylidyne(5, 6-chloro-3-oxo-1H-indene-2, 1(3H)-diylidene)]] bis[propanedinitrile]
- BTP-eC9: 2, 2′- [[12, 13-Bis(2-butyloctyl)-12, 13-dihydro-3, 9-dinonylbisthieno[2″, 3″:4′, 5′]thieno[2′, 3′:4, 5] pyrrolo [3, 2-e:2′, 3′-g][2, 1, 3] benzothiadiazole-2, 10-diyl] bis [methylidyne(5, 6-chloro-3-oxo-1H-indene-2, 1(3H)-diylidene)]] bis [propanedinitrile]

B.1.2 Film Fabrication

Substrate Preparation

Before films were spin coated on glass substrates, the substrates were cleaned in deionized water, acetone, and 2-propanol by sequential sonication for 10 minutes. The cleaned substrates were dried with nitrogen gas, baked on a hot plate at 110°C for 10 minutes, and treated in a UV-Ozone cleaner (Ossila, L2002A2-UK) for 20 minutes.

Film Deposition

Table B.1 lists each material, solvent, concentration, and spin speed used, as well as the resulting thickness. Each material listed in Table 5.1 was made by dissolving the relevant material in the listed solvent by stirring overnight and spin coating onto glass substrates. The thickness was measured via ellipsometry (J.A. Woollam M-2000 Spectroscopic Ellipsometer).

Material	Solvent	Concentration (mg/mL)	SpinSpeed (rpm)	Thickness (nm)
PM6	CF	14	8000	16
P3HT-Regiorandom	CB	12	2000	47
PTB7-Th	CF	14	8000	17
PCDTBT	CB	7	2000	19
$PC_{60}BM$	CB	14	1000	50
P3HT-Regioregular	CB	20	2000	67
ITIC	CF	20	4000	54
IT4F	CF	20	4000	57
Y6	CF	20	8000	61
BTP-eC9	CF	20	8000	36

Table B.1: Solvent, concentration, and spin speed used to fabricate films for each material and resulting thickness.

B.2 Time Resolved Photoluminescence

The thin films were held in a cryostat (Linkam LTS420) under a constant flow of nitrogen gas to prevent photo-oxidation [246], and an initial density of excitons ($\rho_0 = P_{\text{abs}}/\pi\omega^2 f_{\text{rep}} E_{\text{ph}} d$, P_{abs}-absorbed laser power, f_{rep}-reprate and ω-spotsize of the laser, E_{Ph}-incident photon energy, d-film thickness) is injected by an ultrafast laser source (Pharos PHM02-2H-3H), 515 nm, 25 kHz, 300 fs. The resulting photoluminescence is collimated, filtered to remove scattered pump light, and focused into the streak camera (Hamamatsu C14831).

B.3 Spotsize Measurement

The spotsize for the TRPL and pulsed-PLQY measurements were obtain through the knife edge method [247], in which the transmitted power is fit to the function

$$P_{\text{T}} = 0.5 \left[1 - \text{erf}\left(\sqrt{2} \frac{(x - x_0)}{\omega} \right) \right] \tag{B.1}$$

where P_T is the normalised transmitted power, erf is the error function, and ω is the spotsize. These measurements are shown in Figure B.1 for both the TRPL case (200 mm focal length pump lens) and the pulsed-PLQY case (no pump lens).

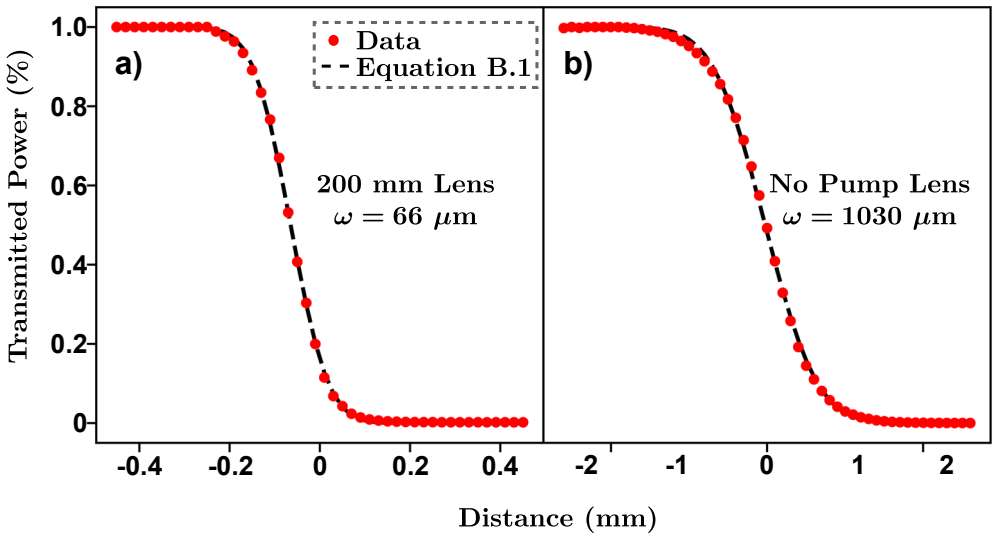

Figure B.1: Knife-edge spot-size measurements for (a) 200 mm focal length lens and (b) no pump lens.

B.4 Error Analysis

η_{PL}

The two main sources of error in the data presented in Figure 5.4 are the error in the measurement of film thickness, leading to an error in the calculation of the initial density, and measurement errors accounting for variations in film thickness. To account for the error in the initial density (σ_{ρ_0}) the error in the film thickness (σ_d) is propagated as

$$\sigma_{\rho_0} = \frac{\partial \rho_0}{\partial d}\sigma_d = \rho_0 \frac{\sigma_d}{d} \tag{B.2}$$

therefore, the 10% error in thickness measurements corresponds to a 10% error in excitation density. Any errors in measurement and variations in film thickness ($\sigma_{\eta_{\mathrm{PL}}}$) are accounted for by repeating each measurement 5 times on different spots on each sample and taking the statistical mean and standard deviation to represent each data point and error bars.

$\gamma\tau$

The error in $\gamma\tau$ was found by fitting all 5 normalised trials of η_{PL} to Equation 5.5. The covariance of the fitting parameter was used as a value for $\sigma_{\gamma\tau}$.

Table I

The errors in Table 5.1 are propagated in the usual way and added in quadrature. The error in L_D (σ_{L_D}) is given by the error in $\gamma\tau$ and R_0 (σ_{R_0}, assumed to be half the value of R_0) as

$$\sigma_{L_D} = \left[\left(\frac{\partial L_D}{\partial \gamma\tau}\sigma_{\gamma\tau}\right)^2 + \left(\frac{\partial L_D}{\partial R_0}\sigma_{R_0}\right)^2\right]^{1/2} \tag{B.3}$$

$$\sigma_{L_D} = \frac{1}{2}\left[\left(\frac{L_D}{\gamma\tau}\sigma_{\gamma\tau}\right)^2 + \left(\frac{L_D}{R_0}\sigma_{R_0}\right)^2\right]^{1/2} \tag{B.4}$$

The error in γ is found from the error in $\gamma\tau$ and τ ($\sigma_\tau = 10$ ps) as

$$\sigma_\gamma = \left[\left(\frac{\partial \gamma}{\partial \gamma\tau}\sigma_{\gamma\tau}\right)^2 + \left(\frac{\partial \gamma}{\partial \tau}\sigma_{\tau}\right)^2\right]^{1/2} \tag{B.5}$$

$$\sigma_\gamma = \left[\left(\frac{\sigma_{\gamma\tau}}{\tau}\right)^2 + \left(\frac{\gamma}{\tau}\sigma_{\tau}\right)^2\right]^{1/2} \tag{B.6}$$

The error in the diffusion coefficient (σ_D) is found from the error in $\gamma\tau$, R_0, and τ as

$$\sigma_D = \left[\left(\frac{\partial D}{\partial \gamma\tau}\sigma_{\gamma\tau}\right)^2 + \left(\frac{\partial D}{\partial \tau}\sigma_{\tau}\right)^2 + \left(\frac{\partial D}{\partial R_0}\sigma_{R_0}\right)^2\right]^{1/2} \tag{B.7}$$

$$\sigma_D = \left[\left(\frac{\sigma_{\gamma\tau}}{4\pi R_0\tau}\right)^2 + \left(\frac{D}{\tau}\sigma_{\tau}\right)^2 + \left(\frac{D}{R_0}\sigma_{R_0}\right)^2\right]^{1/2} \tag{B.8}$$

B.5 Pulsed-PLQY Measurements

The low density TRPL and relative η_{PL} data and corresponding fits are show in Figures B.2-B.11. The top panel in each Figure shows the TRPL data (blue) on a log-linear scale, the data used to fit for τ (green) and the fitting (black line). Indicated on the upper panel is the density of the initial excitation. The lower panel shows the relative η_{PL} data as a function of initial density (blue) and the fit to Equation 5.5 (black line). Indicated on the lower panel are some of the calculated values listed in Table 5.1.

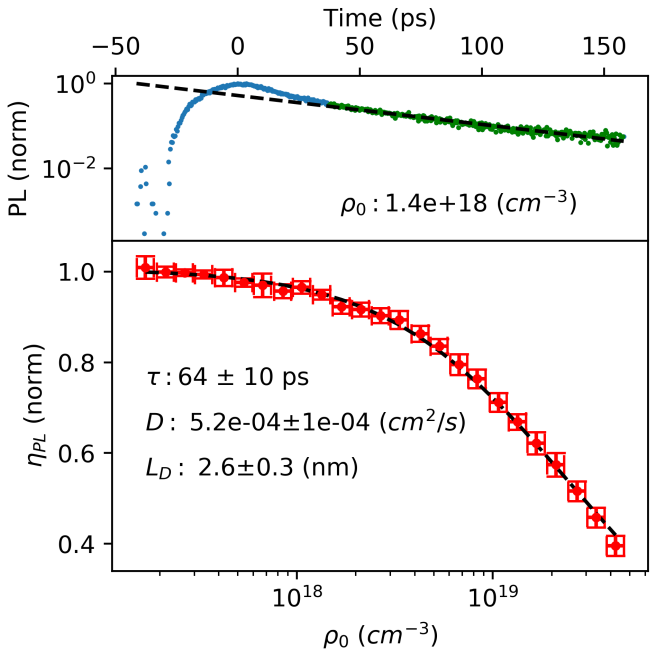

Figure B.2: (Top Panel) TRPL and (lower panel) η_{PL} for **PM6**.

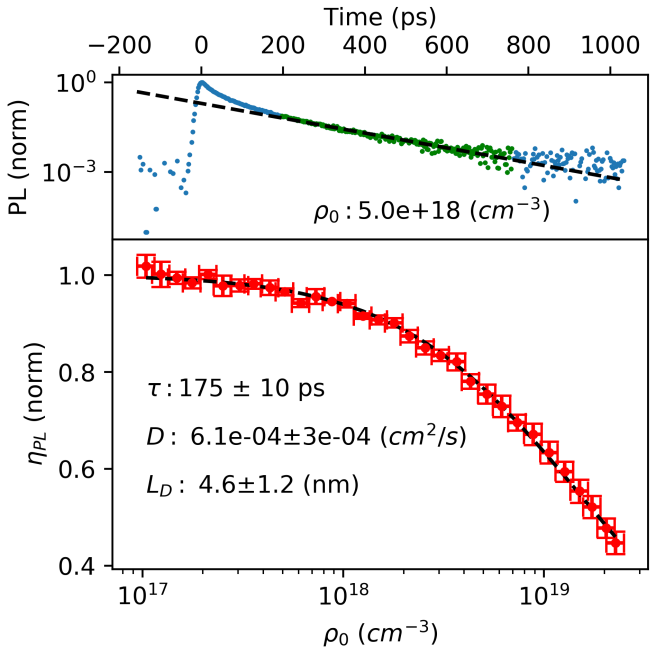

Figure B.3: (Top Panel) TRPL and (lower panel) η_{PL} for **P3HT regiorandom**.

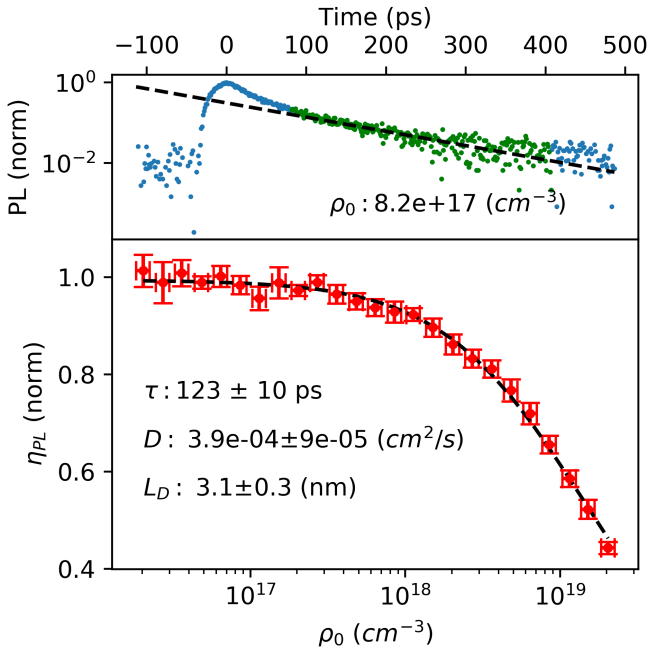

Figure B.4: (Top Panel) TRPL and (lower panel) η_{PL} for **PTB7-Th**.

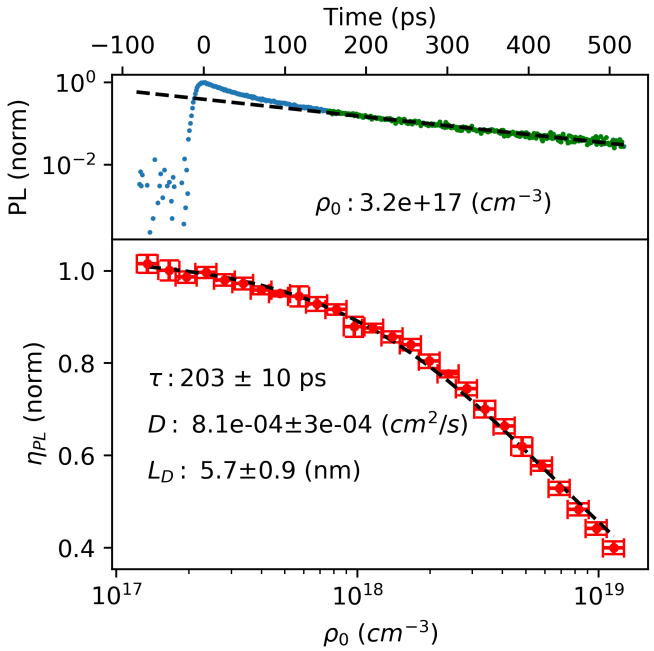

Figure B.5: (Top Panel) TRPL and (lower panel) η_{PL} for **PCDTBT**.

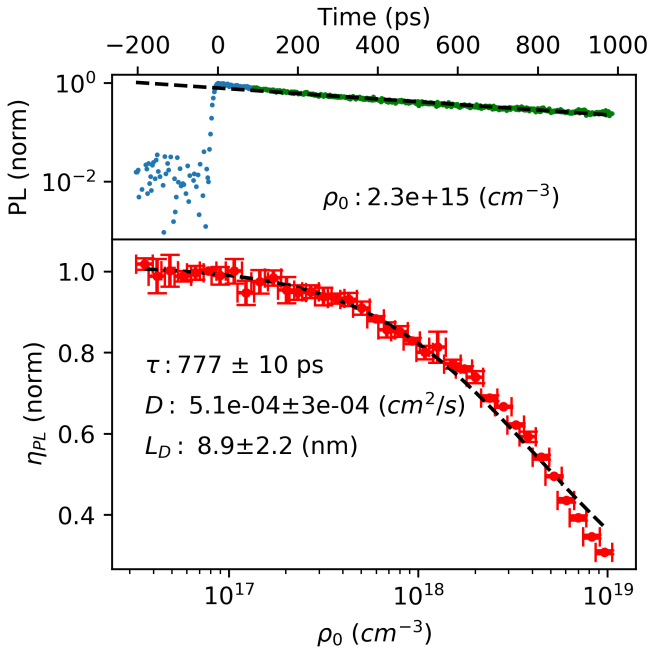

Figure B.6: (Top Panel) TRPL and (lower panel) η_{PL} for **$PC_{60}BM$**.

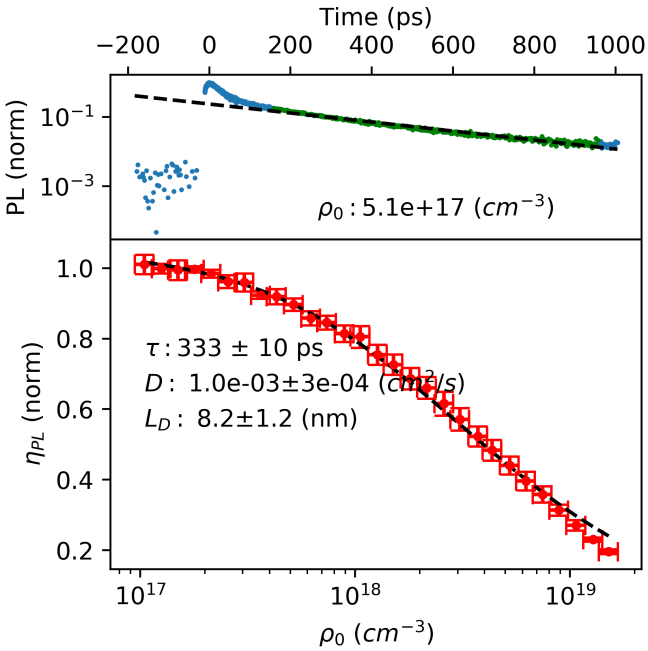

Figure B.7: (Top Panel) TRPL and (lower panel) η_{PL} for **P3HT regioregular**.

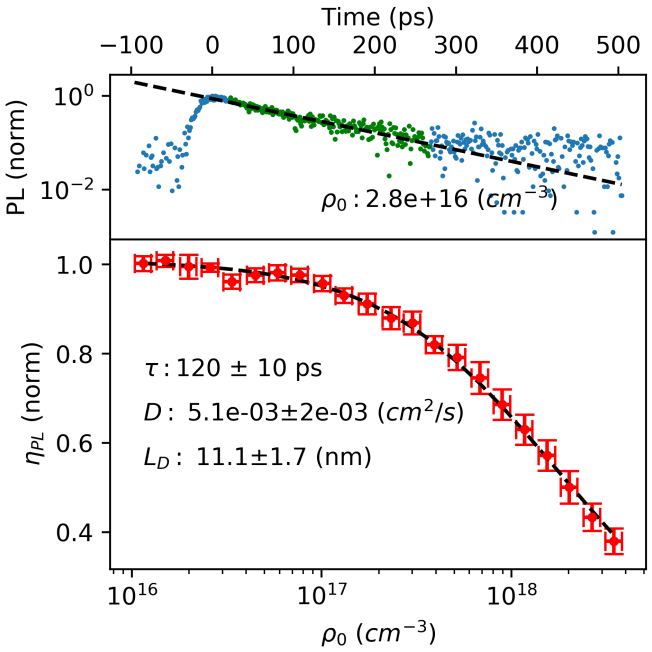

Figure B.8: (Top Panel) TRPL and (lower panel) η_{PL} for **ITIC**.

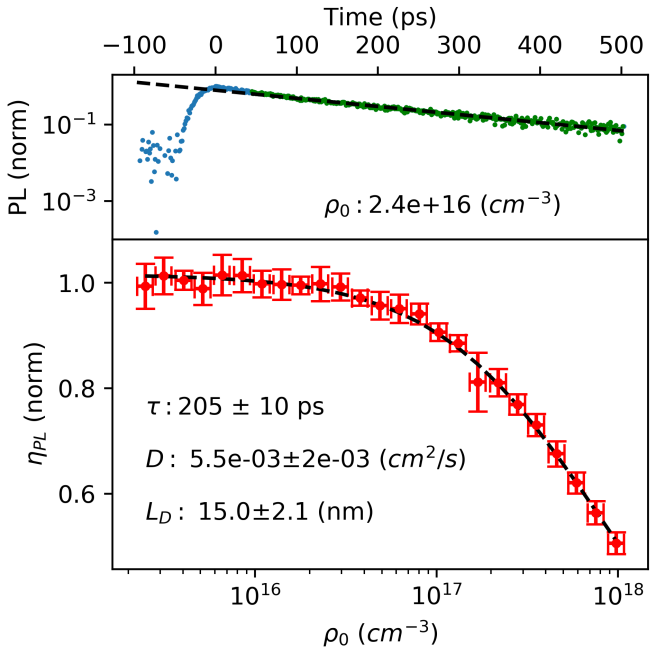

Figure B.9: (Top Panel) TRPL and (lower panel) η_{PL} for **IT4F**.

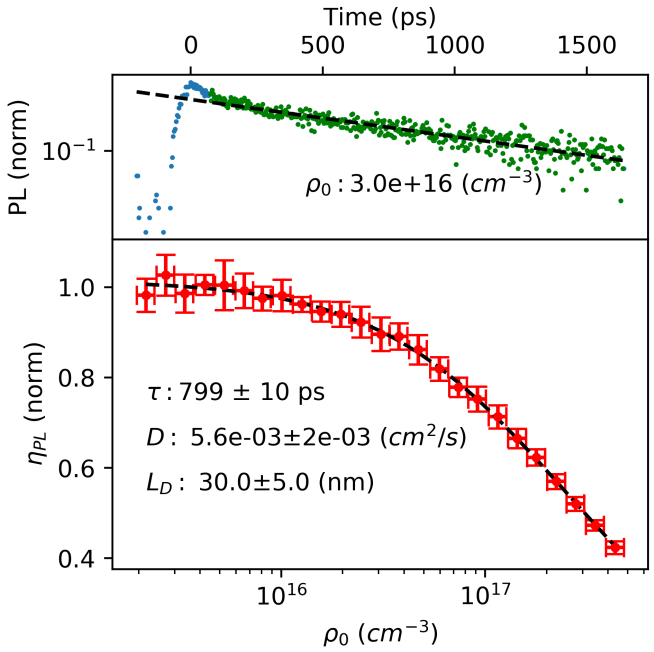

Figure B.10: (Top Panel) TRPL and (lower panel) η_{PL} for **Y6**.

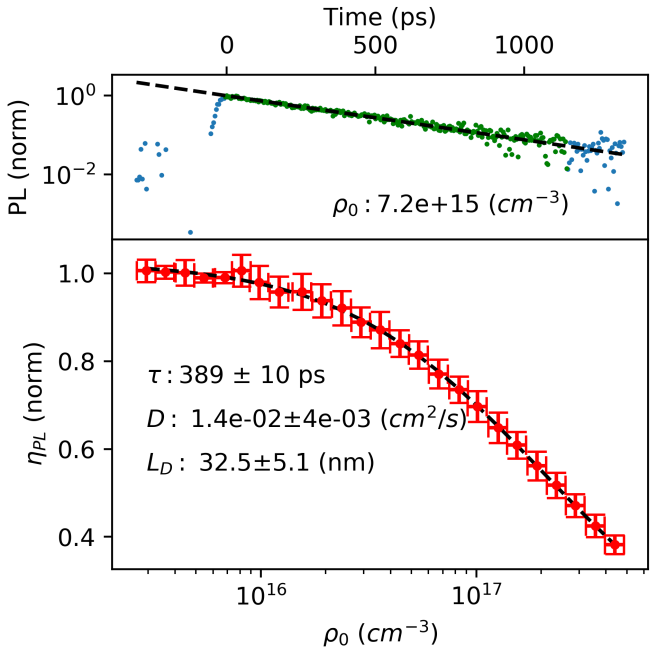

Figure B.11: (Top Panel) TRPL and (lower panel) η_{PL} for **BTP-eC9**.

B.6 Monte-Carlo Simulation Parameters

Table B.2 lists the parameters used in the Monte-Carlo simulations shown in Figure 5.1 and 5.2. Details about the implementation of the 3D Monte-Carlo simulations are outlined in Appendix F.

Parameter	**Value**
τ	300 ps
dx	0.774597 nm
dt	1 ps
N_{minimum}	8000
z-thickness	50 nm

Table B.2: Parameters used in Monte-Carlo simulation shown in Figure 5.1. N_{minimum} is the lower limit to the number of excitons at the start of each simulation.

Appendix C

Relationship Between Charge Carrier Dynamics and Exciton Dynamics

C.1 Materials

C.1.1 Chemical Definitions

- CN; Chloronaphthalene (C10H7Cl)
- DIO; 1,8-Diiodooctane
- PEDOT:PSS; Poly(3,4-ethylenedioxythiophene) polystyrene sulfonate.
- PDINO-3F; 2, 9-Bis[3-(dimethyloxidoamino) propyl] anthra [2, 1, 9-def:6, 5, 10-d′ e′ f′] diisoquinoline-1, 3, 8, 10(2H,9H)-tetrone
- MoO_3; Molybdenum trioxide
- PDBD-T; Poly[[4, 8-bis[5-(2-ethylhexyl)-2-thienyl]benzo [1, 2-b:4, 5-b′] dithiophene-2, 6-diyl] -2, 5-thiophenediyl[5, 7-bis(2-ethylhexyl)-4, 8-dioxo-4H, 8H-benzo [1, 2-c:4, 5-c′]dithiophene-1, 3-diyl]]
- EH-IDTBR; (5Z)-3-ethyl-2-sulfanylidene-5- [[4- [9, 9, 18, 18- tetrakis (2 - ethylhexyl)- 15-[7- [(Z)- (3- ethyl- 4- oxo- 2- sulfanylidene-1, 3- thiazolidin-5- ylidene) methyl]- 2, 1, 3-benzothiadiazol-4-yl]- 5, 14-dithiapentacyclo[10.6.0.03, 10.04,8.013, 17]octadeca- 1(12), 2, 4(8), 6, 10, 13(17), 15-heptaen- 6- yl]-2, 1, 3-benzothiadiazol- 7- yl] methylidene]- 1, 3- thiazolidin-4-one
- PM6; Poly[(2, 6-(4, 8-bis(5-(2-ethylhexyl-3-fluoro) thiophen-2-yl) - benzo [1, 2-b:4, 5 - b′] dithiophene))- alt- (5, 5- (1′, 3′-di-2-thienyl- 5′, 7′- bis (2-ethylhexyl) benzo [1′, 2′-c:4′, 5′-c′] dithiophene-4, 8- dione)]
- PTB7-Th; Poly[4, 8-bis(5-(2-ethylhexyl)thiophen-2-yl) benzo[1, 2-b; 4, 5-b′] dithiophene-2, 6-diyl-alt-(4- (2- ethylhexyl)- 3- fluorothieno[3,4- b]thiophene-)- 2- carboxylate-2- 6- diyl)]

- PCDTBT; Poly[N-9′-heptadecanyl-2, 7-carbazole-alt-5, 5-(4′, 7′-di-2-thienyl-2′, 1′, 3′-benzothiadiazole)]
- $PC_{60}BM$: ([6, 6]-Phenyl-C_{60}-butyric acid methyl ester)
- $PC_{71}BM$: ([6, 6]-Phenyl-C_{71}-butyric acid methyl ester)
- BQR; benzodithiophene-quaterthiophene-rhodanine [248]
- ITIC; (5Z)-3- ethyl-2- sulfanylidene-5-[[4-[9, 9, 18, 18-tetrakis(2-ethylhexyl)-15-[7- [(Z)-(3- ethyl- 4- oxo- 2- sulfanylidene-1, 3-thiazolidin-5-ylidene) methyl]-2, 1, 3-benzothiadiazol-4-yl] -5, 14- dithiapentacyclo [10.6.0.03, 10.04,8.013,17] octadeca- 1(12), 2, 4(8), 6,10, 13(17), 15- heptaen-6-yl]- 2, 1, 3- benzothiadiazol-7-yl] methylidene]- 1, 3-thiazolidin-4-one
- Y6; 2, 2'-[[12, 13-Bis(2-butyloctyl)-12, 13-dihydro-3, 9-dinonylbisthieno [b″, 3″:4″, 5″]thieno[2″, 3″:4,5] pyrrolo [3, 2-e:2′, 3′-g] [2, 1, 3] benzothiadiazole-2, 10-diyl] bis [methylidyne(5, 6-chloro-3-oxo-1H-indene-2, 1(3H)-diylidene)]] bis[propanedinitrile]
- BTP-eC9; 2,2′- [[12, 13-Bis(2-butyloctyl)-12, 13-dihydro-3, 9- dinonylbisthieno [2″, 3″:4′, 5′] thieno [2′, 3′:4, 5] pyrrolo [3, 2-e:2′, 3′-g] [2, 1, 3] benzothiadiazole-2, 10-diyl] bis[methylidyne(5, 6-chloro-3-oxo-1H-indene-2, 1(3H)-diylidene)]] bis [propanedinitrile]

PEDOT:PSS was purchased from Heraeus. PM6, Y6, BTP-eC9, EH-IDTBR, ITIC, and PDINO were purchased from Solarmer. PBDB-T was purchased from Nanjing Zhiyan. Ptb7-Th, PCDTBT, $PC_{61}BM$, and $PC_{71}BM$ were purchased from Ossilla. BQR was was prepared based on the synthetic procedure explained by Geraghty et.al [248].

C.2 Materials Fabrication

C.2.1 Thin Film Fabrication

Before films were spin coated on glass substrates, the substrates were cleaned in deionized water, acetone, and 2-propanol by sequential sonication for 10 minutes. The cleaned substrates were dried with nitrogen gas, and treated in a UV-Ozone cleaner (Ossila, L2002A2-UK) for 20 minutes. Table C.1 lists each material, solvent, concentration, and spin speed used, as well as the resulting thickness of each film fabricated. Each film listed in Table C.1 was made by dissolving the relevant material in the listed solvent by stirring for at least 2 hours and spin

coating onto glass substrates at the listed spin speed. Some materials such as BQR and DCB-based films required additional post-spin coating preparation as outlined in the relevant parts of Appendix C.2.3.

C.2.2 Bi-layer Film Fabrication

Bi-layer films were fabricated using the spontaneous spreading method [208–210]. In this method Y6 was dissolved in chlorobenzene at 45°C, spin coated onto clean glass substrates, and annealed for 10 min at 70° C. The variation in thickness was controlled by varying both the concentration, from 2.3 to 12.8 mg/mL, and spin speed, from 2000-3000 rpm. The thickness was verified via ellipsometry utilising samples deposited onto silicon substrates, under identical conditions. Table C.2 lists the concentration, spin speeds, and resulting thickness of each Y6 film. Once the Y6 layer was deposited onto the glass substrates, Ptb7-Th solution was prepared with concentration of 10 mg/mL in 0.9:0.1 chlorobenzene:DIO, and stirred at 45° for $>$ 2 hours. Before deposition, the solution was allowed to cool for $>$ 1 hour at room temperature. 10 μL was dropped into a 10 cm petri dish filled with deionized water and allowed to spread out and dry over the course of 2 minutes, creating a film 20 nm thick. Once the film was dry it was transferred to each Y6 device creating the structure drawn in the inset of Figure C.3b.

C.2.3 Device Fabrication

Before devices were fabricated on commercial patterned ITO glass substrates, the substrates were cleaned in deionized water, acetone, and 2-propanol by sequential sonication for 10 minutes. The cleaned substrates were dried with nitrogen gas, and treated in a UV-Ozone cleaner (Ossila, L2002A2-UK) for 20 minutes.

BQR:PC_{71}BM: BQR:PC_{71}BM devices were fabricated in the conventional device architecture (ITO/PEDOT:PSS/BQR:PC_{71}BM/Ca/Al).
PEDOT:PSS/deionized water (1:3) solution was filtered through a 0.45 μm PVDF filter before being spin-coated on ITO substrates at 5000 rpm for 20 seconds and annealed at 150° C for 10 minutes to form a 20 nm film. BQR:PC_{71}BM was dissolved in toluene with a donor: acceptor ratio of 1:1 by weight and a total concentration of 48 mg/mL. The solution was stirred at 60° C for 3 hours before being spin-coated at 1000 rpm to form a film of thickness 240 nm. At this stage the as-cast (AC) devices were moved directly to the evaporator while the solvent annealed (SA) devices were further exposed to a Tetrahydrofuran environment in a closed petri dish for 20 seconds and then thermally annealed at 90° C for 10 minutes. 20 nm of calcium and 100 nm of aluminum were evaporated as the top electrode.

Material	**Solvent**	**Concentration (mg/mL)**	**Spin Speed (rmp)**	**Thickness (nm)**
BQR	Toluene	20	3000	75
$PC_{71}BM$	DCB	10	1000	30
BQR:$PC_{71}BM$	Toluene	16	3000	54
PCDTBT:$PC_{60}BM$	DCB	20	3000	30
PCDTBT	DCB	20	3000	42
$PC_{60}BM$	DCB	20	3000	22
PCDTBT:$PC_{60}BM$	DCB	20	3000	30
PBDB-T:EH-IDTBR	99.5:0.5 CB:DIO	14	3000	69
PM6	CF	8	3000	54
ITIC	CF	10	3000	70
PM6:ITIC	99.5:0.5 CF:DIO	5	3000	35
Y6	CF	10	3000	40
PM6:Y6	99.5:0.5 CF:CN	5	2000	34
Ptb7-Th:Y6	99.5:0.5 CF:CN	8	3000	45
BTP-eC9	CF	10	3000	45
PM6:BTP-eC9	99.5:0.5 CF:DIO	8.5	3000	45

Table C.1: Solvent, concentration, spin speed, and resulting thickness for all neat semiconductor and BHJ films deposited.

Thickness (nm)	Concentration (mg/mL)	Spin Speed (rpm)
17.7	3.2	3000
25	5.4	3000
29.5	6.4	3000
33	9.6	3000
40	12.8	3000
48.7	16	2000
54.4	20	3000
66	22	3000
74.5	20	2000

Table C.2: Concentration and spin speeds used to fabricate Y6 layers in the Y6/Ptb7-Th bi-layer films.

PBDB-T:EH-IDTBR PBDB-T:EH-IDTBR devices were fabricated in the inverted device architecture (ITO/ZnO/BQR:$PC_{71}BM$/MoO_3/Ag). A ZnO solution was prepared by dissolving 200 mg of zinc acetate dihydrate in 2-methoxyethanol (2 mL) and ethanolamine (56 μL). The solution was stirred overnight under ambient conditions and spin-coated onto ITO substrates (4000 rpm resulting in a thickness of approximately 30 nm) followed by thermal annealing at 200° C for 60 minutes. PBDB-T:EH-IDTBR was dissolved in a (99.5:0.5) CB:DIO solution with a donor:acceptor ratio of 1:1 by weight and a total concentration of 14 mg/mL. The solution was stirred at 60° C for $>$ 2 hours before being spin-coated at 1500 rpm and thermally annealed at 100° C to form a film of thickness 120 nm. 7 nm of MoO_3 and 100 nm of aluminum were evaporated as the top electrode.

PM6:ITIC PM6:ITIC devices were fabricated in the conventional device architecture (ITO/PEDOT:PSS/PM6:ITIC/PDINO-3F/Ag).
PEDOT:PSS/deionized water (1:3) solution was filtered through a 0.45 μm PVDF filter before being spin-coated on ITO substrates at 5000 rpm for 20 seconds and annealed at 150° C for 10 minutes to form a 20 nm film. PM6:ITIC was dissolved in a (99.5:0.05) CF:DIO solution with a donor:acceptor ratio of 1:1 by weight and a total concentration of 14 mg/mL. The solution was stirred at 60° C for $>$ 2 hours before being spin-coated at 3000 rpm and thermally annealed at 70° C to form a film of thickness 100 nm. Finally, a 0.5 mg/mL PDINO-3F in methanol solution was spin-coated on at 5000 rpm to form 10 nm films, and 100 nm of Ag was evaporated as the top electrode.

PM6:Y6 PM6:Y6 devices were fabricated in the conventional device architecture (ITO/PEDOT:PSS/PM6:Y6/PDINO-3F/Ag).
PEDOT:PSS/deionized water (1:3) solution was filtered through a 0.45 μm PVDF filter before being spin-coated on ITO substrates at 5000 rpm for 20 seconds and annealed at 150° C for 10 minutes to form a 20 nm film. PM6:Y6 was dissolved in a (99.5:0.05) CF:CN solution with a donor:acceptor ratio of 1:1.2 by weight and a total concentration of 17 mg/mL. The solution was stirred at 60° C for $>$ 2 hours before being spin-coated at 3000 rpm and thermally annealed at 70° C to form a film of thickness 100 nm. Finally, a 0.5 mg/mL PDINO-3F in methanol solution was spin-coated on at 5000 rpm to form 10 nm films, and 100 nm of Ag was evaporated as the top electrode.

Ptb7-Th:Y6 Ptb7-Th:Y6 devices were fabricated in the conventional device architecture (ITO/PEDOT:PSS/Ptb7-Th:Y6/PDINO-3F/Ag). PEDOT:PSS/deionized water (1:3) solution was filtered through a 0.45 μm PVDF filter before being spin-coated on ITO substrates at 5000 rpm for 20 seconds and annealed at 150° C for 10 minutes to form a 20 nm film. Ptb7-Th:Y6 was dissolved in a (99.5:0.05) CF:CN solution with a donor:acceptor ratio of 1:1 by weight and a total concentration of 16 mg/mL. The solution was stirred at 60° C for $>$ 2 hours before being spin-coated at 2000 rpm and thermally annealed at 70° C to form a film of thickness 100 nm. Finally, a 0.5 mg/mL PDINO-3F in methanol solution was spin-coated on at 5000 rpm to form 10 nm films, and 100 nm of Ag was evaporated as the top electrode.

PM6:BTP-eC9 PM6:BTP-eC9 devices were fabricated in the conventional device architecture (ITO/PEDOT:PSS/PM6:BTP-eC9/PDINO-3F/Ag).
PEDOT:PSS/deionized water (1:3) solution was filtered through a 0.45 μm PVDF filter before being spin-coated on ITO substrates at 5000 rpm for 20 seconds and annealed at 150° C for 10 minutes to form a 20 nm film. PM6:BTP-eC9 was dissolved in a (99.5:0.05) CF:DIO solution with a donor:acceptor ratio of 1:1.2 by weight and a total concentration of 17 mg/mL. The solution was stirred at 60° C for $>$ 2 hours before being spin-coated at 3000 rpm and thermally annealed at 70° C to form a film of thickness 100 nm. Finally, a 0.5 mg/mL PDINO-3F in methanol solution was spin-coated on at 5000 rpm to form 10 nm films, and 100 nm of Ag was evaporated as the top electrode.

C.3 Experimental Techniques

C.3.1 Domain Size Measurements

Derivation of Equation 6.4 and 6.6

Singlet-singlet exciton annihilation can occur in an OSC as described in Section 5.2. The rate equation for the ρ in a single phase of an organic semiconductor consisting of a blend of two materials is the sum of the natural decay (determined by the natural lifetime τ), the rate of extraction from the occupied phase to the opposing phase (determined by k_{eff}), and the exciton-exciton annihilation rate (determined by the annihilation coefficient $\gamma = 4\pi D R_0$, with D and R_0 being the diffusion coefficient and capture radius if the occupied phase, respectively)

$$\frac{d\rho}{dt} = -\frac{\rho}{\tau} - k_{\text{eff}}\rho - \gamma\rho^2, \tag{C.1}$$

Combining the linear terms in Equation C.1 yields

$$\frac{d\rho}{dt} = -\frac{\rho}{\tau_{\text{eff}}} - \gamma\rho^2, \tag{C.2}$$

$$\tau_{\text{eff}} = \frac{\tau}{1 + \tau k_{\text{eff}}}. \tag{C.3}$$

The solution to Equation C.2 is

$$\rho(t) = \frac{\rho_0 \exp\left(-t/\tau_{\text{eff}}\right)}{1 + \gamma\rho_0\tau_{\text{eff}}\left[1 - \exp\left(-t/\tau_{\text{eff}}\right)\right]}, \tag{C.4}$$

where ρ_0 is the initial density in the occupied phase. The total number of excitons that decay due to natural decay according to Equations C.1 is $\rho_\tau = \int_0^\infty \rho(t)/\tau dt$. Additionally, the photoluminescence efficiency is given by $\eta_{\text{PL}} = \rho_\tau \eta_{\text{PL},0}/\rho_0$ where $\eta_{\text{PL},0}$ is the low-density photoluminescence quantum efficiency. Therefore, in a neat film ($k_{\text{eff}} = 0$, $\tau_{\text{eff}} = \tau$) the density dependence of the photoluminescence quantum yield can be expressed as

$$\eta_{\text{PL,neat}} = \eta_{\text{PL},0}\frac{\ln\left[1 + \rho_0\gamma\tau\right]}{\rho_0\gamma\tau}, \tag{C.5}$$

consistent with Equation 5.5. As described in Chapter 5, the product of $\gamma\tau$ can be used to calculate the diffusion length directly from $L_D = \sqrt{\gamma\tau/4\pi R_0}$. Whereas, in a blended film ($k_{\text{eff}} \neq 0$) the same procedure can be used to obtain the photoluminescence quantum efficiency from one phase alone as

$$\eta_{\text{PL,blend}} = \eta_{\text{PL},0}\frac{\ln\left[1 + \rho_0\gamma\tau_{\text{eff}}\right]}{\rho_0\gamma\tau_{\text{eff}}} \tag{C.6}$$

The exciton extraction rate from the occupied phase to the opposing phase is dependent on the efficiency of exciton diffusion towards the interface (η_{diff}) and the efficiency of electrons (hole) transfer during channel I (II) charge transfer or the efficiency of FRET transfer from the occupied to opposing phase ($\eta_{\text{CT/FRET}}$) [3]. The efficiency of diffusion depends on the domain size (L) and the diffusion length (L_D) of the occupied phase as $\eta_{\text{diff}} = 2L_D/L \times \tanh\left[L/2L_D\right]$, while the efficiency of charge transfer depends on the competition between the charge transfer rate at the interface or the FRET transfer rate near the interface, and the natural decay. In general the efficiency of exciton dissociation (P_S) can be expressed as the competition between the effective extraction rate and natural decay rate with in the phase, which can be related to η_{diff} and $\eta_{\text{CT/FRET}}$ as

$$P_S = \frac{k_{\text{eff}}}{1/\tau + k_{\text{eff}}} = \left[\frac{1}{\eta_{\text{diff}}} + \frac{1}{\eta_{\text{CT/FRET}}} - 1\right]^{-1}. \tag{C.7}$$

Combining Equation C.3 and C.7 and multiplying by γ the effective lifetime in the occupied phase can be related to the efficiency of exciton extraction as

$$P_S = 1 - \frac{\gamma\tau_{\text{eff}}}{\gamma\tau} = \left[\frac{1}{\eta_{\text{diff}}} + \frac{1}{\eta_{\text{CT/FRET}}} - 1\right]^{-1} \tag{C.8}$$

Under conditions where FRET is inefficient and charge transfer is efficient ($\eta_{\text{CT}} \rightarrow 1$), the system becomes diffusion limited and Equation C.8 becomes

$$1 - \frac{\gamma\tau_{\text{eff}}}{\gamma\tau} - \frac{2L_D}{L}\tanh\left[\frac{L}{2L_D}\right] = 0. \tag{C.9}$$

In the case where FRET is an efficient process, $\eta_{\text{FRET}} \gg \eta_{\text{diff}}$ as the exciton approaches the donor acceptor interface. Leading to a diffusion limited system in which Equation C.8 can be expressed

$$1 - \frac{\gamma\tau_{\text{eff}}}{\gamma\tau} - \frac{2L_D}{L_{\text{eff}}}\tanh\left[\frac{L_{\text{eff}}}{2L_D}\right] = 0. \tag{C.10}$$

Therefore, measuring $\gamma\tau$ on a neat film and $\gamma\tau_{\text{eff}}$ from one phase of a blended film one can solve Equation C.9 for the size of the phase separated domain, L, or Equation C.10 for the size of the domain from the frame of reference of the exciton L_{Eff}.

Apparatus

Figure C.1 shows a schematic diagram of the apparatus used to measure pulsed-PLQY on neat semiconductors and bulk-heterojunctions. The light source (Pharos

PHM02-2H-3H) emits an ultrafast pulse at 515 nm, at a 25 kHz repetition rate, and a pulse duration was approximately 300 fs. The light passes through an acousto-optic modulator (AOM-commonly known as a chopper) which modulates the light at 273 Hz. The laser light is then directed towards the sample with various mirrors and telescopes (not shown here), which is held in a cryostat (Linkam-LTS420) under a constant flow of nitrogen gas. The spotsize of the unfocused light was measured to be 1.03 mm. The resulting photoluminesence (PL) is collimated, filtered by use of a long- or short-pass filter at the appropriate wavelength for the system under test, and focused onto the active area of the amplified photo-diode (Femto OE-300-Si-30). The output signal of the diode is fed into the lock-in amplifier (Stanford Research Systems SR860). The lock-in measures the response of the photo-diode at the frequency of the chopper. This detected light, in principle, is the PL of the sample, however; care must be taken to remove any scattered light from the pump beam, a long-pass 550 nm filter is placed in front of the diode to remove any scattered pump light. The pump scatter can be evaluated by blocking the collection pathway near the sample, such that any scattered pump light will reach the detector in the absence of the PL. Here the pump scatter (with the laser set at the power corresponding to the largest initial density used) was reduced to 100X the smallest photoluminescence signal before taking measurements.

The initial density of excitons in the film (ρ_0) is calculated from the absorbed power ($\mathrm{P_{abs}}$), the laser spot-size (ω), repetition rate (RR), film thickness (d), photon energy (E_{Ph}), and f, given by Equation 6.7.

$$\rho_0 = \frac{\mathrm{P_{abs}}}{\pi\omega^2 \mathrm{RR} d E_{\mathrm{ph}}} f. \tag{C.11}$$

C.3.2 Current-Voltage Characteristics

The current density versus voltage (J–V) curves of the devices (pixel area: $0.036\mathrm{cm}^2$) were measured through a shadow mask using an Ossila Solar Cell I–V Test System. The simulator was calibrated by a standard silicon reference cell certified by the National Renewable Energy Laboratory.

C.3.3 Absolute Photoluminescence Quantum Yield

The absolute Photoluminescence Quantum Yield was measured on a Hamamatsu Quantaurus-QY Absolute PL quantum yield spectrometer (C11347-11).

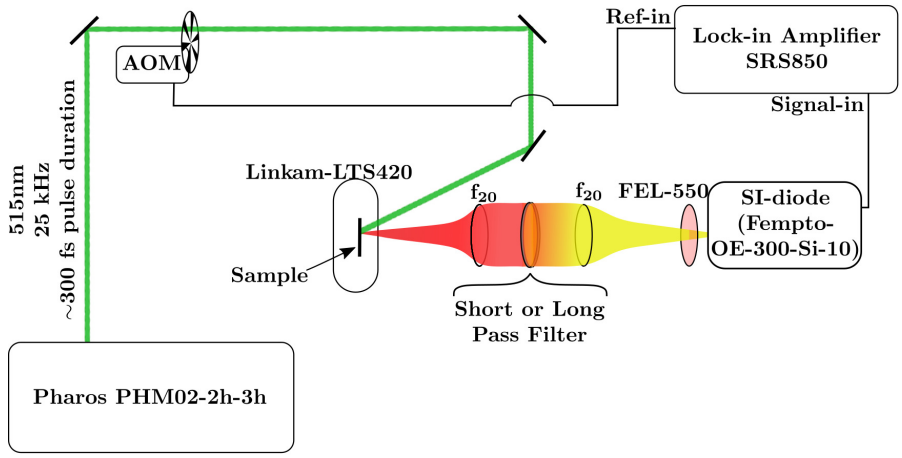

Figure C.1: Experimental setup for measuring pulsed-PLQY on neat semiconductors and bulk-heterojunctions. f_{20}-lens of focal length 20 mm, FEL-550-long-pass 550 nm filter, AOM-acoustical optical modulator (chopper).

C.3.4 Thickness Measurements

The film thickness was measured from ellipsometry data (J.A. Woollam M-2000 Spectroscopic Ellipsometer). Samples used to measure ellipsometry data were on cleaned and sonicated silicon substrates prepared under identical conditions to those in Table C.1 and C.2, and Appendix C.2.2.

C.3.5 Index of Refraction Measurements

The index of refraction, used to measure R_{FRET}, were measured using the NK-Finder code developed elsewhere [60]. The required transmission measurements were performed using a Perkin Elmer UV/VIS/NIR spectrometer (LAMBDA 950).

C.4 Verifying Domain Size Measurements

C.4.1 Monte-Carlo Simulations

To investigate the exciton dynamics within a blended organic film a Monte-Carlo hopping model was implemented. Monte-Carlo simulations were chosen as they have been shown to accurately account for exciton dynamics within organic semiconductors and BHJs [118, 155–157, 249]. Furthermore, the use of Monte-Carlo

simulations allows for the verification of experimentally extracted values under conditions where physical quantities, such as diffusion length, lifetime, and domain size, are known precisely. The simulations were simplified to capture only the relevant physics, such that the experimental procedure can be verified under ideal conditions. First a cylindrical domain, with diameter specified as the domain size, of sufficient volume (V) to accommodate the input density was created with nearest-neighbour spacing of dx. The lattice is then randomly populated with N excitons ($N = \rho_0 V$). Once the lattice has been initialized the simulation is evolved in time with a temporal step-size dt, defining the diffusion coefficient as $D = dx^2/dt$. The cylinder is given periodic boundary conditions along the axis of the cylinder while the radius of the cylinder defines the donor acceptor interface.

The inset in Figure C.2b indicates the various pathways an exciton in the simulation can evolve. The orange circles indicate an exciton hopping to an adjacent site along the major axes. The choice of site to hop to is given by the Gillespie algorithm with equal probability for movement in each direction but limited to nearest neighbor pairs, and a maximum hopping rate given by the inverse of the temporal step size [250]. The amount of time the exciton occupies this new site (the dwell time, τ_{Dwell}) is given by the total hopping rate away from the site (Γ_i) as $\tau_{\text{Dwell}} = T/\Gamma_i$, where T is a pseudo-random number generated from an exponential distribution with unit expectation value and unit variance. The probability of natural decay is given by the input natural lifetime (τ) as dt/τ. Therefore, after each dwell time a pseudo-random number on a unit interval is generated, and an exciton decays naturally when this is smaller than the decay probability. The green circles in the inset of Figure C.2b indicate exciton-exciton annihilation, where any exciton within one lattice spacing of another will decay nonradiatively such that $R_0 = dx$. The final pathway for an exciton to evolve is extraction, as indicated by the black circle and arrow. Extraction, in the simulations, occurs when an exciton is $\geq L/2$ away from the central point of the lattice. Once an exciton is extracted it can be re-injected back to the lattice point from which it was extracted with probability defined by the energetic difference between the charge-transfer state and the singlet exciton state ($\Delta E_{\text{CT/S}}$) as $P = k_{\text{inj}}/1 + k_{\text{inj}}$, $k_{\text{inj}} = \exp\left[-\Delta E_{\text{CT/S}}/k_B T\right]$. In these simulations $\Delta E_{\text{CT/S}} = 1$ eV, while $T = 300$K to limit the effects of re-injection.

Once the system has sufficiently evolved in time the photoluminescence quantum yield can be calculated as the ratio of excitons decayed via natural decay to the initial density within the film. Figure C.2a shows the simulated normalised η_{PL} for selected domain sizes. The black line indicates the expected shape of Equation C.6 given the input dx, dt, and τ, which will be reproduced in the case of an infinite domain [3]. Note that the smaller domains have more noise in the simulated results due to increasing extraction from the domain, reducing

the overall η_{PL}. Each η_{PL} verus ρ_0 curve is then fit to Equation C.6 and Equation C.9 is used to calculate L. The results of this analysis are shown in Figure C.2b, where the measured domain diameter is plotted as a function of the input domain diameter. This analysis reproduces the domain diameter within a

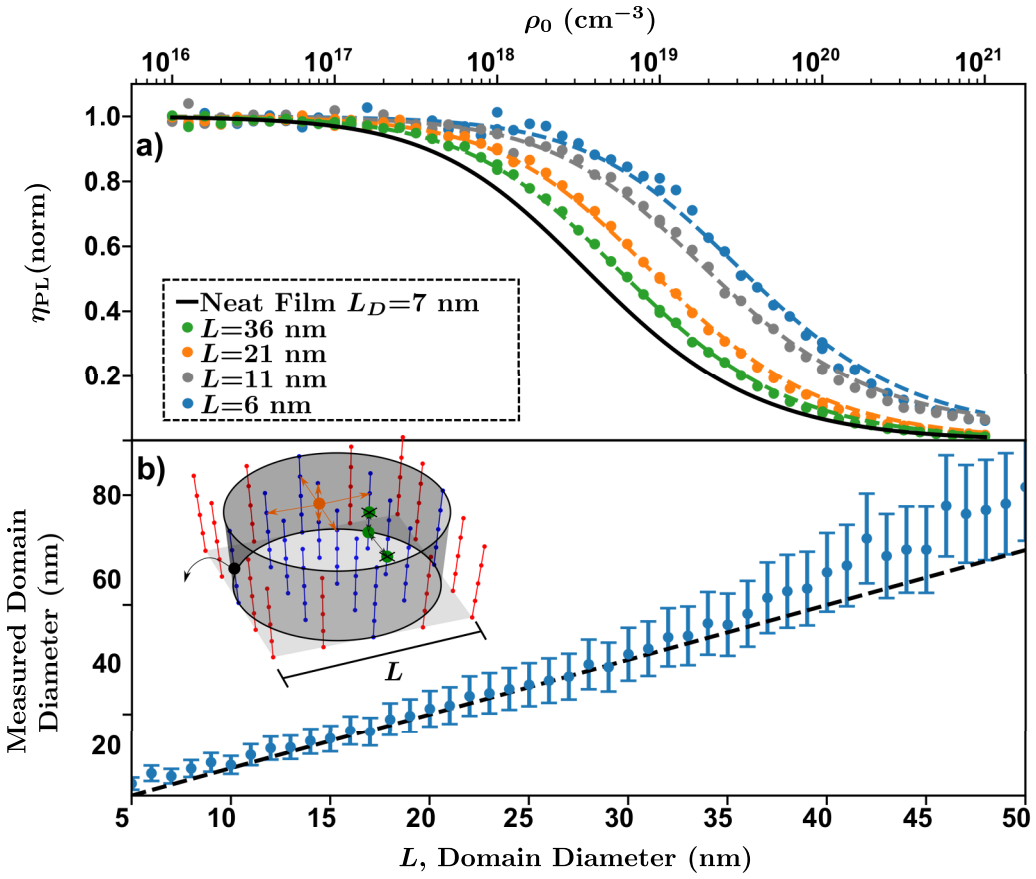

Figure C.2: Monte-Carlo simulations of domain size experiment on cylindrical domain. (a) Normalized photoluminescence quantum yield as a function of initial density for selected domain diameters. (b) Domain diameter extracted from the simulated experiment as a function of input domain diameter. Inset to panel b-Cartoon layout of occupied and opposing domain lattice as well as various pathways for excitons to evolve in the simulation. Blue circles and lines indicate lattice points within the occupied domain, red circles and lines indicate lattice points in the opposing domain. Orange circles indicate hopping transport along major axes, green circles indicate exiton-exciton annihilaiton, black circle indicates extraction from occupied phase to a charge-transfer state. Periodic boundary conditions are used in the vertical direction.

reasonable error (for more information on error analysis see Appendix C.7.3).

C.4.2 Bi-Layer Measurements

To verify the efficacy of Equation C.9 and the analysis laid out in Appendix C.4.1 bi-layer thin films were fabricated using the spontaneous spreading method with Y6 thickness varying between 18 and 75 nm [208–210]. The inset in Figure C.3b shows a cartoon depiction of the bilayer film and the experimental conditions. Y6 was chosen as the active layer while Ptb7-Th was chosen as the quenching layer. These materials were selected as they have large difference between both their respective χ and IP levels, creating an efficient charge-transfer mechanism at the interface for both channel I and II transfer, while the efficiency of FRET transfer from Y6 to Ptb7-Th is very low and from Ptb7-Th to Y6 is high (see Appendix C.5.5), as well, the absorption of Y6 is much greater than Ptb7-Th at the excitation wavelength (515 nm). These conditions result in most excitons generated being active in the Y6 phase before quenching occurs. Therefore, in this particular system, the pump laser excites an exciton in the Y6 phase which diffuses throughout the film, either decaying naturally or quenching at the interface between the Y6 and Ptb7-Th, as indicated in the inset in Figure C.3b.

Pulsed-PLQY is used to measure the relative η_{PL} as a function of initial density for each film thickness, Figure C.3b shows these data. Each data set is then fit to Equation C.6 and Equation C.9 is used to calculate L. In the case of bilayers Equation C.9 is modified such that $\eta_{\mathrm{diff}} = L_D/L \times \tanh\left[L/L_D\right]$ to account for quenching at only one interface [172, 211]. Figure C.3c shows the resulting optically measured thickness as a function of the thickness measured via ellipsometry. For each thickness there is agreement between the optical measured thickness and the ellipsometry thickness within error. This experiment validates the use of Equation C.8 in general and Equation C.9 for this particular system.

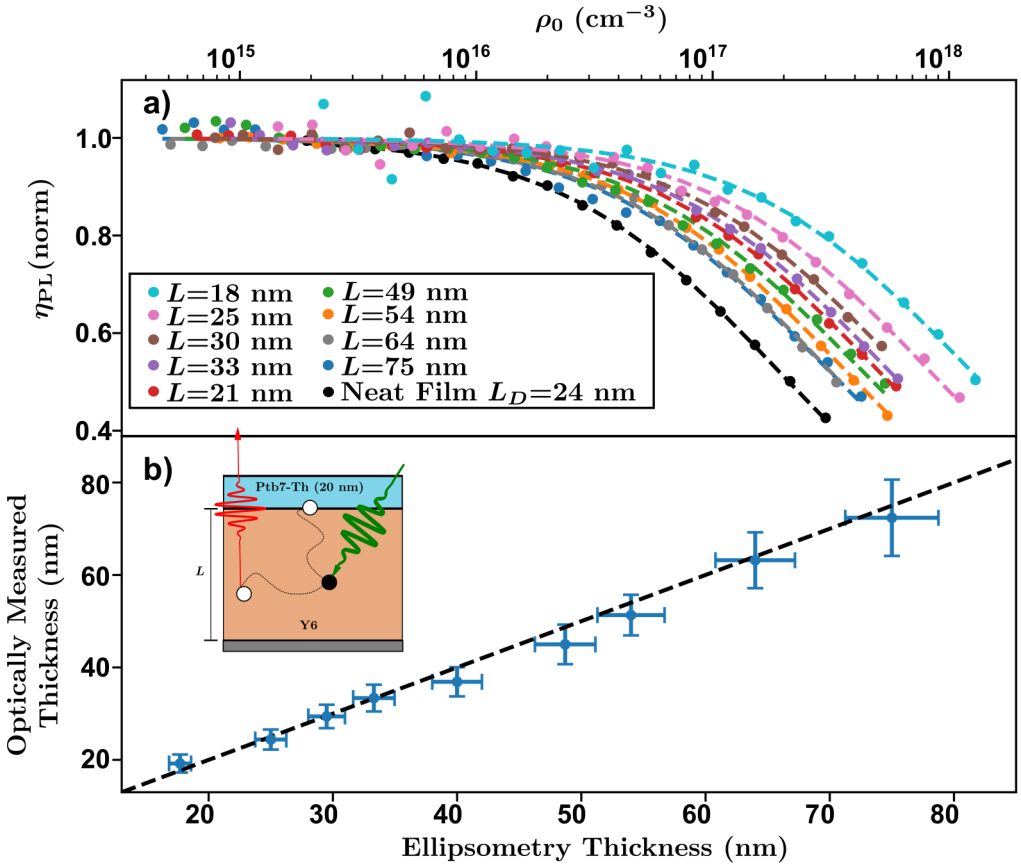

Figure C.3: Bilayer puled-PLQY data. (a) Relative photoluminescence quantum yield as a function of initial density for each thickness. (b) Optically measured thickness of Y6 layer as a function of ellipsometry measured thickness. Inset-schematic of the bilayers and experiment, green pulse indicates incident photon, red pulse indicates photoluminescence from the Y6 phase, black circle indicates exciton created in Y6 phase, white circles indicate excitons decaying either naturally within the Y6 phase, or through quenching at the Y6 Ptb7-Th interface.

C.5 Experimental Data

C.5.1 J-V Characersitics

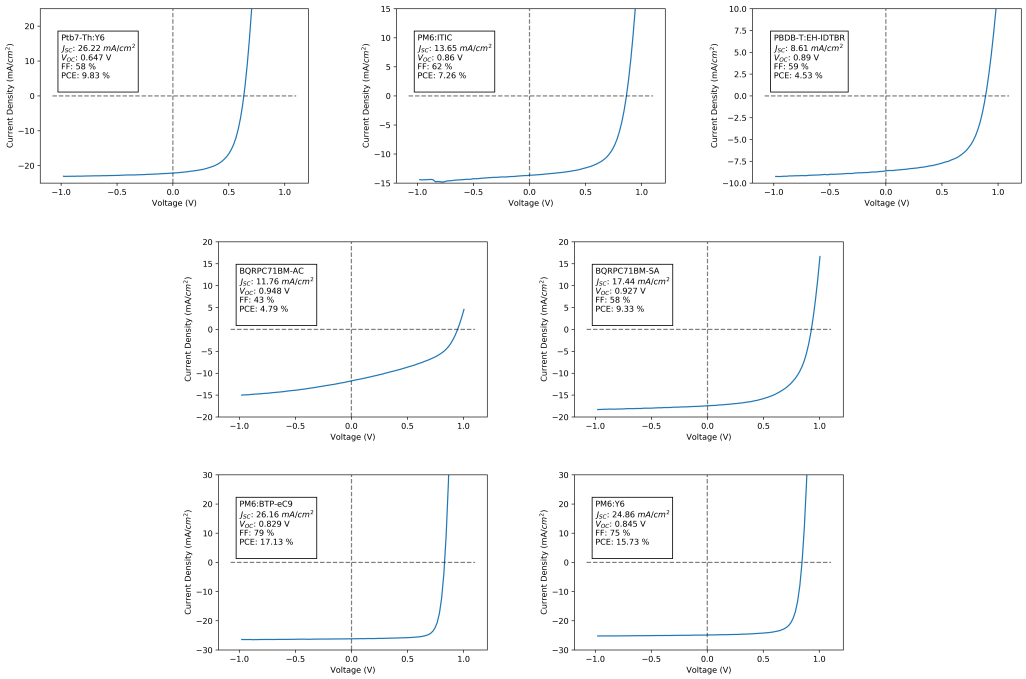

Figure C.4: Current Density versus Voltage for devices with best PCE for each system studied.

C.5.2 Quasi-Steady-State Photoluminescence

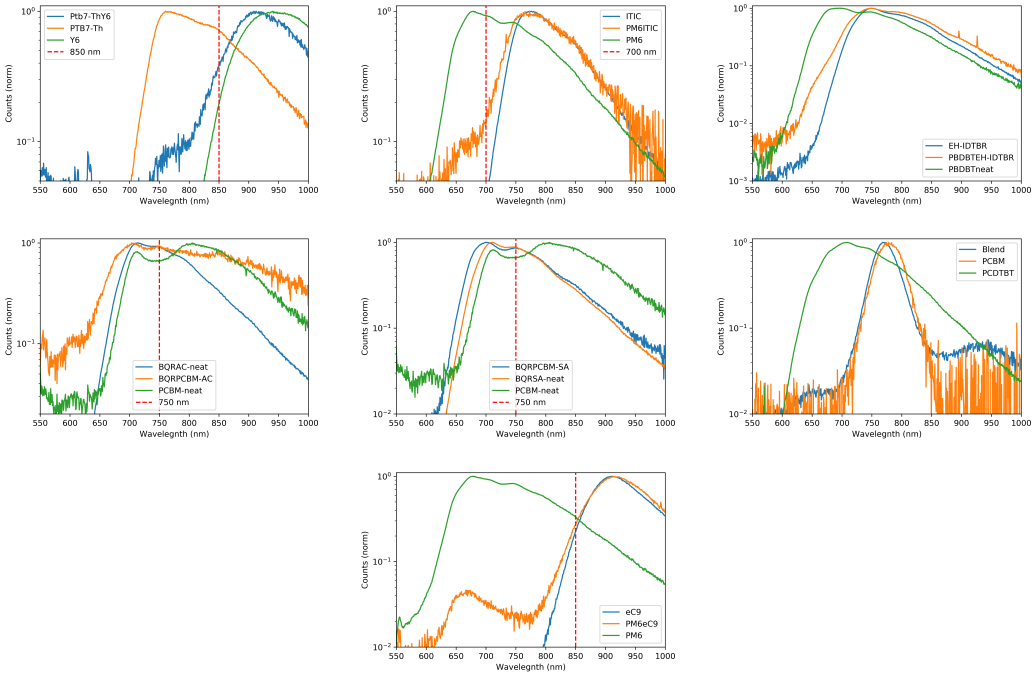

Figure C.5: Normalised quasi-steady-state photoluminescence of thin films. Red line indicates placement of long- and short-pass filters utilised in pulsed-PLQY data in Figure C.8.

C.5.3 Absolute-PLQY

The absolute PLQY value for various neat semiconductors was measured on thin films using a tunable wavelength, absolute PL quantum yield spectrometer equipped with an integrating sphere (Hamamatsu Quantaurus-QY C11347-11). Figure C.6 shows the relevant spectra used to calculate $\eta_{\mathrm{PL},0}$ for each neat semiconductor. The blue curve indicates the reference (pump) spectra utilising the internal monochromator while the other colors indicate the absorption and photoluminescence response from each neat film. The peak of the reference spectra was set to the same wavelength as the pump wavelength utilised in pulsed-PLQY experiments (515 nm).

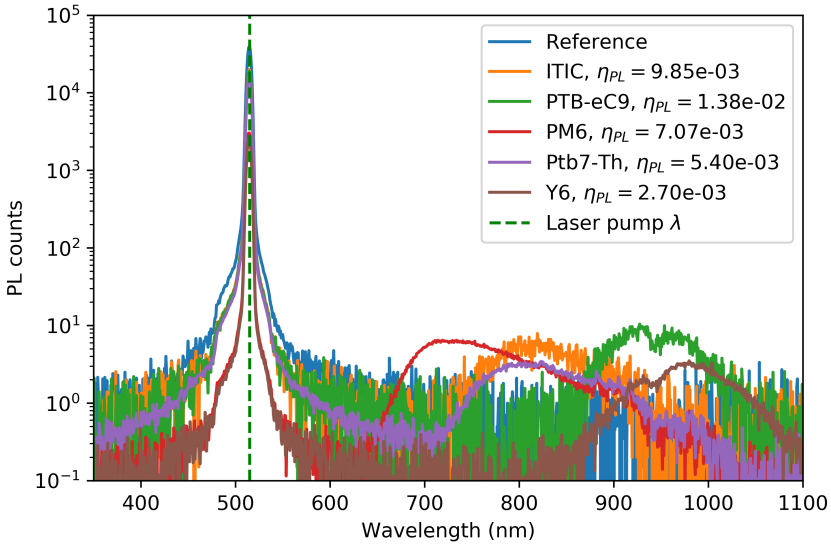

Figure C.6: Absolute PLQY measurements for neat semiconductors.

C.5.4 Pulsed-PLQY Data

Evaluation of Heavily Quenched Donor Phase

In the case of PM6:Y6 it is found that the fraction of absorbed excitons available for EEA in the donor phase is 0.029, indicating that the density of excitons in this phase is two orders of magnitude lower than that of a neat PM6 thin film with similar thickness. When pulsed-PLQY was performed on PM6:Y6 BHJ with a short-pass 750 nm filter in the collection pathway irreversible damage was caused to the film at initial densities above 10^{15} cm^{-3}, as shown in the left panel of Figure C.7. The right panel of Figure C.7 shows the pulsed-PLQY for the PM6 phase of PM6:Y6 up until these densities and that of neat PM6, the red dotted line represents the expected behaviour for the system if the domain size is 10 nm (as estimated from PL quenching). It is clear from these data that damage to the BHJ film occurs at densities far below what is required to measure P_S and hence the donor domain size of this system.

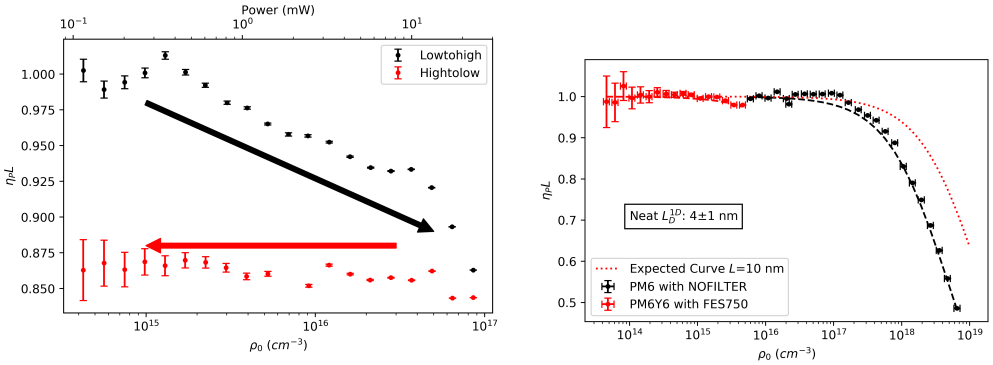

Figure C.7: Pulsed-PLQY data on the PM6 phase of PM6:Y6 BHJ indicating (left panel) the damage threshold for the experiment and (right) the measurement capabilities of the apparatus under these conditions.

Additional Data

Figure C.8 shows the pulsed-PLQY data collected on films of each system studied.

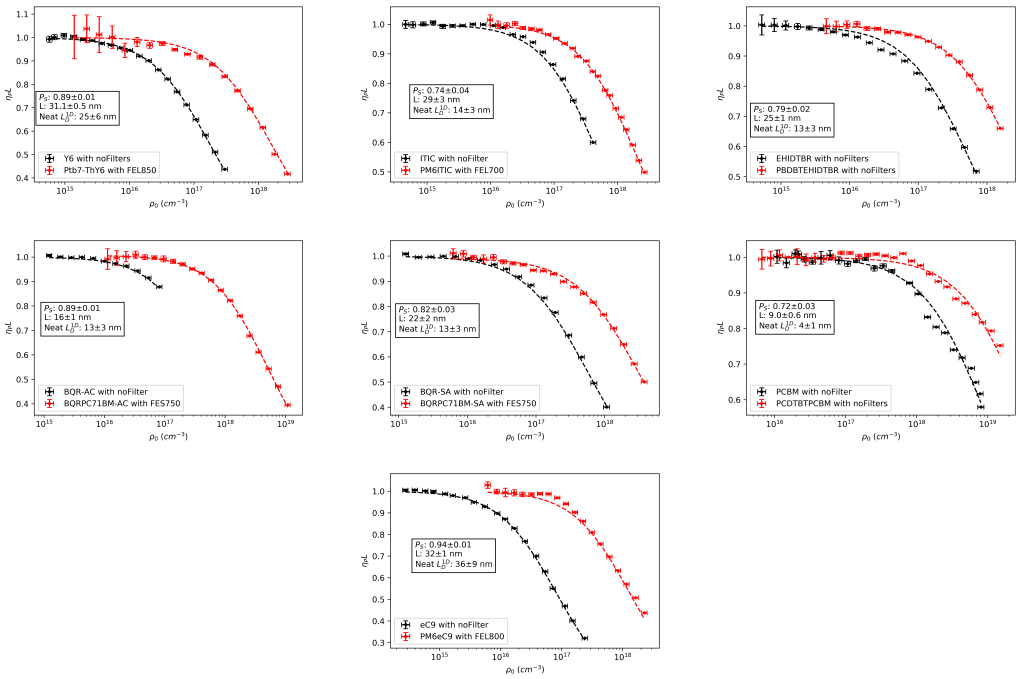

Figure C.8: Pulsed-PLQY data on neat (black circles) and single phase of the BHJ (red circles) of BHJ films with indicated short- or long-pass filters in the collection path.

C.5.5 Förester Resonant Energy Transfer Rate and Radii

As described in Section 3.1.1, the rate of Förster Resonance Energy Transfer (k_{FRET}) from one molecule to another depends on the separation between the molecules (r) and the FRET radii (R_{FRET}), defined as the distance at which the FRET transfer rate and natural decay rate are equivalent

$$k_{\mathrm{FRET}} = \frac{1}{\tau_0}\left(\frac{R_{\mathrm{FRET}}}{r}\right)^6, \tag{C.12}$$

where τ_0 is the lifetime of the molecule from which the transfer is occurring. R_{FRET} is defined by the overlap integral between the emission and absorption of

the two molecules. A commonly used expression to calculate R_{FRET} in nm is [97]

$$R_{\mathrm{FRET}} = \left[\left(\frac{9\ln\left[10\right]}{128\pi^5 N_A} \times 10^{17}\right)\left(\frac{\kappa^2 \eta_{\mathrm{PL},0} J\left(\lambda\right)}{n^4}\right)\right]^{1/6}, \tag{C.13}$$

where N_A is Avogadro's number in mol^{-1}, κ is the dipole orientation factor, assumed here to be 2/3 corresponding to a random orientation of molecules, $\eta_{\mathrm{PL},0}$ is the absolute photoluminescence quantum yield of the occupied molecule, λ is the wavelength, n is the index of refraction, and $J\left(\lambda\right)$ is the overlap integral defined as

$$J\left(\lambda\right) = \int_0^\infty \epsilon\left(\lambda\right) \lambda^4 F\left(\lambda\right) d\lambda, \tag{C.14}$$

where $F\left(\lambda\right)$ is the emission spectra of the molecule from which the transfer is occurring (normalised to an area of unity) and $\epsilon\left(\lambda\right)$ is the attenuation coefficient (in units of $\mathrm{mol}^{-1}\mathrm{cm}^{-1}$) of the molecules to which the energy is being transferred, given by

$$\epsilon\left(\lambda\right) = \frac{\alpha\left(\lambda\right) M_w}{d}, \tag{C.15}$$

where α is the absorption coefficient, M_w is the molecular weight of the corresponding molecule, and $d = 1.2kg/L$ [97]. The index of refraction is taken as the spectral dependence of the index of refraction weighted to the overlap spectra $J\left(\lambda\right)$

$$\eta\left(\lambda\right) = \frac{\int_0^\infty \epsilon\left(\lambda\right) \lambda^4 F\left(\lambda\right) n\left(\lambda\right) d\lambda}{J\left(\lambda\right)}. \tag{C.16}$$

Figure C.9 shows $F(\lambda)$, $\epsilon(\lambda)$, and $n(\lambda)$ of the various films measured in Chapter 6, indicated on each plot is the relevant overlap area (black cross-hatched area), the calculated R_{FRET} and the relevant d_{100} molecular spacing [186–188, 190, 192, 212, 251].

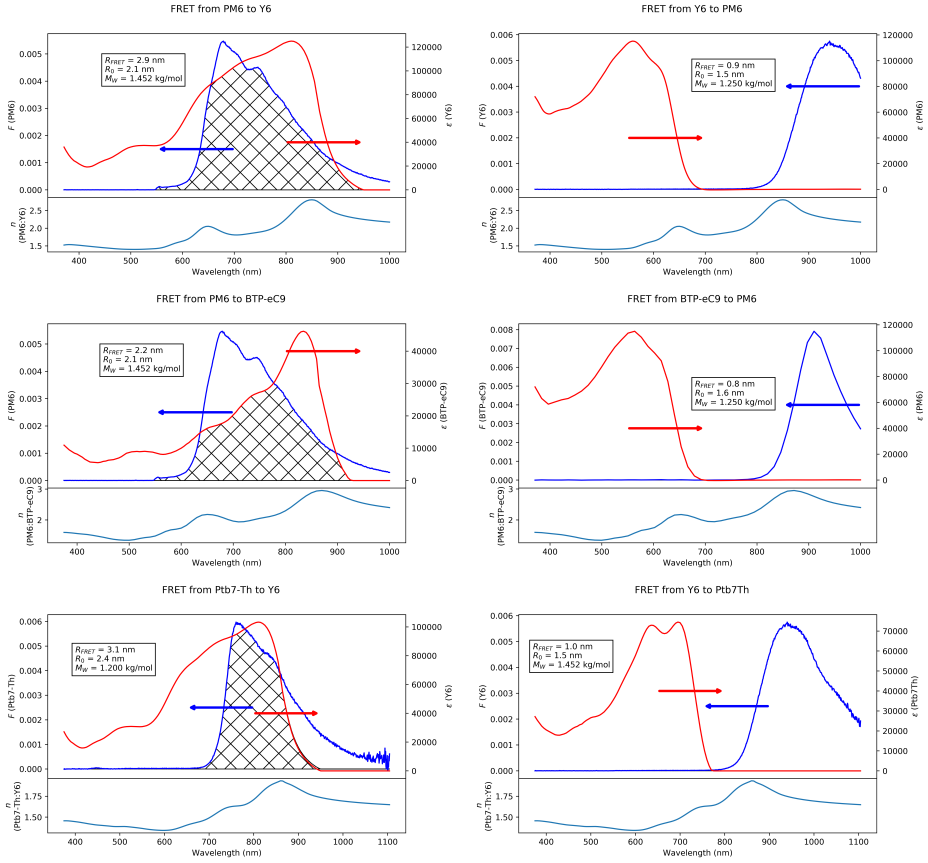

Figure C.9: Calculation of FRET radii for (Top Left) PM6 to Y6 energy transfer, (top right) Y6 to PM6 energy transfer, (center left) PM6 to BTP-eC9 energy transfer, and (center right) BTP-eC9 to PM6 energy transfer, (lower left) Ptb7-Th to Y6 energy transfer, and (lower right) Y6 to Ptb7-Th energy transfer.

C.5.6 Resistance-Dependent Photovoltage Measurements

The mobility measurements were taken utilising Resistance-Dependent Photovoltage technique [104]. The same pump laser as in the photoluminescence and pulsed-PLQY experiments with the repetition rate reduced 3 orders of magnitude using a built-in pulse picker. Data was taken on a Oscilloscope (Rohde & Schwarz RTM3004) triggered by a fast-photodiode (Femto HSA-X). Identical apparatus' has been utilised in prior publications to quantify the mobility through the transit time (t_r) of the carriers as $\mu = d^2/V_{\text{bi}}t_r$, where d is active layer thickness and $V_{\text{bi}} = 1.1$ V [149, 252]. Figure C.10 shows the data and analysis for the mobility

measurements on PBDB-T:EH-IDTBR, PM6:ITIC, and Ptb7-TH:Y6, while SA and AC BQR:$PC_{71}BM$ were taken from reference [213], PCDTBT:$PC_{60}BM$ from reference [253], and PM6:Y6 and PM6:BTP-eC9 were taken from reference [149].

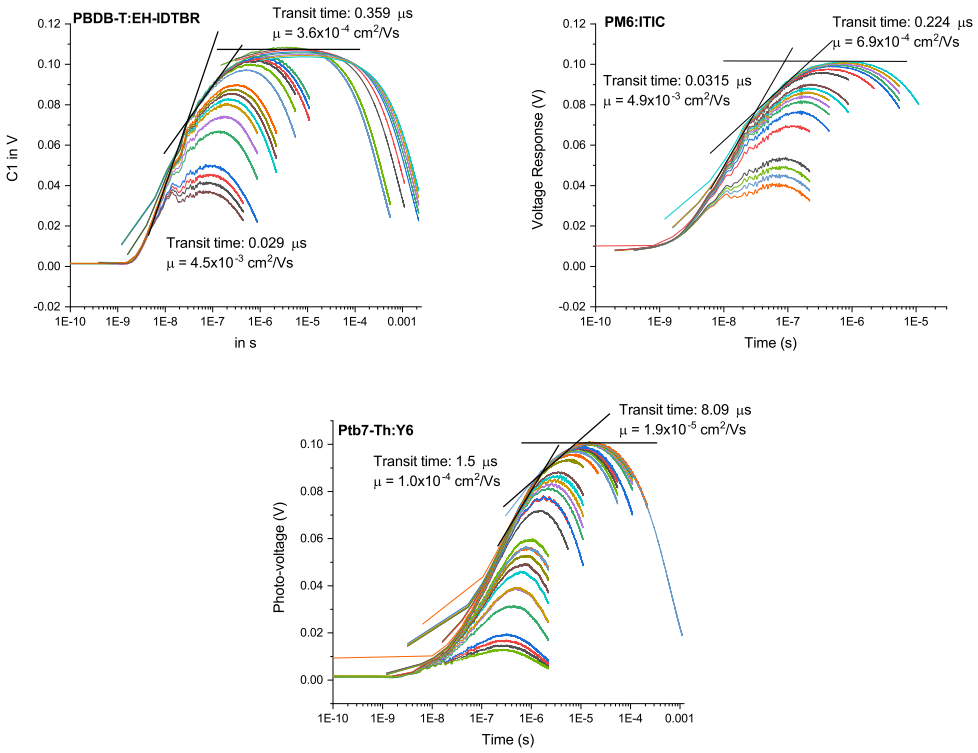

Figure C.10: Resistance dependent photo-voltage measurements for (top left) PBDB-T:EH-IDTBR, (top right) PM6:ITIC, and (lower) Ptb7-Th:Y6 bulk-heterojunctions.

C.6 Calculating Encounter Rates

Following the method outlined by Heiber et. al [112] the bimolecular recombination rate is calculated as

$$k_{\text{sim}} = \frac{q}{\epsilon\epsilon_0} f(L) 2M_{g(L)}\left(\mu_e, \mu_h\right), \tag{C.17}$$

where q is the fundamental charge, ϵ and ϵ_0 are the relative and vacuum permitivity, μ_e and μ_h are the electron and hole mobilities, $f(L)$ is a single valued function

found from fitting simulated Monte-Carlo results $M_{g(L)}$ is the generalised mean of the electron and hole mobilities given by

$$M_{g(L)}\left(\mu_e, \mu_h\right) = \left(\frac{\mu_e^{g(L)} + \mu_h^{g(L)}}{2}\right)^{1/g(L)} \tag{C.18}$$

where $g(L)$ is an additional single valued function found from Monte-Carlo simulations and digitised for use in this work [112]. Once k_{sim} is calculated the geometric reduction factor can be calculated as $\gamma_{\text{enc}} = k_{\text{sim}}/k_L$.

C.7 Error Analysis

The errors in each quantity are propagated in the usual way and added in quadrature.

C.7.1 Diffusion Length

The error in L_D (σ_{L_D}) is dependent on the error in $\gamma\tau$ ($\sigma_{\gamma\tau}$ given by the fitting error) and R_0 (σ_{R_0} given as half the value of R_0) as

$$\sigma_{L_D} = \left[\left(\frac{\partial L_D}{\partial \gamma\tau}\sigma_{\gamma\tau}\right)^2 + \left(\frac{\partial L_D}{\partial R_0}\sigma_{R_0}\right)^2\right]^{1/2} \tag{C.19}$$

$$\sigma_{L_D} = \frac{1}{2}\left[\left(\frac{L_D}{\gamma\tau}\sigma_{\gamma\tau}\right)^2 + \left(\frac{L_D}{R_0}\sigma_{R_0}\right)^2\right]^{1/2} \tag{C.20}$$

C.7.2 Exciton Quenching Efficiency

The uncertainty in the exciton quenching efficiency (σ_{P_S}) is taken as half the difference between fittings to Equation C.5 and Equation C.6 resulting in the largest and smallest P_S possible. Figure C.11 shows this analysis for a the PM6 phase of a PM6:Y6 BHJ film. The dark blue fitting results in the maximum value for P_S while the cyan fitting results in the minimum value for P_S. The difference between these results is 0.01 leading to $\sigma_{P_S} = 0.005$.

C.7.3 Domain Size

The domain size is calculated by finding the zeros of the function $f(L)$, expressed in Equation C.9, such that

$$f(L) = P_S(\gamma\tau_{\text{eff}}, \gamma\tau_{\text{neat}}) - \eta_{\text{diff}}(L, L_D) = 0 \tag{C.21}$$

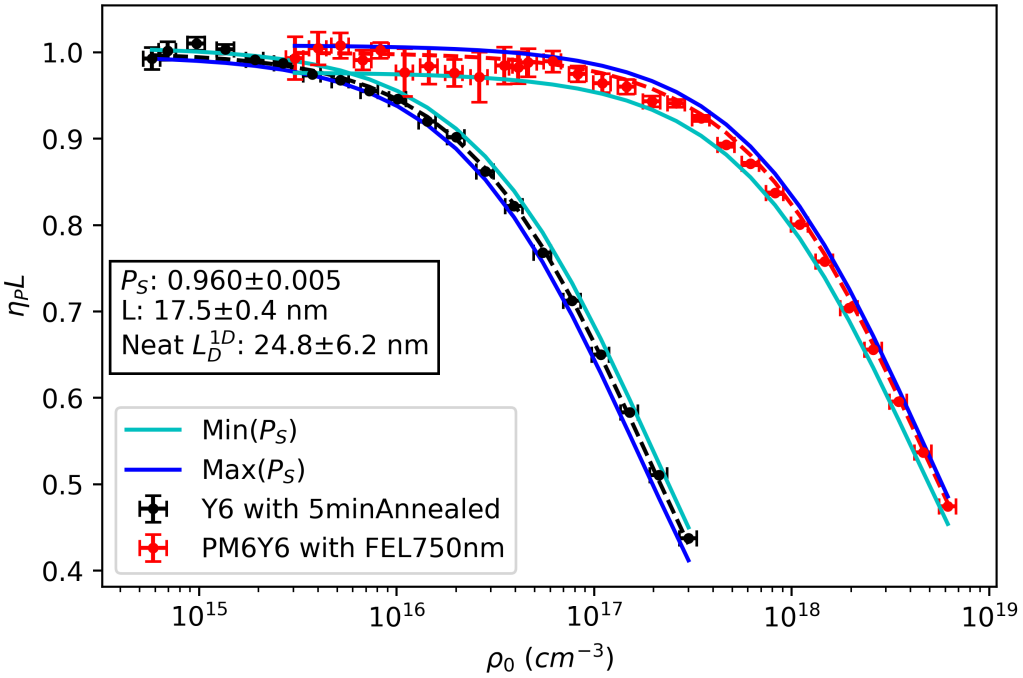

Figure C.11: Example of error analysis shown for the Y6 phase in a PM6:Y6 system heterojunction thin film. The dark blue fitting results in the maximum value for P_S while the cyan fitting results in the minimum value for P_S.

where P_S is given by the Equation C.8 and $\eta_{\text{diff}} = L_D/L \times \tanh[L/L_D]$. To find the error in L (σ_L) Equation C.21 is implicitly differentiated such that the uncertainty in f (σ_f) is given by

$$(\sigma_f)^2 = (f_{P_S}\sigma_{P_S})^2 - (f_{\eta_{\text{diff}}}\sigma_{\eta_{\text{diff}}})^2 \tag{C.22}$$

$$\tag{C.23}$$

and the uncertainty in η_{diff} is given by $(\sigma_\eta)^2 = \left((\eta_{\text{diff}})_{L_D}\,\sigma_{L_D}\right)^2 + \left((\eta_{\text{diff}})_L\,\sigma_L\right)^2$, where the subscript notation indicates partial derivatives ($f_x = \frac{\partial f}{\partial x}$). Solving for σ_L we find

$$(\sigma_L)^2 = \frac{1}{\left((\eta_{\text{diff}})_L\right)^2}\left[(\sigma_f)^2 + (\sigma_{P_S})^2 + \left((\eta_{\text{diff}})_{L_D}\,\sigma_{L_D}\right)^2\right] \tag{C.24}$$

σ_f is defined as the value of $f(L)$ for L which minimises Equation C.9, σ_{P_S} and σ_{L_D} are defined in Appendix C.7.1 and C.7.2 respectively. Consolidating all these

together results in the uncertainty in L

$$(\sigma_L)^2 = \left\{ (\sigma_f)^2 + (\sigma_{P_S})^2 + \left(\frac{2}{L} \tanh\left[\frac{L}{2L_D}\right] - \frac{1}{L_D} \operatorname{sech}^2\left[\frac{L}{2L_D}\right] \right)^2 (\sigma_{L_D})^2 \right\} \times \left\{ \frac{-2L_D}{L^2} \tanh\left[\frac{L}{2L_D}\right] + \frac{1}{L} \operatorname{sech}^2\left[\frac{L}{2L_D}\right] \right\}^{-2} \tag{C.25}$$

Appendix D

Direct Quantification of Quasi-Fermi Level Splitting in Organic Semiconductor Devices

D.1 Simulations

Figure 7.4

The parameters used for the electroluminescence and EM-PLQY simulations in Figure 1 are shown in Table D.1.

Parameter	Value
T	300 K
ϵ	3.4
N_{V}, N_{C}	10^{26} m^{-3}
$\mu_{n,p}$	10^{-8} m^2/Vs
Donor IP	4.7 eV
Acceptor χ	3.6 eV
Anode WF	4.7 eV
Cathode WF	3.6 eV
$S_{n,\mathrm{cat}}$, $S_{p,\mathrm{An}}$	10^6 m/s
$S_{n,\mathrm{an}}$, $S_{p,\mathrm{Cat}}$	10^{-50} m/s
d	100 nm
β	$0.01k_L$ m^3/s
G	6×10^{27} m^{-3}
ω_v	$2\pi \times 377$ Hz

Table D.1: Simulated parameters used for simulating the data in Figure 7.4 and D.1.

Figure D.1a shows the current-voltage characteristics, while Figure D.1b shows the photoluminescence and current response from the simulated EM-PLQY under one sun conditions (b). From the J-V curve, the V_{OC} is 0.728 V and the J_{sc} is 9.5

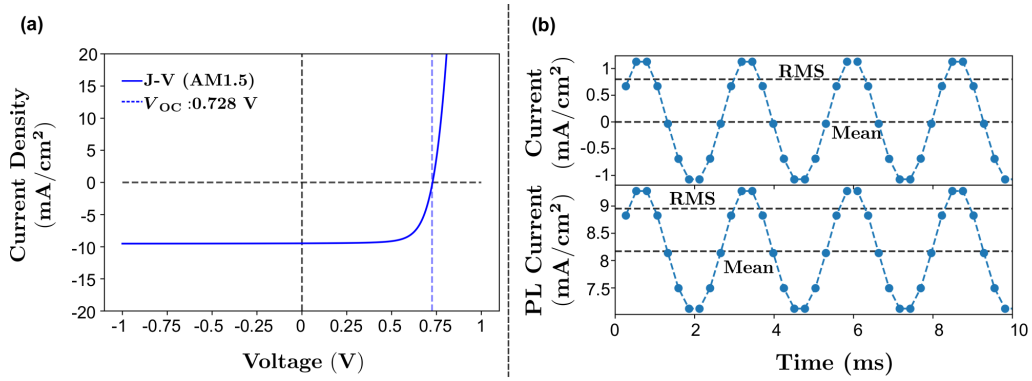

Figure D.1: Simulated (a) steady-state IV characteristics under artificial AM1.5 conditions and (b) device current and photoluminescence current as a function of time, resulting from a simulated EM-PLQY experiment. Table D.1 shows simulation parameters used.

mA/cm^2. The current response from the EM-PLQY experiments is sinusoidal centered around 0 with a RMS response of 0.8 mA/cm^2. This corresponded to a $V_{\text{off}} = 0.723$ V and $\Delta V = 6.5$ mV, which were subsequently used to create the steady state simulations in Figure 1. The PL response has a positive offset, due to the steady state PL, overlaid with a sinusoidal response in phase with the current. The RMS value for the PL current was given as 0.78 mA/cm^2. From these data the η_{EMPL} is defined as:

$$\eta_{\text{EMPL}} = \frac{J_{\text{PL}}^{\text{RMS}}(\omega_v)}{J^{\text{RMS}}(\omega_v)} \times 100\% \sim 98\%, \tag{D.1}$$

since here all the bulk recombination is assumed to be radiative.

Figure 7.5

Table D.2 shows the parameters used to simulate the data in Figure 7.5. Here the parameters are held the same as in Table D.1, except the surface recombination velocity is raised for holes at the cathode while the cathode work function is increased stepwise. This causes surface recombination to occur at the cathode while the anode stays perfectly selective [232]. Further the external quantum efficiency of the ideal simulation (η_{bulk}) is assumed to be 5×10^{-6} leading to $V_{\text{OC}}^{\text{rad}} = E_{\text{G}} - k_{\text{B}}T \ln[\beta_{\text{rad}} N_{\text{V}} N_{\text{C}}/G]$ where $\beta_{\text{rad}} = \eta_{\text{bulk}}\beta$. Figure D.2a shows the current-voltage characteristics for these cells. As the injection barrier is increased, the V_{OC} decreases due to surface recombination, while J_{SC} is unaffected. Figure D.2b shows the simulated quasi-Fermi levels at V_{OC} and indicates how the QFLS is calculated for each case.

Parameter	Value
T	300 K
ϵ	3.4
N_{V}, N_{C}	10^{26} m^{-3}
$\mu_{n,p}$	10^{-8} m$^2/Vs$
Donor IP	4.7 eV
Acceptor χ	3.6 eV
Anode WF	4.7 eV
Cathode WF	3.6,3.65,3.7,3.75,3.8,3.85,3.9 eV
$S_{p,\mathrm{An}}$, $S_{p,\mathrm{Cat}}$, $S_{n,\mathrm{Cat}}$	10^{6} m/s
$S_{n,\mathrm{An}}$	10^{-50} m/s
d	100 nm
β	$0.01k_L$ m^3/s
G	6×10^{27} m^{-3}
ω_v	$2\pi \times 377$ Hz
η_{bulk}	5×10^{-6}

Table D.2: Parameters used for simulating the data from Figure 7.5 and Figure D.2.

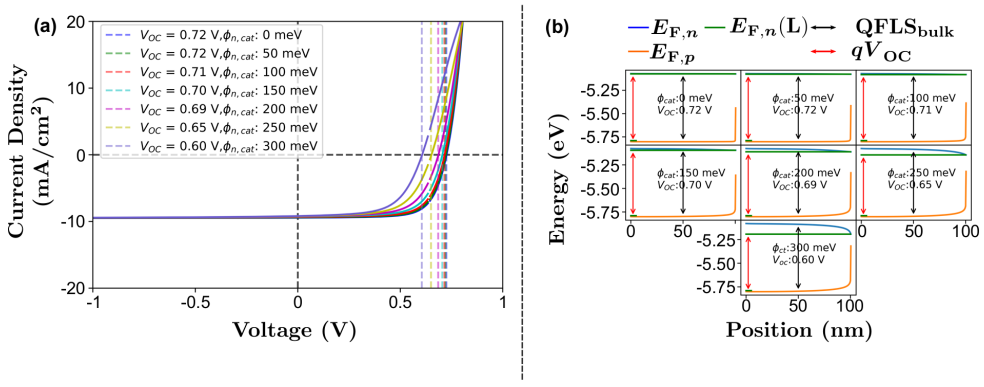

Figure D.2: Simulated (a) current-voltage characteristics and (b) quasi-Fermi levels at open circuit conditions for each electron injection barrier at the cathode simulated using parameters in Table D.2 and shown in Figure 7.5.

D.2 Calibration of Apparatus

D.2.1 In Situ Calibration

The electroluminescence apparatus shown in Figure 7.4a suffers from a reduction in measured emission due to limitations in geometric and spectral light-collection efficiency. In order to compensate for this the absolute η_{EL} was measured with a absolute external quantum efficiency apparatus (Hamamatsu C9920-12). These data are used to calibrate the home-built electroluminescence apparatus ($\eta_{\mathrm{EL}}^{\mathrm{Raw}}$) for each device. Figure D.3 shows the η_{EL} measured by the Hamamatsu and home-built apparatus for the device with a PDINO/Ag cathode (device 1 Table D.3) as a function of injected current. In this case the scaling factor between the home-built and Hamamatsu systems is 9.7×10^2. This factor is then used to scale the η_{EMPL} measurement for the same device. This was carried out for each device and the scaling factors are shown in Table D.3. In the case of device 7, no electroluminescence emission was measurable, so a scaling factor of 1×10^3 was assumed for the η_{EMPL}.

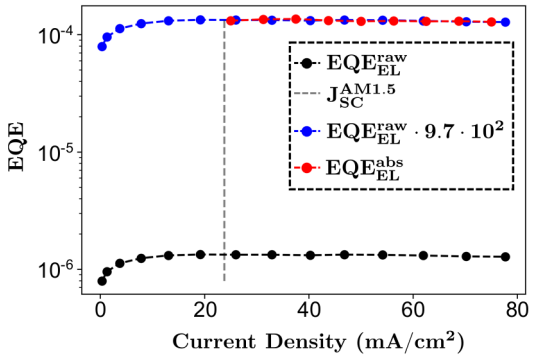

Figure D.3: Electroluminescence external quantum efficiency as a function of injected current for (red) Hamamatsu system (black) unscaled and (blue) scaled home-built apparatus as shown in Figure 7.4. Device used here has structure ITO/PEDOT:PSS/PM6:Y6/PDINO/Ag (device 1 Table D.3).

D.2.2 Perturbation Strength

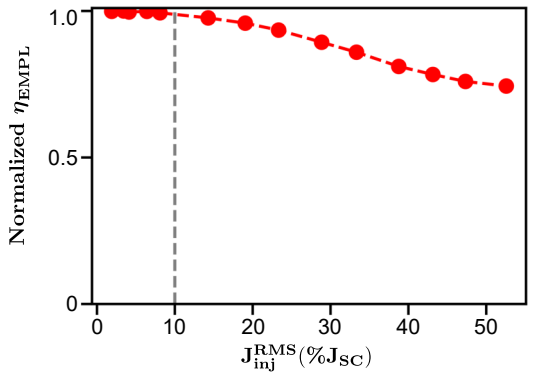

Figure D.4: Normalised η_{EMPL} as a function of the strength of the modulating current. The device used here is ITO/PEDOT:PSS/PM6:Y6/PDINO/Ag (device 1 Table D.3), and the illumination was such that the measured J_{SC} was approximately $J_{SC}^{AM1.5}$

To verify that the current injected by the modulated voltage is not strong enough to significantly disturb the system, and possibly alter the QFLS, η_{EMPL} was measured varying the magnitude of the injected current modulation. Figure D.4 shows the normalised η_{EMPL} as a function of the RMS value for the injected current sine wave as a percentage of the short-circuit current. Here the optimised device architecture was employed and an illumination corresponding to a measured short-circuit current of roughly $J_{SC}^{AM1.5}$ was chosen. There is less than 2% variance between the 1% and 10% J_{SC} measurements indicating that an injected current RMS of $0.1J_{SC}$ (indicated by the dotted black line) is within the small perturbation regime and Equation 7.10 is valid.

D.2.3 Modulation Frequency

To verify that the modulation frequency was slow enough to allow carriers to recombine as they would under steady-state situation the η_{EMPL} was measured as a function of modulation frequency. Figure D.5 shows the normalised η_{EMPL} as a function of modulation frequency. There is no change in η_{EMPL} for modulation frequencies up to and 377 Hz, shown vertical grey line, above the frequency used in the measurements shown in Figure 7.7 and 7.8.

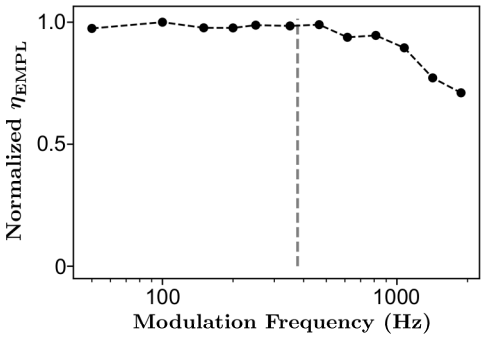

Figure D.5: Normalised η_{EMPL} as a function of modulation frequency. The device used here is ITO/PEDOT:PSS/PM6:Y6/PDINO/Ag (device 1 Table D.3), and the illumination was such that the measured J_{SC} was approximately $J_{\mathrm{SC}}^{\mathrm{AM1.5}}$

D.3 Devices

D.3.1 Measuring $V_{\mathrm{OC}}^{\mathrm{rad}}$

As outlined in Section 2.3.1, the radiative limit of the V_{OC} can be calculated from the photovoltaic external quantum efficiency ($\mathrm{EQE_{PV}}$) as:

$$V_{\mathrm{OC}}^{\mathrm{rad}} = \frac{k_{\mathrm{B}}T}{q} \ln\left[\frac{J_{\mathrm{ph}}}{J_0^{\mathrm{rad}}} + 1\right], \tag{D.2}$$

$$J_{\mathrm{ph}} = q\int_{E_0}^{\infty} \mathrm{EQE_{PV}}\Phi_{\mathrm{sun}}dE, \tag{D.3}$$

$$J_0^{\mathrm{rad}} = q\int_{E_0}^{\infty} \mathrm{EQE_{PV}}\Phi_{\mathrm{BB}}dE. \tag{D.4}$$

Where E_0 is typically the lower energy limit available from the measurement of $\mathrm{EQE_{PV}}$. Figure D.6 shows the sensitive $\mathrm{EQE_{PV}}$ as a function of photon energy and calculated $V_{\mathrm{OC}}^{\mathrm{rad}}$ as a function of the lower integral limit for the device with a PDINO/Ag cathode (device 1 Table D.3). In the case of sensitive $\mathrm{EQE_{PV}}$ where midgap trap states are present, the $V_{\mathrm{OC}}^{\mathrm{rad}}$ measurement is taken from the onset of mid-gap trap states (1.05 eV) and is found to be 1.077 V, as described in previous works [107].

D.3.2 Device Architectures

Table D.3 lists the device cathodes and measured photovoltaic parameters, as measured under artificial one sun (AM1.5). Each device has the structure

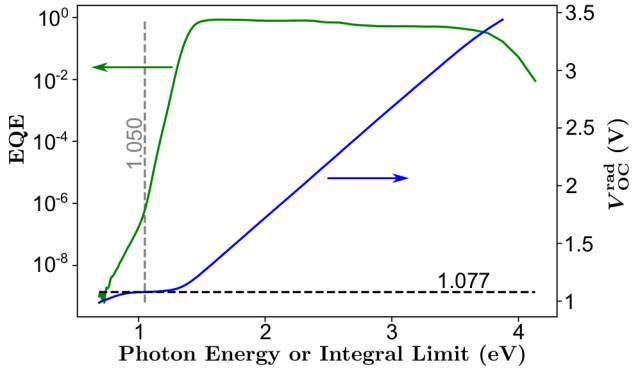

Figure D.6: Photovoltaic external quantum efficiency as a function of photon energy (green), and calculated radiative V_{OC} limit as a function of integral lower limit (blue). Device used here has structure ITO/PEDOT:PSS/PM6:Y6/PDINO/Ag (device 1 Table D.3).

ITO/PEDOT:PSS/PM6:Y6/cathode, except for device 7 which has the structure ITO/PM6:Y6/Ag.

Device	Cathode	V_{OC} (V)	J_{SC} (mA/cm^2)	FF (%)	PCE (%)	Scaling Factor
1	PDINO/Ag	0.847	23.8	75.8	15.3	9.7×10^2
2	PFN-Br/Ag	0.849	23.7	74.9	15	1.8×10^3
3	Ca/Al	0.821	21.7	70.6	12.6	1.7×10^3
4	Ag	0.787	24.2	68	13.0	1.7×10^3
5	Cu	0.667	22.1	60	9.0	1×10^3
6	Al	0.545	16.2	59.4	5.2	1.3×10^3
7	No Interlayers	0.325	21.0	39.5	2.7	1×10^3

Table D.3: Device properties of devices used in Figure 7.1, 7.7, and 7.8. Devices 1 through 6 have structure ITO/PEDOT:PSS/PM6:Y6/Cathode, device 7 has structure ITO/PM6:Y6/Ag. Scaling factor is worked out experimentally for each device as described in Appendix D.3.1.

D.4 Materials

Chemical Definitions

- PM6: Poly(3, 4-ethylenedioxythiophene) polystyrene sulfonate (PEDOT:PSS); poly[(2, 6-(4, 8-bis (5- (2-ethylhexyl-3-fluoro)thiophen-2-yl)- benzo[1, 2-b:4, 5-b′] dithiophene))- alt-(5, 5-(1′,3′-di - 2 - thienyl- 5′, 7′-bis (2-ethylhexyl) benzo [1′, 2′-c:4′, 5′-c′] dithiophene-4, 8- dione)]
- Y6: 2, 2′-((2Z, 2′Z)-((12, 13-bis (2-ethylhexyl)-3, 9-diundecyl-12, 13- dihydro-[1, 2, 5] thiadiazolo [3, 4-e]thieno[2″,3″:4′,5′] thieno [2′,3′:4, 5] pyrrolo [3, 2-g] thieno [2′, 3′:4, 5] thieno [3, 2-b] indole-2, 10-diyl) bis(methanylylidene)) bis(5, 6-difluoro-3-oxo-2, 3-dihydro-1H-indene-2, 1-diylidene)) dimalononitrile
- PDINO: 2, 9-Bis [3-(dimethyloxidoamino)propyl] anthra [2, 1, 9-def:6, 5, 10-d′e′f′] diisoquinoline-1, 3, 8, 10(2H, 9H)- tetrone

PEDOT:PSS was purchased from Heraeus. PM6, Y6, and PDINO were purchased from Solarmer. ITO was purchased from Kintec Company.

Device Fabrication

Commercial patterned ITO coated glass substrates were cleaned in deionize water, acetone, and 2-propanol by sequential sonication for 10 minutes. The cleaned substrates were first dried by nitrogen and then baked on hotplate at 110° C for 10 minutes. Afterwards, the substrates were treated in a UV-Ozone cleaner (Ossila, L2002A2-UK) for 20 minutes before the deposition of hole transport layer. PEDOT: PSS solution was diluted with the same volume of water and then cast at 4000 rpm on ITO substrate to form a 10 nm film. Then, all the substrates were transferred into a glovebox to deposit the active layer and cathode. PM6:Y6 was dissolved in a 16 mg ml-1 CF:CN (99.5:0.5) solution with a donor: acceptor ratio of 1:1.2, and spin-coated at 3000 rpm to form 100 nm active layer. PM6:Y6 films were then thermal annealed at 110° C for 10 mins. Afterwards, PM6:Y6 solar cells with different cathodes were fabricated as shown below:
ITO/PEDOT:PSS/PM6:Y6/PDINO/Ag: 1 mg ml-1 PDINO solution was spin-coated on PM6:Y6 film at 2000 rpm to form a 10 nm film, and 100 nm of Ag was evaporated as the top electrode.
ITO/PEDOT:PSS/PM6:Y6/PFN-Br/Ag: 0.5 mg ml-1 PFN-Br solution was spin-coated on PM6:Y6 film at 3000 rpm to form a 2 nm film, and 100 nm of Ag was evaporated as the top electrode.
ITO/PEDOT:PSS/PM6:Y6/Ca/Al: 5 nm of Ca and 100 nm of Al were

evaporated as the top electrode.
ITO/PEDOT:PSS/PM6:Y6/Ag: 100 nm of Ag was evaporated as the top electrode.
ITO/PEDOT:PSS/PM6:Y6/Cu: 100 nm of Cu was evaporated as the top electrode.
ITO/PEDOT:PSS/PM6:Y6/Al: 100 nm of Al was evaporated as the top electrode.
ITO/PM6:Y6/Ag: Specifically, for ITO/PM6:Y6/Ag device, the pre-cleaned ITO substrates were treated in a UV-Ozone cleaner (Ossila, L2002A2-UK) for 20 minutes and transferred into glovebox to deposit PM6:Y6 active layer. Then 100 nm PM6:Y6 active layer was spin-coated on ITO substrate and thermal annealed with the same recipe as above. Afterwards, 100 nm of Ag was evaporated on PM6:Y6 active layer as the top electrode.

D.5 Error Analysis

The three primary sources of error in the calculation of $\Delta V_{\mathrm{OC}}^{\mathrm{NR}}$ are the sample temperature, the lock-in current ($J_{\text{Lock-in}}$), and the oscilloscope current (J_{Osc}). The errors are worked out in the standard way and added in quadrature.

$$\Delta\left(\Delta V_{\mathrm{OC}}^{\mathrm{NR}}\right)=\sqrt{\left(\Delta T\frac{\partial\left(\Delta V_{\mathrm{OC}}^{\mathrm{NR}}\right)}{\partial T}\right)^{2}+\left(\Delta J_{\text{Lock-in}}\frac{\partial\left(\Delta V_{\mathrm{OC}}^{\mathrm{NR}}\right)}{\partial J_{\text{Lock-in}}}\right)^{2}+\left(\Delta J_{\mathrm{Osc}}\frac{\partial\left(\Delta V_{\mathrm{OC}}^{\mathrm{NR}}\right)}{\partial J_{\mathrm{Osc}}}\right)^{2}}. \tag{D.5}$$

Where the error in the lock-in is quantified as the background signal measured by the lock-in when the laser is on but no voltage is applied to the device for a given lock-in time constant, the error in the oscilloscope was estimated to be 5 μA for EM-PLQY measurements and 100 μA for electroluminescence measurements, the error in the temperature is assumed to be 5° K.

Appendix E

Transfer Matrix Modelling

To model the generation inside an active layer of a solar cell one must model the electric fields propagating both left and right inside a stack of dielectric layers making up the cell. The incident electric field must first pass through an incoherent glass layer (meaning that the glass is thick enough that there is no phase relationship between the left and right propagating electric fields) proceeded by a stack of coherent dielectric layers each with a thickness d_j and complex refractive induces $\tilde{\eta}_j = n_j + i\kappa_j$. Figure E.1 shows a schematic depiction of such a stack of layers. For any wavelength (λ) the intensity of light on the active layer ($I(x)$) can be written as:

$$I(x,\lambda) = I_0(\lambda)T_{(\text{air}\to\text{glass})}(\lambda)T_{(\text{glass}\to\text{stack})}(\lambda)I^{\text{norm}}(x,\lambda). \tag{E.1}$$

In which I_0 is the intensity of light on the glass layer, $T_{(\text{air}\to\text{glass})}$ is the transmission coefficient of the incoherent glass layer, $T_{(\text{glass}\to\text{stack})}$ is the transmission coefficient of the coherent stack, and $I^{\text{norm}}(x)$ is the normalised intensity at each point in the active layer. Each layer will have an associated transfer matrix ($\mathbf{P}_j$) and interface matrix ($\mathbf{I}_{j\to j+1}$), corresponding to the electric field propagation through layer j and between layer j and $j+1$ respectively. The transfer matrix

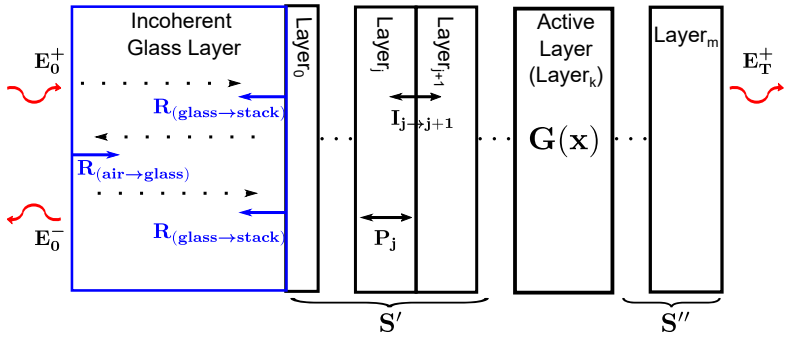

Figure E.1: Dielectric Stack representing solar cell. Light is incident from left side on incoherent glass layer. Stack is made up of m layers with active layer at layer k.

for the entire stack can be written as:

$$\boldsymbol{S}^{\text{stack}} = \sum_{i=0}^{m} \mathbf{P}_j \mathbf{I}_{j\to j+1} = \begin{bmatrix} S_{0,0}^{\text{stack}} & S_{0,1}^{\text{stack}} \\ S_{1,0}^{\text{stack}} & S_{1,1}^{\text{stack}} \end{bmatrix}. \tag{E.2}$$

Which can be used to calculate the total reflection coefficient from the stack:

$$R_{\text{stack}} = \left\| \frac{S_{1,1}^{\text{stack}}}{S_{0,1}^{\text{stack}}} \right\|^2. \tag{E.3}$$

E.1 Incoherent Glass Layer

To model the intensity of light entering the dielectric stack consider the two walls of the incoherent glass layer. The incoming intensity I_0 will pass though the left interface with transmission of $T_{(\text{air}\to\text{glass})}$, propagate through the glass, reflect off the right interface with reflection of $R_{(\text{glass}\to\text{stack})}$, propagate to the left interface and reflect again with reflection $R_{(\text{air}\to\text{glass})}$ and so on. The intensity of light transmitted by the glass can be calculated from the infinite series:

$$T_{(\text{glass}\to\text{stack})} = T_{(\text{air}\to\text{glass})} \left[1 + R_{(\text{glass}\to\text{stack})} R_{(\text{air}\to\text{glass})} + \left(R_{(\text{glass}\to\text{stack})} R_{(\text{air}\to\text{glass})} \right)^2 \cdots \right], \tag{E.4}$$

$$T_{(\text{glass}\to\text{stack})} = \frac{T_{(\text{air}\to\text{glass})}}{1 - R_{(\text{air}\to\text{glass})} R_{(\text{glass}\to\text{glass})}}. \tag{E.5}$$

While the transmission and reflection coefficients from air to glass can be written:

$$T_{(\text{air}\to\text{glass})} = \left\| \frac{2 n_{\text{air}} n_{\text{glass}} \cos(\phi_i) \cos(\phi_{\text{glass}})}{\tilde{\eta}_{\text{air}} \cos(\phi_{\text{glass}}) + \tilde{\eta}_{\text{glass}} \cos(\phi_i)} \right\|^2, \tag{E.6}$$

$$R_{(\text{air}\to\text{glass})} = \left\| \frac{n_{\text{air}} \cos(\phi_{\text{glass}}) - n_{\text{glass}} \cos(\phi_i)}{n_{\text{air}} \cos(\phi_{\text{glass}}) + n_{\text{stack}} \cos(\phi_i)} \right\|^2, \tag{E.7}$$

where ϕ_i is the angle the incident light makes with the glass layer and ϕ_{glass} is the angle of transmission of the incident light into the glass layer.

E.2 Coherent Stack

As each layer in the stack is on the order of the wavelength of light, as such right and left propagating electric fields within each layer will preserve their phase

relationship and interfere accordingly. Under these conditions the phase and interface matrices in each layer is given by:

$$\mathbf{P}_j = \begin{bmatrix} e^{-i\xi_j d_j} & 0 \\ 0 & e^{i\xi_j d_j} \end{bmatrix}, \tag{E.8}$$

$$\mathbf{I}_{j\to j+1} = \frac{1}{t_{j\to j+1}} \begin{bmatrix} 1 & r_{j\to j+1} \\ r_{j\to j+1} & 1 \end{bmatrix}, \tag{E.9}$$

where the phase change is given by $\xi_j d_j = 2\pi\tilde{q}_j d_j/\lambda$ ($\tilde{q}_j = \sqrt{\tilde{n}^2 - \tilde{n}_0^2 \sin(\phi_0)}$). t are r are the complex Fresnel reflection coefficients which, in the case for purely p-polarized waves, are given by:

$$r_{j\to j+1} = \frac{\tilde{n}_j^2\tilde{q}_{j+1} - \tilde{n}_{j+1}^2\tilde{q}_j}{\tilde{n}_j^2\tilde{q}_{j+1} + \tilde{n}_{j+1}^2\tilde{q}_j}, \tag{E.10}$$

$$t_{j\to j+1} = \frac{\tilde{n}_j\tilde{n}_{j+1}\tilde{q}_{j+1}}{\tilde{n}_j^2\tilde{q}_{j+1} + \tilde{n}_{j+1}^2\tilde{q}_j}, \tag{E.11}$$

$$\tilde{q}_j = \tilde{\eta}_j \cos(\phi_j) = \left[\tilde{\eta}_j^2 - \tilde{\eta}_0^2 \sin(\phi_0)\right]^{1/2}, \tag{E.12}$$

where ϕ_j is the incident angle of light arriving at the left side of surface j and ϕ_0 is the angle of incident light on the left glass surface. The stack can be divided into two sub-stacks, the first starting from layer 0 and running until the interface on the left side of the active layer, the second starting at the right interface of the active layer and running until the right hand side interface of layer m (as shown in Figure E.1). The normalised electric field ($\vec{E}_k(x)$) and the energy dissipation ($Q(x)$) within the active layer are given by the transfer matrix in the first ($\boldsymbol{S}'$) and second ($\boldsymbol{S}''$) sub-stack.

$$\vec{E}_k(x) = \frac{S'_{0,0} \times \exp\left[-i\xi_k(d_k - x)\right] + S''_{1,0} \times \exp\left[-i\xi_k(d_k - x)\right]}{S'_{0,0}S''_{0,0} \times \exp\left[-i\xi_k d_k\right] + S'_{0,1}S''_{1,0} \times \exp\left[-i\xi_k d_k\right]}, \tag{E.13}$$

$$Q(x) = \frac{1}{2} c\epsilon_0\alpha_k\eta_k \left|\vec{E}_k(x)\right|^2, \tag{E.14}$$

where the absorption coefficient is given by $\alpha = 4\pi\kappa_k/\lambda$.

E.3 Simulation

Figure E.2 shows the flowchart for this program, the user input is the thickness and spectral dependent complex refractive index of each layer in the stack. The program then loops through each wavelength calculating the generation at each position for that wavelength. The total generation at each position is then given by:

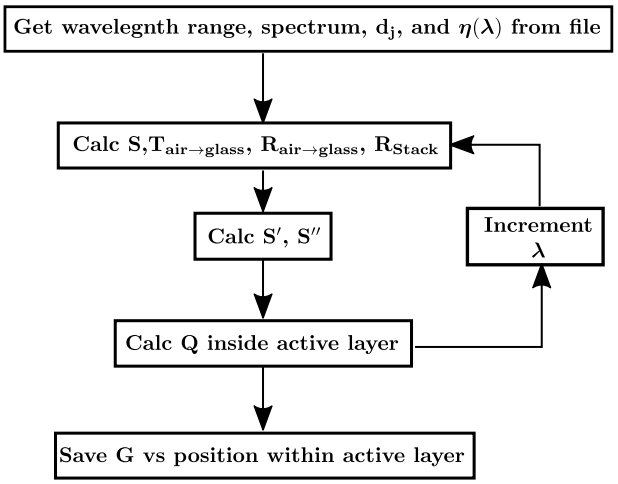

Figure E.2: Flowchart for Transfer Matrix Modelling program

$$G_{\text{Total}}(x) = \int_{\lambda_{\text{start}}}^{\lambda_{\text{end}}} Q(x, \lambda_i) \frac{\lambda_i}{hc} d\lambda_i. \tag{E.15}$$

The output file saves the $G_{\text{Total}}(x)$ and the position within the active layer for each input wavelength.

Appendix F

Monte-Carlo Modelling

To model the exciton dynamics within an organic semiconductor a Monte-Carlo hopping model using a gaussian density of states, Miller-Abrahams hopping rate, and a Gillipse algorithm was created incorporating exciton-exciton annihilation. The inputs to the program include the initial density of excitons (ρ_0), the diffusion constant of the lattice (D), the natural (low density) lifetime of the excitons (τ), the temporal step size of the simulation (dt), the gaussian disorder in the lattice sites (σ_d), and the minimum number of excitons required in the simulation (N_0). The flowchart for this program can be seen in Figure F.1, and can be divided into three sub-sections initialising the lattice, populating the lattice, and evolving the system in time.

F.1 Initialising the Lattice

The spacial distance between sites is calculated from diffusion coefficient and the natural lifetime as $dx = \sqrt{6D\tau}$, and dimensions are generated for the given geometry of the simulation.

1. **Infinite Thin Film** In the case of an infinite thin film (such as those simulations used in Chapter 5) the z dimension is considered the thin dimension, defined by an input parameter z_{nm}, and has reflecting boundary conditions, while the x and y dimensions are considered infinite and have periodic boundary conditions. The size of the lattice in the z direction is calculated as $z = z_{\mathrm{nm}}/dx$. The x and y dimensions are then calculated from ρ_0, N, and z as $x = y = \sqrt{N_0/\rho_0 z(dx)^3}$

2. **Limited Cylindrical Domain** In the case of a single cylindrical domain (such as the simulations laid out in Chapter 6) the z-dimension is considered infinite with periodic boundary conditions while the x and y dimensions form a cylindrical plane of a radius defined by an input parameter r, which defines the size of the x and y dimension of the lattice ($x = y = r/dx$). The size of the z-dimension is then calculated as $z = N_0/\rho_0 xy(dx)^3$

Once the dimensions have been defined, a lattice is generated with the total number of sites equalling $N = xyz$, where the energy of each lattice site is defined

from the gaussian density of states expressed by the disorder. The hopping rate between site i and site j can be defined from Miller-Abrahams rate:

$$\Gamma_{ij} = \nu_0 \exp\left[-\gamma r_{ij}\right] \begin{cases} \exp\left[-\frac{\Delta E_{ij}}{k_B T}\right], \Delta E_{ij} > 0 \\ 1, \Delta E_{ij} \leq 0 \end{cases}, \tag{F.1}$$

where ΔE_{ij} is the energetic difference between site i and j, ν_0 is the maximum hopping rate given as the inverse of the temporal step size, r_{ij} is the distance between sites, γ is the inverse localisation radius, stating how well the carriers can tunnel between sites. The total rate for a carrier to leave a site is given by the sum of all the possible pathways away from this site.

$$\Gamma_i = \sum_1^k \Gamma_{ik}. \tag{F.2}$$

F.2 Populating the Lattice

Once the lattice is created N_0 excitons are placed at random on the lattice by generating N_0 pseudo random numbers. This can be done simply with equal probability of generating a number between 0 and N for an even distribution. Additionally this can be done for any desired distribution; for example the distribution injected from a Gaussian laser spot would form a Gaussian distribution, which can be simulated by generating N_0 random numbers on a normal distribution with standard deviation equal to the laser spot-size. In the algorithm established here this is accomplished via the use of the Marsaglia Polar Method [254].

F.3 Evolving in Time

The amount of time an exciton spends on each lattice site (the 'dwell time') is given by the total hopping rate away from the site:

$$\tau_{\text{Dwell}} = T/\Gamma_i. \tag{F.3}$$

Where T is a pseudo-random value generated from an exponential distribution with unit expectation value and unit variance. As shown in Figure F.1 evolving each exciton in time consists of 4 possible routes, during each time step for each exciton the program checks:

i If the exciton is already decayed; ignore and move onto the next one.

ii If any of the nearest neighbours are occupied decay this exciton via exciton-exciton annihilation. This is considered a non-radiative decay event.

iii In the case where excitons can be extracted and reinjected at an interface.

(a) Check if exciton is on border and extract.

(b) Check if exciton is extracted and calculate probability of reinjection. If pseudo-random number generated is less than the probability of reinjection, then reinject the exciton.

iv Generate a pseudo-random number between 0 and 1. If this is less than dt/τ decay this exciton radiatively.

v If the dwell time has passed move the exciton via the Gillipse algorithm (see Appendix F.3.1).

This algorithm runs until the all excitons have decayed.

F.3.1 Gillipse Algorithm

In the Gillipse algorithm the probability that an exciton will move from one site to another (P_{ij}) is given by the ratio of that sites hopping rate to the total rate away from the site as

$$P_{ij} = \frac{\Gamma_{ij}}{\Gamma i}. \tag{F.4}$$

While the selected site to hop to (j) from site i is decided by generating a pseudo-random number (x) between 0 and 1 and finding j such that

$$\sum_{l=0}^{j} P_{il} \leq x. \tag{F.5}$$

In this case the excitons can move along any of the major axis meaning that the total number of pathways away from each (non boundary) site is 6.

F.3.2 Extraction and Reinjection

In the simulations used to calculate the domain size, described in Chapter 6, excitons on the edge of the domain can be extracted from and reinjected into the primary phase being simulated. If the position of the exciton away from the center of the lattice is larger than the simulated domain size, then the exciton is automatically extracted from the lattice and is considered decayed (non-radiative).

The probability for reinjection into the lattice is given by $k_{\text{inj}}/(k_{\text{inj}}+1)$ where k_{inj} is the rate of re-injection into the lattice, give by $k_{\text{inj}} = \exp\left[-\frac{\Delta E_{\text{inj}}}{K_B T}\right]$ where ΔE_{inj} is the energetic barrier to reinject an exciton into the lattice, ultimately determined by the energetic difference between the singlet exciton and the charge transfer state.

F.4 Scaling of Algorithm

There are two parts to the scaling of this simulation, the one is the creation of the lattice and the other is the temporal evolution. The lattice requires creating $x_{\text{Dim}} y_{\text{Dim}} z_{\text{Dim}}$ points each with a site energy, hopping rates, and occupation number (each represented by a vector class in C++), therefore this part of the algorithm scales polynomially with N. Apart from this the size of each vector grows with N, leading to memory issues at low densities (large lattices). To circumvent this issue the Sunbird supercomputer was used to run these simulations, allowing for a drastic increase in memory as well as each density to be run on parallel processors. This creates the need for each density to be run on a separate 'stream' on the lattice, such that excitons from other simulations do not interact. This increased the size of memory taken up by the lattice but decreased the time the simulations take. To attempt to decrease the time taken to implement the lattice, 'on-the-fly' Monte-Carlo was implemented. In this algorithm no quantity is calculated unless it is necessary; for example, the hopping rates of various lattice points may never be calculated if it is never occupied by an exciton. The temporal evolution of the system requires multiple checks for each exciton on the lattice and therefore also scales polynomially with N.

F.5 Physical Parameters

Once a particular simulation has been completed various quantities can be saved as outputs such as the route and exciton takes through the lattice, the start and end coordinates of each exciton, the time and type (radiative, annihilation, extraction) of decay each exciton undergoes, or the overall η_{PL} of the simulation. From these quantities the various outputs of the simulated experiments described in Chapter 5 and 6 can be computed and saved. The effective diffusion length $L_{D,\text{eff}}$ can be calculated for an ensemble of electrons from the Euclidean distance travelled by each exciton (L_i) as

$$L_{D,\text{eff}} = \sqrt{\frac{\sum_0^N (L_i)^2}{N}} \tag{F.6}$$

which will converge to the input diffusion length ($L_{D,\text{input}} = \sqrt{2mD\tau}$, where m is the dimensionality) in the low-density limit.

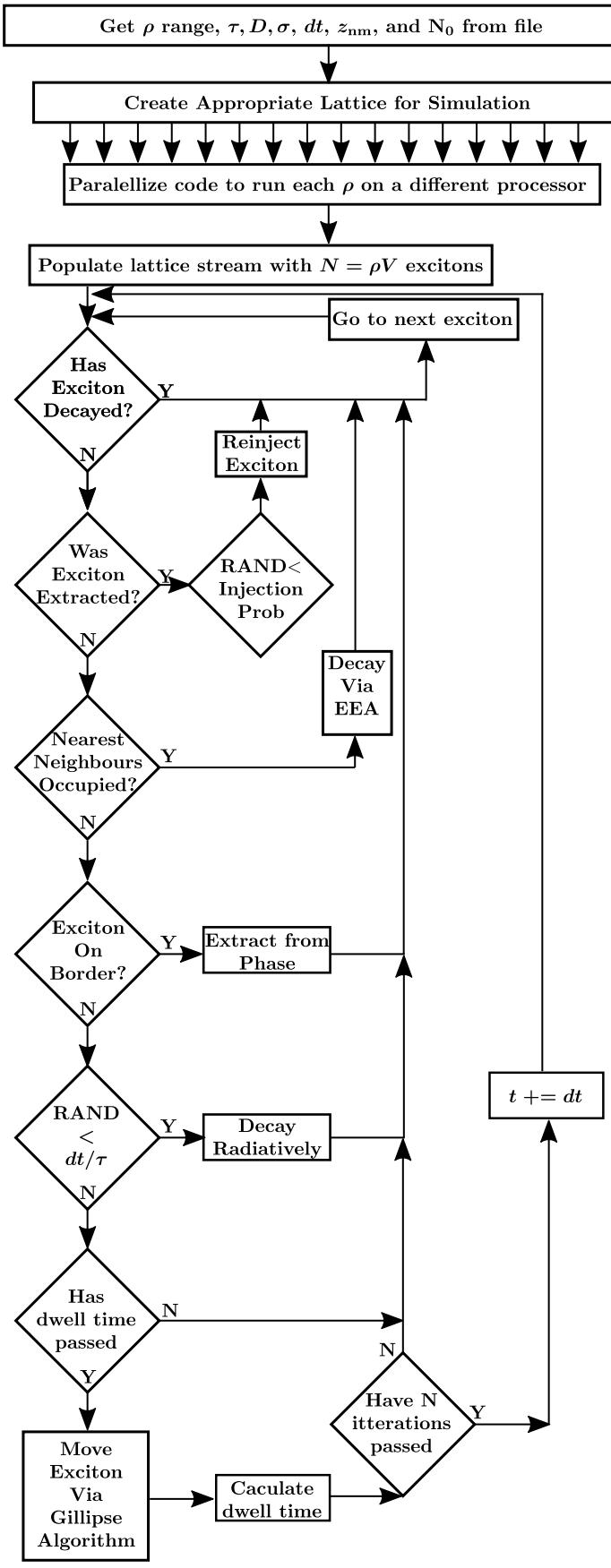

Figure F.1: Flow chart for multiple exciton time resolved photoluminescence simulations. ρ-initial exciton density, τ-natural exciton density, D-diffusion coefficient, σ_d-disorder parameter, dt-temporal step size, z_{nm}-film thickness, N_0-Minimum number of excitons on lattice, V-Volume of lattice, EEA-exciton-exciton annihilation, RAND-pseudo-random number between 0 and 1, t-simulation time.

Appendix G

Drift-Diffusion Modelling

The purpose of the drift diffusion model is to solve for the electron and hole concentrations and electric potential across the active area of a device contingent on the applied voltage at the contacts and the charge generation occurring within the active layer of the device. Once the carrier concentrations and potential are determined, observable values, such as device current or photoluminescence, can be calculated and compared to experimental results. This is achieved by discretizing the active area and simultaneously solving the Poisson and continuity equations in and between each voxel [255]. The poisson equation in a material of relative permittivity ϵ, can be found from the internal electric field(F)

$$\frac{d}{dx}\epsilon\epsilon_0 F = \rho \quad F = -\frac{d}{dx}\psi, \tag{G.1}$$

$$\frac{d^2}{dx^2}\psi = -\frac{q}{\epsilon\epsilon_0}\left[p - n\right]. \tag{G.2}$$

Where ρ is the total charge density, ψ is the electric-potential, n (p) is the electron (hole) densities within the device, q is the elementary charge, and ϵ_0 is the vacuum permittivity. The continuity equation can be found from Maxwell's addition to Ampère's circuit law

$$\frac{d}{dx}J + q\frac{d}{dt}(p - n) = 0. \tag{G.3}$$

The net generation-recombination rate of free electrons and holes occurring within a device is given by the difference between the sum of the intrinsic ($\beta {n^*}^2$, where n^* is the intrinsic carrier density) and external (G) generation, and the bi-molecular recombination of electron-hole pairs (βnp). The recombination constant (β) is defined as a multiple of the Langevin recombination

$$\beta = \beta_0 k_L = \beta_0 \frac{q}{\epsilon}\left(\mu_\mathrm{p} + \mu_\mathrm{n}\right), \beta_0 \leq 1 \tag{G.4}$$

From this the continuity equations for electrons and holes are found separately

$$\frac{1}{q}\frac{d}{dx}J_n - \frac{d}{dt}n = -\left[G - \beta\left(np - {n^*}^2\right)\right], \tag{G.5}$$

$$\frac{1}{q}\frac{d}{dx}J_p + \frac{d}{dt}p = G - \beta\left(np - {n^*}^2\right). \tag{G.6}$$

Where J_n (J_p) is the electron (hole) current density within the device. Which can be related to the carrier diffusion coefficient ($D_{n/p}$) through the drift-diffusion equations

$$J_n = qn\mu_n F + qD_n \frac{d}{dx} n, \tag{G.7}$$

$$J_p = qp\mu_p F - qD_p \frac{d}{dx} p. \tag{G.8}$$

Where the diffusion coefficient is given by the generalised Einstein equation

$$D_{n/p} = \frac{\mu_{n/p} k_B T}{q}. \tag{G.9}$$

Simultaneously discretizing and solving the Poisson (Equation G.2), and the continuity equations (Equation G.5 and G.6) in one dimension will lead to solutions to the electron and hole densities across a device for a given set of boundary conditions [255–257].

G.1 Discretizing and Solving the Poisson equation

To discretize the poisson equation consider the electric potential on site x_i (ψ_i). The electric potential between sites x_i and x_{i+1} will be dependent on the potential at site x_i and the derivative away from this site. Taylor expanding the potential at the site $x_{i+1/2}$, using step sizes of Δx

$$\psi_{i+1/2} = \psi_i + \frac{\Delta x}{2}\frac{d}{dx}\psi_i + \frac{\Delta x^2}{4}\frac{d^2}{dx^2}\psi_i + \frac{\Delta x^3}{8}\frac{d^3}{dx^3}\psi_i + O(h^4). \tag{G.10}$$

Taking the derivative at $x = i + 1/2$

$$\frac{d}{dx}\psi_{i+1/2} = \frac{d}{dx}\psi_i + \frac{\Delta x}{2}\frac{d^2}{dx^2}\psi_i + \frac{3\Delta x^2}{4}\frac{d^3}{dx^3}\psi_i. \tag{G.11}$$

Likewise, at $x = i - 1/2$

$$\frac{d}{dx}\psi_{i-1/2} = \frac{d}{dx}\psi_i - \frac{\Delta x}{2}\frac{d^2}{dx^2}\psi_i + \frac{3\Delta x^2}{4}\frac{d^3}{dx^3}\psi_i. \tag{G.12}$$

Truncating and using these results the Poisson equation (Equation G.2) can be written as

$$\frac{d^2}{dx^2}\psi_i = \frac{\frac{d}{dx}\psi_{i+1/2} - \frac{d}{dx}\psi_{i-1/2}}{\Delta x} + O(h^2) = \frac{q}{\epsilon}\left[n_i - p_i\right]. \tag{G.13}$$

Taking the difference between ψ_{i+1} and ψ_i to obtain $\frac{d}{dx}\psi_{i+1/2}$, Equation G.13 can be written

$$\frac{d^2}{dx^2}\psi_i = \frac{\psi_{i+1} - 2\psi_i + \psi_{i-1}}{(\Delta x)^2} = \frac{q}{\epsilon}\left[n_i - p_i\right]. \tag{G.14}$$

These expressions can be normalised using $\tilde{\psi}_i = \psi/V_{\text{th}}$, $V_{\text{th}} = k_B T/q$, $\tilde{x} = x/d$, $\Delta\tilde{x} = \Delta x/d$, $\tilde{n} = n/N_0$, $\tilde{p} = p/N_0$, $N_0 = \epsilon\epsilon_0 V_{\text{th}}/qd^2$ to

$$\tilde{\psi}_{i+1} - 2\tilde{\psi}_i + \tilde{\psi}_{i-1} = (\Delta\tilde{x})^2\left[\tilde{n}_i - \tilde{p}_i\right] \tag{G.15}$$

Equation G.15 is known as the Normalised Discretized Poisson Equation.

Starting with an initial guess of ψ, n, and p across the active area, an iterative approach (over the variable k) can be used to minimise the energy across the active area for a given set of boundary conditions ψ_{-1} and ψ_d. Under these conditions $\tilde{\psi}_i^{k+1} = \tilde{\psi}_i^k + \delta\tilde{\psi}_i$. The ϕ dependence of the electron and hole concentrations can be approximated as

$$\tilde{n}_i\left(\tilde{\psi}_i^{k+1}\right) = \tilde{n}_i e^{\tilde{\psi}_i^k + \delta\tilde{\psi}^k}, \tag{G.16}$$

$$\tilde{n}_i^{k+1} = \tilde{n}_i^k e^{\delta\psi} \sim \tilde{n}_i^k\left(1 + \delta\psi\right), \tag{G.17}$$

$$\tilde{p}_i\left(\tilde{\psi}_i^{k+1}\right) = \tilde{p}_i e^{\tilde{\psi}_i^k - \delta\tilde{\psi}^k}, \tag{G.18}$$

$$\tilde{p}_i^{k+1} = \tilde{p}_i^k e^{\delta\psi} \sim \tilde{p}_i^k\left(1 - \delta\psi\right). \tag{G.19}$$

Applying these conditions to Equation G.15

$$\tilde{\psi}_{i+1}^{k+1} - 2\tilde{\psi}_i^{k+1} + \tilde{\psi}_{i-1}^{k+1} = (\Delta\tilde{x})^2\left[\tilde{n}_i^k\left(1 + \delta\psi\right) - \tilde{p}_i^k\left(1 - \delta\psi\right)\right], \tag{G.20}$$

$$= (\Delta\tilde{x})^2\left[\tilde{n}_i^k\left(1 + \tilde{\psi}_i^{k+1} - \tilde{\psi}_i^k\right) - \tilde{p}_i^k\left(1 - \tilde{\psi}_i^{k+1} + \tilde{\psi}_i^k\right)\right]. \tag{G.21}$$

Which can be rearranged to read

$$\tilde{\psi}_{i+1}^{k+1} - \left[2 + (\Delta\tilde{x})^2\left(\tilde{n}_i^k + \tilde{p}_i^k\right)\right] + \tilde{\psi}_i^{k+1} + \tilde{\psi}_{i-1}^{k+1} = (\Delta\tilde{x})^2\left(\tilde{n}_i^k + \tilde{p}_i^k\right) - (\Delta\tilde{x})^2\left(\tilde{n}_i^k + \tilde{p}_i^k\right)\tilde{\psi}_i^k. \tag{G.22}$$

Equation G.22 expresses the terms of $\tilde{\psi}_i^{k+1}$ in terms of $\tilde{n}_i^k$ and $\tilde{p}_i^k$. Expressing Equation G.22 for each point ($0 < i < N$) as a matrix results in

$$\begin{bmatrix} a_0^k & 1 & \cdots & \cdots & 0 \\ 1 & a_1^k & 1 & \cdots & 0 \\ 0 & 1 & a_2^k & \cdots & \\ & \ddots & \ddots & \ddots & \\ 0 & \cdots & 1 & a_{N-1}^k & 1 \\ 0 & \cdots & \cdots & \cdots 1 & a_N^k \end{bmatrix} \begin{bmatrix} \tilde{\psi}_0^{k+1} \\ \tilde{\psi}_1^{k+1} \\ \vdots \\ \vdots \\ \tilde{\psi}_{N-1}^{k+1} \\ \tilde{\psi}_N^{k+1} \end{bmatrix} = \begin{bmatrix} b_0^k - \tilde{\psi}_{-1} \\ b_1^k \\ \vdots \\ \vdots \\ b_{n-1}^k \\ b_n^k - \tilde{\psi}_{N+1} \end{bmatrix}, \tag{G.23}$$

where

$$a_i^k = -\left(2 + \tilde{n}_i^k + \tilde{p}_i^k\right)(\Delta\tilde{x}), \tag{G.24}$$

$$b_i^k = (\Delta\tilde{x})\,\tilde{n}_i^k - (\Delta\tilde{x})\,\tilde{p}_i^k - (\Delta\tilde{x})\left(\tilde{n}_i^k + \tilde{p}_i^k\right)\tilde{\psi}_i^k. \tag{G.25}$$

Diagonalizing this matrix and iterating over k allows for the minimisation of the overall energy to a given tolerance. Concurrently, the energetics of the electron and hole densities must be minimised as well via the continuity equation.

G.2 Discretizing and Solving the Continuity Equations

To discretize the continuity equations consider the current moving between two sites i and $i+1$ as $J_n|_{i+1/2}$. In general, the electron current density is given by

$$J_n(x) = -qn\mu_n\frac{d}{dx}\psi(x) + qD_n\frac{d}{dx}n(x). \tag{G.26}$$

Expanding this expression to second order around a point $x_{i+1/2}$

$$\begin{aligned} J_n(x)|_{i+1/2} + (x - (x_i + \Delta x/2))\,\frac{d}{dx}J_n(x)|_{i+1/2} + O\left(\Delta x^2\right) \\ = -qn\mu_n\frac{d}{dx}\psi(x) + qD_n\frac{d}{dx}n(x), \end{aligned} \tag{G.27}$$

$$qn\mu_n\frac{d}{dx}\psi(x) - qD_n\frac{d}{dx}n(x) \sim J_n(x)|_{i+1/2} + (x - (x_i + \Delta x/2))\frac{d}{dx}J_n(x)|_{i+1/2}. \tag{G.28}$$

over the interval $x \subset [x_i, x_{i+1}]$ this has solutions [257]

$$J_n|_{i+1/2} = \frac{\tilde{\mu}_n}{\Delta\tilde{x}}\left[B\left(\tilde{\psi}_{i+1} - \tilde{\psi}_i\right)\tilde{n}_{i+1} - B\left(\tilde{\psi}_i - \tilde{\psi}_{i+1}\right)\tilde{n}_i\right], \tag{G.29}$$

where

$$B(y) = \frac{y}{e^y - 1}. \tag{G.30}$$

The normalised discretized version of equation G.5 can be written as

$$\begin{aligned} \nabla\cdot\tilde{J} \sim \frac{-\tilde{\mu_n}}{(\Delta\tilde{x})^2}\left\{B\left(\tilde{\psi}_{i+1} - \tilde{\psi}_i\right)\tilde{n}_{i+1}^t\left[B\left(\tilde{\psi}_i - \tilde{\psi}_{i+1}\right) + B\left(\tilde{\psi}_i - \tilde{\psi}_{i-1}\right)\right]\tilde{n}_i^t + \right. \\ \left. B\left(\tilde{\psi}_{i-1} - \tilde{\psi}_i\right)\tilde{n}_{i-1}^t\right\} = \tilde{G} - \tilde{\beta}\left(\tilde{n}_i^t\tilde{p}_i - \tilde{n^*}^2\right) + \frac{\tilde{n}_i^{t-1} - \tilde{n}_i^t}{\Delta\tilde{t}}, \end{aligned} \tag{G.31}$$

where $\tilde{n}_i^{t-1}$ is the electron density from the previous time step. Rearranging this for known and unknown terms

$$B\left(\tilde{\psi}_{i-1}-\tilde{\psi}_i\right)\tilde{n}_{i-1}^t-\left[B\left(\tilde{\psi}_i-\tilde{\psi}_{i+1}\right)+B\left(\tilde{\psi}_i-\tilde{\psi}_{i-1}\right)+\frac{\left(\tilde{\Delta x}\right)^2}{\tilde{\mu}_n}\left\{\tilde{\beta}\tilde{p_i}^t+\frac{1}{\Delta\tilde{t}}\right\}\right]\tilde{n}_i^t$$
$$+B\left(\tilde{\psi}_{i+1}-\tilde{\psi}_i\right)\tilde{n}_{i+1}^t=-\frac{(\Delta\tilde{x})^2}{\tilde{\mu}}\left[\tilde{G}+\tilde{\beta}\tilde{n}^{*2}+\frac{\tilde{n}_i^{t-1}}{\Delta\tilde{t}}\right], \tag{G.32}$$

creates a systems of equations that can be formulated into a matrix of the form

$$\begin{bmatrix} a_0^k & c_0^k & \cdots & \cdots & 0 \\ b_1^k & a_1^k & c_1^k & \cdots & 0 \\ 0 & b_2^k & a_2^k & \cdots & \\ & \ddots & \ddots & \ddots & \\ 0 & \cdots & b_{n-1}^k & a_{n-1}^k & c_{n-1}^k \\ 0 & \cdots & \cdots & \cdots b_n^k & a_n^k \end{bmatrix}\begin{bmatrix}\tilde{n}_0^{k+1}\\ \tilde{n}_1^{k+1}\\ \vdots\\ \vdots\\ \tilde{n}_{n-1}^{k+1}\\ \tilde{n}_n^{k+1}\end{bmatrix}=\begin{bmatrix} d_0^k-\mathrm{BC}_0\\ d_1^k\\ \vdots\\ \vdots\\ d_{n-1}^k\\ d_n^k-\mathrm{BC_d}\end{bmatrix}. \tag{G.33}$$

In which

$$a_i=B\left(\tilde{\psi}_i-\tilde{\psi}_{i+1}\right)+B\left(\tilde{\psi}_i-\tilde{\psi}_{i-1}\right)+\frac{\left(\tilde{\Delta x}\right)^2}{\tilde{\mu}_n}\left\{\tilde{\beta}\tilde{p_i}^t+\frac{1}{\Delta\tilde{t}}\right\}, \tag{G.34}$$

$$b_i=-B\left(\tilde{\psi}_{i+1}-\tilde{\psi}_i\right), \tag{G.35}$$

$$c_i=-B\left(\tilde{\psi}_{i-1}-\tilde{\psi}_i\right), \tag{G.36}$$

$$d_i=\frac{(\Delta x)^2}{\tilde{\mu}_n}\left[G+\tilde{\beta}\tilde{n}^{*2}+\frac{\tilde{n}_i^{t-1}}{\Delta\tilde{t}}\right], \tag{G.37}$$

$$a_n=B\left(\tilde{\psi}_d-\tilde{\psi}_{d-1}\right)+\frac{(\Delta x)^2}{\tilde{\mu}_n}\tilde{S}_{n,cath}, \tag{G.38}$$

$$\mathrm{BC}_0=\frac{(\Delta x)^2}{\tilde{\mu}_n}\tilde{S}_{n,an}\tilde{n}_0, \tag{G.39}$$

$$\mathrm{BC_d}=\frac{(\Delta x)^2}{\tilde{\mu}_n}\tilde{S}_{n,cath}\tilde{n}_n. \tag{G.40}$$

In which a_0, a_n, b_n, c_0, n_0, and n_n have forms that depend on the boundary conditions laid out in Appendix G.3. $\tilde{S}_{n,an/ct}$ are the surface recombination velocities discussed in Section 3.2.4. By diagonalizing Matrix G.33 one can find $\tilde{n}^{k+1}$ in terms of the known terms $\tilde{\psi}^{k+1}$. By iterating between the Poisson and continuity

equations one can minimise the energetics of both expressions to an arbitrary tolerance. Thus obtaining the electron and hole concentrations and electric potential across the device for a given boundary condition. Figure G.1 shows the flow chart for the of the program.

Likewise, the hole continuity equation can be discretized to obtain

$$B\left(\tilde{\psi}_i-\tilde{\psi}_{i-1}\right)\tilde{p}_{i-1}^{t}-\left[B\left(\tilde{\psi}_{i-1}-\tilde{\psi}_i\right)+B\left(\tilde{\psi}_{i+1}-\tilde{\psi}_i\right)+\frac{\left(\tilde{\Delta x}\right)^2}{\tilde{\mu}_p}\left\{\tilde{\beta}\tilde{n}_i+\frac{1}{\Delta\tilde{t}}\right\}\right]\tilde{p}_i^{t}$$
$$+B\left(\tilde{\psi}_i-\tilde{\psi}_{i+1}\right)\tilde{p}_{i+1}^{t}=-\frac{\left(\Delta\tilde{x}\right)^2}{\tilde{\mu}}\left[\tilde{G}+\tilde{\beta}\tilde{n}^{*2}+\frac{\tilde{p}_i^{t-1}}{\Delta\tilde{t}}\right] \tag{G.41}$$

from which a Matrix similar to G.33 can be formed.

G.3 Boundary Conditions

In OPV-based solar cells the conduction level is defined by the acceptor χ while the valence level is defined by the donor IP. The effective energy gap is described by the difference between these values $E_{\mathrm{G}} = \mathrm{IP}_{\mathrm{Donor}} - \chi_{\mathrm{Acceptor}}$ (see Figure G.2). While the anode is held at zero potential the potential boundary condition at the cathode will be given by the difference between the applied (V) and built in (V_{bi}) voltage

$$\int_0^d F(x,t)dx = V - V_{\mathrm{bi}}. \tag{G.42}$$

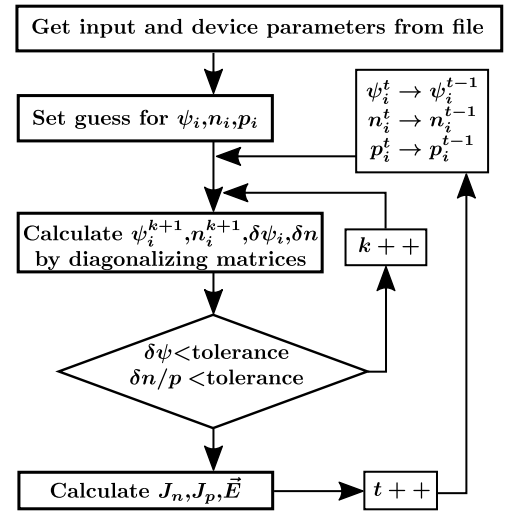

Figure G.1: Flow Chart for Drift-Diffusion Algorithm

Surface recombination occurs when there are non-radiative pathways for carrier recombination near the contacts. The charge carrier current can be described by

a kinetic model with a surface recombination velocity ($S_{n/p,\mathrm{An/Cat}}$) at the cathode and anode, given by the product of the carrier thermal velocity through the lattice, the capture cross section, and the density of pathways at the contact-semiconductor interface [43]. The density of carriers generated at the various contacts defines the electron and hole density boundary conditions, given by thermonic emission theory as [258, 259]

$$n_{\mathrm{An}} = N_{\mathrm{C}} \exp\left(-\phi_{n,\mathrm{An}}/k_{\mathrm{B}}T\right), \tag{G.43}$$
$$n_{\mathrm{Cat}} = N_{\mathrm{C}} \exp\left(-\phi_{n,\mathrm{Cat}}/k_{\mathrm{B}}T\right), \tag{G.44}$$
$$p_{\mathrm{An}} = N_{\mathrm{V}} \exp\left(-\phi_{p,\mathrm{An}}/k_{\mathrm{B}}T\right), \tag{G.45}$$
$$p_{\mathrm{Cat}} = N_{\mathrm{V}} \exp\left(-\phi_{p,\mathrm{Cat}}/k_{\mathrm{B}}T\right). \tag{G.46}$$

The electron or hole current flowing between the semiconductor and the anode or the cathode are given by the difference between the carrier concentrations at the device interface ($n(0,d)/p(0,d)$) and at the contact ($n_{\mathrm{An/Cat}}/p_{\mathrm{An/Cat}}$)

$$J_{n,\mathrm{An}} = qS_{n,\mathrm{An}}\left(n(0) - n_{\mathrm{An}}\right), \tag{G.47}$$
$$J_{p,\mathrm{An}} = -qS_{p,\mathrm{An}}\left(p(0) - p_{\mathrm{An}}\right), \tag{G.48}$$
$$J_{n,\mathrm{Cat}} = -qS_{n,\mathrm{Cat}}\left(n(d) - n_{\mathrm{Cat}}\right), \tag{G.49}$$
$$J_{p,\mathrm{Cat}} = qS_{p,\mathrm{Cat}}\left(p(d) - p_{\mathrm{Cat}}\right), \tag{G.50}$$

which defines the boundary conditions for J_n and J_p, and therefore those given in Equations G.39 and G.40.

G.4 Calculating Physical Quantities

Once the electron and hole densities have been calculated, measurable quantities can be calculated. The time dependent total current can be calculated as

$$J_{\mathrm{tot}}(t) = \frac{1}{d}\int_0^d \left(J_n + J_p\right) dx + \frac{\epsilon\epsilon_0}{d}\frac{\partial V}{\partial t}. \tag{G.51}$$

Photoluminescence (PL) can be calculated as

$$\mathrm{PL} = f_r \int_0^d \beta n(x) p(x) dx, \tag{G.52}$$

where f_r is the proportion of recombination that is radiative. The conduction and valence levels ($E_{\mathrm{C/V}}$) and quasi-Fermi ($E_{\mathrm{F}n/p}$) levels can be calculated as

$$E_{\mathrm{C}}(x) = -\chi_n - q\psi(x), \tag{G.53}$$
$$E_{\mathrm{V}}(x) = E_c(x) - E_{\mathrm{G}}, \tag{G.54}$$
$$E_{\mathrm{F}n}(x) = k_{\mathrm{B}}T \ln\left[n(x)/N_{\mathrm{C}}\right] + E_{\mathrm{C}}(x), \tag{G.55}$$
$$E_{\mathrm{F}p}(x) = -k_{\mathrm{B}}T \ln\left[p(x)/N_{\mathrm{V}}\right] + E_{\mathrm{V}}(x). \tag{G.56}$$

The spacial dependence of the quasi-Fermi level splitting can be calculated as

$$E_{\mathrm{QFLS}}(x) = E_{\mathrm{F}n}(x). - E_{\mathrm{F}p}(x) \tag{G.57}$$

In general, the V_{OC} is given by the difference between the anode and cathode quasi-Fermi levels, which, in turn, takes the form [232, 236]

$$qV_{\mathrm{oc}} = E_{\mathrm{F}n}(d) - E_{\mathrm{F}p}(0). \tag{G.58}$$

Where the electron and hole quasi-Fermi levels are given by equations G.55 and G.56.

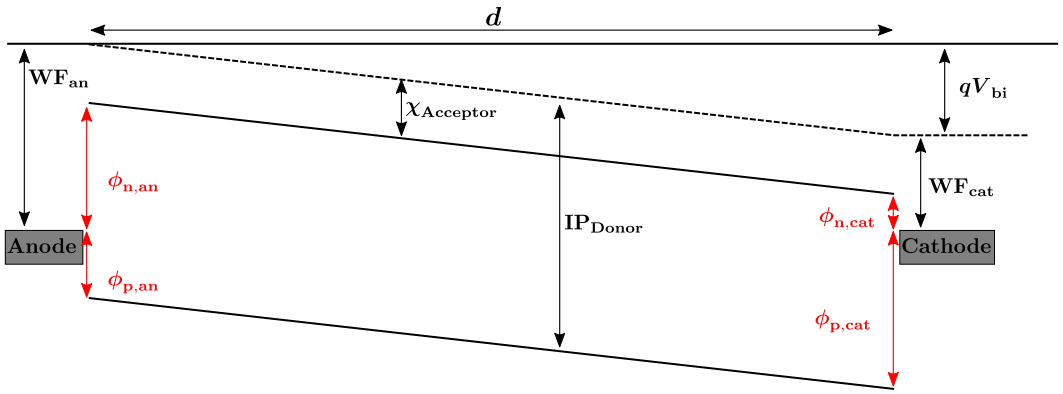

Figure G.2: Energy levels used to calculate the conduction and valence levels as well as injection barriers at the anode and cathode. d-junction thickness, WF-work function, ϕ-injection barrier, V_{bi}-built in voltage, χ-electron affinity.

Bibliography

[1] Drew B Riley, Paul Meredith, Ardalan Armin, and Oskar J Sandberg. Role of exciton diffusion and lifetime in organic solar cells with a low energy offset. The Journal of Physical Chemistry Letters, 13:4402–4409, 2022.

[2] Drew B Riley, Oskar J Sandberg, Wei Li, Paul Meredith, and Ardalan Armin. Quasi-steady-state measurement of exciton diffusion lengths in organic semiconductors. Physical Review Applied, 17(2):024076, 2022.

[3] Drew B Riley, Oskar J Sandberg, Nora M Wilson, Wei Li, Stefan Zeiske, Nasim Zarrabi, Paul Meredith, Ronald Österbacka, and Ardalan Armin. Direct quantification of quasi-fermi-level splitting in organic semiconductor devices. Physical Review Applied, 15(6):064035, 2021.

[4] Alessandro Volta. Xvi. del modo di render sensibilissima la più debole elettricità sia natural, sia artificiale. Philosophical Transactions of the Royal Society of London, pages 237–280, 1782.

[5] Thomas Johann Seebeck. Magnetische polarisation der metalle und erze durch temperatur-differenz. W. Engelmann, 1895.

[6] Michael Faraday. Xx. experimental researches in electricity.—fourth series. Philosophical Transactions of the Royal Society of London, pages 507–522, 1833.

[7] KARL Ferdinand Braun. Electrical oscillations and wireless telegraphy. Nobel Lecture, December, 11(1909):226–245, 1909.

[8] Walter H Brattain and John Bardeen. Surface properties of germanium. The Bell System Technical Journal, 32(1):1–41, 1953.

[9] William Shockley. The theory of p-n junctions in semiconductors and p-n junction transistors. Bell System Technical Journal, 28(3):435–489, 1949.

[10] Jack St Clair Kilby. Turning potential into realities: The invention of the integrated circuit (nobel lecture). ChemPhysChem, 2(8-9):482–489, 2001.

[11] A Slocum and John Northrup Shive. Shot dependence of p-n junction phototransistor noise. Journal of Applied Physics, 25(3):406–406, 1954.

[12] Silvano Donati. Photodetectors: devices, circuits and applications. John Wiley & Sons, 2021.

[13] Charles E Fritts. On a new form of selenium cell, and some electrical discoveries made by its use. American Journal of Science, 3(156):465–472, 1883.

[14] Russell S Ohl. Light-sensitive electric device, June 25 1946. US Patent 2,402,662.

[15] Kunta Yoshikawa, Hayato Kawasaki, Wataru Yoshida, Toru Irie, Katsunori Konishi, Kunihiro Nakano, Toshihiko Uto, Daisuke Adachi, Masanori Kanematsu, Hisashi Uzu, et al. Silicon heterojunction solar cell with interdigitated back contacts for a photoconversion efficiency over 26%. Nature energy, 2(5):1–8, 2017.

[16] Jingjing Liu, Yao Yao, Shaoqing Xiao, and Xiaofeng Gu. Review of status developments of high-efficiency crystalline silicon solar cells. Journal of Physics D: Applied Physics, 51(12):123001, 2018.

[17] Ardalan Armin, Wei Li, Oskar J Sandberg, Zuo Xiao, Liming Ding, Jenny Nelson, Dieter Neher, Koen Vandewal, Safa Shoaee, Tao Wang, et al. A history and perspective of non-fullerene electron acceptors for organic solar cells. Adv. Energy. Mater., 11(15):2003570, 2021.

[18] Lucio Claudio Andreani, Angelo Bozzola, Piotr Kowalczewski, Marco Liscidini, and Lisa Redorici. Silicon solar cells: toward the efficiency limits. Advances in Physics: X, 4(1):1548305, 2019.

[19] Jan Benick, Armin Richter, Ralph Müller, Hubert Hauser, Frank Feldmann, Patricia Krenckel, Stephan Riepe, Florian Schindler, Martin C Schubert, Martin Hermle, et al. High-efficiency n-type hp mc silicon solar cells. IEEE journal of photovoltaics, 7(5):1171–1175, 2017.

[20] Brendan M Kayes, Hui Nie, Rose Twist, Sylvia G Spruytte, Frank Reinhardt, Isik C Kizilyalli, and Gregg S Higashi. 27.6% conversion efficiency, a new record for single-junction solar cells under 1 sun illumination. In 2011 37th IEEE Photovoltaic Specialists Conference, pages 000004–000008. IEEE, 2011.

[21] Mark Wanlass. Systems and methods for advanced ultra-high-performance inp solar cells. Technical report, National Renewable Energy Lab.(NREL), Golden, CO (United States), 2017.

[22] Mark Wanlass. Systems and methods for advanced ultra-high-performance inp solar cells, March 7 2017. US Patent 9,590,131.

[23] Martin Green, Ewan Dunlop, Jochen Hohl-Ebinger, Masahiro Yoshita, Nikos Kopidakis, and Xiaojing Hao. Solar cell efficiency tables (version 57). Progress in photovoltaics: research and applications, 29(1):3–15, 2021.

[24] Christie L Cutting, Monojit Bag, and D Venkataraman. Indoor light recycling: a new home for organic photovoltaics. J. Mater. Chem. C, 4(43):10367–10370, 2016.

[25] Nicholas C Davy, Melda Sezen-Edmonds, Jia Gao, Xin Lin, Amy Liu, Nan Yao, Antoine Kahn, and Yueh-Lin Loo. Pairing of near-ultraviolet solar cells with electrochromic windows for smart management of the solar spectrum. Nat. Energy, 2(8):1–11, 2017.

[26] Gregory Burwell, Oskar J Sandberg, Wei Li, Paul Meredith, Matt Carnie, and Ardalan Armin. Scaling considerations for organic photovoltaics for indoor applications. Solar RRL, page 2200315, 2022.

[27] N Thejo Kalyani and SJ Dhoble. Organic light emitting diodes: Energy saving lighting technology—a review. Renew. Sust. Energ. Rev., 16(5):2696–2723, 2012.

[28] F Pelayo García de Arquer, Ardalan Armin, Paul Meredith, and Edward H Sargent. Solution-processed semiconductors for next-generation photodetectors. Nat. Rev. Mater., 2(3):1–17, 2017.

[29] Sébastien Chénais and Sebastien Forget. Recent advances in solid-state organic lasers. Polym. Int., 61(3):390–406, 2012.

[30] Tanya Kumari, Sang Myeon Lee, So-Huei Kang, Shanshan Chen, and Changduk Yang. Ternary solar cells with a mixed face-on and edge-on orientation enable an unprecedented efficiency of 12.1%. Energy & Environmental Science, 10(1):258–265, 2017.

[31] Wenchao Zhao, Sunsun Li, Huifeng Yao, Shaoqing Zhang, Yun Zhang, Bei Yang, and Jianhui Hou. Molecular optimization enables over 13% efficiency in organic solar cells. Journal of the American Chemical Society, 139(21):7148–7151, 2017.

[32] Jianqiang Qin, Lixiu Zhang, Chuantian Zuo, Zuo Xiao, Yongbo Yuan, Shangfeng Yang, Feng Hao, Ming Cheng, Kuan Sun, Qinye Bao, et al. A chlorinated copolymer donor demonstrates a 18.13% power conversion efficiency. Journal of Semiconductors, 42(1):010501, 2021.

[33] Ke Jin, Zuo Xiao, and Liming Ding. D18, an eximious solar polymer! Journal of Semiconductors, 42(1):010502–010502, 2021.

[34] Yong Cui, Ye Xu, Huifeng Yao, Pengqing Bi, Ling Hong, Jianqi Zhang, Yunfei Zu, Tao Zhang, Jinzhao Qin, Junzhen Ren, et al. Single-junction organic photovoltaic cell with 19% efficiency. Advanced Materials, 33(41):2102420, 2021.

[35] Yunhao Cai, Yun Li, Rui Wang, Hongbo Wu, Zhihao Chen, Jie Zhang, Zaifei Ma, Xiaotao Hao, Yong Zhao, Chunfeng Zhang, et al. A well-mixed phase formed by two compatible non-fullerene acceptors enables ternary organic solar cells with efficiency over 18.6%. Advanced Materials, 33(33):2101733, 2021.

[36] Qishi Liu, Yufan Jiang, Ke Jin, Jianqiang Qin, Jingui Xu, Wenting Li, Ji Xiong, Jinfeng Liu, Zuo Xiao, Kuan Sun, et al. 18% efficiency organic solar cells. Sci. Bull., 65(4):272–275, 2020.

[37] Oskar J Sandberg and Ardalan Armin. Energetics and kinetics requirements for organic solar cells to break the 20% power conversion efficiency barrier. The Journal of Physical Chemistry C, 125(28):15590–15598, 2021.

[38] Paul Meredith, Wei Li, and Ardalan Armin. Nonfullerene acceptors: A renaissance in organic photovoltaics? Advanced Energy Materials, 10(33):2001788, 2020.

[39] Marius Grundmann. The physics of semiconductors. In Graduate Texts in Physics, volume 3, page 989. Springer Cham, 2010.

[40] N. W. Ashcroft and N. D. Mermin. Solid State Physics. Holt-Saunders, 1976.

[41] Charles Kittel and Paul McEuen. Introduction to solid state physics. John Wiley & Sons, 2018.

[42] Jenny A Nelson. The physics of solar cells. World Scientific Publishing Company, 2003.

[43] Peter Würfel and Uli Würfel. Physics of solar cells: from basic principles to advanced concepts. John Wiley & Sons, 2016.

[44] David G Seiler, JR Lowney, Chris L Littler, and MR Loloee. Temperature and composition dependence of the energy gap of hg1- x cd x te by two-photon magnetoabsorption techniques. Journal of Vacuum Science & Technology A: Vacuum, Surfaces, and Films, 8(2):1237–1244, 1990.

[45] Martin Feneberg, Robert AR Leute, Benjamin Neuschl, Klaus Thonke, and Matthias Bickermann. High-excitation and high-resolution photoluminescence spectra of bulk aln. Physical Review B, 82(7):075208, 2010.

[46] Xu She, Alex Q Huang, Oscar Lucia, and Burak Ozpineci. Review of silicon carbide power devices and their applications. IEEE Transactions on Industrial Electronics, 64(10):8193–8205, 2017.

[47] Chi Zhang, Srdjan Srdic, Srdjan Lukic, Yonghan Kang, Edward Choi, and Ehsan Tafti. A sic-based 100 kw high-power-density (34 kw/l) electric vehicle traction inverter. In 2018 IEEE Energy Conversion Congress and Exposition (ECCE), pages 3880–3885. IEEE, 2018.

[48] Shaolin Yu, Jianing Wang, Xing Zhang, Yuanjian Liu, Nan Jiang, and Wenbo Wang. The potential impact of using traction inverters with sic mosfets for electric buses. IEEE Access, 9:51561–51572, 2021.

[49] Kevin J Chen, Oliver Häberlen, Alex Lidow, Chun lin Tsai, Tetsuzo Ueda, Yasuhiro Uemoto, and Yifeng Wu. Gan-on-si power technology: Devices and applications. IEEE Transactions on Electron Devices, 64(3):779–795, 2017.

[50] Yueshi Guan, Yijie Wang, Dianguo Xu, and Wei Wang. A 1 mhz half-bridge resonant dc/dc converter based on gan fets and planar magnetics. IEEE Transactions on Power Electronics, 32(4):2876–2891, 2016.

[51] Giuseppe Iannaccone, Christian Sbrana, Iacopo Morelli, and Sebastiano Strangio. Power electronics based on wide-bandgap semiconductors: Opportunities and challenges. IEEE Access, 2021.

[52] F Pelayo García de Arquer, Dmitri V Talapin, Victor I Klimov, Yasuhiko Arakawa, Manfred Bayer, and Edward H Sargent. Semiconductor quantum dots: Technological progress and future challenges. Science, 373(6555):eaaz8541, 2021.

[53] Shuiyuan Wang, Xiaoxian Liu, and Peng Zhou. The road for 2d semiconductors in the silicon age. Advanced Materials, page 2106886, 2021.

[54] Kai Wang, Dong Yang, Congcong Wu, Mohan Sanghadasa, and Shashank Priya. Recent progress in fundamental understanding of halide perovskite semiconductors. Progress in Materials Science, 106:100580, 2019.

[55] Peter Wurfel. The chemical potential of radiation. Journal of Physics C: Solid State Physics, 15(18):3967, 1982.

[56] H Barry Bebb and EW Williams. Photoluminescence i: theory. In Semiconductors and semimetals, volume 8, pages 181–320. Elsevier, 1972.

[57] Helmut A Müser. Thermodynamische behandlung von elektronenprozessen in halbleiter-randschichten. Zeitschrift für Physik, 148(3):380–390, 1957.

[58] Alexis De Vos. Efficiency of some heat engines at maximum-power conditions. American Journal of Physics, 53(6):570–573, 1985.

[59] William Shockley and Hans J Queisser. Detailed balance limit of efficiency of p-n junction solar cells. Journal of applied physics, 32(3):510–519, 1961.

[60] Robin Kerremans, Christina Kaiser, Wei Li, Nasim Zarrabi, Paul Meredith, and Ardalan Armin. The optical constants of solution-processed semiconductors—new challenges with perovskites and non-fullerene acceptors. Advanced Optical Materials, 8(16):2000319, 2020.

[61] Earl J McCartney. Optics of the atmosphere: scattering by molecules and particles. 1976.

[62] C Donolato. A reciprocity theorem for charge collection. Applied Physics Letters, 46(3):270–272, 1985.

[63] C Donolato. An alternative proof of the generalized reciprocity theorem for charge collection. Journal of Applied Physics, 66(9):4524–4525, 1989.

[64] Martin A Green. Generalized relationship between dark carrier distribution and photocarrier collection in solar cells. Journal of applied physics, 81(1):268–271, 1997.

[65] Uwe Rau. Reciprocity relation between photovoltaic quantum efficiency and electroluminescent emission of solar cells. Physical Review B, 76(8):085303, 2007.

[66] Thomas Kirchartz, Anke Helbig, Wilfried Reetz, Michael Reuter, Jürgen H Werner, and Uwe Rau. Reciprocity between electroluminescence and quantum efficiency used for the characterization of silicon solar cells. Progress in Photovoltaics: Research and Applications, 17(6):394–402, 2009.

[67] Thomas Kirchartz, Jenny Nelson, and Uwe Rau. Reciprocity between charge injection and extraction and its influence on the interpretation of electroluminescence spectra in organic solar cells. Physical Review Applied, 5(5):054003, 2016.

[68] Thomas Kirchartz and Uwe Rau. Detailed balance and reciprocity in solar cells. physica status solidi (a), 205(12):2737–2751, 2008.

[69] Anna Köhler and Heinz Bässler. Electronic processes in organic semiconductors: An introduction. John Wiley & Sons, 2015.

[70] Jacov Frenkel. On the transformation of light into heat in solids. ii. Physical Review, 37(10):1276, 1931.

[71] Vladimir Valentinovich Egorov and Mikhail V Alfimov. Theory of the j-band: from the frenkel exciton to charge transfer. Physics-Uspekhi, 50(10):985, 2007.

[72] Marc Dvorak, Su-Huai Wei, and Zhigang Wu. Origin of the variation of exciton binding energy in semiconductors. Physical review letters, 110(1):016402, 2013.

[73] Th Forster. Energiewanderung und fluoreszenz. Naturwissenschaften, 33(6):166–175, 1946.

[74] T Förster. Energy transfer and fluorescence between molecules. Ann. Phys., 437(1-2):55–75, 1948.

[75] Robert M Clegg. Förster resonance energy transfer—fret what is it, why do it, and how it's done. Laboratory techniques in biochemistry and molecular biology, 33:1–57, 2009.

[76] John David Jackson. Classical electrodynamics. American Association of Physics Teachers, 1999.

[77] BR Masters. Paths to förster's resonance energy transfer (fret) theory. The European Physical Journal H, 39(1):87–139, 2014.

[78] Th Föster. Intermolecular energy migration and fluorescence. Ann Phys, 2:55–75, 1948.

[79] Garth A Jones and David S Bradshaw. Resonance energy transfer: from fundamental theory to recent applications. Frontiers in Physics, 7:100, 2019.

[80] Kim F Wong, Biman Bagchi, and Peter J Rossky. Distance and orientation dependence of excitation transfer rates in conjugated systems: beyond the förster theory. The Journal of Physical Chemistry A, 108(27):5752–5763, 2004.

[81] Edward Condon. A theory of intensity distribution in band systems. Physical Review, 28(6):1182, 1926.

[82] James Franck and EG Dymond. Elementary processes of photochemical reactions. Transactions of the Faraday Society, 21(February):536–542, 1926.

[83] Theodor Förster and O Sinanoglu. Modern quantum chemistry. Academic Press, New York, 3:93–137, 1965.

[84] Paul WM Blom and MCJM Vissenberg. Charge transport in poly (p-phenylene vinylene) light-emitting diodes. Materials Science and Engineering: R: Reports, 27(3-4):53–94, 2000.

[85] Ivan I Fishchuk, Andrey Kadashchuk, Sebastian T Hoffmann, Stavros Athanasopoulos, Jan Genoe, Heinz Bässler, and Anna Köhler. Unified description for hopping transport in organic semiconductors including both energetic disorder and polaronic contributions. Physical Review B, 88(12):125202, 2013.

[86] Esther M Conwell. Impurity band conduction in germanium and silicon. Physical Review, 103(1):51, 1956.

[87] Allen Miller and Elihu Abrahams. Impurity conduction at low concentrations. Physical Review, 120(3):745, 1960.

[88] K Feron, X Zhou, WJ Belcher, and PC Dastoor. Exciton transport in organic semiconductors: Förster resonance energy transfer compared with a simple random walk. Journal of Applied Physics, 111(4):044510, 2012.

[89] Albert Einstein. Über die von der molekularkinetischen theorie der wärme geforderte bewegung von in ruhenden flüssigkeiten suspendierten teilchen. Annalen der physik, 4, 1905.

[90] Ardalan Armin, Ivan Kassal, Paul E Shaw, Mike Hambsch, Martin Stolterfoht, Dani M Lyons, Jun Li, Zugui Shi, Paul L Burn, and Paul Meredith. Spectral dependence of the internal quantum efficiency of organic solar cells: Effect of charge generation pathways. J. Am. Chem. Soc., 136(32):11465–11472, 2014.

[91] Lorena Perdigón-Toro, Huotian Zhang, Anastasia Markina, Jun Yuan, Seyed Mehrdad Hosseini, Christian M Wolff, Guangzheng Zuo, Martin Stolterfoht, Yingping Zou, Feng Gao, et al. Barrierless free charge generation in the high-performance pm6: Y6 bulk heterojunction non-fullerene solar cell. Advanced Materials, 32(9):1906763, 2020.

[92] Youzhan Li, He Liu, Jiang Wu, Hao Tang, Hailong Wang, Qingqing Yang, Yingying Fu, and Zhiyuan Xie. Additive and high-temperature processing boost the photovoltaic performance of nonfullerene organic solar cells fabricated with blade coating and nonhalogenated solvents. ACS Appl. Mater. Inter., 13(8):10239–10248, 2021.

[93] Maria Saladina, Pablo Simón Marqués, Anastasia Markina, Safakath Karuthedath, Christopher Wöpke, Clemens Göhler, Yue Chen, Magali Allain, Philippe Blanchard, Clément Cabanetos, et al. Charge photogeneration in non-fullerene organic solar cells: Influence of excess energy and electrostatic interactions. Advanced Functional Materials, 31(8):2007479, 2021.

[94] Lorena Perdigón-Toro, Le Quang Phuong, Stefan Zeiske, Koen Vandewal, Ardalan Armin, Safa Shoaee, and Dieter Neher. Excitons dominate the emission from pm6: Y6 solar cells, but this does not help the open-circuit voltage of the device. ACS Energy Letters, 6:557–564, 2021.

[95] Daniel Balzer, Thijs JAM Smolders, David Blyth, Samantha N Hood, and Ivan Kassal. Delocalised kinetic monte carlo for simulating delocalisation-enhanced charge and exciton transport in disordered materials. Chemical Science, 12(6):2276–2285, 2021.

[96] Daniel Balzer and Ivan Kassal. Even a little delocalisation produces large kinetic enhancements of charge-separation efficiency in organic photovoltaics. arXiv preprint arXiv:2108.05032, 2021.

[97] Safakath Karuthedath, Julien Gorenflot, Yuliar Firdaus, Neha Chaturvedi, Catherine SP De Castro, George T Harrison, Jafar I Khan, Anastasia Markina, Ahmed H Balawi, Top Archie Dela Peña, et al. Intrinsic efficiency limits in low-bandgap non-fullerene acceptor organic solar cells. Nat. Mater., 20(3):378–384, 2021.

[98] Tracey M Clarke and James R Durrant. Charge photogeneration in organic solar cells. Chemical reviews, 110(11):6736–6767, 2010.

[99] Charles L Braun. Electric field assisted dissociation of charge transfer states as a mechanism of photocarrier production. The Journal of chemical physics, 80(9):4157–4161, 1984.

[100] Paul Langevin. Recombinaison et mobilites des ions dans les gaz. Ann. Chim. Phys, 28(433):122, 1903.

[101] Leiping Duan, Yu Zhang, Haimang Yi, Faiazul Haque, Rong Deng, Huilan Guan, Yingping Zou, and Ashraf Uddin. Trade-off between exciton dissociation and carrier recombination and dielectric properties in y6-sensitized nonfullerene ternary organic solar cells. Energy Technology, 8(1):1900924, 2020.

[102] A Pivrikas, G Juška, Attila J Mozer, M Scharber, K Arlauskas, NS Sariciftci, H Stubb, and R Österbacka. Bimolecular recombination coefficient as a sensitive testing parameter for low-mobility solar-cell materials. Physical review letters, 94(17):176806, 2005.

[103] P Parkinson, J Lloyd-Hughes, MB Johnston, and LM Herz. Efficient generation of charges via below-gap photoexcitation of polymer-fullerene blend films investigated by terahertz spectroscopy. Physical Review B, 78(11):115321, 2008.

[104] Martin Stolterfoht, Bronson Philippa, Ardalan Armin, Ajay K Pandey, Ronald D White, Paul L Burn, Paul Meredith, and Almantas Pivrikas. Advantage of suppressed non-langevin recombination in low mobility organic solar cells. Applied Physics Letters, 105(1):99_1, 2014.

[105] Ardalan Armin, Jegadesan Subbiah, Martin Stolterfoht, Safa Shoaee, Zeyun Xiao, Shirong Lu, David J Jones, and Paul Meredith. Reduced recombination in high efficiency molecular nematic liquid crystalline: fullerene solar cells. Advanced Energy Materials, 6(22):1600939, 2016.

[106] G Juška, K Arlauskas, J Stuchlik, and R Österbacka. Non-langevin bimolecular recombination in low-mobility materials. Journal of non-crystalline solids, 352(9-20):1167–1171, 2006.

[107] Nasim Zarrabi, Oskar J Sandberg, Stefan Zeiske, Wei Li, Drew B Riley, Paul Meredith, and Ardalan Armin. Charge-generating mid-gap trap states define the thermodynamic limit of organic photovoltaic devices. Nature communications, 11(1):1–10, 2020.

[108] Samantha N Hood and Ivan Kassal. Entropy and disorder enable charge separation in organic solar cells. The journal of physical chemistry letters, 7(22):4495–4500, 2016.

[109] Safa Shoaee, Ardalan Armin, Martin Stolterfoht, Seyed Mehrdad Hosseini, Jona Kurpiers, and Dieter Neher. Decoding charge recombination through charge generation in organic solar cells. Solar RRL, 3(11):1900184, 2019.

[110] Julien Gorenflot, Michael C Heiber, Andreas Baumann, Jens Lorrmann, Matthias Gunz, Andreas Kämpgen, Vladimir Dyakonov, and Carsten Deibel. Nongeminate recombination in neat p3ht and p3ht: Pcbm blend films. Journal of Applied Physics, 115(14):144502, 2014.

[111] LJA Koster, VD Mihailetchi, and PWM Blom. Bimolecular recombination in polymer/fullerene bulk heterojunction solar cells. Applied physics letters, 88(5):052104, 2006.

[112] Michael C Heiber, Christoph Baumbach, Vladimir Dyakonov, and Carsten Deibel. Encounter-limited charge-carrier recombination in phase-separated organic semiconductor blends. Physical review letters, 114(13):136602, 2015.

[113] Rudolph A Marcus. On the theory of oxidation-reduction reactions involving electron transfer. i. The Journal of chemical physics, 24(5):966–978, 1956.

[114] Noel Sydney Hush. Adiabatic theory of outer sphere electron-transfer reactions in solution. Transactions of the Faraday Society, 57:557–580, 1961.

[115] Rudolph A Marcus. Electron transfer reactions in chemistry. theory and experiment. In Protein electron transfer, pages 249–272. Garland Science, 2020.

[116] Wei-Qiao Deng and William A Goddard. Predictions of hole mobilities in oligoacene organic semiconductors from quantum mechanical calculations. The Journal of Physical Chemistry B, 108(25):8614–8621, 2004.

[117] HuiXue Li, XiaoFeng Wang, and ZhiFeng Li. Theoretical study of the effects of different substituents of tetrathiafulvalene derivatives on charge transport. Chinese Science Bulletin, 57(31):4049–4056, 2012.

[118] Robin GE Kimber, Edward N Wright, Simon EJ O'Kane, Alison B Walker, and James C Blakesley. Mesoscopic kinetic monte carlo modeling of organic photovoltaic device characteristics. Physical Review B, 86(23):235206, 2012.

[119] Heinz Bässler. Charge transport in disordered organic photoconductors. a monte carlo simulation study. Physica Status Solidi B (Basic Research);(Germany), 175(1), 1993.

[120] WF Pasveer, Jeroen Cottaar, C Tanase, Reinder Coehoorn, PA Bobbert, PWM Blom, DM De Leeuw, and MAJ Michels. Unified description of charge-carrier mobilities in disordered semiconducting polymers. Physical review letters, 94(20):206601, 2005.

[121] Reinder Coehoorn, WF Pasveer, PA Bobbert, and MAJ Michels. Charge-carrier concentration dependence of the hopping mobility in organic materials with gaussian disorder. Physical Review B, 72(15):155206, 2005.

[122] Heinz Bässler and Anna Köhler. Charge transport in organic semiconductors. Unimolecular and supramolecular electronics I, pages 1–65, 2011.

[123] Reinder Coehoorn and Peter A Bobbert. Effects of gaussian disorder on charge carrier transport and recombination in organic semiconductors. physica status solidi (a), 209(12):2354–2377, 2012.

[124] Hong Ma, Hin-Lap Yip, Fei Huang, and Alex K-Y Jen. Interface engineering for organic electronics. Advanced Functional Materials, 20(9):1371–1388, 2010.

[125] Peicheng Li and Zheng-Hong Lu. Interface engineering in organic electronics: Energy-level alignment and charge transport. Small Science, 1(1):2000015, 2021.

[126] Li Tian, Qifan Xue, Zhicheng Hu, and Fei Huang. Recent advances of interface engineering for non-fullerene organic solar cells. Organic Electronics, 93:106141, 2021.

[127] Conyers Herring and MH Nichols. Thermionic emission. Reviews of modern physics, 21(2):185, 1949.

[128] Alexander Wagenpfahl, Carsten Deibel, and Vladimir Dyakonov. Organic solar cell efficiencies under the aspect of reduced surface recombination velocities. IEEE Journal of Selected Topics in Quantum Electronics, 16(6):1759–1763, 2010.

[129] Kristina M Knesting, Huanxin Ju, Cody W Schlenker, Anthony J Giordano, Andres Garcia, O'Neil L Smith, Dana C Olson, Seth R Marder, and David S Ginger. Ito interface modifiers can improve v oc in polymer solar cells and suppress surface recombination. The Journal of Physical Chemistry Letters, 4(23):4038–4044, 2013.

[130] Thomas Kirchartz, Florent Deledalle, Pabitra Shakya Tuladhar, James R Durrant, and Jenny Nelson. On the differences between dark and light ideality factor in polymer: fullerene solar cells. The Journal of Physical Chemistry Letters, 4(14):2371–2376, 2013.

[131] Jens Reinhardt, Maria Grein, Christian Bühler, Martin Schubert, and Uli Würfel. Identifying the impact of surface recombination at electrodes in

organic solar cells by means of electroluminescence and modeling. Advanced Energy Materials, 4(11):1400081, 2014.

[132] S Boukli Hacène and T Benouaz. Influence of charge carrier mobility and surface recombination velocity on the characteristics of p3ht: Pcbm organic solar cells. Physica Status Solidi (a), 211(4):862–868, 2014.

[133] Scot Wheeler, Florent Deledalle, Nurlan Tokmoldin, Thomas Kirchartz, Jenny Nelson, and James R Durrant. Influence of surface recombination on charge-carrier kinetics in organic bulk heterojunction solar cells with nickel oxide interlayers. Physical Review Applied, 4(2):024020, 2015.

[134] Irene Zonno, Benedikt Krogmeier, Verena Katte, Dana Lübke, Alberto Martinez-Otero, and Thomas Kirchartz. Discriminating between surface and bulk recombination in organic solar cells by studying the thickness dependence of the open-circuit voltage. Applied Physics Letters, 109(18):183301, 2016.

[135] Oskar J Sandberg and Ardalan Armin. On the effect of surface recombination in thin film solar cells, light emitting diodes and photodetectors. Synthetic Metals, 254:114–121, 2019.

[136] Akchheta Karki, Joachim Vollbrecht, Alexander J Gillett, Steven Shuyong Xiao, Yali Yang, Zhengxing Peng, Nora Schopp, Alana L Dixon, Sangcheol Yoon, Max Schrock, et al. The role of bulk and interfacial morphology in charge generation, recombination, and extraction in non-fullerene acceptor organic solar cells. Energy & Environmental Science, 13(10):3679–3692, 2020.

[137] Noel C Giebink, Gary P Wiederrecht, Michael R Wasielewski, and Stephen R Forrest. Thermodynamic efficiency limit of excitonic solar cells. Physical Review B, 83(19):195326, 2011.

[138] A Luque, A Martí, and L Cuadra. Thermodynamics of solar energy conversion in novel structures. Physica E: Low-dimensional Systems and Nanostructures, 14(1-2):107–114, 2002.

[139] IG Hill, A Kahn, ZG Soos, and RA Pascal Jr. Charge-separation energy in films of π-conjugated organic molecules. Chemical Physics Letters, 327(3-4):181–188, 2000.

[140] Andrej Classen, Christos L Chochos, Larry Lüer, Vasilis G Gregoriou, Jonas Wortmann, Andres Osvet, Karen Forberich, Iain McCulloch, Thomas Heumüller, and Christoph J Brabec. The role of exciton lifetime for charge

generation in organic solar cells at negligible energy-level offsets. Nature Energy, 5(9):711–719, 2020.

[141] Ture F Hinrichsen, Christopher CS Chan, Chao Ma, David Paleček, Alexander Gillett, Shangshang Chen, Xinhui Zou, Guichuan Zhang, Hin-Lap Yip, Kam Sing Wong, et al. Long-lived and disorder-free charge transfer states enable endothermic charge separation in efficient non-fullerene organic solar cells. Nature communications, 11(1):1–10, 2020.

[142] Jenny E Donaghey, Ardalan Armin, Paul L Burn, and Paul Meredith. Dielectric constant enhancement of non-fullerene acceptors via side-chain modification. Chemical Communications, 51(74):14115–14118, 2015.

[143] JPA Souza, L Benatto, G Candiotto, LS Roman, and M Koehler. Binding energy of triplet excitons in nonfullerene acceptors: The effects of fluorination and chlorination. The Journal of Physical Chemistry A, 126(8):1393–1402, 2022.

[144] Yufan Zhu, Fuwen Zhao, Wei Wang, Yawen Li, Shiming Zhang, and Yuze Lin. Exciton binding energy of non-fullerene electron acceptors. Advanced Energy and Sustainability Research, 3(4):2100184, 2022.

[145] Martin A Green. Accuracy of analytical expressions for solar cell fill factors. Solar cells, 7(3):337–340, 1982.

[146] Dieter Neher, Juliane Kniepert, Arik Elimelech, and L Koster. A new figure of merit for organic solar cells with transport-limited photocurrents. Scientific reports, 6(1):1–9, 2016.

[147] Zuo Xiao, Xue Jia, Dan Li, Shizhe Wang, Xinjian Geng, Feng Liu, Junwu Chen, Shangfeng Yang, Thomas P Russell, and Liming Ding. 26 mA/cm^2 Jsc from organic solar cells with a low-bandgap nonfullerene acceptor. Sci. Bull., 62(22):1494–1496, 2017.

[148] Xiaosha Wang, Honggang Chen, Jun Yuan, Qingya Wei, Jing Li, Lihui Jiang, Jun Huang, Yongfang Li, Yungui Li, and Yingping Zou. Precise fluorination of polymeric donors towards efficient non-fullerene organic solar cells with enhanced open circuit voltage, short circuit current and fill factor. J. Mater. Chem. A, 9(26):14752–14757, 2021.

[149] Wei Li, Stefan Zeiske, Oskar J Sandberg, Drew B Riley, Paul Meredith, and Ardalan Armin. Organic solar cells with near-unity charge generation yield. Energy & Environmental Science, 14(12):6484–6493, 2021.

[150] Flurin D Eisner, Mohammed Azzouzi, Zhuping Fei, Xueyan Hou, Thomas D Anthopoulos, T John S Dennis, Martin Heeney, and Jenny Nelson. Hybridization of local exciton and charge-transfer states reduces nonradiative voltage losses in organic solar cells. Journal of the American Chemical Society, 141(15):6362–6374, 2019.

[151] Dani M Stoltzfus, Jenny E Donaghey, Ardalan Armin, Paul E Shaw, Paul L Burn, and Paul Meredith. Charge generation pathways in organic solar cells: assessing the contribution from the electron acceptor. Chem. Rev., 116(21):12920–12955, 2016.

[152] Carsten Deibel and Vladimir Dyakonov. Polymer–fullerene bulk heterojunction solar cells. Rep. Prog. Phys., 73(9):096401, 2010.

[153] Qingxin Guo, Yahui Liu, Ming Liu, Hao Zhang, Xiquan Qian, Jinjin Yang, Jing Wang, Wenyue Xue, Qian Zhao, Xinjun Xu, et al. Enhancing the performance of organic solar cells by prolonging the lifetime of photogenerated excitons. Advanced Materials, 32(50):2003164, 2020.

[154] Christian G Bottenfield, Fanan Wei, Hui Joon Park, L Jay Guo, and Guangyong Li. Investigation of printing-based graded bulk-heterojunction organic solar cells. Energy Technology, 3(4):414–422, 2015.

[155] Peter K Watkins, Alison B Walker, and Geraldine LB Verschoor. Dynamical monte carlo modelling of organic solar cells: The dependence of internal quantum efficiency on morphology. Nano letters, 5(9):1814–1818, 2005.

[156] Nasim Zarrabi, Aren Yazmaciyan, Paul Meredith, Ivan Kassal, and Ardalan Armin. Anomalous exciton quenching in organic semiconductors in the low-yield limit. The journal of physical chemistry letters, 9(20):6144–6148, 2018.

[157] Waldemar Kaiser, Johannes Popp, Michael Rinderle, Tim Albes, and Alessio Gagliardi. Generalized kinetic Monte–Carlo framework for organic electronics. Algorithms, 11(4):37, 2018.

[158] Sylvia J Lou, Jodi M Szarko, Tao Xu, Luping Yu, Tobin J Marks, and Lin X Chen. Effects of additives on the morphology of solution phase aggregates formed by active layer components of high-efficiency organic solar cells. Journal of the American Chemical Society, 133(51):20661–20663, 2011.

[159] Upendra Neupane, Behzad Bahrami, Matt Biesecker, Mahdi Farrokh Baroughi, and Qiquan Qiao. Kinetic monte carlo modeling on organic solar cells: Domain size, donor-acceptor ratio and thickness. Nano energy, 35:128–137, 2017.

[160] Hyojung Cha, Scot Wheeler, Sarah Holliday, Stoichko D Dimitrov, Andrew Wadsworth, Hyun Hwi Lee, Derya Baran, Iain McCulloch, and James R Durrant. Influence of blend morphology and energetics on charge separation and recombination dynamics in organic solar cells incorporating a non-fullerene acceptor. Advanced Functional Materials, 28(3):1704389, 2018.

[161] Sreelakshmi Chandrabose, Kai Chen, Alex J Barker, Joshua J Sutton, Shyamal KK Prasad, Jingshuai Zhu, Jiadong Zhou, Keith C Gordon, Zengqi Xie, Xiaowei Zhan, et al. High exciton diffusion coefficients in fused ring electron acceptor films. Journal of the American Chemical Society, 141(17):6922–6929, 2019.

[162] Yuliar Firdaus, Vincent M Le Corre, Safakath Karuthedath, Wenlan Liu, Anastasia Markina, Wentao Huang, Shirsopratim Chattopadhyay, Masrur Morshed Nahid, Mohamad I Nugraha, Yuanbao Lin, et al. Long-range exciton diffusion in molecular non-fullerene acceptors. Nature communications, 11(1):1–10, 2020.

[163] Alexander J Ward, Arvydas Ruseckas, and Ifor DW Samuel. A shift from diffusion assisted to energy transfer controlled fluorescence quenching in polymer–fullerene photovoltaic blends. J. Phys. Chem. C, 116(45):23931–23937, 2012.

[164] Oleksandr V Mikhnenko, Hamed Azimi, Markus Scharber, Mauro Morana, Paul WM Blom, and Maria Antonietta Loi. Exciton diffusion length in narrow bandgap polymers. Energy Environ. Sci., 5(5):6960–6965, 2012.

[165] Hai Wang, Hai-Yu Wang, Bing-Rong Gao, Lei Wang, Zhi-Yong Yang, Xiao-Bo Du, Qi-Dai Chen, Jun-Feng Song, and Hong-Bo Sun. Exciton diffusion and charge transfer dynamics in nano phase-separated P3HT/PCBM blend films. Nanoscale, 3(5):2280–2285, 2011.

[166] M Theander, Arkady Yartsev, Donatas Zigmantas, Villy Sundström, W Mammo, M. R. Andersson, and Olle Inganäs. Photoluminescence quenching at a polythiophene/C_{60} heterojunction. Phys. Rev. B, 61(19):12957, 2000.

[167] Wade A Luhman and Russell J Holmes. Investigation of energy transfer in organic photovoltaic cells and impact on exciton diffusion length measurements. Adv. Funct. Mater., 21(4):764–771, 2011.

[168] OV Mikhnenko, F Cordella, AB Sieval, JC Hummelen, PWM Blom, and MA Loi. Temperature dependence of exciton diffusion in conjugated polymers. J. Phys. Chem. B, 112(37):11601–11604, 2008.

[169] A Haugeneder, M Neges, C Kallinger, W Spirkl, U Lemmer, J Feldmann, Ullrich Scherf, E Harth, A Gügel, and Klaus Müllen. Exciton diffusion and dissociation in conjugated polymer/fullerene blends and heterostructures. Phys. Rev. B, 59(23):15346, 1999.

[170] Oleksandr V Mikhnenko, Fabrizio Cordella, Alexander B Sieval, Jan C Hummelen, Paul WM Blom, and Maria Antonietta Loi. Exciton quenching close to polymer- vacuum interface of spin-coated films of poly (p-phenylenevinylene) derivative. J. Phys. Chem. B, 113(27):9104–9109, 2009.

[171] Shawn R Scully and Michael D McGehee. Effects of optical interference and energy transfer on exciton diffusion length measurements in organic semiconductors. J. App. Phys., 100(3):034907, 2006.

[172] Denis E Markov, Emiel Amsterdam, Paul WM Blom, Alexander B Sieval, and Jan C Hummelen. Accurate measurement of the exciton diffusion length in a conjugated polymer using a heterostructure with a side-chain cross-linked fullerene layer. J. Phys. Chem. A, 109(24):5266–5274, 2005.

[173] Paul E Shaw, Arvydas Ruseckas, and Ifor DW Samuel. Exciton diffusion measurements in poly (3-hexylthiophene). Adv. Mater., 20(18):3516–3520, 2008.

[174] AJ Lewis, A Ruseckas, OPM Gaudin, GR Webster, PL Burn, and IDW Samuel. Singlet exciton diffusion in MEH-PPV films studied by exciton–exciton annihilation. Org. Electron., 7(6):452–456, 2006.

[175] E Engel, K Leo, and M Hoffmann. Ultrafast relaxation and exciton–exciton annihilation in PTCDA thin films at high excitation densities. Chem. Phys., 325(1):170–177, 2006.

[176] Steffan Cook, Akihiro Furube, Ryuzi Katoh, and Liyuan Han. Estimate of singlet diffusion lengths in PCBM films by time-resolved emission studies. Chem. Phys. Lett., 478(1-3):33–36, 2009.

[177] Steffan Cook, Han Liyuan, Akihiro Furube, and Ryuzi Katoh. Singlet annihilation in films of regioregular poly (3-hexylthiophene): Estimates for singlet diffusion lengths and the correlation between singlet annihilation rates and spectral relaxation. J. Phys. Chem. C, 114(24):10962–10968, 2010.

[178] Yun Long, Gordon J Hedley, Arvydas Ruseckas, Mithun Chowdhury, Thomas Roland, Luis A Serrano, Graeme Cooke, and Ifor DW Samuel. Effect of annealing on exciton diffusion in a high performance small molecule

organic photovoltaic material. ACS Appl. Mater. Inter., 9(17):14945–14952, 2017.

[179] Yiwei Zhang, Muhammad T Sajjad, Oskar Blaszczyk, Andrew J Parnell, Arvydas Ruseckas, Luis A Serrano, Graeme Cooke, and Ifor DW Samuel. Large crystalline domains and an enhanced exciton diffusion length enable efficient organic solar cells. Chem. Mater., 31(17):6548–6557, 2019.

[180] Muhammad Tariq Sajjad, Arvydas Ruseckas, Lethy Krishnan Jagadamma, Yiwei Zhang, and Ifor DW Samuel. Long-range exciton diffusion in non-fullerene acceptors and coarse bulk heterojunctions enable highly efficient organic photovoltaics. J. Mater. Chem. A, 8(31):15687–15694, 2020.

[181] Song Yi Park, Sreelakshmi Chandrabose, Michael B Price, Hwa Sook Ryu, Tack Ho Lee, Yun Seop Shin, Ziang Wu, Woojin Lee, Kai Chen, Shuixing Dai, et al. Photophysical pathways in efficient bilayer organic solar cells: The importance of interlayer energy transfer. Nano Energy, 84:105924, 2021.

[182] Oleksandr V Mikhnenko, Paul WM Blom, and Thuc-Quyen Nguyen. Exciton diffusion in organic semiconductors. Energy & Environmental Science, 8(7):1867–1888, 2015.

[183] Subrahmanyan Chandrasekhar. Stochastic problems in physics and astronomy. Rev. Mod. Phys., 15(1):1, 1943.

[184] Nardeep Kumar, Qiannan Cui, Frank Ceballos, Dawei He, Yongsheng Wang, and Hui Zhao. Exciton-exciton annihilation in MoSe 2 monolayers. Phys. Rev. B, 89(12):125427, 2014.

[185] Eric Linardy, Dinesh Yadav, Daniele Vella, Ivan A Verzhbitskiy, Kenji Watanabe, Takashi Taniguchi, Fabian Pauly, Maxim Trushin, and Goki Eda. Harnessing exciton–exciton annihilation in two-dimensional semiconductors. Nano Lett., 20(3):1647–1653, 2020.

[186] Jun Yuan, Yunqiang Zhang, Liuyang Zhou, Guichuan Zhang, Hin-Lap Yip, Tsz-Ki Lau, Xinhui Lu, Can Zhu, Hongjian Peng, Paul A Johnson, Mario Leclerc, Yong Cao, Jacek Ulanski, Yongfang Li, and Yingping Zou. Single-junction organic solar cell with over 15% efficiency using fused-ring acceptor with electron-deficient core. Joule, 3(4):1140–1151, 2019.

[187] Kedar D Deshmukh, Rukiya Matsidik, Shyamal KK Prasad, Naresh Chandrasekaran, Adam Welford, Luke A Connal, Amelia CY Liu, Eliot Gann, Lars Thomsen, Dinesh Kabra, et al. Impact of acceptor fluorination on the

performance of all-polymer solar cells. ACS Appl. Mater. Inter., 10(1):955–969, 2018.

[188] Michael Wong-Stringer, James E Bishop, Joel A Smith, David K Mohamad, Andrew J Parnell, Vikas Kumar, Cornelia Rodenburg, and David G Lidzey. Efficient perovskite photovoltaic devices using chemically doped PCDTBT as a hole-transport material. J. Mater. Chem. A, 5(30):15714–15723, 2017.

[189] Ping-Hsun Chu, Gang Wang, Boyi Fu, Dalsu Choi, Jung Ok Park, Mohan Srinivasarao, and Elsa Reichmanis. Synergistic effect of regioregular and regiorandom poly (3-hexylthiophene) blends for high performance flexible organic field effect transistors. Adv. Electron. Mater., 2(2):1500384, 2016.

[190] Jiangquan Mai, Yiqun Xiao, Guodong Zhou, Jiayu Wang, Jingshuai Zhu, Ni Zhao, Xiaowei Zhan, and Xinhui Lu. Hidden structure ordering along backbone of fused-ring electron acceptors enhanced by ternary bulk heterojunction. Adv. Mater., 30(34):1802888, 2018.

[191] Ruijie Ma, Yuzhong Chen, Tao Liu, Yiqun Xiao, Zhenghui Luo, Maojie Zhang, Siwei Luo, Xinhui Lu, Guangye Zhang, Yongfang Li, et al. Improving the performance of near infrared binary polymer solar cells by adding a second non-fullerene intermediate band-gap acceptor. J. Mater. Chem. C, 8(3):909–915, 2020.

[192] Yong Cui, Huifeng Yao, Jianqi Zhang, Kaihu Xian, Tao Zhang, Ling Hong, Yuming Wang, Ye Xu, Kangqiao Ma, Cunbin An, et al. Single-junction organic photovoltaic cells with approaching 18% efficiency. Adv. Mater., 32(19):1908205, 2020.

[193] Yanbo Wang, Yamin Zhang, Nailiang Qiu, Huanran Feng, Huanhuan Gao, Bin Kan, Yanfeng Ma, Chenxi Li, Xiangjian Wan, and Yongsheng Chen. A halogenation strategy for over 12% efficiency nonfullerene organic solar cells. Advanced Energy Materials, 8(15):1702870, 2018.

[194] Fuwen Zhao, Huotian Zhang, Rui Zhang, Jun Yuan, Dan He, Yingping Zou, and Feng Gao. Emerging approaches in enhancing the efficiency and stability in non-fullerene organic solar cells. Advanced Energy Materials, 10(47):2002746, 2020.

[195] Oh Kyu Kwon, Mohammad Afsar Uddin, Jung-Hwa Park, Sang Kyu Park, Thanh Luan Nguyen, Han Young Woo, and Soo Young Park. A high efficiency nonfullerene organic solar cell with optimized crystalline organizations. Advanced materials, 28(5):910–916, 2016.

[196] Huifeng Yao, Long Ye, Junxian Hou, Bomee Jang, Guangchao Han, Yong Cui, Gregory M Su, Cheng Wang, Bowei Gao, Runnan Yu, et al. Achieving highly efficient nonfullerene organic solar cells with improved intermolecular interaction and open-circuit voltage. Advanced materials, 29(21):1700254, 2017.

[197] Yunsen Zhao, Zinan Wu, Xin Liu, Ziping Zhong, Rihong Zhu, and Jiangsheng Yu. Revealing the photo-degradation mechanism of pm6: Y6 based high-efficiency organic solar cells. Journal of Materials Chemistry C, 9(39):13972–13980, 2021.

[198] Zhengke Li, Kui Jiang, Guofang Yang, Joshua Yuk Lin Lai, Tingxuan Ma, Jingbo Zhao, Wei Ma, and He Yan. Donor polymer design enables efficient non-fullerene organic solar cells. Nature communications, 7(1):1–9, 2016.

[199] Jingyang Xiao, Minrun Ren, Guichuan Zhang, Jianbin Wang, Donglian Zhang, Linlin Liu, Ning Li, Christoph J Brabec, Hin-Lap Yip, and Yong Cao. An operando study on the photostability of nonfullerene organic solar cells. Solar Rrl, 3(7):1900077, 2019.

[200] Long Ye, Wenchao Zhao, Sunsun Li, Subhrangsu Mukherjee, Joshua H Carpenter, Omar Awartani, Xuechen Jiao, Jianhui Hou, and Harald Ade. High-efficiency nonfullerene organic solar cells: critical factors that affect complex multi-length scale morphology and device performance. Advanced Energy Materials, 7(7):1602000, 2017.

[201] Xueping Yi, Zhengxing Peng, Bing Xu, Dovletgeldi Seyitliyev, Carr Hoi Yi Ho, Evgeny O Danilov, Taesoo Kim, John R Reynolds, Aram Amassian, Kenan Gundogdu, et al. Critical role of polymer aggregation and miscibility in nonfullerene-based organic photovoltaics. Advanced Energy Materials, 10(8):1902430, 2020.

[202] Guoping Li, Liang-Wen Feng, Subhrangsu Mukherjee, Leighton O Jones, Robert M Jacobberger, Wei Huang, Ryan M Young, Robert M Pankow, Weigang Zhu, Norman Lu, et al. Non-fullerene acceptors with direct and indirect hexa-fluorination afford¿ 17% efficiency in polymer solar cells. Energy & Environmental Science, 15(2):645–659, 2022.

[203] Joshua H Carpenter, Adrian Hunt, and Harald Ade. Characterizing morphology in organic systems with resonant soft x-ray scattering. Journal of Electron Spectroscopy and Related Phenomena, 200:2–14, 2015.

[204] Tao Liu, Zhenghui Luo, Qunping Fan, Guangye Zhang, Lin Zhang, Wei Gao, Xia Guo, Wei Ma, Maojie Zhang, Chuluo Yang, et al. Use of two

structurally similar small molecular acceptors enabling ternary organic solar cells with high efficiencies and fill factors. Energy & Environmental Science, 11(11):3275–3282, 2018.

[205] Qi Liu, Jin Fang, Jingnan Wu, Lei Zhu, Xia Guo, Feng Liu, and Maojie Zhang. Tuning aggregation behavior of polymer donor via molecular-weight control for achieving 17.1% efficiency inverted polymer solar cells. Chinese Journal of Chemistry, 39(7):1941–1947, 2021.

[206] Yanan Shi, Yilin Chang, Kun Lu, Zhihao Chen, Jianqi Zhang, Yangjun Yan, Dingding Qiu, Yanan Liu, Muhammad Abdullah Adil, Wei Ma, et al. Small reorganization energy acceptors enable low energy losses in non-fullerene organic solar cells. Nature Communications, 13(1):1–10, 2022.

[207] Brian A Collins and Eliot Gann. Resonant soft x-ray scattering in polymer science. Journal of Polymer Science, 60(7):1199–1243, 2022.

[208] Jonghyeon Noh, Seonju Jeong, and Jung-Yong Lee. Ultrafast formation of air-processable and high-quality polymer films on an aqueous substrate. Nature communications, 7(1):1–9, 2016.

[209] Fallon JM Colberts, Martijn M Wienk, Ruurd Heuvel, Weiwei Li, Vincent M Le Corre, L Jan Anton Koster, and René AJ Janssen. Bilayer–ternary polymer solar cells fabricated using spontaneous spreading on water. Advanced Energy Materials, 8(32):1802197, 2018.

[210] Tack Ho Lee, Won-Woo Park, Song Yi Park, Shinuk Cho, Oh-Hoon Kwon, and Jin Young Kim. Planar organic bilayer heterojunctions fabricated on water with ultrafast donor-to-acceptor charge transfer. Solar RRL, 5(8):2100326, 2021.

[211] DE Markov, C Tanase, PWM Blom, and J Wildeman. Simultaneous enhancement of charge transport and exciton diffusion in poly (p-phenylene vinylene) derivatives. Physical Review B, 72(4):045217, 2005.

[212] Muhammad T Sajjad, Yiwei Zhang, Paul B Geraghty, Valerie D Mitchell, Arvydas Ruseckas, Oskar Blaszczyk, David J Jones, and Ifor DW Samuel. Tailoring exciton diffusion and domain size in photovoltaic small molecules by annealing. Journal of Materials Chemistry C, 7(26):7922–7928, 2019.

[213] Kyra N Schwarz, Paul B Geraghty, Valerie D Mitchell, Saeed-Uz-Zaman Khan, Oskar J Sandberg, Nasim Zarrabi, Bryan Kudisch, Jegadesan Subbiah, Trevor A Smith, Barry P Rand, et al. Reduced recombination and

capacitor-like charge buildup in an organic heterojunction. Journal of the American Chemical Society, 142(5):2562–2571, 2020.

[214] Yong Cui, Huifeng Yao, Jianqi Zhang, Tao Zhang, Yuming Wang, Ling Hong, Kaihu Xian, Bowei Xu, Shaoqing Zhang, Jing Peng, et al. Over 16% efficiency organic photovoltaic cells enabled by a chlorinated acceptor with increased open-circuit voltages. Nature communications, 10(1):1–8, 2019.

[215] Qishi Liu, Yufan Jiang, Ke Jin, Jianqiang Qin, Jingui Xu, Wenting Li, Ji Xiong, Jinfeng Liu, Zuo Xiao, Kuan Sun, et al. 18% efficiency organic solar cells. Science Bulletin, 65(4):272–275, 2020.

[216] Koen Vandewal, Abay Gadisa, Wibren D Oosterbaan, Sabine Bertho, Fateme Banishoeib, Ineke Van Severen, Laurence Lutsen, Thomas J Cleij, Dirk Vanderzande, and Jean V Manca. The relation between open-circuit voltage and the onset of photocurrent generation by charge-transfer absorption in polymer: fullerene bulk heterojunction solar cells. Advanced Functional Materials, 18(14):2064–2070, 2008.

[217] Koen Vandewal, Kristofer Tvingstedt, Abay Gadisa, Olle Inganäs, and Jean V Manca. On the origin of the open-circuit voltage of polymer–fullerene solar cells. Nature materials, 8(11):904–909, 2009.

[218] Koen Vandewal, Kristofer Tvingstedt, Abay Gadisa, Olle Inganäs, and Jean V Manca. Relating the open-circuit voltage to interface molecular properties of donor: acceptor bulk heterojunction solar cells. Physical Review B, 81(12):125204, 2010.

[219] Koen Vandewal, Zaifei Ma, Jonas Bergqvist, Zheng Tang, Ergang Wang, Patrik Henriksson, Kristofer Tvingstedt, Mats R Andersson, Fengling Zhang, and Olle Inganäs. Quantification of quantum efficiency and energy losses in low bandgap polymer: Fullerene solar cells with high open-circuit voltage. Advanced Functional Materials, 22(16):3480–3490, 2012.

[220] Naveen Kumar Elumalai and Ashraf Uddin. Open circuit voltage of organic solar cells: an in-depth review. Energy & Environmental Science, 9(2):391–410, 2016.

[221] Derya Baran, Thomas Kirchartz, Scot Wheeler, Stoichko Dimitrov, Maged Abdelsamie, Jeffrey Gorman, Raja Shahid Ashraf, Sarah Holliday, Andrew Wadsworth, Nicola Gasparini, et al. Reduced voltage losses yield 10% efficient fullerene free organic solar cells with¿ 1 v open circuit voltages. Energy & Environmental Science, 9(12):3783–3793, 2016.

[222] Markus C Scharber, David Mühlbacher, Markus Koppe, Patrick Denk, Christoph Waldauf, Alan J Heeger, and Christoph J Brabec. Design rules for donors in bulk-heterojunction solar cells—towards 10% energy-conversion efficiency. Advanced Materials, 18(6):789–794, 2006.

[223] VD Mihailetchi, PWM Blom, JC Hummelen, and MT Rispens. Cathode dependence of the open-circuit voltage of polymer: fullerene bulk heterojunction solar cells. Journal of Applied Physics, 94(10):6849–6854, 2003.

[224] Ian L Braly, Dane W deQuilettes, Luis M Pazos-Outón, Sven Burke, Mark E Ziffer, David S Ginger, and Hugh W Hillhouse. Hybrid perovskite films approaching the radiative limit with over 90% photoluminescence quantum efficiency. Nature Photonics, 12(6):355–361, 2018.

[225] Martin Stolterfoht, Pietro Caprioglio, Christian M Wolff, José A Márquez, Joleik Nordmann, Shanshan Zhang, Daniel Rothhardt, Ulrich Hörmann, Yohai Amir, Alex Redinger, et al. The impact of energy alignment and interfacial recombination on the internal and external open-circuit voltage of perovskite solar cells. Energy & Environmental Science, 12(9):2778–2788, 2019.

[226] Yong Cao, Ian D Parker, Gang Yu, Chi Zhang, and Alan J Heeger. Improved quantum efficiency for electroluminescence in semiconducting polymers. Nature, 397(6718):414–417, 1999.

[227] Ullrich Mitschke and Peter Bäuerle. The electroluminescence of organic materials. Journal of Materials Chemistry, 10(7):1471–1507, 2000.

[228] Andrew C Grimsdale, Khai Leok Chan, Rainer E Martin, Pawel G Jokisz, and Andrew B Holmes. Synthesis of light-emitting conjugated polymers for applications in electroluminescent devices. Chemical Reviews, 109(3):897–1091, 2009.

[229] Martin A Green, Jianhua Zhao, Aihua Wang, Peter J Reece, and Michael Gal. Efficient silicon light-emitting diodes. Nature, 412(6849):805–808, 2001.

[230] Thomas Kirchartz and Uwe Rau. Electroluminescence analysis of high efficiency cu (in, ga) se 2 solar cells. Journal of Applied Physics, 102(10):104510, 2007.

[231] Thomas Kirchartz, Uwe Rau, Martin Hermle, Andreas W Bett, Anke Helbig, and Jürgen H Werner. Internal voltages in ga in p/ ga in as/ ge

multijunction solar cells determined by electroluminescence measurements. Applied Physics Letters, 92(12):123502, 2008.

[232] Oskar J Sandberg, Anton Sundqvist, Mathias Nyman, and Ronald Österbacka. Relating charge transport, contact properties, and recombination to open-circuit voltage in sandwich-type thin-film solar cells. Physical Review Applied, 5(4):044005, 2016.

[233] Annika Spies, Mathias List, Tanmoy Sarkar, and Uli Würfel. On the impact of contact selectivity and charge transport on the open-circuit voltage of organic solar cells. Advanced Energy Materials, 7(5):1601750, 2017.

[234] Le Quang Phuong, Seyed Mehrdad Hosseini, Oskar J Sandberg, Yingping Zou, Han Young Woo, Dieter Neher, and Safa Shoaee. Quantifying quasi-fermi level splitting and open-circuit voltage losses in highly efficient non-fullerene organic solar cells. Solar RRL, page 2000649, 2020.

[235] Wolfgang Tress. Organic solar cells. In Organic Solar Cells, pages 67–214. Springer, 2014.

[236] Oskar J Sandberg, Mathias Nyman, and Ronald Österbacka. Effect of contacts in organic bulk heterojunction solar cells. Physical Review Applied, 1(2):024003, 2014.

[237] Sherali Zeadally, Faisal Karim Shaikh, Anum Talpur, and Quan Z Sheng. Design architectures for energy harvesting in the internet of things. Renewable and Sustainable Energy Reviews, 128:109901, 2020.

[238] Rakeshkumar Mahto, Deepak Sharma, Reshma John, and Chandrasekhar Putcha. Agrivoltaics: A climate-smart agriculture approach for indian farmers. Land, 10(11):1277, 2021.

[239] Eshwar Ravishankar, Melodi Charles, Yuan Xiong, Reece Henry, Jennifer Swift, Jeromy Rech, John Calero, Sam Cho, Ronald E Booth, Taesoo Kim, et al. Balancing crop production and energy harvesting in organic solar-powered greenhouses. Cell Reports Physical Science, 2(3):100381, 2021.

[240] Ashu K Bansal, Shuoben Hou, Olena Kulyk, Eric M Bowman, and Ifor DW Samuel. Wearable organic optoelectronic sensors for medicine. Advanced Materials, 27(46):7638–7644, 2015.

[241] Kazunori Kuribara, He Wang, Naoya Uchiyama, Kenjiro Fukuda, Tomoyuki Yokota, Ute Zschieschang, Cherno Jaye, Daniel Fischer, Hagen Klauk, Tatsuya Yamamoto, et al. Organic transistors with high thermal stability for medical applications. Nature communications, 3(1):1–7, 2012.

[242] Quinn Burlingame, Melissa Ball, and Yueh-Lin Loo. It's time to focus on organic solar cell stability. Nature Energy, 5(12):947–949, 2020.

[243] Hao Ren, Jing-De Chen, Yan-Qing Li, and Jian-Xin Tang. Recent progress in organic photodetectors and their applications. Advanced Science, 8(1):2002418, 2021.

[244] Aren Yazmaciyan, Paul Meredith, and Ardalan Armin. Cavity enhanced organic photodiodes with charge collection narrowing. Advanced Optical Materials, 7(8):1801543, 2019.

[245] Boming Xie, Ruihao Xie, Kai Zhang, Qingwu Yin, Zhicheng Hu, Gang Yu, Fei Huang, and Yong Cao. Self-filtering narrowband high performance organic photodetectors enabled by manipulating localized frenkel exciton dissociation. Nature communications, 11(1):1–9, 2020.

[246] Heinz Gerischer and Adam Heller. The role of oxygen in photooxidation of organic molecules on semiconductor particles. J. Phys. Chem., 95(13):5261–5267, 1991.

[247] A Yoshida and T Asakura. A simple technique for quickly measuring the spot size of gaussian laser beams. Opt. Laser Technol., 8(6):273–274, 1976.

[248] Paul B Geraghty, Calvin Lee, Jegadesan Subbiah, Wallace WH Wong, James L Banal, Mohammed A Jameel, Trevor A Smith, and David J Jones. High performance p-type molecular electron donors for opv applications via alkylthiophene catenation chromophore extension. Beilstein journal of organic chemistry, 12(1):2298–2314, 2016.

[249] Heinz Bässler. Charge transport in disordered organic photoconductors. a monte carlo simulation study. Physica Status Solidi B (Basic Research);(Germany), 175(1), 1993.

[250] Daniel T Gillespie. Exact stochastic simulation of coupled chemical reactions. J. Phys. Chem., 81(25):2340–2361, 1977.

[251] Jin Hyuck Heo, Muhammad Jahandar, Sang-Jin Moon, Chang Eun Song, and Sang Hyuk Im. Inverted CH 3 NH 3 Pbi 3 perovskite hybrid solar cells with improved flexibility by introducing a polymeric electron conductor. J. Mater. Chem. C, 5(11):2883–2891, 2017.

[252] Stefan Zeiske, Oskar J Sandberg, Nasim Zarrabi, Wei Li, Paul Meredith, and Ardalan Armin. Direct observation of trap-assisted recombination in organic photovoltaic devices. Nature Communications, 12(1):1–7, 2021.

[253] Armantas Melianas, Fabian Etzold, Tom J Savenije, Frédéric Laquai, Olle Inganäs, and Martijn Kemerink. Photo-generated carriers lose energy during extraction from polymer-fullerene solar cells. Nature communications, 6(1):1–8, 2015.

[254] George Marsaglia and Thomas A Bray. A convenient method for generating normal variables. SIAM review, 6(3):260–264, 1964.

[255] Siegfried Selberherr. Analysis and simulation of semiconductor devices. Springer Science & Business Media, 2012.

[256] Lambert JA Koster, ECP Smits, VD Mihailetchi, and PWM Blom. Device model for the operation of polymer/fullerene bulk heterojunction solar cells. Physical Review B, 72(8):085205, 2005.

[257] Donald L Scharfetter and Hermann K Gummel. Large-signal analysis of a silicon read diode oscillator. IEEE Transactions on electron devices, 16(1):64–77, 1969.

[258] Emlyn Huw Rhoderick. Metal-semiconductor contacts. IEE Proceedings I-Solid-State and Electron Devices, 129(1):1, 1982.

[259] Alexander Wagenpfahl, Daniel Rauh, Moritz Binder, Carsten Deibel, and Vladimir Dyakonov. S-shaped current-voltage characteristics of organic solar devices. Physical Review B, 82(11):115306, 2010.